ELECTRONIC AND MAGNETIC PROPERTIES OF TWO DIMENSIONAL ELECTRON GASES AT COMPLEX OXIDE INTERFACES FOR DIFFERENT POLAR SYSTEMS AND CRYSTALLOGRAPHIC ORIENTATIONS

ANIL ANNADI

M. TECH

(INDIAN INSTITUTE OF TECHNOLOGY KHARAGPUR, INDIA)

A THESIS SUBMITTED

FOR THE DEGREE OF DOCTOR OF PHILOSOPHY IN SCIENCE

DEPARTMENT OF PHYSICS

NATIONAL UNIVERSITY OF SINGAPORE

2013

DECLARATION

I hereby declare that the thesis is my original work and it has been written by me in its entirety. I have duly acknowledged all the sources of information which have been used in this thesis.

This thesis has also not been submitted for any degree in any university previously.

_____

Anil Annadi

24 August 2013

Table of Contents

Acknowledgements

The achievement and final outcome of this thesis work required a lot of assistance and support from many people and I am extremely fortunate to have them all around me during my PhD. Whatever I have achieved through this PhD is all with the assistance and support they provide and I would not forget them all to acknowledge.

First and foremost I would like to express deepest admiration to my supervisor Asst. Prof. Ariando. I thank him for showing continuous support and belief in me. He always gave me a chance to get elevated to come up and I have no second opinion to say that without his support and ideas in designing the projects this research work would not at all have possible to realize and made it within the time frame. Especially the patience he showed towards me during my initial stage of my PhD. I always enjoyed our regular project discussions and his open approach towards the research projects really helped me to design most of the current research work.

I would like to express my gratitude to Prof. T. Venkatesan, greatly called as Prof. Venky for his supervision. Apart from research I must say Prof. Venky's influence in my individual personality development is wordless. I must say that the research experiences in his carrier and tips that he shared with us during the discussion sessions are great valuable and cannot be learned from any textbooks. I used to attend his discussion sessions whenever there is an opportunity to get motivated and to improve myself.

I would like to thank all my Nanocore colleagues for their motivation and kind help during my research work. I appreciate Dr. Gopi and Dr. Arkajit and Dr. Wang Xiao for their moral support during my initial days. The research and interpersonal skills learned from them helped me a lot to pick up the pace in research. A special thanks to Adi putra who associated with me in performing some of experimental works. A personal thank to my colleague Amar with whom I shared most of the research hours and discussions in the Lab. I thank my other

lab collegues Dr.Surajit, Dr.Sinu Mathew, Dr. Abhimanyu, Pranjal and Tarapada. I was very lucky to have them as Post doctoral fellows. I would like to thank my group members Liu Zhiqi, Dr. Wieming, Shengwie Zheng, Dr. Zhen Huang, Yongliang, Teguh, Michal Dykas, Abijit and Harsan Ma. I would like to express gratitude to Dr. Dhar, Dr. Andrivo for their valuable inputs to the research and project discussions.

I am glad to associate with the NUSNNI-Nanocore institute which often described by Prof. Venky as “Bell Core” in Singapore. The research culture in the Institute gave me the liberty to think out of box to design some of my projects. The institute really gave me an opportunity to work closely with distinguished and highly regarded professors in the research community which I believe would have not possible for me without the association with the Nanocore institute. I thank Prof. Hans Hilgenkamp for his valuable inputs in my research projects during his visits to Nanocore. I thank my research collaborators Prof. S. Meakawa, Prof. J. Levy, Prof. J. M. D. Coey, Dr. S. Yunoki, Dr. B. Gu and Dr. Q. Zhang for their support in collaboration works which made my PhD thesis a complete work. I am very thankful for the institute for providing the financial aid all throughout my PhD tenure to participate in many international conferences that gave me an opportunity to present my research work at international level and excel myself. The institute offered me an excellent opportunity to work with various ethnic groups that gave an opportunity to learn different work ethics that helped me personally to improve in all aspects especially to work in and as a group. I thank all the institute staff for the help and support.

The most important driving force of motivation is obviously my family. Being known as home sick guy it was very difficult for me to be in abroad and carry on studies, it was a tough decision to take at that time to do PhD abroad and I thank all my family members who encouraged me for my desire to pursue higher education abroad with no second opinion. Special thanks to my father and sisters who always motivated me and had faith in me that I can do well. Their ever

continuous love and affection showed towards me was made it to complete my PhD.

They may be last in the list but not least, my friends, who are actually a little world for me in Singapore. I express my deepest appreciation towards my dear friends Mahesh, Sudheer, Prashanth, Malli, Girijha, Sandhya, Durga, Chandu, Pawan, Bablu, Satyanarayana, Vinayak, Suresh and Ashok. The journey with them in these 4 years in Singapore has been memorable in my personal life. The discussions regarding to social life, science and research were a great process of learning for me.

Finally I would like to express my thankfulness to National university of Singapore for giving me this opportunity to pursue the PhD degree and for its financial aid provided during the PhD tenure and for the conferences. Special thanks especially to the department of Physics which provided me an opportunity to carry out the research work under various grant programs and utilizing various facilities.

Abstract

Owing to structural, charge, orbital or spin reconstruction at their interfaces, complex oxide heterostructures have emerged as an avenue for creation of exotic phenomena that are absent in their bulk constituents. One of the most exciting among such heterostructures is the interface between two band insulators $LaAlO_3$ and $SrTiO_3$. When these two perovskite type oxides are brought together along the (100) orientation, a highly conducting two dimensional electron gas (2DEG) emerges at their interface. Further, this interface has also been shown to host various exotic phases such as tunable metal-insulator ground state, superconductivity and magnetism. Thus far these entire novel properties that are discussed at the $LaAlO_3/SrTiO_3$ interfaces have been studied extensively based on the interfaces constructed using ABO_3 type polar $LaAlO_3$ on non-polar (100)-oriented $SrTiO_3$ only. The main objective of this thesis is to explore the electronic and magnetic properties of the two dimensional electron gases at such interfaces along different crystallographic orientations and in various combinations of polar/non-polar oxide interfaces, providing us further understanding of the nature of carrier confinement, magnetic interactions and origin of conductivity of the two dimensional electron gases.

In order to understand the nature of magnetic ordering, the $LaAlO_3/SrTiO_3$ (100) interfaces were studied under various growth parameters such as LAO layer thickness and oxygen pressure during the growth. The nature of magnetic interactions at the interface is investigated through specific magneto transport measurements such as anisotropic magneto resistance (AMR) and planar Hall effect (PHE). A specific fourfold oscillation in the AMR and the observation of large PHE is observed. The carrier confinement effects of electron gas on the AMR are evaluated and it was found that the fourfold oscillation appears only for the case of 2DEG samples while it is twofold for the 3D conducting samples. These confinement effects suggest that the magnetic interactions are predominant at the interface, and further indicate the in-plane nature of magnetic ordering

possibly arising from Ti $3d_{xy}$ orbitals. Further the AMR behaviour is found sensitive to the external gate electric field which offers tunability of magnetic interactions via gate electric fields. The gate tunability of the magnetic interactions infers the significant role of spin-orbit coupling at these interfaces. As the fourfold oscillation fits well to the phenomenological model for a cubic symmetry system, this oscillation behaviour is attributed to the anisotropy in the magnetic scattering arising from the interaction of itinerant electrons with the localized magnetic moments coupled to the crystal symmetry via spin-orbit interaction. The tunability of magnetic interactions with external electric fields via anisotropic magneto resistance shows the potential of the $LaAlO_3/SrTiO_3$ interface system for spin-based electronics.

The role of the A and B cations of the ABO_3 type polar layer on interface characteristics has been investigated using various combinations of polar/non-polar oxide ($NdAlO_3/SrTiO_3$, $PrAlO_3/SrTiO_3$ and $NdGaO_3/SrTiO_3$) interfaces which are similar in nature to the $LaAlO_3/SrTiO_3$ interface. Significantly, these interfaces were found to support formation of 2DEG. It is further understood that the combined effects of interface strain provided by the lattice mismatch of polar layers to $SrTiO_3$ and electron correlations arising from octahedral distortions in $SrTiO_3$ appear to control the characteristics of the 2DEG. Further, a metal-insulator transition in conductivity is observed for $NdAlO_3/SrTiO_3$ interfaces with $NdAlO_3$ film thickness. This suggests that polarization discontinuity induced electronic reconstruction could also be the possible origin of conductivity for these interfaces. The $NdAlO_3$ film thickness dependent transport study of 2DEG at $NdAlO_3/SrTiO_3$ interfaces reveals an emergence of two-dimensional variable range hopping at low temperatures, suggesting the strong role of interface strain in governing its electronic properties.

As previously discussed, the occurrence of 2DEG at the $LaAlO_3/SrTiO_3$ interface is believed to be driven by polarization discontinuity leading to an electronic reconstruction. In this scenario, the crystal orientation plays an important role and no conductivity would be expected, for example for the interface between $LaAlO_3$

and (110)-oriented $SrTiO_3$, which should not have a polarization discontinuity. Here we demonstrate that a high mobility 2DEG can also arise at this $LaAlO_3/SrTiO_3$ (110) interface. The (110) interface shows transport property and $LaAlO_3$ layer critical thickness for the metal-to-insulator transition similar to those of (100) interfaces, but with a strong anisotropic characteristic along the two in-plane crystallographic directions. This anisotropic behaviour is further found to be sensitive to the oxygen growth condition. Density functional theory calculation reveals that electronic reconstruction, and thus conductivity, is still possible at this (110) interface by considering the energetically favourable (110) interface structure, *i.e.* buckled TiO_2/LaO, in which the polarization discontinuity is still present. Along with lifting the crystallographic constraint, the observed highly anisotropic nature of the 2DEG at $LaAlO_3/SrTiO_3$ (110) interface is potential for anisotropic superconductivity and magnetism, and offers a possibility for 1-D device concepts. The nature of spin-orbit interaction was investigated at the $LaAlO_3/SrTiO_3$ (110) interface through magneto conductance analysis in the weak localization regimes. It was found that a spin relaxation mechanism is operating at this interface, and the Rashba type spin-orbit interaction. However it was also observed that a significant anisotropy in spin-orbit coupling is present for the (110) interfaces with respect to crystallographic directions. Further significant difference in strength of spin-orbit interaction between the in-plane and out-of-plane external magnetic fields is observed, suggesting multiple contributions for spin-orbit interactions.

Patterning of 2DEG at the $LaAlO_3/SrTiO_3$ remains as one of the key issues in transforming this interface to device applications. The potetial of using energetic ion beam exposure for structuring the interface was investigated. It was found that this method can be utilized to manipulate the conductivity at the $LaAlO_3/SrTiO_3$ interface by inducing localizations, enabling us to create an insulating ground state through the localization of mobile electrons via structural changes in $SrTiO_3$. These structural changes in $SrTiO_3$ were revealed by the appearance of first-order polar TO_2, and TO_4 vibration modes associated with Ti-O bonds in the Raman spectra. A resist-free single step direct patterning of conducting oxide interface

$LaAlO_3/SrTiO_3$ utilizing ion beam exposure is demonstrated, which is of importance for oxide electronics.

List of publications

[1] A.Annadi, Q. Zhang, X. Renshaw Wang, N. Tuzla, K. Gopinadhan, W.M. Lu, A. Roy Barman, Z.Q. Liu, A. Srivastava, S. Saha, Y.L. Zhao, S.W. Zheng, S. Dhar, E. Olsson, B. Gu, S. Yunoki, S. Maekawa, H. Hilgenkamp, T. Venkatesan, Ariando*, *Anisotropic two dimensional electron gas at the $LaAlO_3/SrTiO_3$ (110) interface.* **Nature Communications 4, 1838 (2013)**. Selected as **Science Magazine Editors' Choice**: Jelena Stajic, *Unexpected Conductivity*, **Science** 14 June 2013: **Vol. 340 no. 6138 p. 1267**.

[2] S. Mathew*, A. Annadi*, T. Asmara, T. K. Chan, K. Gopinadhan, A. Srivastava, Ariando, M. B. H. Breese, A. Rusydi, T. Venkatesan, *Tuning the interface conductivity of $LaAlO_3/SrTiO_3$ using ion beams: An approach for the oxide patterning*. (**Equal contribution**), **ACS Nano, DOI: 10.1021/nn4028135, (In press).**

[3] A. Annadi, Z. Huang, K. Gopinadhan, X. Wang, A Srivastava, Z.Q. Liu, H. Ma, T. Sarkar, T. Venkatesan, Ariando*, *Anisotropic Magneto Resistance and Planar Hall effect at the LAO/STO Heterointerfaces: Effect of Carrier Confinement on Magnetic Interaction.* **Physical Review B 87, 201102 (2013) - Rapid Communications**.

[4] A. Annadi, A. Putra, A. Srivistava, X. Wang, Z. Huang, Z.Q. Liu, T. Venkatesan, Ariando*, *Evolution of variable range hopping in strongly localized 2DEG at the $NdAlO_3/SrTiO_3$ heterostructures.* **Applied Physics Letters, 101, 231604 (2012)**.

[5] A. Annadi, A. Putra, Z.Q. Liu, X. Wang, K. Gopinadhan, Z. Huang, S. Dhar, T. Venkatesan, Ariando*, *Electronic correlation and strain effects at the interfaces between polar and nonpolar complex oxides.* **Physical Review B 86, 085450 (2012)**.

[6] A. Roy Barman, A. Annadi, K. Gopinadhan, W.M. Lu, Ariando, S. Dhar, T. Venkatesan*, *Interplay between carrier and cationic defect concentration in ferromagnetism of anatase $Ti_{(1-x)}Ta_{(x)}O_{(2)}$ thin films.* **AIP Advances 2, 012148 (2012)**.

[7] Ariando, X. Wang, G. Baskaran, Z.Q. Liu, J. Huijben, J.B. Yi, A. Annadi, A. Roy Barman, A. Rusydi, S. Dhar, Y.P. Feng, J. Ding, H. Hilgenkamp, T. Venkatesan, *Electronic Phase Separation at the $LaAlO_3/SrTiO_3$ Interface.* **Nature Communications 2, 188 (2011)**.

[8] X. Wang, W.M. Lu, A. Annadi, Z.Q. Liu, S. Dhar, K. Gopinadhan, T. Venkatesan, Ariando*, *Magnetoresistance of 2D and 3D Electron Gas in $LaAlO_3/SrTiO_3$ Heterostructures: Influence of Magnetic Ordering, Interface Scattering and Dimensionality*. **Physical Review B 84, 075312 (2011)**.

[9] A. Roy Barman, M.R. Motapothula, A. Annadi, K. Gopinadhan, Y.L. Zhao, Z. Yong, I. Santoso, Ariando, M.B.H. Breese, A. Rusydi, S. Dhar, T. Venkatesan*, *Multifunctional $Ti_{1-x}Ta_xO_2$: Ta Doping or Alloying?* **Applied Physics Letters, 98, 072111 (2011)**.

[10] Z.Q. Liu, C.J. Li, W.M. Lu, X.H. Huang, Z. Huang, S.W. Zeng, X.P. Qiu, L.S. Huang, A. Annadi, J.S. Chen, J.M.D. Coey, T. Venkatesan, Ariando*, *Origin of the two dimensional electron gas at $LaAlO_3/SrTiO_3$ interfaces- The role of oxygen vacancies and electronic reconstruction.* **Physical Review X 3, 021010 (2013)**.

[11] Z.Q. Liu, D.P. Leusink, Y.L. Zhao, X. Wang, X.H. Huang, W.M. Lu, A. Srivastava, A. Annadi, S.W. Zeng, K. Gopinadhan, S. Dhar, T. Venkatesan, Ariando*, *Metal-Insulator Transition in $SrTiO_{3-x}$ Thin Film Induced by Frozen-out Carriers.* **Physical Review Letters, 107, 146802 (2011)**.

[12] Z.Q. Liu, W.M. Lu, X.Wang, B. M. Zhang, Z. Huang, K. Gopinadhan, S. W. Zeng, A. Annadi, T. Venkatesan, Ariando*, *Tailoring electronic properties of the $SrRuO_3$ thin films in $SrRuO_3/LaAlO_3$ superlattices.* **Applied Physics Letters, 101, 223105 (2012)**.

[13] S.W. Zeng, X. Wang, W.M. Lu, Z. Huang, M. Motapothula, Z.Q. Liu, Y.L. Zhao, A. Annadi, S. Dhar, H. Mao, W. Chen, T. Venkatesan, Ariando*, *Metallic state in La-doped $YBa_2Cu_3O_y$ thin films with n-type charge carriers.* **Physical Review B 86, 045124 (2012)**.

[14] Z.Q. Liu, W.M. Lu, X. Wang, A. Annadi, Z. Huang, S.W. Zeng, T. Venkatesan, Ariando*, *Magnetic-field induced resistivity minimum with in-plane linear magnetoresistance of the Fermi liquid in $SrTiO_3$ single crystals.* **Physical Review B 85, 155114 (2012)**.

[15] A. Srivistava, T.S. Herng, S. Saha, B. Nina, A. Annadi, N. Naomi, Z.Q. Liu, S. Dhar, Ariando, J. Ding, T. Venkatesan*, *Coherently coupled ZnO and VO2 interface studied by photoluminescence and electrical transport across a phase transition*. **Applied Physics Letters, 100, 241907 (2012)**.

[16] Z.Q. Liu, Z. Huang, W.M. Lu, K. Gopinadhan, X. Wang, A. Annadi, T. Venkatesan, Ariando*, *Atomically flat interface between a single-terminated*

$LaAlO_3$ substrate and $SrTiO_3$ thin film is insulating. **AIP Advances 2, 012147 (2012)**.

[17] W.M. Lu, X. Wang, Z.Q. Liu, S. Dhar, A. Annadi, K. Gopinadhan, A. Roy Barman, T. Venkatesan, Ariando*, *Metal-Insulator Transition at A Depleted $LaAlO_3/SrTiO_3$ Interface: Evidence for Charge Transfer Variations Induced by SrTiO3 Phase Transitions*. **Applied Physics Letters, 99, 172103 (2011)**.

[18] Z.Q. Liu, D.P. Leusink, W.M. Lu, X. Wang, X.P. Yang, K. Gopinadhan, L.Y. Teng, Y.L. Zhao, A. Annadi, A. Roy Barman, S. Dhar, Y.P. Feng, H.B. Su, G. Xiong, T. Venkatesan, Ariando*, *Resistive Switching Mediated by The Formation of Quasi Conduction Band in A Large Band Gap Insulating Oxide*. **Physical Review B 84, 165106 (2011)**.

[19] Y. L. Zhao, A. Roy Barman, S. Dhar, A. Annadi, M. Motapothula, Jinghao Wang, Haibin Su, M. Breese, T. Venkatesan, and Q. Wang. *Scaling of flat band potential and dielectric constant as a function of Ta concentration in Ta-TiO_2 epitaxial films.* **AIP Advances 1, 022151 (2011)**.

Submitted

[1] A. Annadi, K. Gopinadhan, A. Srivastava, T. Venkatesan, Ariando, *Study on Anomaly transport behavior of 2DEG at the LAO/STO (110) interface: Impact of electric field and structural phase transitions of STO*.

[2] A. Annadi, T. Venkatesan, Ariando, *Investigation of Surface Reconstructions at $SrTiO_3$ (110) Using Reflection High Energy Electron Diffraction (RHEED) Technique*. Procedia Engineering.

[3] K. Gopinadhan*, A. Annadi, Q. Zhang, B. Gu, S. Yunoki, S. Maekawa, Ariando, T. Venkatesan, *Nature of spin orbit coupling at LAO/STO (110) interfaces*. (equal contribution)

[4] T. C. Asmara, A. Annadi, I. Santoso, P. K. Gogoi, A. Kotlov, H. M. Omer, M. Rübhausen, T. Venkatesan, Ariando, A. Rusydi, *Charge transfer mechanisms in $LaAlO_3/SrTiO_3$ revealed by high-energy optical conductivity*.

Conference presentations

1. **ICMAT-2011, Singapore. (Poster presentation:** *Two-dimensional electron gas at the LAO/STO interfaces, crystallographic and strain effects*, received **best poster award**)

2. **International school of oxide electronics-2011, Corsica, France.** (**Poster presentation:** *Unexpected 2-dimensional electron gas at the LAO/STO (110) interfaces*)

3. **APS March meeting-2012, Boston, USA.** (**Oral presentation**: *Unexpected 2-dimensional electron gas at the LAO/STO (110) interfaces*).

4. **World oxide electronics (WOE-19), Apeldoorn, The Netherlands -2012. (Poster presentation:** *Electron correlation and strain effects at polar non polar complex oxide interfaces*).

5. **MRS-Singapore, Singapore, 2012. (Poster presentation:** *Nature of spin-orbit coupling at LAO/STO (110) interface*).

6. **ICMAT-2013, Singapore. (Poster presentation:** *Symmetry and carrier confinement effects on magnetic interactions at LAO/STO interface*).

List of figures

at 300 K, here δn_s defined as the difference in n_s of as-deposited and irradiated sample sections (($\delta n_s = n_{s\ (as\text{-}deposited)} - n_{s\ (irradiated)}$).

Figure 8.3: Magnetoresistance (MR) of the (8 uc) $LaAlO_3/SrTiO_3$ sample sections with different proton fluences: (a) Out of plane MR at 2 K for different ion fluences. (b) Out of plane MR at 2, 5, 10 and 20 K for the sample section irradiated with 2×10^{17} ions cm^{-2}. (c) In-plane and out of plane MR measured for the sample section in (b) at 2 K. (d) Angle dependent anisotropic magneto resistance measurement for the corresponding sample portion.

Figure 8.4: Raman spectrum obtained for (8 uc) LAO/STO interface sample portions irradiated with different proton ion doses and as deposited portion. The Transverse TO_2 and TO_4 modes at 165 and 540 cm^{-1} and a longitudinal LO_4 mode at about 800 cm^{-1} emerges with respect to proton ion dose respectively.

Figure 8.5: Raman spectrum obtained for bare STO sample portion with and without irradiation.

Figure 8.6: Raman spectrum obtained for LAO/STO sample portions irradiated with different proton ion doses. Schematic represents the 500 μm patterns line made with different proton ion dose.

Figure 8.7: Raman spectrum mapped for a TO_4 mode at 540 cm^{-1} for patterned lines (500 μm) of LAO/STO sample portions irradiated with different proton ion doses showing a clear intensity difference with ion irradiation dose. The resistance behaviour with temperature measured for the corresponding patterned lines displaying the metal to insulator transition with increase in proton ion irradiation dose.

Fugure 8.8: (a) Scanning electron microscopy (SEM) image of the patterned LAO/STO sample: (a) using a 2 MeV proton fluence of 6×10^{17} ions cm^{-2} with a mask of Hall bar geometry (in this case proton beam (6×10^{17} ions cm^{-2}) was irradiated on to the sample using a tensile metal mask; the irradiated portion locally become insulating allows patterning the structure). (b) 500 keV helium ions at a fluence of 1×10^{16} ions cm^{-2} with a gold mask of size 5 μm.

List of symbols and abbreviations

$\boldsymbol{\mu}$	Mobility
$\boldsymbol{n_s}$	Carrier density
$\boldsymbol{\theta}$	Angle
$\boldsymbol{\Omega}$	Ohms
$\boldsymbol{Å}$	Angstrom
□	Square area
ρ	Resistivity
$\boldsymbol{R_s}$	Sheet resistance
V	Volts and Voltage
Vg	Gate voltage
$\boldsymbol{I}$	Current
$\boldsymbol{H}$	Magnetic field
T	Temperature
E	Electric field
e	Electron charge
ε	Dielectric constant

uc Unit cell

RHEED Reflection high energy electron diffraction

PLD Pulsed laser deposition

AFM Atomic force microscopy

PPMS Physical property measurement system

VRH Variable range hopping

AMR Anisotropic magneto resistance

PHE Planar Hall effect

P_{O2} Oxygen partial pressure

Chapter 1

Introduction

1.1. Introduction to complex oxides

Most of the current electronic and optical devices are based on semiconductor technology which has current density as the only knob for tunability. To keep pace with the growing demand for smarter and faster electronics, miniaturization of this technology is needed as to be able to incorporate more and more logics in a single device. However, this trend at some point will hit a brick wall of atomic size and quantum limit. It is widely suggested that this limitation may be overcome by introducing multifunctionalities and thus providing multi knobs (such as magnetism and ferroelectricity) in the device. This thus calls for the challenge to look for new materials with multifunctionality.

One class of such materials is the metal-oxides, which exhibit properties with a wide spectrum of tunability, such as from optically opaque to transparent, electrically insulator to metallic and superconducting, dielectric to ferroelectric and diamagnetic to ferromagnetic. Most importantly in oxide materials these properties can co-exist, and some of these properties can be cross-coupled that can lead to multi-functional devices. In fact most materials found in nature are oxides, which are crystals made of oxygen and at least one other element bound together with regular spacing. A few most common examples are silica (silicon and oxygen), rust (iron and oxygen), and porcelain (aluminum, silicon, oxygen, and water). A sub class of oxide materials further called complex oxides exhibits some truly exceptional properties for example high temperature superconductivity [1], which is the ability to transport the electricity with no power loss even up to elevated temperatures, although much lower than the freezing temperature of water.

What make complex oxides so unique is the large variety of ways the oxygen and other atoms can be packed together and the tendency for the electrons to interact with each other results in the strong electron correlation nature in these oxides. Unlike free electron systems here the electrons are no more individual and they are correlated with coulomb interactions, meaning that the electrons may act collectively instead of on their own. These properties are not present in metals like gold or the semiconductors used to run modern day computers.

Various methods have been developed to further manipulate the properties in complex oxides via tuning the electronic correlations. Some examples of novel properties that have been introduced through manipulating electronic correlations are the superconductivity in Cu-based oxides [1], colossal magneto resistance (CMR) in Mn-based oxides [2]. The latter can be introduced by manipulating the valence of the Mn transition metal. Furthermore, complex oxides can respond actively to external stimuli for example to elemental doping [1], magnetic field [2], electric field [3] and strain [4] showing the potential for creating new functionalities for development of oxide based devices. In recent years, the focus shifted more to the hetero structures and interfaces constructed from various combinations of oxide materials that showed fascinating emergent phenomena [5, 6] such as low dimensional superconductivity [7], magneto-electric coupling [8] and quantum Hall effect [9] making oxide heterostructures and interfaces a new avenue for creating novel states.

1.2. Novel phenomena at oxide interfaces

With the advancement in the technology of thin film growth, the control for creating interfaces between dissimilar materials has reached an unprecedented level of perfection at atomic level. This coupled with the sensitivity of charge, spin, and orbital degree of freedom to the breaking of their symmetry and atomic structure at the interface, makes combination of various complex oxide materials a new playground for creating physical phenomena which are not present in its constituent materials. In these artificial heterostructures, electronic, orbital, and

atomic reconstructions driven by charge transfer, exchange interactions, and strain effects can lead to exotic electronic states that are bound to the interface [10, 11, 12]. The engineering and/or spontaneous emergence of unique material properties at the interfaces and their co-existance with various other material properties made these oxide interfaces a possible candidate for multifunctional oxide electronics.

Over the years, numerous combinations of oxide heterostructures and interfaces have been investigated under different parameters. Recent examples are the emergence of ferromagnetism at the interface between antiferromagnetic (AF) insulators $LaFeO_3$ and $LaCrO_3$ [13]; in this case the d orbital coupling across the interface is shown to be the origin for the emergence of the magnetism. Further examples are magnetism at the interface of $CaMnO_3$ (AF insulator) and $CaRuO_3$ (paramagnetic metal) [14] and magnetism at $LaMnO_3$ (AF) /$SrTiO_3$ (diamagnetic) interface [15]; a charge transfer mechanism across the interface is shown to be the responsible mechanism for the above observed phenomena. The orbital reconstructions at the interface between $(Y,Ca)Ba_2Cu_3O_7$ and $La_{0.67}Ca_{0.33}MnO_3$ [16], colossal ionic conductivity at interfaces of epitaxial ZrO_2:Y_2O_3/$SrTiO_3$ [17], superconducting temperature enhancement at the interface between La_2CuO_4 and $La_{1.55}Sr_{0.45}CuO_4$ [18], and dielectric constant enhancement at ultrathin $PbTiO_3$ [19] are some more examples of different intriguing properties observed at complex oxide interfaces which further augment the spectrum of multifunctional oxides.

Amongst all, the recent discovery of two-dimensional electron gases (2DEG) with high mobility reported at $SrTiO_3$ [20, 21] and ZnO [22] based systems further set examples for truly emergent phenomena that can be realized in oxide materials. The first of such types of 2DEG is demonstrated at the atomically abrupt interface between two band perovskite insulators $LaAlO_3$ and $SrTiO_3$ by Ohtomo *et al.* [21] and then at the interface of Mg doped ZnO/ZnO heterostrucutre [22].

In particular, the observation of the 2DEG with high mobility at the interface between two insulators $LaAlO_3$ and $SrTiO_3$ is extremely fascinating because it

demonstrated a novel path way to generate new properties at the interfaces that do not exist in either of the bulk materials. In subsequent years this $LaAlO_3/SrTiO_3$ interface system is further shown to accommodate several unusual phenomena such as superconductivity and magnetism that made this system a novel play ground to explore the interface physics.

1.3. Scope and outline of the thesis

The main aim of this thesis work is to investigate and explore the $LaAlO_3/SrTiO_3$ (defined as LAO/STO in later part of discussions) and proto-type heterointerfaces in new directions; investigating new combinations of oxide interfaces and to tune the electronic properties in novel approaches. Ever since the discovery of 2DEG at the LAO/STO interface in 2004, a lot of significant and exciting results have been demonstrated experimentally. However, the understanding of underlying physics and origin of most of the properties such as origin of conductivity and magnetism is lacking which remained as puzzles even till now owing to the complexness of interface physics. To fully utilize these materials, exploration of the properties in novel device concepts, a clear knowledge about the origin and underlying physics of various properties is essential.

Considering the broad scope of research on LAO/STO interface, here we particularly focus on the topics related to the origin of conductivity through varius combinations of oxide interfaces, the nature of magnetic interactions and spin-orbit interaction through electro and magneto transport, and to develop an easy way to pattern the 2DEG at the LAO/STO interface for device concepts. The approach adapted to these research directions and the outline of the thesis work is discussed below.

Since its discovery in 2004, the origin of the 2DEG is still under lively debate due to the complexness of the interface physics, although it is widely believed that the conductivity relates to a concept of polarization discontinuity at the interface where defects also shown to influence the conductivity. To address the issue and better provide further insights for the understanding of the mechanism, the

interface system is explored using different configurations, including using various crystallographic orientations and different oxide layers which are similar in nature to LAO/STO. This problem is addressed in two specific approaches, in crystallographic point of view by investigating the LAO/STO interface along different orientations specifically (100) and (110), and investigation of various combinations of polar/non-polar oxide ABO_3/STO (A= La, Nd, Pr, B= Al, Ga) interfaces.

One of the exciting ongoing research areas in LAO/STO based interfaces is the exploration of the unconventional magnetic ordering and spin-orbit interaction at the interface. Several experimental techniques reveal the presence of magnetism at the interface; however there is little knowledge about the nature of the magnetic interactions. The dilute nature of the magnetism somewhat limit the probing capability of the magnetic property using conventional magnetization techniques. In this thesis work the nature of magnetic interactions are investigated with more specific electro and magneto transport and electric field measurements. Further the influence of various interface configurations and parameters such as dimensionality and spin-orbit interaction effects on such magnetic interactions are examined.

The structuring and patterning of the 2DEG at the LAO/STO interface system has remained as one of the challenges towards interface device fabrication due to the difficulty in accessing the buried interface. Thus far all the approaches employed to pattern the 2DEG involved with multiple step processes during the film growth. The etching techniques using focused ion beam involving heavy ions are also undesired for the patterning of these interfaces due to the creation of defect induced conductivity in STO. Highlighting the fundamental issue to create a pattern of these conducting regimes involves with achieving insulating states locally, in this work the properties of LAO/STO interface are investigated using the low Z-proton beam irradiation technique and the results shows that this method can be utilized to manipulate the conductivity at the LAO/STO. A resist-

free single step direct patterning of conducting oxide interface of LAO/STO utilizing ion beam exposure has been explored.

During this thesis work, in the course of investigation of above mentioned key issues, I was able to resolve, discover and explain some new and important aspects of the LAO/STO interface such as the strong localization behavior, the anisotropic nature, and the structural property of the STO on the conductivity of 2DEG. These results are discussed herein this thesis work.

These different topics are divided into chapters and are listed below. The literature review related to LAO/STO based interface system is presented in chapter 2 and the experimental techniques used for thin film fabrication and characterization are discussed in chapter 3. Chapter 4 to chapter 8 discusses the experimental results of this thesis work. The summary of the thesis work and scope of future work are discussed in chapter 9.

Chapter 2

In this chapter a detailed literature review for the LAO/STO interface system is presented. The literature review discusses various aspects of the LAO/STO interface system that includes the origin for the high mobility conduction, emergent novel phenomena at LAO/STO the interface and demonstrated device concepts for the technological applications. Here I also discuss perovskite type oxide materials, and basic properties of commonly known perovskite oxides such as $SrTiO_3$, $LaAlO_3$ and $BaTiO_3$ are presented.

Chapter 3

This chapter gives a brief description to various experimental techniques that are employed for characterization of the samples. I will discuss the thin film growth methodology that includes the pre, post-deposition steps and basic thin film characterization results. Further a brief background theory for various types of experimental methods is also presented.

Chapter 4

This chapter describes the growth and properties of LAO/STO (100) interface investigated under various conditions such as thickness of LAO layer and growth oxygen pressure. The magnetic origin at the interface is probed by more specific magnetic measurements such as anisotropic magneto resistance (AMR) and planar Hall effect (PHE). These are further performed with respect to dimensionality of conducting channel, electric field and growth oxygen pressure. Interestingly, the evolution of fourfold oscillation is observed in AMR for two dimensional systems. From the experimental observations, it is shown that the magnetic interactions are very strong near the interface and electron orbital occupancies are very much preferred near the interface.

Chapter 5

Thus for studies on polar/nonpolar oxide interfaces have been carried out extensively which involve a polar $LaAlO_3$ layer. In this study, the role of the A and B cationic sites of the ABO_3 type polar layer investigated by preparing various combinations of polar/nonpolar ($NdAlO_3/SrTiO_3$, $PrAlO_3/SrTiO_3$ and $NdGaO_3/SrTiO_3$) oxide interfaces which are similar in nature to LAO/STO interface. The experimental results illustrated that the properties of the formed 2DEG such as carrier density and mobility can be controlled by electronic correlations and strain at the interface offered by these polar layers. The highly mismatch $NdAlO_3/SrTiO_3$ interface is further explored under various parameters such as $NdAlO_3$/ layer thickness and deposition pressure. The results show a strong localizion for the 2DEG with thickeness of $NdAlO_3$ layers and the magneto transport reveals an evolution of variable range hopping transport in this strongly localized regime.

Chapter 6

This chapter reports the growth and properties of the LAO/STO interface grown on (110) oriented STO substrate. The experiments demonstrate the formation of

high mobility 2DEG at the interface. The LAO/STO (110) interface exhibits a metal-insulator transition with a LAO critical thickness of 4 unit cells. Structural analysis and theoretical calculations were performed in order to understand the origin of this unexpected conductivity at the (110) interface. Density functional theory calculation reveals that electronic reconstruction, and thus conductivity, is still possible at this (110) interface by considering the energetically favourable (110) interface structure. The results are compared and contrasted with the (100) interface, where the (110) interfaces display a strong crystallographic anisotropy in conductivity. The anisotropic character of the 2DEG is investigated with respect to the growth pressure, and electric field effect. The (110) interfaces were further showed the trans-conductance charecteristics similar to field effect transistor.

Chapter 7

This chapter reports proton beam irradiation studies on the properties of 2DEG at the LAO/STO (100) interface. In this study, the samples of LAO/STO were selectively irradiated with various proton beam fluences. The transport properties reveal that as the ion beam fluence increases the conducting state can be transformed into an insulating state above a critical ion fluence irradiation. This metal to insulator transition is induced by the localization of mobile electrons because of structural changes in STO lattice, revealed by Raman spectroscopy measurements. In the irradiated regime the centro-symmetry of the STO is broken which is evidenced by the observation of TO_2 and TO_4 vibration modes in Raman spectroscopy which corresponds to Ti-O bonds. The ability to create insulating ground state locally in the conducting oxides demonstrates a novel way to structure the buried conducting interface without any extra etching or intermediate lithography steps.

Chapter 8

This chapter discusses the nature of spin orbit interaction at the LAO/STO (110) interfaces. The intrinsic anisotropy present in the (110) interface system is further expected to influence the spin-orbit interaction strength at the interface. The stenght of the spin-orbit interaction is investigated through magneto transport studies in the weak localization regime with gate elelctric field. Measuremets were carried out on LAO/STO (110) interfaces and it is found that the spin-orbit strength is significantly different, and shows anisotropy with respect to the crystallographic directions. The in-plane and out-of-plane magnetic field dependence magneto resistance measurement results reveal that there is an additional contribution to the Rashba spin-orbit interaction.

Chapter 9

This final chapter summarizes the important results and outcome of the thesis work. Finally, the outlook towards the challenge for the future work in this field of oxide interfaces will be discussed.

References:

[1] M. K. Wu, J. R. Ashburn, C. J. Torng, P. H. Hor, R. L. Meng, L. Gao, Z. J. Huang, Y. Q. Wang, and C. W. Chu, "Superconductivity at 93K in a new mixed-phase Y-Ba-Cu-O compund system at ambient pressure," *Physical Review Letters*, 58, 908-910 (1987).

[2] S. Jin, T. H. Tiefel, M. Mccormack, R. A. Fastnacht, R. Ramesh, and L. H. Chen, "Thousandfold change in resistivity magnetoresistive La-Ca-Mn-O films," *Science*, 264, 413-415 (1994).

[3] C. H. Ahn, J.-M. Triscone, and J. Mannhart, "Electric field effect in correlated oxide systems," *Nature*, 424, 1015-1018 (2003).

[4] K. J. Choi, M. Biegalski, Y. L. Li, A. Sharan, J. Schubert, R. Uecker, P. Reiche, Y. B. Chen, X. Q. Pan, V. Gopalan, L.-Q. Chen, D. G. Schlom, and C. B. Eom, "Enhancement of ferroelectricity in strained $BaTiO_3$ thin films," *Science*, 306, 1005-1009 (2004).

[5] H. Y. Hwang, Y. Iwasa, M. Kawasaki, B. Keimer, N. Nagaosa, and Y. Tokura, "Emergent phenomena at oxide interfaces," *Nature Materials*, 11, 103-113 (2012).

[6] J. Chakhalian, A. J. Millis, and J. Rondinelli, "Whither the oxide interfaces," *Nature Materials*, 11, 92-94 (2012).

[7] K. Ueno, S. Nakamura, H. Shimotani, A. Ohtomo, N. Kimura, T. Nojima, H. Aoki, Y. Iwasa, and M. Kawasaki, "Electric-field-induced superconductivity in an insulator," *Nature Materials*, 7, 855–858 (2008).

[8] H. Yamada, Y. Ogawa, Y. Ishii, H. Sato, M. Kawasaki, H. Akoh, and Y. Tokura, "Engineered interface of magnetic oxides," *Science*, 305, 646–648 (2004).

[9] Y. Kozuka, A. Tsukazaki, D. Maryenko, J. Falson, S. Akasaka, K. Nakahara, S. Nakamura, S. Awaji, K. Ueno, and M. Kawasaki, "Insulating phase of a two-dimensional electron gas in $Mg_xZn_{1-x}O$/ZnO heterostructures below $\nu = 1/3$," *Physical Review B*, 84, 033304 (2011).

[10] Y. Tokura, and N. Nagaosa, "Orbital physics in transition-metal oxides," *Science*, 288 (5465), 462-468 (2000).

[11] E. Dagotto, and Y. Tokura, "Strongly correlated electronic materials: present and future," *MRS Bulletin*, 33, 1037–1045 (2008).

[12] P. Zubko, S. Gariglio, M. Gabay, P. Ghosez, and J.-M. Triscone, "Interface physics in complex oxide heterostructures," *Annual Review of Condense Matter Physics*, 2, 141 (2011).

[13] K. Ueda, H. Tabata, and T. Kawai, Ferromagnetism in $LaFeO_3$-$LaCrO_3$ superlattices, *Science*, 280 1064 (1998).

[14] K. S. Takahashi, M. Kawasaki, and Y. Tokura, "Interface ferromagnetism in oxide superlattices of $CaMnO_3$/$CaRuO_3$," *Applied Physics Letters*, 79, 1324 (2001).

[15] J. Garcia-Barriocanal, F. Y. Bruno, A. Rivera-Calzada, Z. Sefrioui, N. M. Nemes, M. Garcia-Herna´ndez, J. Rubio-Zuazo, G.R. Castro, M. Varela, S. J. Pennycook, C. Leon, and J. Santamaria, ""Charge leakage" at $LaMnO_3$/$SrTiO_3$ interfaces," *Advanced Materials*, 22, 627–632 (2010).

[16] J. Chakhalian, J. W. Freeland, H.-U. Habermeier, G. Cristiani, G. Khaliullin, M. van Veenendaal, and B. Keimer, "Orbital reconstruction and covalent bonding at an oxide interface," *Science*, 318, 1114-1117 (2007).

[17] J. Garcia-Barriocanal, A. Rivera-Calzada, M. Varela, Z. Sefrioui, E. Iborra, C. Leon, S. J. Pennycook, and J. Santamaria, "Colossal ionic conductivity at interfaces of epitaxial ZrO_2:Y_2O_3/$SrTiO_3$ heterostructures," *Science*, 321, 676-680 (2008).

[18] A. Gozar , G. Logvenov, L. Fitting Kourkoutis, A. T. Bollinger, L. A. Giannuzzi, D. A. Muller, and I. Bozovic, "High-temperature interface superconductivity between metallic and insulating copper oxides," *Nature*, 455, 782-785 (2008).

[19] D. D. Fong, G. B. Stephenson, S. K. Streiffer, Jeffrey A. Eastman, O. Auciello, P. H. Fuoss, C. Thompson, "Ferroelectricity in ultrathin perovskite films," *Science*, 304, 1650-1653 (2004).

[20] A. Ohtomo, D. A. Muller, J. L. Grazul, and H. Y. Hwang, "Artificial charge-modulation in atomic-scale perovskite titanate superlattices," *Nature*, 419, 378-380 (2002).

[21] A. Ohtomo, and H. Y. Hwang, "A high-mobility electron gas at the $LaAlO_3/SrTiO_3$ heterointerface," *Nature*, 427, 423-426 (2004).

[22] A. Tsukazaki, A. Ohtomo, T. Kita, Y. Ohno, H. Ohno, and M. Kawasaki, "Quantum Hall effect in polar oxide heterostructures," *Science*, 315, 1388 (2007).

Chapter 2

The $LaAlO_3/SrTiO_3$ interface

In this section I will discuss perovskite-type ABO_3 oxides, a special type of oxide crystal structure mainly investigated during this research work. This chapter includes the introduction to the crystal structure of perovskites and physical properties of some of the well known perovskite oxides investigated in this thesis. Finally, I will give a detailed literature study of complex oxide interfaces, especially the fascinating LAO/STO oxide interface system which is my main interface system for research.

2.1. ABO_3 perovskite oxides

Perovskite oxide is a class of oxide crystal structure having a chemical formula of ABO_3 with A and B as the cations and comprised of oxygen.

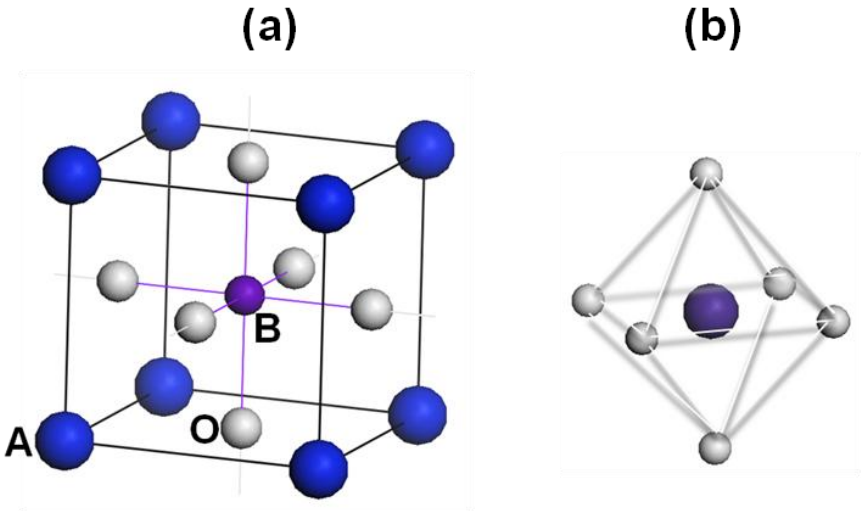

Figure 2.1: (a) Sketch of cubic ABO_3 perovskite structure, (white: oxygen, blue: A-site and purple: B-site atoms respectively). (b) Schematic of the BO_6 octahedron structure where B-atom is surrounded by 6 oxygen atoms.

Perovskite is actually the name of calcium titanium oxide ($CaTiO_3$) mineral named after Russian mineralogist L. A. Perovski [1]. In figure 2.1, an ideal cubic unit cell structure of perovskite is shown. The B-site cation generally occupies the body center position and is caged in oxygen octahedral represented as BO_6 as shown in the figure, whereas A-site cation occupies a corner position of a cube and shared with oxygen. In terms of symmetry, this cubic-symmetry structure has the 'B' cation in a 6-fold coordination, surrounded by an octahedron of oxygen anions, and the 'A' cation in a 12-fold coordination. In this structure A-site cation is generally larger in size than the B-site cation. The atomic sizes of A, B-site cations and their bond angles with oxygen are found to be very crucial and shown to create a wide range of properties.

The nature of A-, B-site cations and combination of both predominantly defines the property of the perovskite type oxides. Owing to the sensitivity of structural transitions associated with crystal structure and subtle manipulation of interactions among charge, orbital, spin degree of freedom, the perovskite materials exhibit a wide class of physical properties. For example, consider the the cases of strontium titanate ($SrTiO_3$) and barium titanate ($BaTiO_3$). $SrTiO_3$ is a quantum paraelectric and insulating material. When the A-site Sr is replaced by Ba atom, then $BaTiO_3$ behaves as ferroelectric material. These emphasize the role of A-site cation to the different properties of these materials. Whereas in another case, when the B-site cation in STO that is Ti is replaced by other transition metal elements such as Manganese (Mn) and rare-earth Ruthenium (Ru), the materials $SrRuO_3$ (para magnetic) and $SrMnO_3$ (anti ferromagnetic) show a magnetic property which arises from the unpaired electron spin. These examples demonstrate new and multi properties may emerge in perovskite oxide by modifying the interplay between the charge, spin and orbital degrees of freedom of the elements.

In this thesis various classes of perovskite-type oxides specially, $SrTiO_3$ and $LaAlO_3$ have been extensively used and investigated. In the following, the basic properties and literature of these different classes of material systems will be introduced.

2.1.1 $SrTiO_3$

$SrTiO_3$ (STO) is a band insulator with a band gap of around 3.2 eV, having a cubic perovskite crystal structure ($a=b=c$) at room temperature with a lattice constant of a= 3.905 Å. It undergoes various low symmetry structural phase transitions at lower temperatures: a cubic to tetragonal phase transition at around 110 K, a tetragonal to orthorhombic phase transition at around 60 K and further orthorhombic to rhombohedral phase transition at around 30 K [2-4]. A schematic of spontaneous lattice distortion of STO various phase transitions is shown in figure 2.2a.

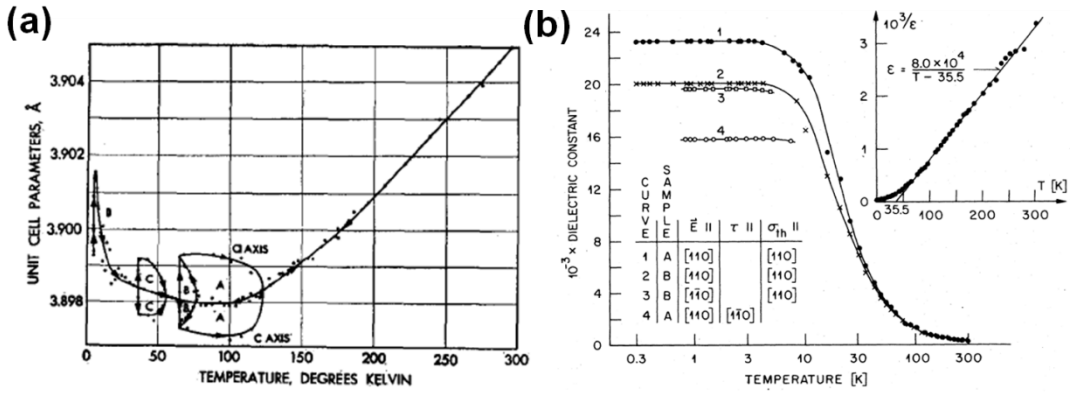

Figure 2.2: (a) Spontaneous lattice distortion of STO with temperature associated with various structural phase transitions. From Lytle *et al*. [2]. (b) Temperature dependece of dielectric constant of STO. From Muller *et al*. [5].

One of the most important properties of the STO is its unusual dielectric response. STO has a dielectric constant value of around 300 at room temperature and increases to a few thousands at low temperatures [5] (shown in figure 2.2b). Further the dielectric response is also shown to be tunable by the electric fields [6]. The large dielectric property of STO made it an ideal material as a gate dielectric in oxide based field effect devices. All these unusual dielectric responses are associated with structural phase transitions at low temperatures. However, eventhough STO undergoes a low symmetry structural phase transitions when it is cooled, it does not show ferroelectric property because of quantum

fluctuations [5] in the material which suppresses the ferroelectric ordering, and thus it is called a quantum paraelectric. This paraelectric state is very sensitive to lattice perturbations, thus subtle changes in lattice structure would create a ferroelectric behavior in STO, the ferroelectricity in STO is shown to be induced by doping [7,8] and strain effects [9,10].

The STO single crystal is a very attractive substrate material for growing oxide thin films due to its lattice match with most of oxides and its high dielectric constant and diamagnetic nature. It has been used as a key substrate for epitaxial growth of high temperature superconducting [11] and magnetic oxide thin films [12]. In recent years, the electronic doping in STO emerged as an exciting area of research in oxides due to the creation of high mobility conduction at the surface and heterostructures involving with STO [13, 14, 15-18]. The charge doping STO is achieved by electrostatic doping, electronic reconstructions and defect creation such as oxygen vacancies. Further advances also include the observation of an unusual optical response of STO where a wide range of photo luminance can be induced by creating defects and oxygen vacancies in the crystal [19].

2.1.2 $LaAlO_3$

$LaAlO_3$ (LAO) is also a band insulator with a wide band gap of 5.6 eV. LAO exists in a rhombohedral phase at room temperature in bulk form and transforms into a cubic phase at temperatures above 875 K [20, 21]. Further, LAO is a dielectric material with dielectric constant of about ~20 at room temperature and it has a low dielectric loss which is suitable for low loss microwave applications [22]. Similar to STO, LAO single crystal has a good lattice match with various perovskite materials usefull for epitaxial growth of oxides thin films such as TiO_2 [23]. The single crystal of LAO can be grown in a pseudo-cubic form with a lattice constant of 3.791 Å. In contrast to STO, LAO show a robust electrically insulating behavior even for defect and vacancy creation in the structure, however, these defects and oxygen vacancies show optical response [24].

2.1.3 $BaTiO_3$

$BaTiO_3$ (BTO) is a special class of perovskite-type crystals with a ferroelectric character. It exhibits a tetragonal structure at room temperature. The tetragonal structure is represented by $a=b\neq c$, where one of the crystallographic axis is elongated or stretched. The structural phase diagram of BTO as a function of temperature is shown in figure 2.3a. BTO undergoes several low symmetric structural phase transitions upon lowering the temperature. Near the low symmetric phase transitions, lattice parameters show a hysteric behaviour in cooling and heating temperature cycles. The ferroelectric property of BTO is associated with a cubic to tetragonal structural phase transition which happens around 120 °C.

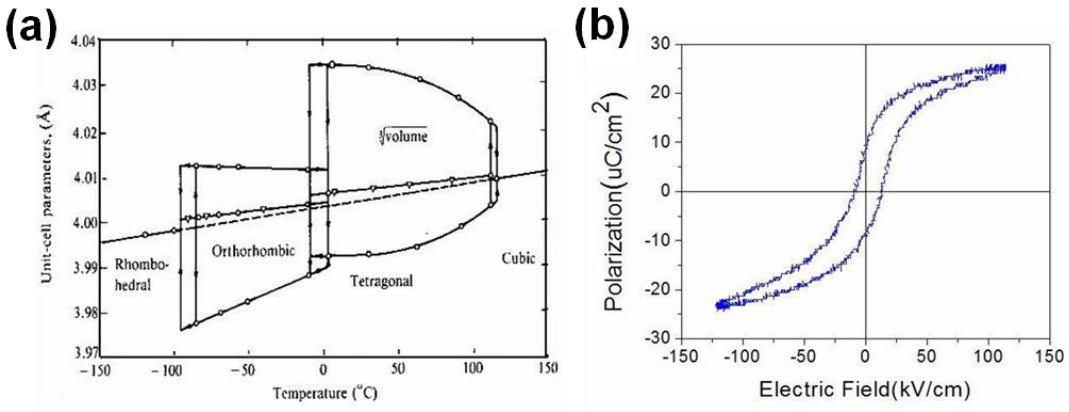

Figure 2.3: (a) Variation of lattice parameters of BTO as a function of temperatura associated with structural phase transitions. From Kingery *et al*. [25]. (b) Typical polarization versus electric field response of BTO thin film, showing the hysterisis a charecteristic of ferroelectric behavior. From Wang *et al*. [26].

In the tetragonal phase, the charge center of Ba atoms moves off-center with respect to Ti sites that create a net charge dipole in a unitcell which is permanent, the coupling of these dipoles further create a spontaneous polarization leading to a ferroelectric property. In bulk case, the room temperature spontaneous polarization of $BaTiO_3$ is about 15 $\mu C/cm^2$ with ferroelectric Curie temperature of

120 °C. A typical ferroelectric behaviour of BTO with electric field is shown in the figure 2.3b [26]. The ferroelectric property in perovskite-type oxides has d a wide range of applications in the ferroelectric based memory, sensors, actuators, and transducers.

All the above oxides are electrically insulators. However there are few oxides which are electrical conductors, the two main examples are $SrRuO_3$ and Nb doped $SrTiO_3$. These conducting perovskite-type oxides are usually used as electronds in all oxide based devices. The other perovskite type oxides investigated in this thesis work are namely, $NaAlO_3$, $PrAlO_3$, $NdGaO_3$, LSAT, Nb doped $SrTiO_3$ and Ba doped $SrTiO_3$. The basic properties of various perovskite oxides are listed in Table.1.

	Crystal structure	Lattice parameters	Electrical property	Magnetic property	Dielectric property
$SrTiO_3$	*cubic*	*a=b=c* *a*= 3.905 *Å*	*insulator*	*diamagnetic*	*paraelectric*
$BaTiO_3$	*tetragonal*	*a=b≠ c* *a*= 3.99 *Å* *c*= 4.04 *Å*	*insulator*	*diamagnetic*	*ferroelectric*
Nb:$SrTiO_3$	*cubic*	*a=b=c* *a*= 3.905 *Å*	*conductor*	*diamagnetic*	
$SrRuO_3$	*orthorombic*	*a ≠b≠ c* *a*= 5.56 *Å* *b*= 5.53 *Å* *c*= 7.84 *Å*	*conductor*	*paramagnetic* *ferromagnetic (<160 K)*	
$LaAlO_3$	*rhombohedral*	*a*= 5.366 *Å* *c*= 13.366 *Å*	*insulator*	*diamagnetic*	*dielectric*
LSAT	*cubic*	*a=b=c* *a*= 3.87 *Å*	*insulator*	*diamagnetic*	*dielectric*
$NdGaO_3$	*orthorombic*	*a*= 5.43 *Å* *b*= 5.50 *Å* *c*= 7.71 *Å*	*insulator*	*paramagnetic*	*dielectric*

Table.1: Crystal structure (at room temperature), lattice parameters, electric, magnetic and dielectric properties of various perovskite oxides. From the data base of Crystec GmbH [27].

2.1.4 Site termination control of ABO_3 oxides

One of the important properties developed relating to the perovskite structure at the atomic level is the possibility to obtain and tailor the perovskite ABO_3 with the specific termination of A-site or B-site on its surface. Along the [001] direction, the ABO_3 perovskite unit cell (uc) can be considered as AO and BO_2 sub-unit-cells or sublayers as shown in figure 2.4a.

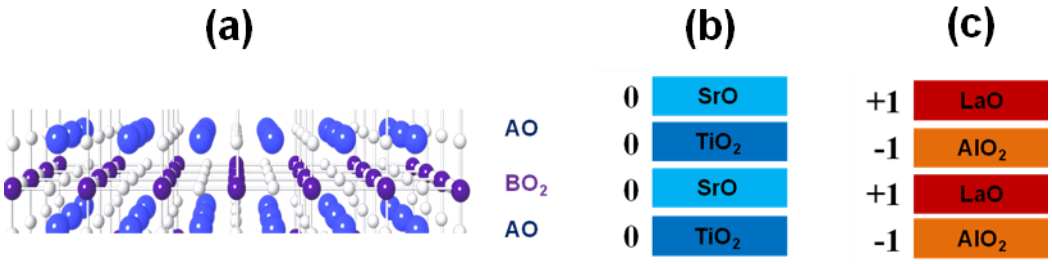

Figure 2.4: (a) Schematic of the ABO_3 perovskite as sub unitcell AO and BO_2 layers along (001) orientation. Sub unitcell representation for (b) a non-polar $SrTiO_3$ and (c) for a polar $LaAlO_3$ [28]. The electrostatic net charge (0, +1, -1) on each sub unitcell layer in both cases is also shown.

These specific terminations of AO and BO_2 can be achieved by suitable chemical etching and thermal treatments of the crystal surfaces, details of treatment methods will be discussed in the subsequent sample preparation section. This single terminated surface has been utilized for layer by layer growth of the thin films with an atomic precision and to prepare abrupt interfaces and hetero structures. Depending on the valence of the cations and the net charge states of these sublayers, a perovskite crystal can be classified as non-polar or polar. For example in the case of the $SrTiO_3$ (100), it can be represented as SrO and TiO_2 sub layers. Here Sr valence is +2 and Ti is +4 and oxygen is -2. Therefore in charge state formalism $SrTiO_3$ can be represented as $Sr^{+2}Ti^{+4}(O^{-2})_3$ with neutral sublayer stacking of $(SrO)^0 - (TiO_2)^0 - (SrO)^0 - (TiO_2)^0$, thus it is called as non-polar. A schematic representation of $SrTiO_3$ as planar charge sheets along (100) is

shown in figure 2.4b. On the other hand for the case of $LaAlO_3$, with La valence is +3 and Al is -3 and oxygen is -2. $LaAlO_3$can be represented as $La^{+3}Al^{+3}(O^{-2})_3$ in charge formalism with a non-neutral sublayer stacking of $(LaO)^{+1} - (AlO_2)^{-1} - (LaO)^{+1} - (AlO_2)^{-1}$ resulting in a polar perovskite along (100) direction (shown in figure 2.4c). Utilizing the specific termination of the perovskite and abruptness of the hetero-structures, various combinations of complex oxide interfaces had been investigated. The best example is the interface between two insulating oxides, the $LaAlO_3/SrTiO_3$ (LAO/STO) interface, which exhibits a 2DEG with high mobility when the interface prepared by depositing $LaAlO_3$ on TiO_2 terminated $SrTiO_3$. In the following, a detailed literature review for the LAO/STO interface is presented, including the basic properties of the LAO/STO interface, mechanisms proposed for the origin of the conductivity, emergent phenomena at the LAO/STO interfaces, and few device concepts demonstrating that the interface system is a potential candidate for oxide electronics.

2.2. 2DEG at the $LaAlO_3/SrTiO_3$ oxide interfaces

In 2004, Ohtomo and Hwang have demonstrated a high mobility 2DEG for the first time at the atomically abrupt interface prepared by depositing $LaAlO_3$ on TiO_2 terminated $SrTiO_3$. After the fascinating discovery of 2DEG at the LAO/STO interface, intensive studies have been conducted to explore different interface material systems, mechanisms and possible devices. The initial studies on the LAO/STO interface are summarized in figure 2.5. Figure 2.5a shows the mobility of the 2DEG at the interface with different sample growth conditions [14]. The mobility values at low temperature are as high as few thousands at low temperature.

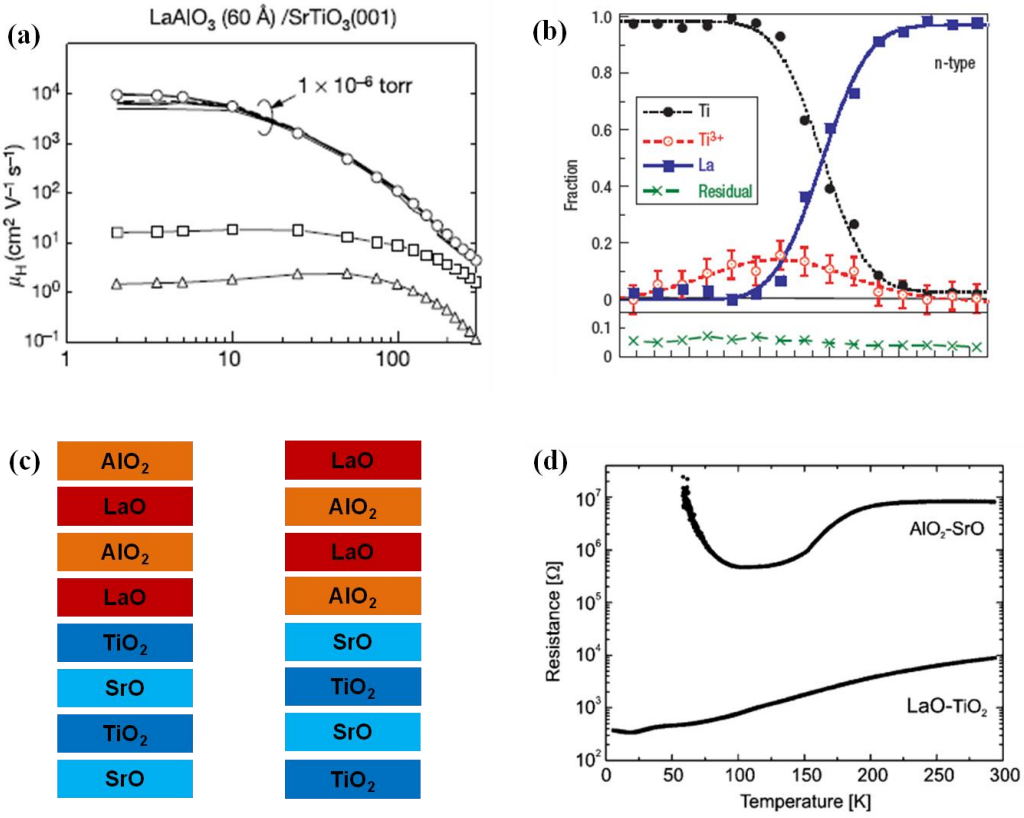

Figure 2.5: (a) The mobility variation with temperature for the 2DEG formed at the LAO/STO interface, here X-coordinate is temperatura in Kelvin. From Ohtomo *et al.* [14]. (b) electron energy loss spectroscopy (EELS) analysis from Transmission electron microscopy (TEM) showing the mixed valence of Ti (3+, 4+) at the interface. From Nakagawa *et al.* [28]. (c) Schematic representation of the two types of LAO/STO interfaces, AlO_2-LaO-TiO_2-SrO interface and LaO-AlO_2-SrO-TiO_2 interface respectively. (d) The experimental observación of conductivity at the interface LaO-TiO_2 and insulating behavior at the AlO_2-SrO interface. From Huijben *et al.* [30] and [14].

Regarding the location of electrons at the interface, transmission microscopy [28] (figure 2.5b) and spectroscopic techniques [29] revealed that electrons occupy Ti sites near the interface through the observation of Ti^{+3} states along with Ti^{+4} [28]. The accecibilty of Ti multivalence (+4 or +3) to accumulate the charge in $SrTiO_3$ allows accommodating 2DEG at the interfaces which further generated the

interest of oxide research community to explore such type of interfaces from various aspects.

In order to understand the interface properties, various combinations of interfaces have been investigated. Specifically, two different types of interfaces are investigated in the LAO/STO system: the AlO_2-LaO/TiO_2-SrO interface and the LaO-AlO_2/SrO-TiO_2 interface (Figure 2.5c). The atomically flat interfaces were constructed by controlling the termination of the STO surface. The remarkable observation from the above experiment is that AlO_2-LaO/TiO_2-SrO interface produces a 2DEG and it is absent in the other structure as shown in Fig. 2.5d [14, 30]. The above results establish that TiO_2 termination is a key to produce a perfect metallic interface, while the interface with SrO termination is shown to produce an insulating interface [31]. The above observation establishes remarkable interface effects achieved by interface termination control. These observations of Ti mixed valence and TiO_2 termination effects can help in understanding the origin of the conductivity at these interfaces.

2.3. Origin of the 2DEG

In spite of extensive research on the LAO/STO interfaces, the origin of high mobility 2DEG is still one of the highly debated topic in the oxide community. Researchers approached the problem of origin of the conductivity with different possible mechanisms. Based on the observations of Ti mixed valence and TiO_2 termination effects at the LAO/STO interface, Nakagawa *et al.* [28] considered the electrostatic states of LAO and STO across the interface and proposed what is widely called the polarization catastrophe model. Besides the polarization catastrophe, other mechanisms are also shown to influence the interface conductivity. The most prominent mechanisms are oxygen vacancies creation [32-34] at the interface during the growth, possible cation intermixing [35] and strain [36] at the interface. In the following a detailed literature review of various mechanisms suggested for the origin is presented.

2.3.1 The polarization catastrophe picture

The model deals with the internal polarizations of the LAO and the STO. The schematic for the polarization catastrophe model is shown in figure 2.6.

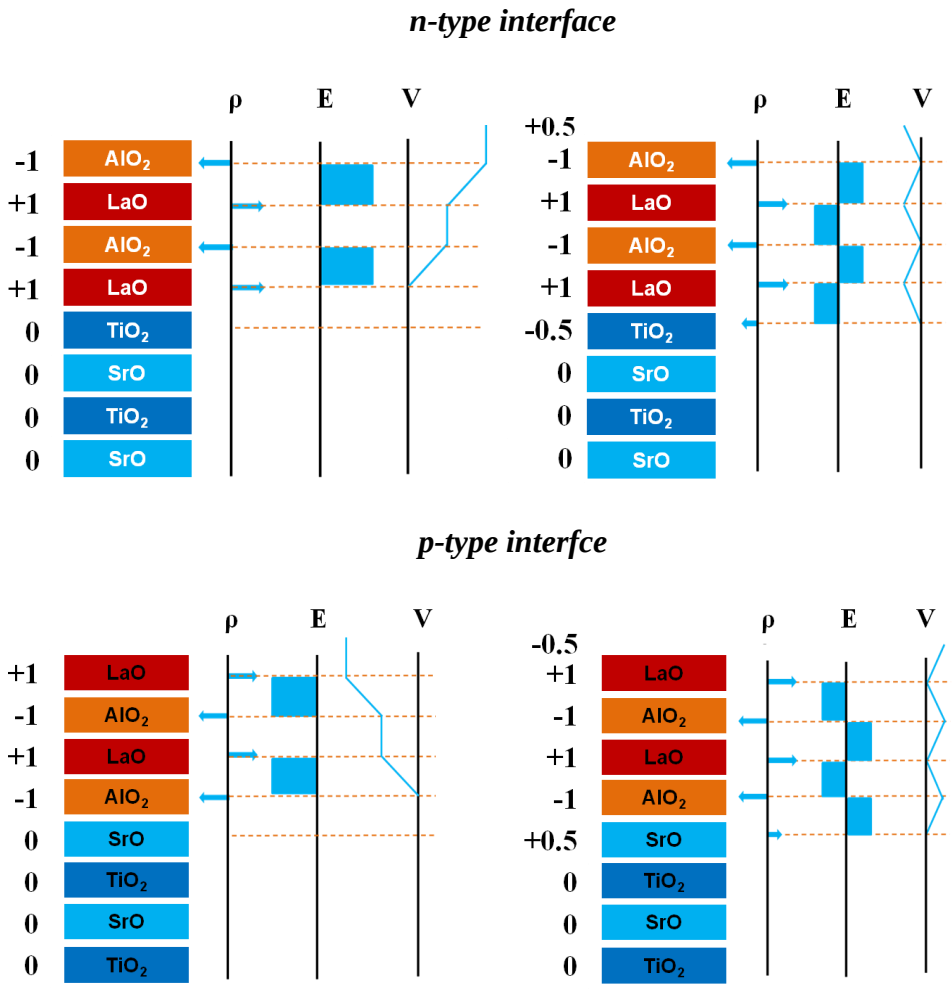

Figure 2.6: The Polarization catastrophe picture for the case of a n-type AlO_2-LaO/TiO_2-SrO interface before reconstruction (top left) and after reconstruction (top right). A case of p-type LaO-AlO_2/SrO-TiO_2 interface before reconstruction (bottom left) and after reconstruction (bottom right). From Nakagawa *et al.* [28].

The LAO along the (100) direction is regarded as a polar material stacked by positively charged sublayers $(LaO)^{+1}$ and negatively charged sublayers $(AlO_2)^{-1}$.

Here, LaO and AlO_2 layers with an alternating net charge in each sub layer actually acts as a charge dipole. In contrast, STO is a non-polar material stacked by the neutral sublayers $(SrO)^0$ and $(TiO_2)^0$ with no intrinsic charge dipole. When the interface structure is AlO_2-LaO/TiO_2-SrO, according to the polarization catastrophe model as illustrated in figure 2.6, due to the polarization discontinuity at the interface, the (001) planes of LAO with alternating net charges (**ρ**) lead to an intrinsic electric field (**E**) in each unit cell of LAO and result in a potential (**V**) build up as the LAO thickness increases, leading to a potential catastrophe in the system. However due to the accessibility of multivalence of Ti states in STO, this potential build up can be avoided by transferring 0.5 electrons per unit cell (uc) to the STO leading to the phenomenon so called electronic reconstruction. In this scenario, after the reconstruction the intrinsic potentials converge within the layers of LAO as shown in the figure. At the AlO_2-LaO/TiO_2-SrO interface, injected electrons results in an n-type conducting interface which is consistent with the experimental observation. On the other hand, for the LaO-AlO_2/SrO-TiO_2 interface structure, the polarization catastrophe model suggests the formation of a p-type interface by creating 0.5 holes per uc at the interface. However the experimental observation shows an insulating interface, in this case a $SrO_{0.75}$ layer is suggested to form as a result of possible atomic reconstruction. Furthermore, experimentally, a robust 4 uc critical thickness of LAO is needed to produce robust 2DEG at the LAO/STO interface by S. Thiel *et al*. [37], this robust metal to insulator transition is further theoretically confirmed by the density functional theory (DFT) calculations [38] through band alignments between LAO and STO. Here it is shown that the electronic states can be generated in STO for the thickness of LAO larger than 4 uc where the built in potential due to the polarization discontinuities exceeds the STO bandgap of 3.2 eV. The conductivity at the interface for LAO larger than 4 uc samples is also claimed to be stable after post oxygen annealing conditions which minimize the oxygen vacancy effects to an extent [37, 39]. These observations drive in favor of electronic reconstructions mechanism at the interfaces.

Although the polarization discontinuity mechanism supports large number of experimental observations as summarized by Schlom *et al*. [40], yet there are several short comings of the model; in the simple picture of electronic reconstructions there will be an hole gas expected at the surface of the LAO in the LAO/STO samples and thus far no real experimental evidence is found for the hole gas on the surface. There have been efforts made to estimate the built in fields in LAO layers [41, 42]. Capacitance measurements [41] were performed across the LAO/STO interface which revealed the presence of intrinsic electric field across LAO of about 80 meVÅ^{-1}. The band alignments and internal electric fields investigated with core level spectroscopy found that the electric fields are very small [42]. Although the above measurements show the presence of built in fields in LAO layers yet these numbers are significantly small compared to ideal polarization catastrophe picture.

In the following I discuss some other suggested possible origins of the interface conductivity; the oxygen vacancy formation in STO and cationic intermixing.

2.3.2 Oxygen vacancy creation and cationic intermixing

In any oxide material preparation the growth parameters especially the oxygen pressure during the growth is very crucial and can influence the properties to great effect. Various research groups investigated the interface properties of LAO/STO interface system under different oxygen growth conditions.

The literature review of the oxygen growth pressure dependence of properties of the LAO/STO interface samples prepared in a wide range of oxygen partial pressures (P_{O2}) is summarized below [32-34,39]. Depending on the P_{O2}, the samples basically fall under two classes, the ones grown at low P_{O2} ($\leq 10^{-5}$ mbar) and the ones grown at high P_{O2} ($\geq 10^{-4}$ mbar). The sheet resistance, R_s, of the samples grown at $P_{O2} \leq 10^{-5}$ mbar (low pressure samples) are ~10 Ω/□ at 300 K and ~1 mΩ/□ at 2 K with an almost temperature-independent carrier density, n_s, of ~10^{16} -10^{17} cm^{-2} and an increase of Hall mobility, μ, to ~10^4 cm^{2}V^{-1}s^{-1} at 2 K. The large n_s of the samples grown in this pressure range indicate 3D like

conductivity that is most likely dominated by oxygen vacancies. The R_s of samples grown at $P_{O2} \geq 10^{-4}$ mbar (high pressure samples) are 9–13 kΩ/□ at 300 K and gradually decrease to ~200 Ω/□ at 2 K; n_s is in the order of ~10^{14} cm^{-2} at 300 K to 2.0–2.5×10^{13} cm^{-2} at 2 K, and the μ increases significantly to ~10^3 $cm^2V^{-1}s^{-1}$ at 2 K.

The origin of oxygen vacancy in these samples is confirmed by the post thermal oxygen annealing experiments. The annealed samples show significant reduction in the carrier densities compared to those for the as-grown samples, which indicates the presence of oxygen vacancy created carriers at the interface [32, 39]. However, the remaining carrier density after post annealing still suggests that other mechanisms may be at work and responsible for the carriers at the interface. The role of oxygen vacancies and the confinement effects of carriers with respect to the growth pressure are investigated by a conducting-atomic force microscopy (C-AFM) measurement [43], the confinement of carriers in low oxygen pressure samples is about a few μm and in the high pressure grown samples and post annealed samples about a few nano meters from the interface. However, although the samples LAO/STO deposited at higher pressures up to 10^{-2} mbar show conductivity, it is not possible to get conductivity in STO by annealing in P_{O2} greater than 10^{-4} mbar [32]. Therefore, the electron gas in LAO/STO prepared in P_{O2} above 10^{-4} mbar does not originate from oxygen vacancy creation but likely from electronic reconstruction. However resent results show the creation of conductivity at bare STO surface by vacuum cleaving [18] and chemical reduction [44] of STO surface by the growth of amorphous over layers results in oxygen vacancy creation in STO and thus conductivity. The above observation shows that the oxygen vacancy creation during the surface preparation and growth of oxide films definitely play a considerable role in governing the conductivity at the interface.

The other most prominent mechanism proposed for the origin of conductivity is the possible cationic intermixing at the atomic level at the interface. In this scenario, the inter diffusion of La into the STO could introduce conductivity due to the electron doping in STO. This model can be simply considered as a

formation of $La_xSr_{1-x}TiO_3$ by atomic intermixing at the LAO/STO interfaces. In this $La_xSr_{1-x}TiO_3$ structure the mixed valence at A-site can (La^{+3} and Sr^{+2}) manipulates the Ti valence (from Ti^{+4} to Ti^{+3}) that create conductivity in this case [45]. High resolution TEM reports suggest cation mixing at the interface to an extent up to few unit cells [35]. However this mechanism cannot explain the critical thickness found for metal-insulator transition and termination effects as discussed above.

As discussed above each mechanism appears to influence the interface conductivity in a specific way, One cannot conclude completely a single mechanism or at least cannot rule out the possibility of multiple mechanisms operating in these interfaces [40]. Further experiments at the atomic level are necessary to come to a solid conclusion to reveal the origin of the conductivity. Nevertheless, this problem of the origin of conductivity challenges the scientific community to find and explore the interface in some new and novel approaches in order to understand the interface physics better from what has been learned so far. Although this still remains as a task to be resolved until today, in recent years the LAO/STO interface system has further shown several unusual properties which are far beyond the expectations from the known interface physics. In the following a brief literature review is presented for emergent phenomena at the LAO/STO interface that co-exist with the 2DEG.

2.4. Superconductivity and magnetism

The surprising discoveries at the LAO/STO interface were not limited to the observation of the high mobility 2DEG at the interface. Exploiting the electron correlation nature and its sensitivity to the external parameters such as growth parameters, strain and electric fields; novel properties have been reported at the LAO/STO interfaces. The most fascinating among all are two dimensional superconductivity and magnetism, and further the co-existence of both at the interface. Along with the high mobility 2DEG at the LAO/STO interface, Reyren *et al*. [46] reported two-dimentional (2D) superconductivity at 200 mK temperature (figure 2.7a). The superconducting phase shows the typical critical

magnetic field and current behavior. The 2D nature of the the superconducting layer is confirmed by coherence length analysis and the upper limit for the dimensionality is found to 10 nm. As shown in figure 2.7b, it was also demonstrated that this superconducting ground state can be tuned to an insulating state by electric fields [47]. Such modulation of ground states is achieved by the electrostatic tuning of the carrier density at the interface by applying external electric fields through the STO back gate. Superconductivity at the interface triggered a lot of interest in the community to investigate further the nature of superconducting behavior.

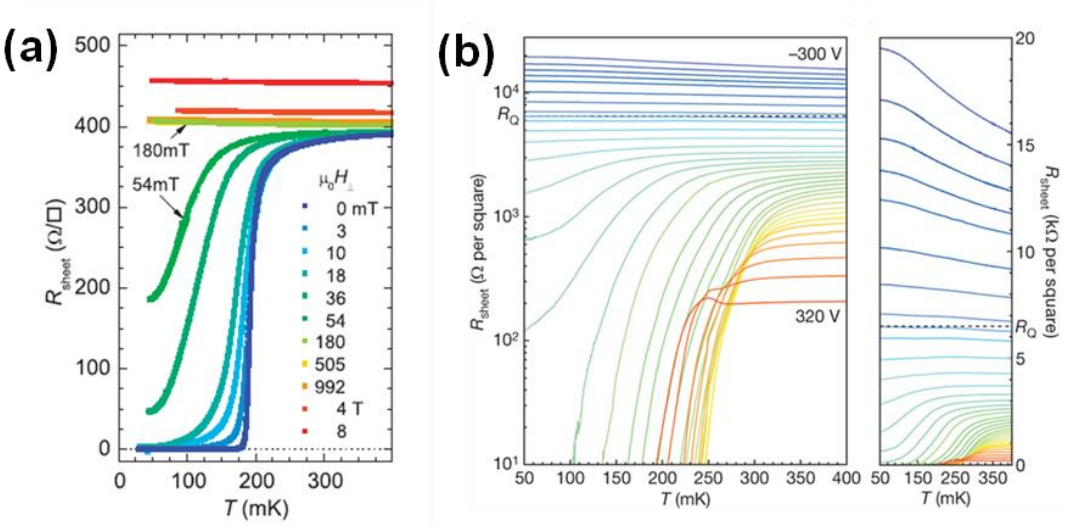

Figure 2.7: (a) Superconducting transition of the LAO/STO interface under different magnetic fields. From Reyren *et al*. [46]. (b) Electric field tuning of the superconducting ground state to normal state at the LAO/STO interface. From Caviglia *et al*. [47].

The other fascinating discovery further at this interface is the magnetic property at this non-magnetic oxide interface. A ferromagnetic state at the n-type LAO/STO interface was predicted for the electrons occupying Ti $3d_{xy}$ orbitals. The magnetic property was investigated through various experimental techniques and is summarized in below figure 2.8. By preparing the LAO/STO samples in a rather broad range of P_{O2} and with thicker LAO films, Brinkman *et al*. [48] investigated

the transport properties of the LAO/STO interfaces. As shown in figure 2.8a, samples prepared under higher P_{O2} exhibit a signature of Kondo behavior.

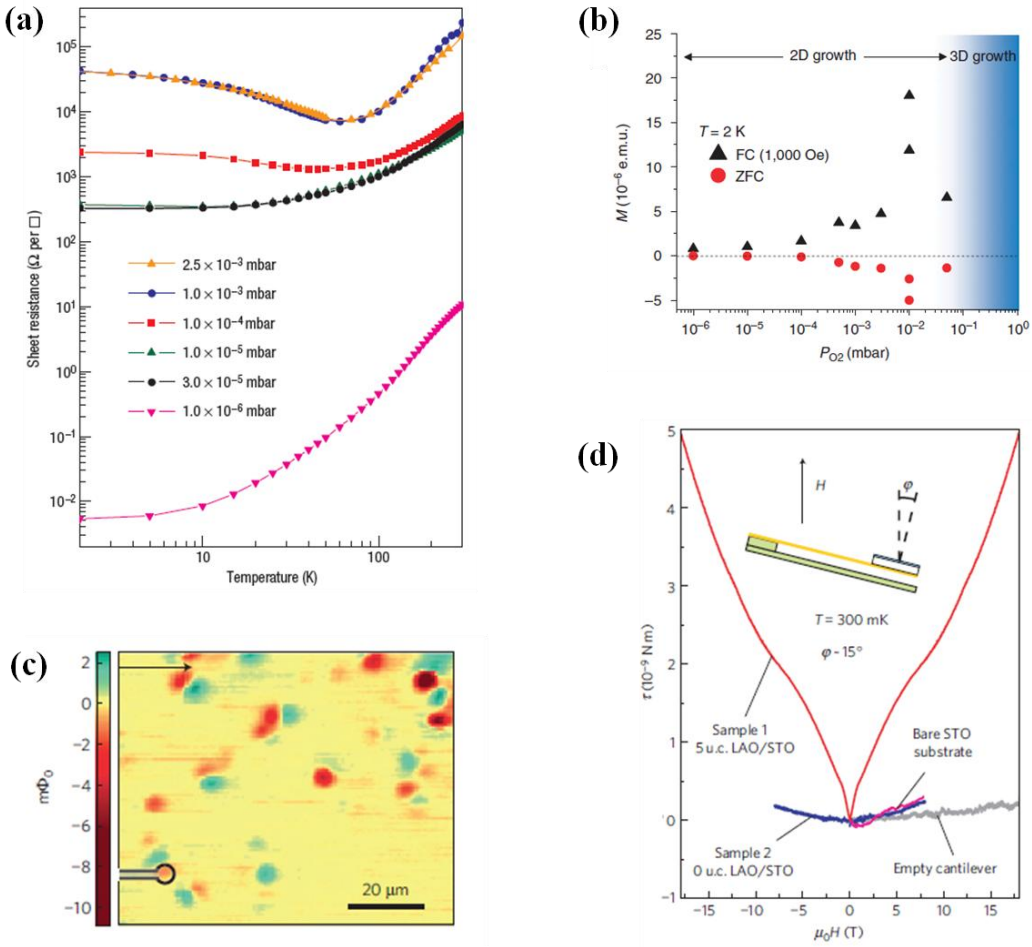

Figure 2.8: (a) Magnetic kondo behaviour at the LAO/STO interface. From Brinkman *et al*. [48]. (b) Magnetic moment measured with SQUID-VSM for the LAO/STO samples deposited at various pressures. From Ariando *et al*. [49]. (c) Direct imaging of magnetic dipoles using scanning SQUID microscope. From Bert *et al*. [50]. (d) Torque magnetometry measurement on the LAO/STO interface samples. From Lu Li *et al*. [51].

At low temperatures the resistance exhibits a magnetic hysteresis like behavior. These observations indicate magnetic ordering in the system. The magnetic origin is attributed to the occupied Ti^{+3} states which have an un-paired electron.This

significant observation of magnetic character at non magnetic oxides stimulated a lot of interest to investigate the magnetic origin in this system. Exploiting higher P_{O2} growth conditions, Ariando *et al*. [49] reported the observation of electronic phase separation at the interface with the co-existence of various magnetic phases such as diamagnetism and ferromagnetism along with the 2DEG. The origin of these various magnetic phases is suggested to arising from the specific occupancy of various Ti 3*d* states. Magnetic moment measurements were performed by vibrating sample magnetometer (VSM), the magnetization (**M**) of the samples prepared under different pressure is shown in figure 2.8b. In accordance with the above reports simultaneous observation of magnetic ordering at the interface is reported by using different measurement techniques such as flux mapping of the magnetic dipoles at the interface [50] (figure 2.8c) and torque magnetometer [51] (figure 2.8d). Significantly, these reports also show the co-existence of superconductivity and magnetism at low temperatures.

In all the above reports the orbital physics at the interface is proposed to play a key role to the magnetic ordering and to the unconventional co-existence of superconductivity and magnetism at the interface. At the LAO/STO interface, the electrons are doped into the STO and these electrons occupy Ti 3*d* orbitals due to the accessibility of the multi valence of the Ti (Ti^{+3}, Ti^{+4}) states. This interpretation is supported by various spectroscopic measurements where the evolution of the Ti^{+3} states in the conducting interfaces is observed [29]. A schematic for the Ti 3*d* orbital picture for STO is shown in figure 2.9.

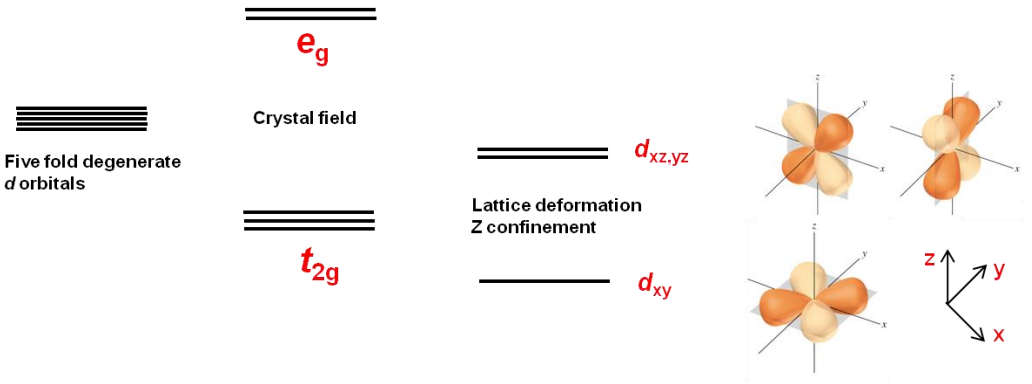

Figure 2.9: Schematic of the Ti 3*d* orbital picture for STO at the LAO/STO interface. The energy levels splits into e_g and t_{2g} states due to crystal field, and further splitting of t_{2g} into in-plane (d_{xy}) and out of plane (d_{yz}, d_{zx}) orbitals due to the interface strain and *z*-confinement.

Due to the crystal field the fivefold degenerate Ti 3*d* orbitals split into two e_g and t_{2g} levels. In the LAO/STO case, doped electrons in STO at the interface occupy the lower Ti t_{2g} states. The t_{2g} level is threefold degenerate consisting of d_{xy}, d_{yz} and d_{zx} orbitals. Both density functional theory (DFT) [52] and spectroscopic measurements [29, 53], show that, in the top TiO_2 layers, t_{2g} states further undergo splitting which is attributed due to the lattice deformation arising from the lattice mismatch between LAO and STO and z-confinement of electrons at the interface. It is further shown that the in-plane d_{xy} states have lower energy than out of plane d_{xz}, d_{yz} which makes d_{xy} the first available states for electrons at the LAO/STO interface. Based on these facts, at the interface, the conductivity is attributed to the itinerant mobile electrons of these Ti^{+3} states, while the origin of magnetism is believed to originate from the localization of electrons in some of these Ti^{+3}states. The supposed localization of these electrons is believed to be the consequence of interface effects such as crystal fields, strain, and electronic disorder. Note here that the d_{xy} orbitals lie within the (001) plane of the interface. Further, owing to this preferential occupancy, particularly to the Ti $3d_{xy}$ orbitals at the interface, various reports have presumed that the magnetization predominantly is in the

plane of the interface. There have been extensive investigations in progress to further understand the orbital physics and possible control over the magnetism.

2.5. Device concepts

To realize high quality devices from this unique interface and thus to transform this 2DEG into useful technologies, reliable patterning of the interface is essential. Patterning of this conducting interface is also of fundamental importance for investigating the above mentioned exotic phases. The patterning of oxide heterostructures is always a challenging task, thus one need to find new and reliable ways. Mannhart's group developed a technique to pattern the buried interface and create device structures [54].

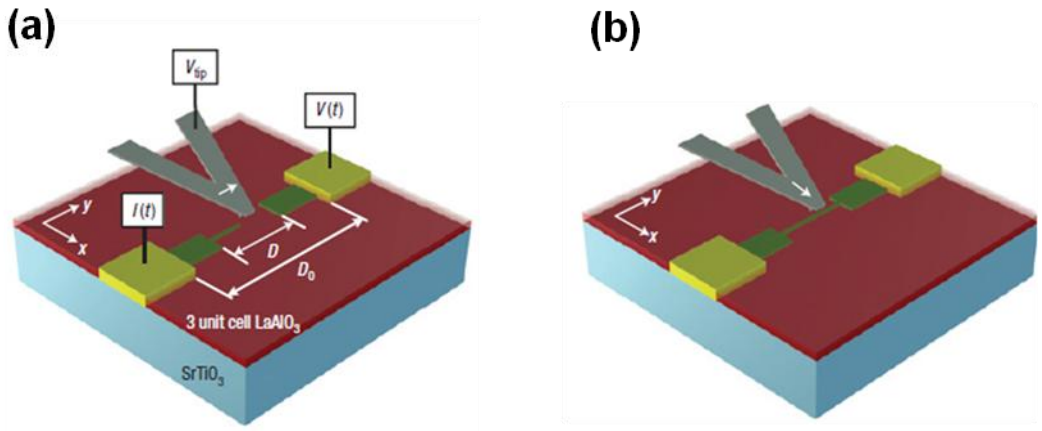

Figure 2.10: (a) Writing process of a conducting line (positive voltage to AFM tip). (b) Erasing process of a conducting line (negative voltage to AFM tip) using AFM lithography. From Cen *et al*. [55].

Pattering of 2DEG can be achieved by growing amorphous LAO film over STO using lithography (this creates a insulating interface) followed by a conventional crystalline LAO/STO interface; this selectively creates a conducting area and thus a patterned 2DEG. J. Levy and co-researchers invented a new way to create a 2DEG at LAO/STO interface by writing and erasing of conducting channels using

C-AFM [55] as shown in figure 2.9. By applying the voltages to a tip of C-AFM probe, the LAO/STO interface is locally reversibly switched between insulating and conducting states. The width of these conducting channels was achieved down to few nanometers paving a way to realize possible quantum device application. However, most of the current electronic industry is based on Si based technology. Therefore to integrate the oxide interface system with current silicon technology, one needs to demonstrate the susccessfull growth of this interface on Si. This significant step was realized by Park *et al*. as they demonstrated the creation of 2DEG at the LAO/STO interface by growing on Silicon [56]. Further, quantum Shubnikov- de Hass oscillations [57] and spin-orbit interaction [58] have been reported at these interfaces which are significant importance for spintronic device concepts. The exciting observation as summarized above demonstrates the potential of the LAO/STO interface for future oxide electronics. However there is still a need to pattern these interfaces in a simple way. In the fallowing we discuss very exciting spin-orbit interaction property at the interface in detail.

2.6. Spin-orbit interaction

Spin-orbit interaction is an interaction of a particle's spin with its motion. The spin-orbit coupling originates from an interaction of the spin with magnetic field that is experienced by the moving electron. The spin-orbit interaction energy Hamiltonian is given by H_{so}

$$H_{SO} = \frac{\hbar}{4c^2m^2}\left[\nabla V(r) \times \hat{P}\right] \cdot \vec{\sigma}.$$

Here $V(r)$ is electric potential, P and σ are momentum associated with motion and spin vectors respectively. The role of $V(r)$ is determined by the crystal potential that arises from atomic cores. We can see from the equation that the strength of the interaction depends on angular momentum L ($L = r \times P$) and spin σ of the electron. Thus, systems with high L and spin are expected to have strong spin-orbit interaction (SOI). As a consequence of the SOI, the spin states splits in the system. When the crystal lattice has a centre of symmetry the spin-orbit

coupling would not influence the band structure much, however the termination of a bulk crystal by a surface or creation of a hetero-structure can break the 3D inversion symmetry at the surfaces or interfaces that can create strong SOI. This specific SOI is called Rashba type spin-orbit interaction [19]. The Rashba spin-orbit coupling is a direct consequence of a symmetry breaking field in the direction perpendicular to the 2D surface. Considering the out of plane direction to be z which is perpendicular to the interface, the Rashba SOI equation is given by

$$H_{SO} = \frac{\hbar}{4c^2m^2}\frac{\partial V}{\partial z}\left(P_x\sigma_y - P_y\sigma_x\right).$$

Here the strength of the SOI depends on the interface electric field and the in plane spin components. The interface electric field could arise from the band discontinuity and confinement of the electrons near the interfaces. The classic examples are GaAs/GaAlAs [60] and InAs/InGaAs [61] heterostructures with 2DEG at the interface. The importance of SOI brought to the forefront in the proposed Datta-Das device [62] where the spin precession of the electron in a conducting channel can be controlled by gate electric field via tunable Rashba SOI. When the gate voltage is applied to the interface it potentially modifies the potential gradient at the interface via the changes in band bending of the bands and electron probability density within the confinement well. Thus the Rashba SOI gives rise to the effective magnetic field that can be controlled by electric field and is given by,

$$B_{SO} = \alpha(P \times e_z),$$

where α is Rashba coefficient and tunable with electric field. When the spin polarized electron is injected in to the conduction channel the electron precess about this B_{SO} with an angle $\Delta\theta = \frac{2m\alpha l}{\hbar}$ as it traverses a distance *l* and allows controlling the spin current of the electrons [63].

The spin-orbit coupling can be examined by magneto transport study of the weak antilocalization (WAL) effect of the conducting channel. The negative magneto conductance is a characteristic of the weak antilocalization of the carriers due to SOI and the strength of this interaction is tunable with gate voltage. Weak antilocalization is a negative correction to the resistivity (actually reduces the positive correction to the resistance which arises due to weak localization of the system) of a system that originates from the SOI. The spin-orbit field basically adds additional phase to carriers as they move around paths which reduces the localization effect. Weak antilocalization has been reported in semiconductor heterostructures [64] which exhibit a large SOI. Further, the tunability of the Rashba SOI can be examined by the magneto transport analysis with gate voltage.

Maekawa-Fukuyama derived a formula [65] to extract SOI from the conductance correction ($\Delta\sigma$) in the diffusive regime and is given by

$$\frac{\Delta\sigma(H)}{\sigma_0} = \Psi\left(\frac{H}{H_i + H_{so}}\right) + \frac{1}{2\sqrt{1-\gamma^2}}\Psi\left(\frac{H}{H_i + H_{so}(1+\sqrt{1-\gamma^2})}\right) - \frac{1}{2\sqrt{1-\gamma^2}}\Psi\left(\frac{H}{H_i + H_{so}(1-\sqrt{1-\gamma^2})}\right)$$

The function $\Psi(z) = \ln z + \psi(1/2 + 1/z)$ is a digamma function. Here H_i and H_{so} are inelastic and spin-orbit field and can be obtained from the fitting results of the data to above formula. The SOI at the LAO/STO interfaces is investigated in this thesis and the experimental results are discussed in the chapter 7.

Having made an attempt to present a back ground for the perovskite oxides and their interfaces, and especially to the LAO/STO interface, in the following chapter I will discuss the techniques employed for the film growth and characterization techniques used to investigate their properties. The experimental results will be presented in the subsequent chapters.

.

References:

[1] http://en.wikipedia.org/wiki/Perovskite_(structure).

[2] F. W. Lytle, "X-Ray diffractometry of low-temperature phase transformations in strontium titanate," *Journal of Applied Physics*, 35, 2212-2215 (1964).

[3] E. Tosatti, and R. Martonak, "Rotational melting in displacive quantum paraelectrics," *Solid Sate Communications*, 92, 167-180 (1994).

[4] S. K. Mishra, and D. Pandey, "Low temperature x-ray diffraction study of the phase transitions in $Sr_{1-X}Ca_XTiO_3$ (x = 0.02, 0.04): evidence for ferrielectric ordering," *Applied Physics Letters*, 95, 232910 (2009).

[5] K. A. Muller, and H. Burkard, "$SrTiO_3$: an intrinsic quantum paraelectric below 4 K," *Physical Review B*, 19, 3593 (1979).

[6] H. -M. Christen, J. Mannhart, E. J. Williams, and Ch. Gerber, "Dielectric properties of sputtered $SrTiO_3$ films," *Physical Review B*, 49, 12095 (1994).

[7] J. G. Bednorz, and K. A. Müller, "$Sr_{1-x}Ca_xTiO_3$: An XY quantum ferroelectric with transition to randomness," *Physical Review Letters*, 52, 2289–2292 (1984).

[8] M. Itoh, R. Wang, Y. Inaguma, T. Yamaguchi, Y-J. Shan, and T. Nakamura, "Ferroelectricity induced by oxygen isotope exchange in strontium titanate perovskite," *Physical Review Letters*, 82, 3540–3543 (1999).

[9] H. Uwe, and T. Sakudo , "Stress-induced ferroelectricity and soft modes in $SrTiO_3$," *Physical Review B*, 13, 271–286 (1976).

[10] J. H. Haeni, P. Irvin, W. Chang, R. Uecker, P. Reiche, Y. L. Li, S. Choudhury, W. Tian, M. E. Hawley, B. Craigo, A. K. Tagantsev, X. Q. Pan, S. K. Streiffer, L. Q. Chen, S. Kirchoefer, J. Levy, and D. G. Schlom, "Room-temperature ferroelectricity in strained $SrTiO_3$," *Nature*, 430, 758 (2004).

[11] M. Kawai, S. Watanabe, and T. Hanada, "Molecular beam epitaxy of $Bi_2Sr_2CuO_x$ and $Bi_2Sr_2Ca_{0.85}Sr_{0.15}Cu_2O_x$ ultra thin films at 300°C," *Journal of Crystal Growth*, 112, 745-752 (1991).

[12] F. Tsui, M. C. Smoak, T. K. Nath, and C. B. Eom, "Strain-dependent magnetic phase diagram of epitaxial $La_{0.67}Sr_{0.33}MnO_3$ thin films," *Applied Physics Letters*, 76, 2421 (2000).

[13] A. Ohtomo, D. A. Muller, J. L. Grazul, and H. Y. Hwang, "Artificial charge-modulationin atomic-scale perovskite titanate superlattices," *Nature*, 419, 378-380 (2002).

[14] A. Ohtomo, and H. Y. Hwang, "A high-mobility electron gas at the LaAlO3/SrTiO3 heterointerface," *Nature*, 427, 423-426 (2004).

[15] M. Lee, J. R. Williams, S. Zhang, C. D. Frisbie, and D. Goldhaber-Gordon, "Electrolyte gate-controlled Kondo effect in $SrTiO_3$," *Physical Review Letters*, 107, 256601 (2011).

[16] J. Son, P. Moetakef, B. Jalan, O. Bierwagen, N. J. Wright, R. E.-Herbert, and S. Stemmer, "Epitaxial $SrTiO_3$ films with electron mobilities exceeding 30,000 $cm^2 V^{-1} s^{-1}$," *Nature Materials*, 9, 482–484 (2010).

[17] W. Meevasana, P. D. C. King, R. H. He, S.-K. Mo, M. Hashimoto, A. Tamai, P. Songsiriritthigul, F. Baumberger, and Z.-X. Shen, "Creation and control of a two-dimensional electron liquid at the bare $SrTiO_3$ surface," *Nature Materials*, 10, 114-118 (2011).

[18] A. F. Santander-Syro, A. F. O. Copie, T. Kondo, F. Fortuna, S. Pailhès, R. Weht, X. G. Qiu, F. Bertran, A. Nicolaou, A. Taleb-Ibrahimi, P. Le Fèvre, G. Herranz, M. Bibes, N. Reyren, Y. Apertet, P. Lecoeur, A. Barthélémy, and M. J. Rozenberg, "Two-dimensional electron gas with universal subbands at the surface of $SrTiO_3$," *Nature*, 469, 189-193 (2011).

[19] D. Kan, T. Terashima, R. Kanda, A. Masuno, K. Tanaka, S. Chu, H. Kan, A. Ishizumi, Y. Kanemitsu, Y. Shimakawa, and M. Takano, "Blue-light emission at room temperature from Ar^+-irradiated $SrTiO_3$," *Nature Materials*, 4, 816 - 819 (2005).

[20] J. Chrosch, and E. K. H. Salje, "Temperature dependence of the domain wall width in $LaAlO_3$," *Journal of Applied Physics*, 85, 722-727 (1999).

[21] S. A. Hayward, S. A. T. Redfern, and E. K. H. Salje, "Order parameter saturation in $LaAlO_3$," *Journal of Physics: Condensed Matter*, 14, 10131-10144 (2002).

[22] R. W. Simon, C. E. Platt, A. E. Lee, G. S. Lee, K. P. Daly, M. S. Wire, J. A. Luine, and M. Urbanik, "Low-loss substrate for epitaxial growth of high-temperature superconductor thin films," *Applied Physics Letters*, 53, 2677 (1988).

[23] A. Roy Barman, M. Motapathula, A. Annadi, K. Gopinadhan, Y. L. Zhao, Z. Yong, I. Santoso, Ariando, M. Breese, A. Rusydi, S. Dhar, and T. Venkatesan, "Multifunctional $Ti_{1-x}Ta_xO_2$: Ta doping or Ta alloying?" *Applied Physics Letters*, 98, 072111 (2011).

[24] J. Q. Chen, X. Wang, Y. H. Lu, A. Roy Barman, G. J. You, G. C. Xing, T. C. Sum, S. Dhar, Y. P. Feng, Ariando, Q.-H. Xu, and T. Venkatesan. "Defect dynamics and spectral observation of twinning in single crystalline $LaAlO_3$ under subbandgap excitation," *Applied Physics Letters*, 98, 041904 (2011).

[25] W. D. Kingery, H. K. Bowen, and D.R. Uhlmann, *op cit*, pp926-927.

[26] Z. Wang, Y. Yang, R. Viswan, J. Li, and D. Viehland (2011), "Control of crystallization and ferroelectric properties of $BaTiO_3$ thin films on alloy substrates," *Ferroelectrics - Material Aspects*, DOI: 10.5772/17488.

[27] *Crystec GmbH*, http://www.crystec.de/crystec-e.html.

[28] N. Nakagawa, H. Y. Hwang, and D. A. Muller, "Why some interfaces cannot be sharp," *Nature Materials*, 5, 204-209 (2006).

[29] M. Salluzzo, J. C. Cezar, N. B. Brookes, V. Bisogni, G. M. De Luca, C. Richter, S. Thiel, J. Mannhart, M. Huijben, A. Brinkman, G. Rijnders, and G. Ghiringhelli, "Orbital reconstruction and the two-dimensional electron gas at the $LaAlO_3/SrTiO_3$ interface," *Physical Review Letters*, 98. 102, 166804 (2009).

[30] M. Huijben, A. Brinkman,G. Koster, G. Rijnders, H. Hilgenkamp, and D. H. A. Blank, "Structure-property relation of $SrTiO_3/LaAlO_3$ interfaces," *Advanced Materials*, 21, 1665-1677, (2009).

[31] J. Nishimura, A. Ohtomo, A. Ohkubo, Y. Murakami, and M. Kawasaki, "Controlled carrier generation at a polarity-discontinued perovskite heterointerface," *Japanese Journal of Applied Physics*, 2004, 43, L1032.

[32] A. Kalabukhov, R. Gunnarsson, J. Borjesson, E. Olsson, T. Claeson, and D. Winkler, "Effect of oxygen vacancies in the $SrTiO_3$ on the electrical properties of the $LaAlO_3/SrTiO_3$ interface," *Physical Review B*, 75, 121404(R) (2007).

[33] W. Siemons, G. Koster, H. Yamamoto, W. A. Harrison, G. Lucovsky, T. H. Geballe, D. H. A. Blank, and M. R. Beasley, "Origin of charge density at $LaAlO_3$ on $SrTiO_3$ heterointerfaces: possibility of intrinsic doping," *Physical Review Letters*, 98, 196802 (2007).

[34] G. Herranz, M. Basletic´, M. Bibes, C. Carre´te´ro, E. Tafra, E. Jacquet, K.Bouzehouane, C. Deranlot, A. Hamzic´, J.-M. Broto, A. Barthe´le´my, and A. Fert, "High mobility in $LaAlO_3/SrTiO_3$ heterostructures: dimensionality, and perspectives," *Physical Review Letters*, 98, 216803(2007).

[35] P. R. Wilmott, S. A. Pauli, R. Herger, C. M. Schlepu¨tz, D. Martoccia, B. D. Patterson, B. Delley, R. Clarke, D. Kumah, C. Coinca, and Y. Yacoby, "Structural basis for the conducting interface between $LaAlO_3$ and $SrTiO_3$," *Physical Review Letters*, 99, 155502 (2007).

[36] C. W. Bark, D. A. Felker, Y. Wang, Y. Zhang, H. W. Jang, C. M. Folkman, J. W. Park, S. H. Baek, H. Zhou, D. D. Fong, X. Q. Pan, E. Y. Tsymbal, M. S. Rzchowski, and C. B. Eom "Tailoring a two-dimensional electron gas at the $LaAlO_3/SrTiO_3$ (001) interface by epitaxial strain," *Proceedings of the National Academy of Sciences*, 108, 4720-4724, (2011).

[37] S. Thiel, G. Hammerl, A. Schmehl, C. W. Schneider, and J. Mannhart, "Tunable quasi-two-dimensional electron gases in oxide heterostructures," *Science*, 313, 1942 (2006).

[38] R. Pentcheva, and W. E. Pickett, "Avoiding the polarization catastrophe in $LaAlO_3$ over layers on $SrTiO_3$ (001) through polar distortion," *Physical Review Letters*, 102, 107602 (2009).

[39] C. Cancellieri, N. Reyren1, S. Gariglio, A. D. Caviglia, A. Fête, and J.-M. Triscone, "Influence of the growth conditions on the $LaAlO_3/SrTiO_3$ interface electronic properties," *Europhysics letters*, 91, 17004 (2010).

[40] D. G. Schlom, and J. Mannhart, "Interface takes charge over Si," *Nature Materials*, 10,168–169 (2011).

[41] G. Singh-Bhalla, C. Bell, J. Ravichandran, W. Siemons, Y. Hikita, S. Salahuddin, A. F. Hebard, H. Y. Hwang, and R. Ramesh, "Built-in and induced polarization across $LaAlO_3/SrTiO_3$ heterojunctions," *Nature Physics* **7**, 80–86 (2011).

[42] M. Takizawa, S. Tsuda, T. Susaki, H. Y. Hwang, and A. Fujimori, "Electronic charges and electric potential at LAO/STO interfaces studied by core-level photoemission spectroscopy," *Physical review B*, 84, 245124 (2011).

[43] M. Basletic, J. -L. Maurice, C. Carrétéro, G. Herranz, O. Copie, M. Bibes, É. Jacquet, K. Bouzehouane, S. Fusil, and A. Barthélémy, "Mapping the spatial distribution of charge carriers in $LaAlO_3/SrTiO_3$ heterostructures," *Nature Materials*, 7, 621(2008).

[44] Y. Chen, N. Pryds, J. E. Kleibeuker, G. Koster, J. Sun, E. Stamate, B. Shen, G. Rijnders, and S. Linderoth, "Metallic and insulating interfaces of amorphous $SrTiO_3$-based oxide heterostructures," *Nano Letters*, 11, 3774-3778 (2011).

[45] T. Higuchi, and H. Y. Hwang, "General considerations of the electrostatic boundary conditions in oxide heterostructures," *arXiv:1105.5779v1*.

[46] N. Reyren, S. Thiel, A. D. Caviglia, L. Fitting Kourkoutis, G. Hammerl, C. Richter, C. W. Schneider, T. Kopp, A. -S. Ruetschi, D. Jaccard, M. Gabay, D. A. Muller, J. -M. Triscone, and J. Mannhart, "Superconducting interfaces between insulating oxides," *Science*, 317, 1196-1199 (2007).

[47] A. D. Caviglia, S. Gariglio, N. Reyren, D. Jaccard, T. Schneider, M. Gabay, S. Thiel, G. Hammerl, J. Mannhart, and J.-M. Triscone, "Electric field control of the $LaAlO_3/SrTiO_3$ interface ground state," *Nature*, 456, 624-627 (2008).

[48] A. Brinkman, M. Huijben, M. Van Zalk, J. Huijben, U. Zeitler, J. C. Maan, W. G. Van Der Wiel, G. Rijnders, D. H. A. Blank, and H. Hilgenkamp,

"Magnetic effects at the interface between non magnetic oxides," *Nature Materials*, 6, 493-496 (2007).

[49] Ariando, X. Wang, G. Baskaran, Z. Q. Liu, J. Huijben, J. B. Yi, A. Annadi, A. Roy Barman, A. Rusydi, Y. P. Feng, J. Ding, H. Hilgenkamp, and T. Venkatesan, "Electronic phase separation at the $LaAlO_3/SrTiO_3$ interface," *Nature Communications*, 2, 188 (2011).

[50] J. A. Bert, B. Kalisky, C. Bell, M. Kim, Y. Hikita, and H. Y. Hwang, "Direct imaging of the coexistence of ferromagnetism and superconductivity at the $LaAlO_3/SrTiO_3$ interface," *Nature Physics*, 7, 767 (2011).

[51] Lu Li, C. Richter, J. Mannhart, and R. C. Ashoori, Coexistence of magnetic order and two-dimensional superconductivity at $LaAlO_3/SrTiO_3$ interfaces, *Nature Physics*, 7, 762 (2011).

[52] R. Pentcheva, and W. E. Pickett, "Charge localization or itineracy at $LaAlO_3/SrTiO_3$ interfaces: Hole polarons, oxygen vacancies, and mobile electrons," *Physical Review B*, 74, 035112 (2006).

[53] M. Sing, G. Berner, K. Goß, A. Müller, A. Ruff, A. Wetscherek, S. Thiel, J. Mannhart, S. A. Pauli, C. W. Schneider, P. R. Willmott, M. Gorgoi, F. Schäfers, and R. Claessen, "Proling the interface electron gas of $LaAlO_3/SrTiO_3$ heterostructures with hard x-ray photoelectron spectroscopy," *Physical Review Letters*, 102, 176805 (2009).

[54] C. W. Schneider, S. Thiel, G. Hammerl, C. Richter, and J. Mannhart, "Microlithography of electron gases formed at interfaces in oxide heterostructures," *Applied Physics Letters*, 89, 122101 (2006).

[55] C. Cen, S. Thiel, G. Hammerl, C. W. Schneider, K. E. Andersen, C. S. Hellberg, J. Mannhart, and J. Levy, "Nanoscale control of an interfacial metal–insulator transition at room temperature," *Nature Materials*, 7, 298-302 (2008).

[56] J. W. Park, D. F. Bogorin, C. Cen, D. A. Felker, Y. Zhang, C. T. Nelson, C. W. Bark, C. M. Folkman, X. Q. Pan, M. S. Rzchowski, J. Levy, and C. B. Eom, "Creation of a two-dimensional electron gas at an oxide interface on silicon," *Nature Communications*, 1, 94 (2010).

[57] A. D. Caviglia, S. Gariglio, C. Cancellieri, B. Sacépé, A. Fête, N. Reyren, M. Gabay, A. F. Morpurgo, and J.-M. Triscone, "Two-dimensional quantum oscillations of the conductance at $LaAlO_3/SrTiO_3$ Interfaces," *Physical Review Letters*, 105, 236802 (2010).

[58] A. D. Caviglia, M. Gabay, S. Gariglio, N. Reyren, C. Cancellieri, and J. -M. Triscone, "Tunable Rashba spin-orbit interaction at oxide Interfaces," *Physical Review Letters*, 104, 126803 (2010).

[59] Yu A Bychkov, E I Rashba, "Properties of a 2D electron gas with lifted spectral degeneracy", *Sov. Phys. JETP Lett*. 39, 78 (1984).

[60] J. P. Eisenstein, H. L. Störmer, V. Narayanamurti, A. C. Gossard, and W. Wiegmann, "Effect of Inversion Symmetry on the Band Structure of Semiconductor Heterostructures", *Phys. Rev. Lett*. 53, 2579 (1984).

[61] J. Nitta, T. Akazaki, H. Takayanagi, and T. Enoki, "Gate Control of Spin-Orbit Interaction in an Inverted $In_{0.53}Ga_{0.47}As/In_{0.52}Al_{0.48}As$ Heterostructure", *Phys. Rev. Lett*. 78, 1335 (1997).

[62] S. Datta and B. Das, "Electronic analog of the electro-optic modulator", *Appl. Phys. Lett*, 56, 665 (1990).

[63] M. B. A. Jalil, S. G. Tan, and T. Fujita, "Spintronics in 2DEG systems", *AAPPS Bulletin* 18, 5, 9 (2008).

[64] P. D. Dresselhaus, C. M. A. Papavassiliou, R. G. Wheeler, and R. N. Sacks, "Observation of spin precession in GaAs inversion layers using antilocalization", *Phys. Rev. Lett*. 68, 106 (1992).

[65] S. Maekawa and H. Fukuyama, "Magnetoresistance in Two-Dimensional Disordered Systems: Effects of Zeeman Splitting and Spin-Orbit Scattering", *J. Phys. Soc. Jpn*. 50, 2516 (1981).

Chapter 3

Thin film fabrication and characterization

This chapter describes various techniques used in sample preparation and characterization of thin films, interfaces and heterostructures investigated in my study. The introduction to thin film fabrication technique, the pulsed laser deposition (PLD) assisted with reflection high energy electron diffraction (RHEED), thin film characterization techniques such as atomic force microscopy (AFM), Rutherford backscattering (RBS), physical property measurement system (PPMS), and structural analysis technique X-ray diffraction (XRD) will be given. Finally I discuss different configurations of electrical characterizations, including electric field effects and magneto transport.

3.1. The Pulsed Laser Deposition

The pulsed laser deposition (PLD) technique was used to fabricate various combinations of oxide interface and heterostructure samples. Since its discovery, PLD played an instrumental role in the field of complex oxide thin films right from the beginning with the demonstration of growth of high T_c superconductors by researchers at Bell Communications Research [1, 2]. A schematic of the PLD setup is shown in Fig. 3.1 which consists of four main components, the laser path, target holder setup, substrate holder setup attached to the heater and a Reflection High Energy Electron Diffraction (RHEED) system to monitor the thin film growth process. In this process, when the laser pulse is absorbed by the target, the material gets ablated and forms plasma. The plasma expands into the surrounding vacuum in the form of a plume of energetic species containing atoms and ions of the target material. These species are then collected on a substrate which is mounted on a heater placed at a specific distance from the target, resuling in a thin film deposition of target material on the substrate.

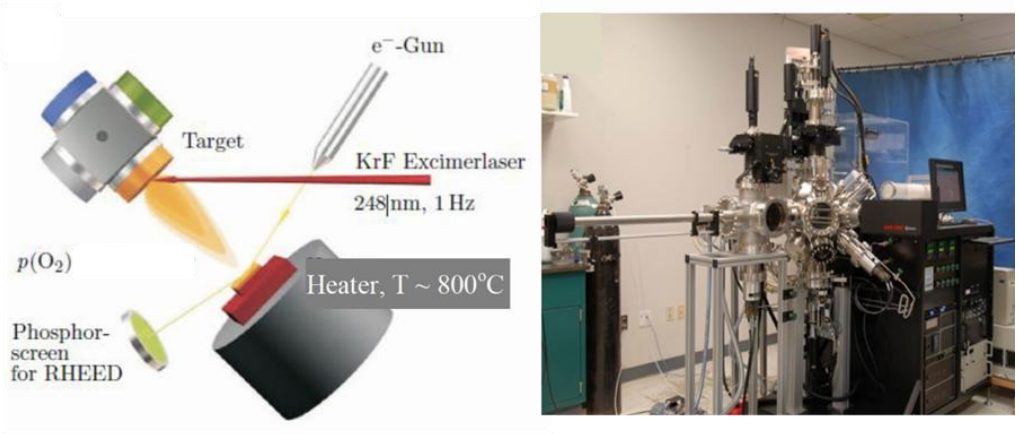

Figure 3.1: A schematic diagram of a pulsed laser deposition system consisting of target, substrate holder and RHEED set up. Pulse laser deposition system with RHEED facility used for the current study in our laboratory.

In this work, a KrF excimer laser with 248 nm wavelength (Lambda Physik Company) and a pulse width of 15 ns with different frequencies ranging from 1-10 Hz was used. The laser energy density for the deposition can be varied by fixing the energy of the laser. To have a uniform ablation, the target was rotated and rastered continuously during the deposition. Similarly, the substrate holder can be rotated during the deposition and its distance from the target can be controlled along the *Z* direction. A radiative heater is used to heat the substrate up to a maximum substrate temperature of 1050 ^{o}C with a heating rate of 5-15 ^{o}C per min. With this basic introduction to the PLD technique, now I discuss the thin film growth methodology including substrate treatment, target preparation and thin film growth process with RHEED monitoring technique.

3.1.1 Thin film growth methodology

One of the most important aspects in thin film growth is the quality of the target material. Targets with specific compositions were prepared in our lab using the solid state reaction method. In this method powders were first weighed according to the reaction formula to form a desired composition, and then these powders were mixed and grinded to form a homogeneous mixture. The mixture is then

sintered at high temperatures for several hours and then pressed to form high density targets. The crystal structure and quality of the targets were verified by the characterization techniques like X-ray difraction and Rutherford back scattering. High quality single crystal substrates for thin film deposition were purchased from CrysTec GmbH. A verity of substrates namely, $SrTiO_3$, $LaAlO_3$, Nb doped $SrTiO_3$, $NdGaO_3$, LSAT ($(LaAlO_3)_{0.3}$-$(Sr_2AlTaO_6)_{0.7}$) were used in this thesis. Prior to the deposition the quality of the substrates was checked under the microscope to avoid unwanted surface contaminations. A general sequence of substrate cleaning procedure was employed before every sample deposition; starting with an ultrasonication of substrate in acetone, then in ionized water, and finally drying the substrate with N_2 gas spray. The selected substrate and target were loaded into the chamber using a load lock attached to the PLD chamber. To have ideal deposition conditions, before the actual deposition process, the PLD chamber pressure was ensured to have a minimum base pressure of 1×10^{-8} Torr. The oxygen gas flow into the chamber is controlled by a mass flow controller (MFC) which has an option of manual/auto mode controls. These modes could control the gas pressures in the range of 1×10^{-1} -10^{-6} Torr. The deposition of thin films is usually performed at high temperatures in the range of 600 -850 ^{o}C. The temperature of the substrate was controlled by a temperature controller attached to the PLD. The most important analysis carried out during the substrate heating process was the RHEED patterns investigation of substrate which gives information of the of substrate surface structure (discussed in later chapters). System shutters in between target and substrate enabled to start and stop the deposition process. After the deposition samples were cooled down to room temperature in deposition pressure with a slow cooling rate employed to avoid the possibility of cracking the thin films due to different thermal expansions. This thesis work deals mostly with the deposition of ultra thin films of few unit cells thickness. The precise control of film thickness at such atomic level was achieved by RHEED monitoring of the film growth during the deposition process. A brief description to the working principle of the RHEED process and analysis of the RHEED data obtained during the film growth is presented below.

3.1.2 RHEED monitoring of growth process

Reflection high energy electron diffraction (RHEED) is a surface characterization technique that works on the principle of diffraction of high energy electrons obtained from the surface of the material. The RHEED process is very sensitive to the sample surface morphology which can be used to probe the crystal symmetry and various surface atomic reconstructions on the surface of the materials. The basic RHEED system contains of two important parts; the electron gun which generates high energy electrons and a camera which collects the diffraction pattern obtained from the substrate. In the RHEED process, the electrons emitted from the electron gun incident on the sample surface at glancing angle and get diffracted from the sample surface and are collected with a CCD (charge coupled device) camera detector (shown in figure 3.2).

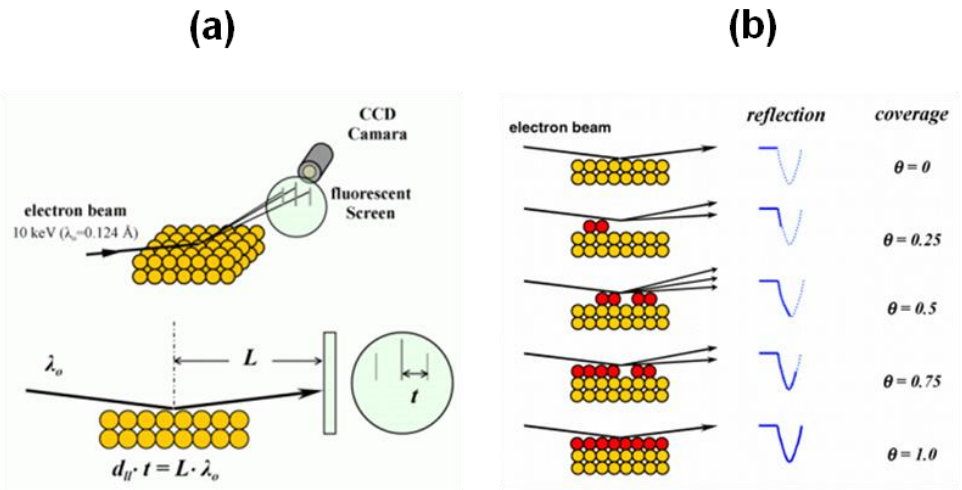

Figure 3.2: (a) Schematic of the RHEED process where the electrons incident on the crystalline material surface and the obtained diffraction pattern collected by a CCD camera. (b) RHEED oscillation period with respect to the coverage of the surface of the film in layer by layer growth mode. From ref [3].

Atoms at the sample surface mostly contribute to the RHEED pattern [3]. The RHEED pattern gives the basic information of the surface crystal structure and

corresponding crystal orientation. However, the most widely used application of the RHEED process is to monitor the growth process and growth rate of the thin film. The basic principle of the growth rate monitoring involves how the coverage of the film surface during the growth oscillates with time. The coverage process of the thin film surface with time for a layer by layer growth method is as shown in the figure 3.2b. As shown in the figure the intensity of the electron diffraction arising from the surfaces during film deposition is actually proportional to the coverage of the surface, which follows the oscillatory behavior (during 0-50% of coverage intensity goes down from maximum to minimum, and during 50-100% of coverage, intensity again goes to maximum due to coverage with newly grown layer), thus enable to monitor the growth of one complete monolayer. The minima in intensity in this process represent the half coverage of the surface, and this should not be misunderstood as a half unit cell growth. Therefore precise counting of these oscillations gives the exact number of unit cells of the thin film grown directly enabling the thickness control of the film. The growth process of monitoring is generally performed by recording the intensity of the 0^{th} order spot in the RHEED pattern. Figure 3.3 shows the RHEED intensity oscillations obtained for the growth of LAO on STO (100) substrate. Clear oscillations allows to control the thickness of the film (here it is 3 unit cells of LAO). The RHEED pattern for before and after the deposition is also shown in the figure. The before deposition pattern corresponds to the STO substrate. The spots in the patterns represent the direct diffraction spots, which give the information of crystal planes in reciprocal space.

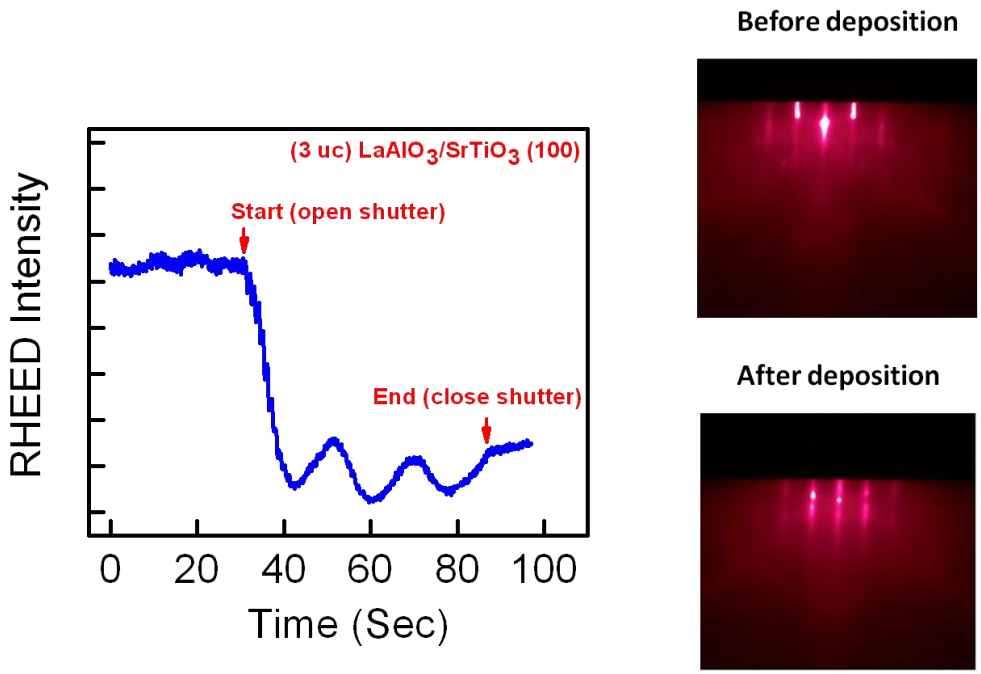

Figure 3.3: RHEED oscillation obtained during the growth of 3 unit cells of LAO on STO (100) oriented substrates. The RHEED patterns obtained before and after the growth of LAO on STO. The pattern obtained for after the growth shows a streak like pattern represent the 2D growth mode for the film with layer by layer by growth mode.

An important observation when comparing before and after deposition patterns is that the RHEED pattern changes from a spot like pattern before deposition to a streak like pattern indicating the growth of 2-dimensional (2D) material on top. The separation between these spots/streaks basically represents the spacing between corresponding crystal planes. The analysis of the spacing will enable to identify the crystal orientation of the film growth. A key criterion to observe RHEED oscillations are of course material should follow the layer by layer growth mode. Any deviation from the layer by layer growth to the so called 3D growth will hinder this process dramatically even though the film grows epitaxial.

3.2. Atomic force microscopy

The important characterization techniques in the study of the thin films are the surface morphology analysis of the samples before and after the growth. To get the precise growth control of the thin films as discussed in the above section one needs to start with atomically flat substrates. Atomic force microscopy (AFM) is the most used technique to analyze the surface morphology of these substrate material surfaces. From AFM analysis, various parameters such as surface roughness, elemental terminations, and height profile of the specific features of the sample surface can be obtained.

The working principle of the AFM is based on the mapping of atomic attraction and or repulsive force between atoms on the sample surface and the AFM tip that is attached to a cantilever. The AFM technique utilizes a short range weak interaction forces (van der Waals). The van der Waals interaction energy of two atoms, located on the r distance from each other can be defined from Lennard-Jones potential equation given by

$$U(r) = U_0 \left\{ -2\left(\frac{r_0}{r}\right)^6 + \left(\frac{r_0}{r}\right)^{12} \right\}$$

In this relation, the total energy (U) is composed of contributions from the long-distance attraction forces (first term) as a result of dipole-dipole interaction between atoms, and the short range repulsion forces (second term). The behaviour of the above relation is shown in figure 3.4.

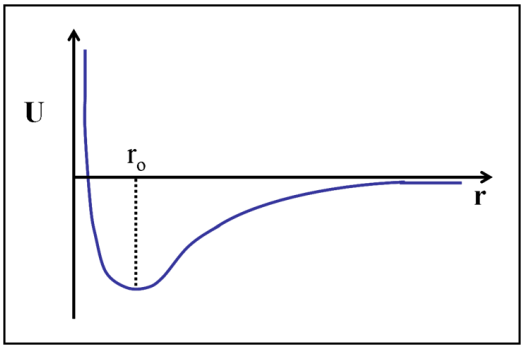

Figure 3.4: Lennard-Jones potential curve

The schematic of the AFM set up is shown in figure 3.5. The basic components in a AFM set up are sample stage, laser diode, photo detector, cantilever with tip and a feed back control unit that generates the equivalent image of the sample surface morphology.

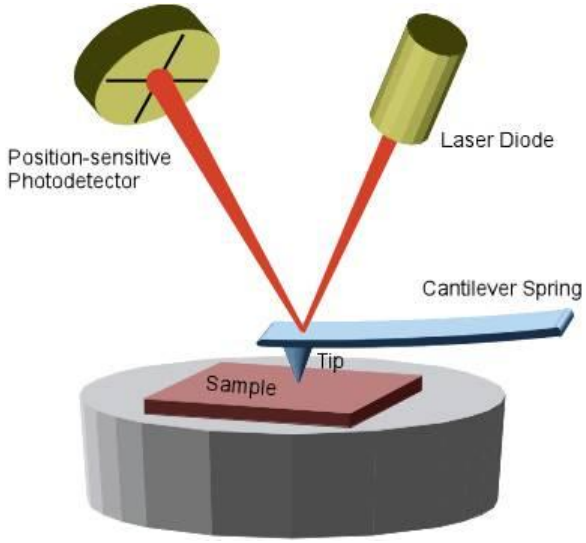

Figure 3.5: Schematic of the AFM set up with the basic components.

The probe used in AFM is a sharp tip attached at the end of a cantilever. The cantilever bends towards or away from the sample surface depending on attractive or repulsive forces from the atoms of the sample surface. The degree of deflection of cantilever is directly proportional to the force between the tip and the sample and is given by

$$F = k.\Delta Z$$

Here F is the force, k is the force constant of cantilever, and ΔZ is the distance between probe and sample. The k coefficients vary in a range of 10^{-3} – 50 N/m. The deflection of cantilever is used for the feedback control to adjust the Z motion of the probe. Since the force between probe and sample is of the order of nano Newton, a very sensitive technique is required to measure the cantilever deflection. The laser based optical technique is used to measure the deflections. These deflection signals are transformed in to real surface morphology using a feed back electric current. For surface sensitive materials the AFM is used in non contact mode also known as tapping mode, in which an AC signal applied instead. In this mode the tip is allowed to vibrate with a specific frequency, which allows interacting with the surface atomic forces better.

3.2.1 Substrate surface analysis

In order to obtain an abrupt interface and atomically sharp hetero structures the first and foremost step is to start with an atomically flat substrate surface. Usually case the purchased substrates contain a mixed termination on the surface due to the milling and polishing steps employed. To prepare an atomically sharp interface and to maintain stoichiometry near interfaces, a single termination substrate surfaces are necessary. Kawasaki *et al.* [4] developed a Buffered hydro florid acid (HF) chemical etching technique to get a single terminated surface for perovskite $SrTiO_3$ substrates, which led a foundation to create abrupt oxide interfaces. In later years this technique was further optimized by researchers from University of Twente [5]. In case of STO (100), using this HF treatment a specific TiO_2 termination can be achieved by the selectively etching SrO. In this process,

STO substrates were first ultrasonicated in DI water to form Sr hydroxide on the surface, and then they were treated with HF for 30 seconds. In this step the formed Sr hydroxides were selectively etches away by HF and creating a TiO_2 termination (here TiO_2 remains nonreactive for HF solution). This chemical treatment then is followed by a thermal treatment step of annealing at 950 °C for 2 hours [5] in air with 5 °C per min ramping up and 3 °C per min while cooing down.

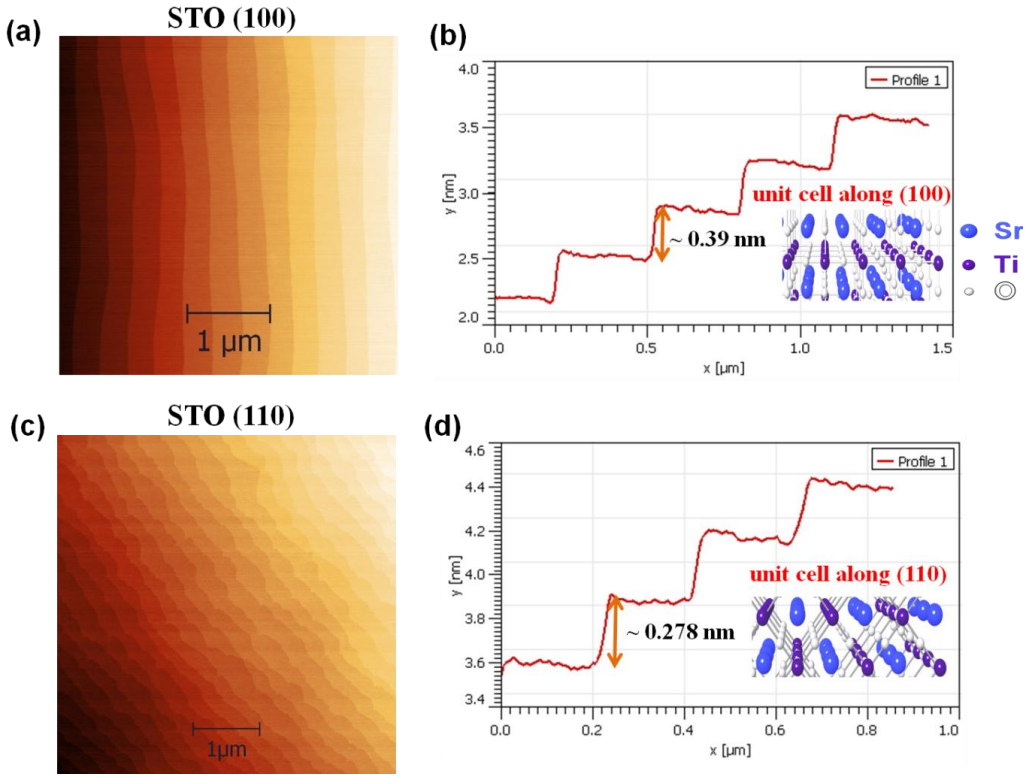

Figure 3.6: (a) AFM topography image of the STO (100) surface after treatment. (b) The AFM height profile showing the step height is equal to a unit cell spacing of (100) STO of 0.39 nm. (c) AFM topography image of the STO (110) surface after treatment.(d) AFM height profile showing the step height is equal to a unit cell spacing of (110) STO of 0.278 nm.

.

Figure 3.6a shows the topography image of STO (100) surface after treatment, the surface contains long terraces structure with the step flow. The step height corresponds to the unit cell height of the STO, which is actually a unit cell distance between two successive TiO_2 layers in (100) direction which is 3.905 Å. Figure 3.6b shows the height profile of the STO(100) surface, which indicates the step height of ~3.9 Å as expected. The terrace width depends on the miscut of the substrates during the polishing of the surfaces. For this thesis work an atomic smooth surfaces of $SrTiO_3$ (110) were also prepared. Atomically smooth surfaces were achieved by employing high temperature treatment with temperature of 1050-1100 ^{o}C with annealing time of 2 -2.5 hours. The corresponding AFM topography image of the STO (110) surface after the treatment is shown in figure 3.6c. Figure 3.6d shows the height profile of the STO (110) surface, indicates the step height of ~2.8 Å which is a unit cell spacing along the (110) direction. Such treated substrates were used for the deposition of LAO/STO interface samples. Atomically flat surfaces for substrates like LSAT and NGO were also obtained through the above thermal treatment process.

3.3. Structural characterization

After a thin film growth it is important to check the crystal quality, growth orientation and most importantly the chemical composition of the film. The investigation of above mentioned properties of grown films was carried out through X-ray diffraction, RBS experiments. In the following a brief background to XRD and RBS techniques is given and the experimental data obtained for the samples is also presented.

3.3.1 X-ray diffraction

X-ray diffraction (XRD) is one of the most fundamental techniques to collect the material structure information. In the XRD process, the atomic structure of a crystal causes a beam of X-rays to diffract into many specific directions. For fixed wave length of incident X-rays, each diffracted angle corresponds to a specific

crystallographic arrangement of atomic planes of the crystal. The periodic arrangement of atoms is generally called as atomic planes. The criterion to have the X-ray diffraction (XRD) is known as the Bragg criterian and is given by the equation

$$2d \sin\theta = n\,\lambda \qquad (n = 1,2,3 \ldots \ldots)$$

Here *d* is the spacing between the crystal atomic planes, θ is the X-ray diffraction angle, λ is the wavelength of the X-rays, and *n* is the order of diffraction. The *d* spacing in a crystal structure depends on the corresponding orientation and lattice constants of a particular crystal structure which is given by

$$d = \frac{1}{\sqrt{\left(\frac{h}{a}\right)^2 + \left(\frac{k}{b}\right)^2 + \left(\frac{l}{c}\right)^2}}$$

Here h, k, l are called miller indices which gives the orientation of the atomic planes, whereas *a*, *b*, and *c* are lattice constants of a crystal structure. Generally the X-ray spectrum is obtained for diffracted x-ray intensity versus 2θ. As there can be a series of differently-spaced planes in a crystalline material, the resultant diffraction spectrum will consist of several peaks at the corresponding θ values. X- ray crystallography library can be used to analyse the obtained spectrum. The growth orientation of the film can be identified by matching the diffraction angle of particular peak position. Once the orientation of the growth is confirmed, from the above Brags formula one can obtain the *d* spacing of the atomic planes and thereby the lattice constants of the thin film. Further the relative intensity and area of the peak generally reflects the crystal quality of the film which can be further precisely analyzed by performing rocking curve of a particular peak. The strain in the thin film can also be extracted from the lattice paramenter by comparing it with the real value.

In this study, a Bruker D8 Discover model X-Ray instrument is used. The X-Rays generated from Cu Kα source which was operated at 40 KV and 20 mA is

incident on the samples mounted on a goniometer stage. The diffracted X-rays are then collected by a detector.

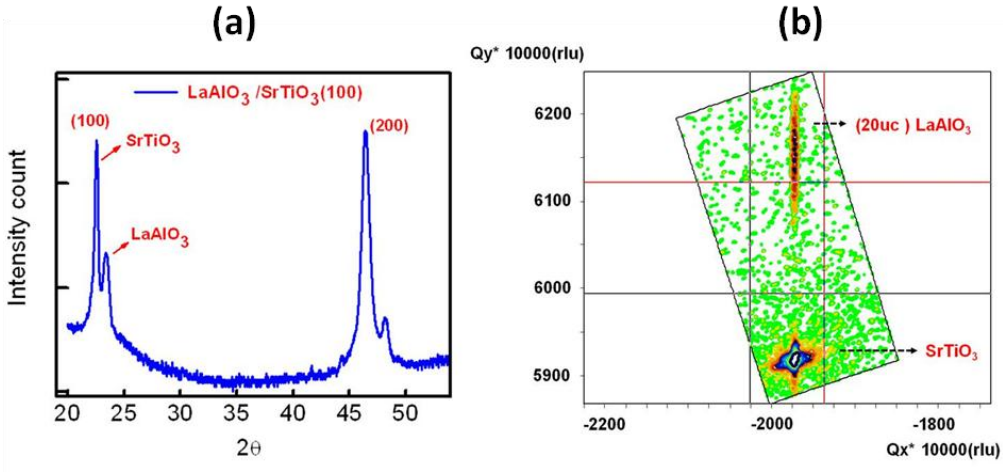

Figure 3.7: (a) The XRD of the LAO/STO (100) sample with 15 nm LAO thickness. (b) The reciprocal mapping image for the LAO/STO (100) sample with 20 uc LAO, showing a coherent growth of LAO film on STO with a strain in LAO layers.

Figure 3.7a shows a XRD spectrum obtained for the LAO/STO (100) sample with LAO thin film having thickness of 15 nm. A 2D detector of VÅNTEC-2000 is used to collect the diffracted X-rays. The epitaxial growth of LAO on STO along the (100) direction can be clearly identified from figure 3.7a. The lattice constant of LAO is estimated from the *d* spacing of (100) planes to be a =3.82 Å. To investigate the strain state in thinner LAO/STO samples, a reciprocal space mapping (RSM) is performed on the sample with 20 uc of LAO on STO (100). Figure 3.7b shows the corresponding RSM image of the sample, showing that LAO is coherently grown on STO and also suggests that LAO is under tensile strain in these thin LAO/STO samples.

3.3.2 Rutherford back scattering

Rutherford backscattering spectrometry (RBS) is a powerful technique for structural and compositional characterization of thin films. Figure 3.8 shows a schematic of RBS process.

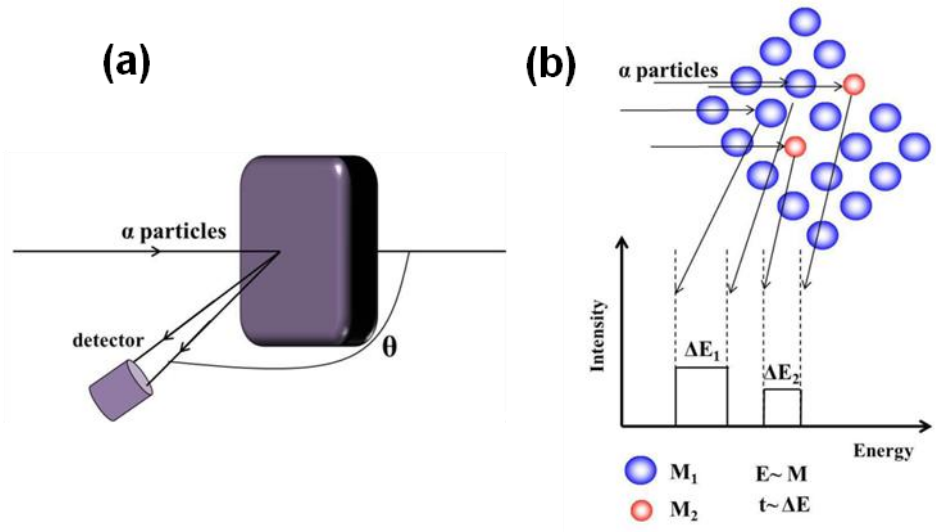

Figure 3.8: (a) Schematic of the Rutherford backscattering (RBS) process. (b) Typical intensity of backscattered α particles versus energy spectrum in a RBS process.

Here a beam of mono energetic α particle ($4He^{+2}$) is generated by an electrostatic accelerator, and directed towards the sample via magnetic steering. When the α particles are irradiated on the sample surface, some of them are elastically back scattered of the surface atoms, while the others enter the sample and lose some energy along the way and are further back scattered by the atoms inside the sample. The number and energy of these backscattered α particles are detected. The RBS spectrum is plotted for the intensity of backscattered particles as a function of energy. Since the collision process between α particle and atom is in elastic, the energy (E) of the backscattered α particle is proportional to the atomic mass (M). The intensity of spectrum at the particular energy is proportional to the atomic mass of corresponding atoms inside the sample, thereby; the elemental

composition of the sample can be readily obtained by spectrum from the area density analysis. The degree of crystalline order in a film can be determined via RBS by operating the system in ion channeling mode, where α particle are allowed to channel through a specific crystallographic planes.

In this study various new combinations of interfaces and heterostructures such as NAO/STO, PAO/STO and NGO/STO were prepared and investigated. The crystal quality and composition of these newly grown samples were investigated through RBS to verify the final composition and crystal quality of the grown thin films. Figure 3.9 shows the RBS spectrum obtained for NAO thin film grown on STO substrate. The positions of elements in NAO film, and STO substrate in the obtained spectrum matches well with the simulated spectrum. Note that the appearance of corresponding elemental peaks at the specific energy is in accordance with the proportional atomic mass relation (Nd appears at higher energy).

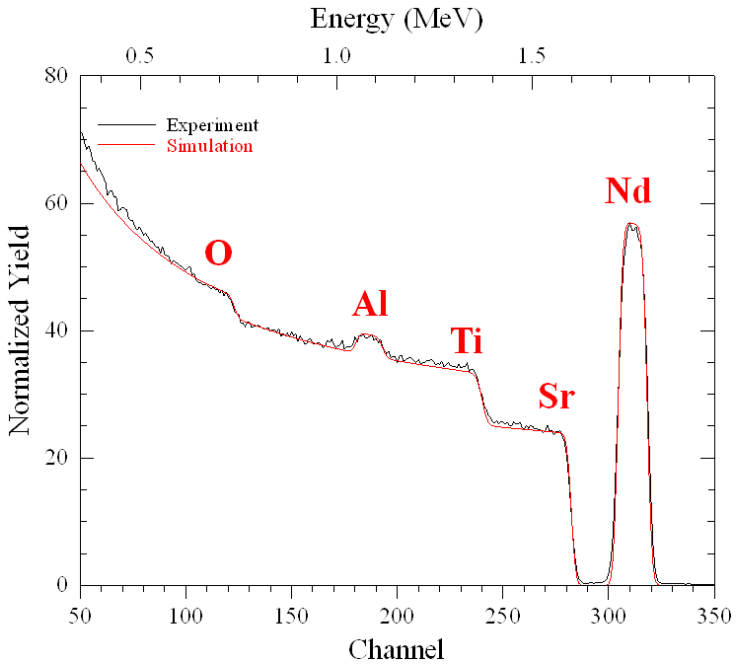

Figure 3.9: The obtained RBS spectrum for the NAO thin film grown on STO (100) substrate, the red curve shows the fitting to the experimental data.

The composition of the thin film is further estimated from intensity spectrum analysis, and the composition is found to be $Nd_{0.2}Al_{0.2}O_{0.59}$ which is almost consistent with the desired stoichiometric $NdAlO_3$composition.The above analysis shows that grown thin films have crystalline quality and maintain stoichiometry during thin film growth.

Having discussed the thin film growth methodology, surface and structural techniques and characterization of substrate and grown thin films, in the following a brief description to the various electrical and magnetic transport measurements that are performed on the samples will be presented.

3.4 Electrical transport measurements

A variety of electrical and magneto transport characterizations on samples were conducted using the Physical Property Measurement System (PPMS, Quantum Design Inc.). The PPMS system is capable of applying magnetic fields up to ± 9T, in a 2- 400 K temperature range with a typical temperature accuracy of ± 0.5%. Temperature can be varied with full sweep capability and ramping rates from 0.02 K/min up to 7 K/min. Temperature stability is ≤ 0.2% for temperatures ≤10 K and 0.02% for temperature >10 K. These transport measurements can also be performed with various magnetic and current orientations to the sample by employing a sample rotator.

The various types of electrical property measurements performed in this work are; basic electronic characterizations including resistance versus temperature, carrier density and mobility and their variation with temperature, magneto resistance (MR), and electric field effects on the interface conducting channel. To perform these electrical measurements Ohmic contacts were made by Al ultrasonic wire bonding onto the sample (performed by West Bond wire bonder machine, with bonding power used from 300-400 W and time of about 30 ms). Since the deposited films mostly have a thickness of a few nanometres, thus penetration of bonded wire from the surface to the interface due to the force allows electrically accessing the interfaces. The Ohmic nature of the contacts is often verified by ***I-V***

measuremet. The samples are typically a square shaped with the dimensions of 5 mm x 5 mm. The conducting behaviour of the samples is investigated by performing resistance versus temperature, R (T) measurements. The R (T) behaviour gives the nature of charge transport. The R (T) measurements were performed in different ways namely Van der Pauw geometry [6] and four point linear geometry as shown in figure 3.10.

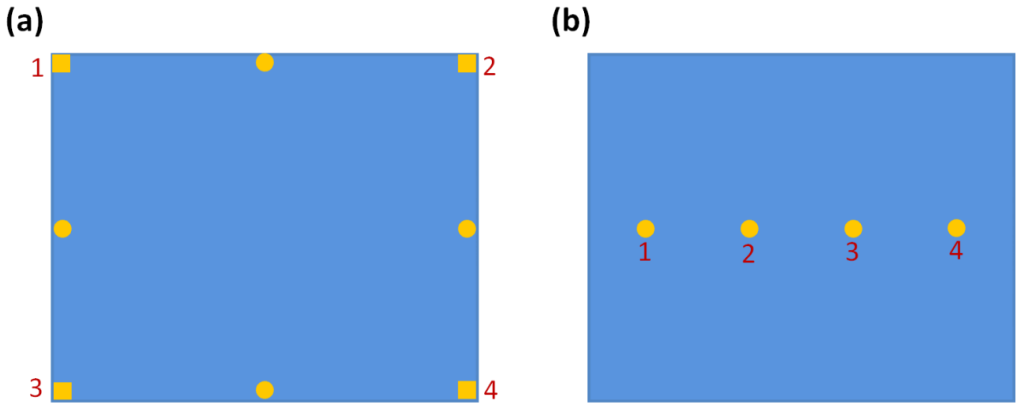

Figure 3.10: Electrical contact geometries: (a) a Van der Pauw geometry, and (b) linear four point geometry.

The Van der Pauw geometry was used to measure the sheet resistance (R_s) and Hall measurements to extract carrier density (n_s) and mobility (μ). In Van der Pauw geometry the electrical contacts were made at the corners of the square sample as shown in figure 3.10a. Here current (***I***) is passed between points 1, 3 or 1, 2 and resistance is measured between 2, 4 or 3, 4, respectively. The resultant R_s is extracted from a Van der Pauw formula. To extract the n_s, contacts were connected in Hall geometry (for example ***I*** is passed between points 1, 4, and Hall resistance is measured between 2, 3). Hall measurements can also be performed by making the contacts at the middle of the edges of the square sample (shown as circular points in the figure 3.10a.). In our observations both Hall geometries yielded similar results. For the Hall measurements the magnetic field was varied between ± 0-9 T. The principle of Hall effect is based on the carrier motion in the

presence of current and perpendicular magnetic field. This results in a charge accumulation at the opposite sides of the sample resulting in Hall voltage and Hall resistance. The carrier density from the Hall measurements can be extracted by a formula given by

$$n = \frac{-1}{R_H \times e}$$

Here R_H is defined as the Hall co-efficient for a material, the R_H can be extracted from the slop of Hall resistance (R_{xy}) versus magnetic field plot which is given by

$$R_H = \frac{R_{xy}}{B}$$

The Hall measurements also give the information about the type of carriers; the sign of R_H distinguishes n-type and p-type charge carriers: negative R_H indicates that the type of carrier is electrons and positive R_H indicates holes.

Figure 3.11 show the Hall resistance versus magnetic field data of a LAO/STO interface sample. The data shows linear variation of R_{xy} with magnetic field. The change of sign of R_{xy} with the polarity of magnetic field is a characteristic of Hall effect. R_H is obtained by extracting the slop of the R_{xy} versus magnetic field plot and thereby the carrier density is derived. The mobility (μ) of carriers was extracted using the relation between conductivity (σ) and carrier density which is given by.

$$\sigma = n\, e\, \mu$$

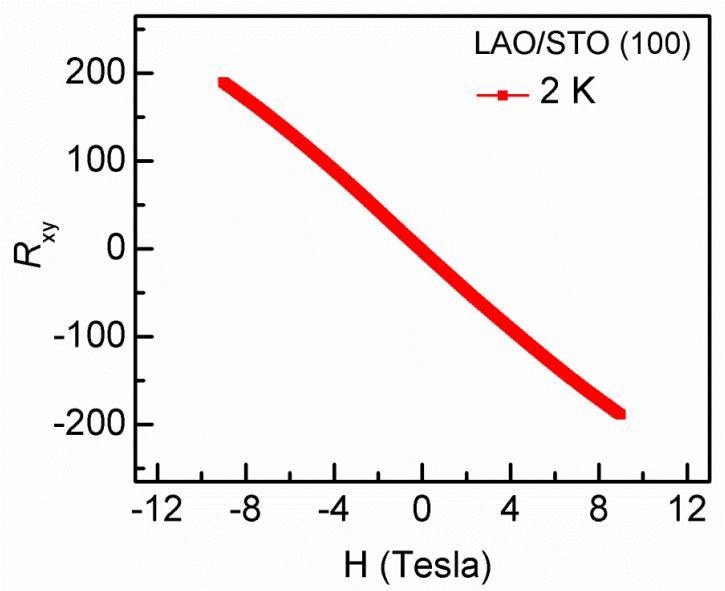

Figure 3.11: R_{xy} versus magnetic field performed on LAO/STO interface.

Generally mobility characterizes the ability of charge carriers to move with in a material. The main factor that defines the mobility is scattering time (τ) and effective mass (m^*) of the carriers (electron here).

$$\mu = \frac{e\,\tau}{m^*}$$

The τ depends on several physical properties of the material and whereas the effective mass m^* depends on the band structure of the material system. Various types of scattering mechanisms such as e-e interactions, e-phonon interactions and a magnetic spin dependent scattering can govern the mobility of the carriers. A distinction among these scattering mechanisms can be made by analysing the temperature dependence of mobility.

In this study, various types of magneto resistance measurements and electric field effect on interface conductivity were performed. To perform the magneto resistance and electric field measurements, linear four probe geometry is used as shown in Fig. 3.10b. The spacing between points was made sure to be equal and

additional care was taken to minimize the issue of misalignment of contact geometry.

3.4.1 Magneto resistance measurements

Magneto resistance (MR) has become one of the important physical properties in material physics ever since the discovery of giant magneto resistance in ferromagnetic layers and colossal magneto resistance (CMR) in manganite systems, which have found a wide range of applications in sensor technology. MR is basically defined as the change in electrical resistance of a material when a magnetic field is applied to the system. The magneto resistance is given by the equation.

$$MR \quad = \frac{R(H) - R(0)}{R(0)} \times 100\ \%$$

$R(H)$, $R(0)$ are the resistance of a material with and without magnetic field, respectively. The origin of MR arises from the influence of scattering of charge carriers in presence of the magnetic field. Depending on the type of scattering involved, MR is classified into various types. The MR that arises from the Lorentz scattering of charge carriers is defined as ordinary MR. When the magnetic field is applied on a current carrying system; electrons experience a cyclotron motion due to Lorentz force which increases the cyclotron frequency of the electron in its closed orbits in quantum limit. However, in a diffusive regime, the electrons would not complete the path to a full circle due to scattering from various scattering centers. This MR only depends on the geometry of the devices and independent of the magnetic property and crystal symmetry of the system. The MR in this case is always positive. Whereas the giant magneto resistance (GMR) which originate from spin dependent scattering of electrons in adjacent ferromagnetic layers that are separated by a metal spacer layer in presence of magnetic field and its direction. The magnitude of GMR depends on the strength

of exchange interaction of electrons between these adjacent layers, is known as Ruderman-Kittel-Kasuya-Yosida (RKKY) interaction [7-9].

In our work, properties at the LAO/STO based hetero interfaces were studied extensively under various MR configurations. The MR experiments were performed in various geometries namely, in-plane and out of plane.

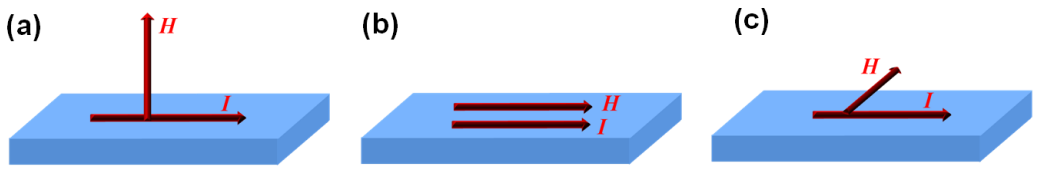

Figure 3.12: Different MR measurement geometries: (a) Out of plane MR. (b) In-plane MR with ***I*** and ***H*** are parallel. (c) In-plane MR with ***I*** and ***H*** perpendicular to each other.

These geometries are defined with respect to the magnetic field and current directions to the sample plane. Figure 3.12a shows MR geometry in out of plane mode, were the ***H*** is applied perpendicular to the plane of the film surface; ***I*** and ***H*** are always perpendicular to each other. In this geometry, the orbital scattering mechanisms such as Lorentz scattering are predominant. Figure 3.12b shows the in-plane MR mode, where the ***H*** and ***I*** are in the plane of the sample surface. As shown, the ***I*** and ***H*** are parallel to each other which results in zero Lorentz force, thus no orbital scattering. For magnetic systems, due to the polarization of magnetic moments in the presence of the external ***H***, there can be MR in this in-plane mode due to the spin dependent scattering. Thus this in plane mode MR is a very useful tool to distinguish orbital scatterings from magnetic spin dependent scattering. Figure 3.12c shows geometry of measuring MR in-pane mode, where the ***H*** and ***I*** are perpendicular to each other but both are in the plane of the sample surface. This mode is useful to investigating the dimensionality effects of

conducting channel, where the orbital scattering strength depends on the dimensionality.

The MR study can help to distinguish numerous physical phenomena. For example, it can clearly gives the distinction among various transport mechanisms starting from metallic, localized (magnetic Kondo scattering) and hopping transports. This distinction can be made by performing the MR in various geometries as described above, and from the temperature dependence of the MR.

In order to investigate the magnetism at the LAO/STO interfaces, we have performed more specific magneto resistance measurements known as anisotropic magneto resistance (AMR) and planar Hall effect (PHE). AMR is a relativistic magneto transport phenomenon that arises from combined effects of spin-orbit interaction and ferromagnetically ordered state coupled to symmetry of the system. In AMR measurement, both ***I*** and ***H*** are always in-plane of the interface and the angle between ***I*** and ***H*** is varied from 0° to 360°. The origin of AMR lies in the anisotropy of the magnetization with respect to the crystal symmetry and spin-orbit interaction. The measurement geometries for both AMR and PHE are shown in the figure 3.13.

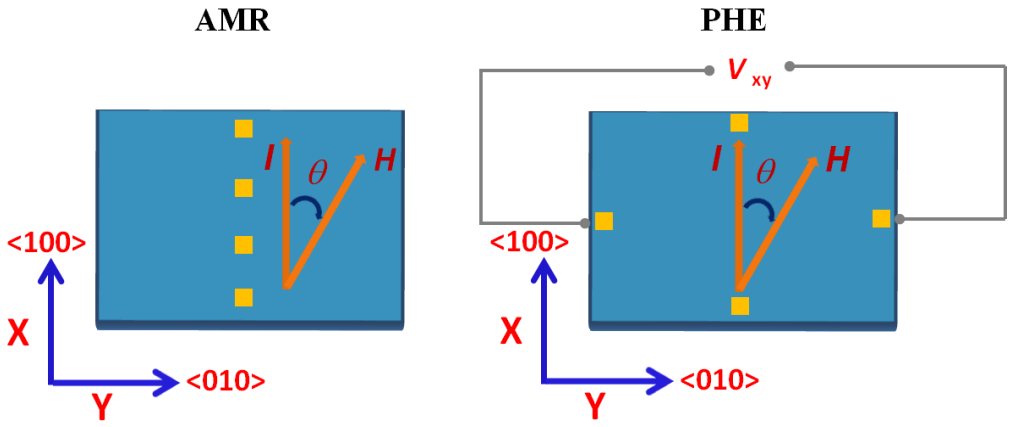

Figure 3.13: Measurement and contact geometry for AMR and PHE.

On the other hand planar Hall effect (PHE) is similar type of magneto resistance measurement but it measures the transverse component of resistivity (ρ_{xy}). In the PHE measurement both the ***I*** and ***H*** are in the plane of the thin film, but resistivity measured in transverse direction.

The mathematical expressions for resistivity components, corresponding to AMR (ρ_{xx}) and PHE (ρ_{xy}), respectively, are given by

$$\rho_{xx} = \rho_{\perp} + (\rho_{||} - \rho_{\perp}) \cos^2 \theta$$

$$\rho_{xy} = \frac{1}{2} (\rho_{||} - \rho_{\perp}) \sin 2\theta$$

Here $\rho_{||}$ and $\rho_{\perp}$ are the resistivity measured when ***I*** and ***H*** parallel and perpendicular respectively and θ is the angle between ***I*** and ***H***. However, the above equations for AMR and PHE are applicable only for general non crystalline and polycrystalline cases. A phenomenological model [10] used for the interpretation of AMR in crystalline samples. The phenomenological model includes the higher order terms in the resistivity tensor considering the symmetry of the systems. The resistivity expression for the AMR in crystalline case is given by MacLaurin's series expansion of resistivity tensor as

$$\rho_{ij} = a_{\mathrm{ij}} + a_{\mathrm{kij}} \alpha_k + \cdots$$

Here a_{ij} , a_{kij} are elements of resistivity tensor of various orders, α is the direction cosines, of the magnetization, where as *i* and *j* are in any of the three orthogonal directions. Due to the symmetry considerations most the terms vanish and for a cubic symmetry system the above expression can be expressed as

$$\rho_{xx} = C_0 + C_1 \cos^2 \theta + C_2 \cos^4 \theta + \cdots$$

$$\rho_{xy} = C_4 \operatorname{Cos} \theta \operatorname{Sin} \theta$$

Here C_0, C_1, C_2 are the coefficients related to the crystalline anisotropy associated with the crystal symmetry of the system [11]. Thus the investigation of AMR and PHE enable to explore the anisotropy of the magnetic property couple to the crystal symmetry. Further, in magnetic systems the observed ρ_{xy} in PHE is linked to the in-plane magnetization with a relation given by

$$\rho_{xy} = \frac{k}{t} M_{||}^2 \sin 2\theta$$

Here $M_{||}$ is the in-plane component of the magnetization, and *t* is the thickness of the film, k is the constant related to anisotropic magneto resistance constant, respectively.

In this thesis work, the investigation of AMR and PHE is carried out under various experimental variables such as temperature, magnetic field and electric field to the interface. These effects are analyzed with respect to the spin-orbit interaction and crystal symmetry of the system by using the phenomenological model discussed above.

3.4.2 Electric field effect

The electric field tuning of the electric properties at the LAO/STO interfaces has been shown to create several novel phenomena such as insulator-metal transition and tunable ground state of two-dimensional superconductivity. The external electric field applied to a material attracts or repels charge carriers, resulting in charge accumulation or depletion from the channel modifing the electric properties dramatically. The characteristic width of the accumulation or depletion regimes is given by the electro static screening length λ_{el}, is also called as Thomas–Fermi length. To have feasible electric field effects large screening lengths are needed i.e effectively 2D system. Conventional metallic systems have very short length scales due to the large carrier densities in the order of 10^{15}cm^{-2} and therefore negligible field effects were observed [12]. On the other hand

LAO/STO interfaces have carrier densities in the order of $10^{13}cm^{-2}$ with dimensions of the conducting channel of few a nanometres which make them ideal for field effect studies. The polarization ($\boldsymbol{\sigma}$), or areal carrier density (charge cm^{-2}) that can be induced at given gate voltage VG applied across an gate insulator of thickness ***t*** is given by

$$\sigma = \int_0^{V_G} \varepsilon_0 \, \varepsilon_r(V)/ \; t \; dV$$

Here $\boldsymbol{\varepsilon_r}$ is the relative dielectric permittivity of the gate dielectric material. The above equation suggests that there can be two ways to increase the electric field effects either by applying large gate voltage or to use a large $\boldsymbol{\varepsilon_r}$ gate material.

In this thesis work, the properties of the 2DEG at the LAO/STO interfaces have studied extensively under the applied electric field. These gating measurements were further utilized in the investigation of properties such as spin-orbit interaction and AMR studies.

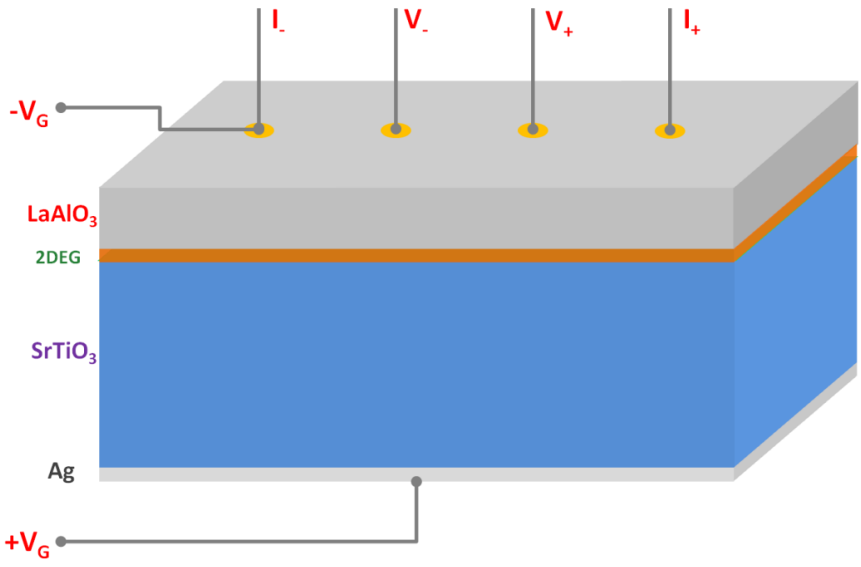

Figure 3.14: Schematic of the electric field effect measurement configuration for the LAO/STO interface sample.

The 2D carrier confinement and tunable carrier density at the LAO/STO interfaces enable to tune the interface properties. The Schematic of the electric field effect device configuration for the LAO/STO interface samples is shown in the figure 3.14. The electric field effect measurements on LAO/STO interfaces were performed by applying the electric potential (voltage) to STO which is used as the gate material. STO (back gate) is preferred over LAO (top gate) due to the large dielectric constant $\boldsymbol{\varepsilon_r}$ of 10,000 at low temperature. This unusual dielectric response of STO at low temperatures let to show the pronounced electric field effect on LAO/STO interfaces. The back electrode for the STO is provided by applying Silver (Ag) epoxy to the STO back surface. During this gate electrode preparation, precautions were taken to avoid any lateral conduction that leaks the charge to the interface. The leakage currents were monitored through a source meter and it was made sure that it is below 1 nA (nano Ampere) during the measurements. The source terminals ($\boldsymbol{I}$_) of the channel are made as common terminal for both gate ($-\mathbf{V}_G$) and channel. The electric contacts for the channel were made through Al wire bonding to the interface. The Ohmic nature of the contacts was verified through ***I-V*** measurements. Linear probe contact geometry is used for conventional resistance measurements and Hall geometry is employed for carrier density measurements. In this study the gate induced electric field effects are performed in the investigation of the spin-orbit interaction. In the following a brief introduction to the spin-orbit interaction is given.

References:

[1] D. Dijkkamp, T. Venkatesan, X.D. Wu, S.A. Shaheen, N. Jisrawi, Y.H. Min-Lee, W.L.McLean, M. Croft, "Preparation of Y-Ba-Cu oxide superconductor thin films using pulsed laser evaporation from high T_c bulk materials," *Appl. Phys. Lett*. 51 619 (1987).

[2] X.D. Wu, T. Venkatesan, A. Inam, X.X. Xi, Q. Li, W.L. McLean, C.C. Chang, D.M.Hwang, R. Ramesh, L. Nazar, B. Wilkens, S.A. Schwartz, R.T. Ravi, J.A. Martinez, P.England, J.M. Tarascon, R.E. Muenchausen, S. Foltyn, R.C. Estler, R.C. Dye, A.R.Garcia, N.S. Nogar, "Pulsed laser deposition of high T_c superconducting thin films: present and future," *Mater. Res. Soc. Symp. Proc.* 191, 129 (1990).

[3] http://www.material.tohoku.ac.jp/~kaimenb/e_genri.html#heed.

[4] M. Kawasaki, K. Takahashi, T. Maeda, R. Tsuchiya, M. Shinohara, O. Ishiyama, T. Yonezawa, M. Yoshimoto, H. Koinuma, "Atomic control of the $SrTiO_3$ crystal surface," *Science*, 266, 1540-1542 (1994).

[5] G. Koster, B. L. Kropman, G. J. H. M. Rijnders, D. H. A. Blank, and H. Rogalla, "Quasi-ideal strontium titanate crystal surfaces through formation of strontium hydroxide," *Appl. Phys. Lett*, 73, 2920-2922 (1998).

[6] L. J. van der Pauw, "A method of measuring the resistivity and Hall coefficient on Lamellae of arbitrary shape," *Philips Technical Review*, 20, 220-224 (1958).

[7] M.A. Ruderman and C. Kittel, "Indirect Exchange Coupling of Nuclear Magnetic Moments by Conduction Electrons", *Phys. Rev.* 96, 99 (1954).

[8] T. Kasuya, "A Theory of Metallic Ferro- and Antiferromagnetism on Zener's Model", *Prog. Theor. Phys*. 16, 45 (1956).

[9] K. Yosida, "Magnetic properties of Cu-Mn alloys", *Phys. Rev.* 106, 893 (1957).

[10] T. R. McGuire, and R. I. Potter, "Anisotropic magneto resistance in ferromagnetic 3*d* alloys", *IEEE Trans. Magn*. 11, 1018 (1975).

[11] C. R. Hu, J. Zhu, G. Chen, J. X. Li, Y. Z. Wu, "Fourfold symmetry of anisotropic magnetoresistance in epitaxial Fe_3O_4 thin films," arXiv:1105.5781.

[12] C. H. Ahn, J. –M. Triscone, and J. Mannhart. "Electric field effect in correlated oxide systems," *Nature* 424, 1015-1018 (2003).

Chapter 4

Investigation of carrier confinement and electric field effects on magnetic interactions at the $LaAlO_3/SrTiO_3$ interfaces

Abstract

In this chapter, the electric and magnetic properties at the LAO/STO (100) interface are investigated under various growth parameters such as LAO layer thickness and oxygen pressure during growth. The LAO/STO interfaces show insulator to metal transition with critical LAO thickness, and a thickness dependence localization behavior. In order to probe the magnetic ordering and its possible anisotropy with crystallography, the magnetic interactions at the interface are investigated through specific anisotropic magneto resistance (AMR) and planar Hall effect (PHE) measurements on LAO/STO (100) interfaces and heterostructure of LAO/STO grown on $NdGaO_3$ (110) substrates. These measurements were performed as a function of magnetic field, temperature and electric field which reveal the presence of the predominant magnetic interactions at the LAO/STO interfaces. Specifically fourfold oscillation in the AMR and large PHE are observed. The carrier confinement effects on the AMR are evaluated and it is found that the fourfold oscillation appears only for the case of 2DEG samples while it is twofold for the 3-dimensional case. The fourfold oscillation fits well to the phenomenological model for a cubic symmetry. Thus this oscillation behavior is attributed to the anisotropy in the magnetic scattering arising from the interaction of itinerant electrons with the localized magnetic moments coupled to the crystal symmetry. The AMR behavior is further found to be sensitive to applied gate electric field, emphasizing the significance of spin-orbit interaction at the interface. These confinement effects suggest that the magnetic interactions are predominant at the interface, and the gate electric field modulation of AMR show the possibility for electric field tuning of magnetic interactions. The observed

large PHE further indicates that the in plane nature of magnetic ordering arises from the in-plane Ti 3d_{xy} orbitals.

4.1. Introduction

As discussed earlier the growth parameters and conditions of the LAO/STO interfaces are very crucial for the properties of the interfaces such as insulator-metal transition with LAO layer thickness, superconductivity and magnetism with oxygen pressure during growth. In spite of the extensive research, a clear picture of interplay between these electronic and magnetic phenomena and the growth parameters and sample configurations is less understood. In this chapter, the electric and magnetic properties at the LAO/STO (100) interface are investigated under various growth parameters such as LAO layer thickness and oxygen pressure during growth, which can be used to control the degree of carrier confinement at the interface.

With this frame work, several LAO/STO interface samples were prepared under different growth parameters. First, the electrical transport properties of the LAO/STO interfaces are investigated, which includes the dependence of the interface conductivity to the LAO thickness and growth oxygen pressure. To investigate the nature of magnetic interactions in the LAO/STO based hetero interfaces, detailed magneto resistance measurements were carried out on several samples under various parameters such as growth oxygen pressure, confinement of electron gas, and electric field. The results for the electric and magnetic interactions at the interface are discussed in the carrier confinement picture.

4.2. Transport properties of the $LaAlO_3/SrTiO_3$ (100) interfaces

4.2.1 $LaAlO_3$ thickness dependence

For the LAO layer thickness dependence study, LAO/STO (100) interface samples with various LAO layer thicknesses were prepared using PLD by ablating LAO target onto the TiO_2 terminated STO (100) substrate. The growth oxygen pressure (P_{O2}) for the samples during the deposition was fixed at 1×10^{-3} Torr. The growth temperature was set to be 720 ^{o}C. Precise control of the thickness of LAO is achieved by RHEED monitoring. Transport and Hall effect

measurements were performed on the samples using standard van der Pauw geometry from which carrier density (n_s) and mobility (μ) of the samples were extracted.

Figure 4.1 shows the variation of room temperature conductivity and the n_s as a function of number of LAO unit cells (uc).

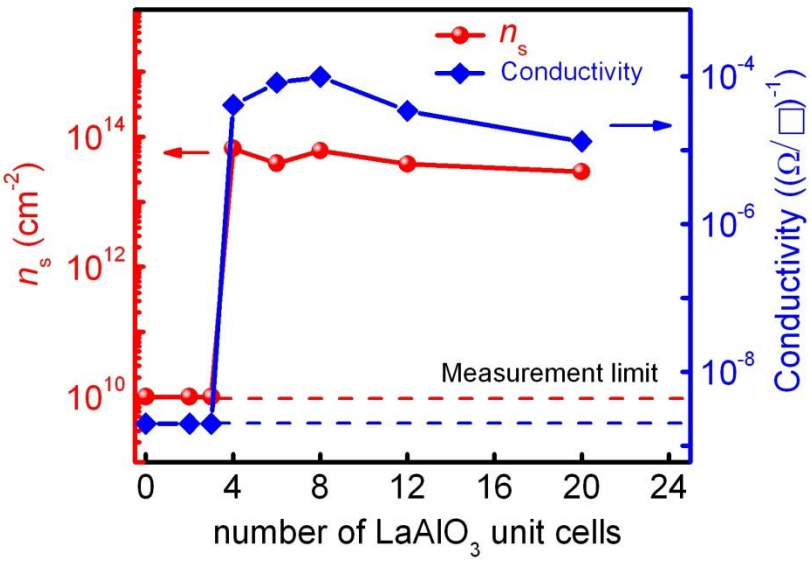

Figure 4.1: Room temperature conductivity and carrier density, n_s of LAO/STO samples as a function of number of LAO unit cells.

Clearly, a distinguishable insulator-to-metal transition in conductivity is found for the samples at about LAO thicknesses of 3-4 uc. The change in conductivity is more than 3 orders of magnitude between the conducting and insulating states (instrument measurement limit). Simultaneously, the n_s also changes almost 3 orders of magnitude across the insulator-to-metal transition. Above the critical thickness of 4 uc, the n_s saturates at a value of the order of 10^{13}cm^{-2}. This insulator-to-metal transition behavior is found only to depend on the thickness of the LAO layers and independent of deposition time (i.e. growth rate of LAO layers). The property of insulator to metal transition at the LAO/STO interface

was first reported by Thiel *et al*. [1]. J. Levy and co-researchers exploited this property for nano-scale charge writing by conducting AFM, where the insulating ground state of a 3 uc sample is manipulated and transformed into a metallic state locally by applying gate voltage to the interface through AFM tip [2].

However, for the samples with thicker LAO layers (> 3 uc) a slight decrease is observed in both conductivity and n_s. To understand this behaviour the temperature dependence of the sheet resistance R_s (T) for the LAO/STO interface samples with various LAO thicknesses was measured in the temperature range between 300 to 2 K. As shown in figure 4.2, the sample with LAO thickness of 4 uc shows a typical metallic behavior with R_s decreasing throughout the temperature range down to 2 K with R_s is about 200 Ω at 2 K, albeit with small localization (upturn in R_s) at low temperatures.

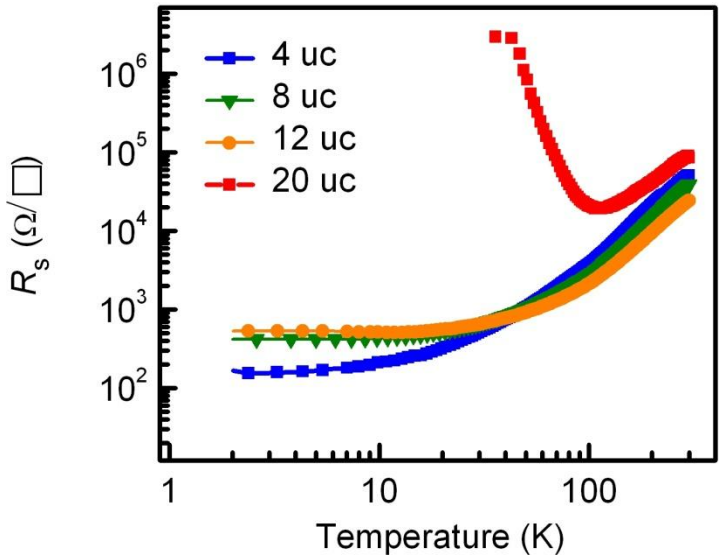

Figure 4.2: The R_s (T) behavior of the LAO/STO samples with various LAO thicknesses.

It is found that these thinner LAO samples have often become superconducting at mK temperatures with relatively higher mobility and they also favorable for

quantum transport. However, as the thickness of LAO increases the samples start to show the localization behavior from weak (8, 12 uc samples) to strong (20 uc) localizations. In these samples, the R_s at 2 K are also found to increase with the increase in LAO thickness. The sample with 20 uc LAO thickness shows a dramatic effect of localization. The 20 uc sample show measurable R_s only up to 20 K with the resistance in order of ~MΩ indicating strong localization of electrons and this result in an insulating state below 20 K. The transport properties presented above are consistent with the published literatures [1, 3]. In the following, the properties of LAO/STO interface are investigated with respect to the samples growth oxygen pressure.

4.2.2 Growth oxygen pressure dependence

To investigate the effect of growth oxygen pressure (P_{O2}) dependence on the LAO/STO interface properties, samples were grown in different P_{O2} ranging from 1×10^{-5} to 5×10^{-3} Torr with a fixed LAO thickness of 8 uc on TiO_2 terminated $SrTiO_3$ (100) substrates. Figure 4.3a shows the R_s (T) behavior for the corresponding samples. The samples grown with $P_{O2} \geq 1\times10^{-4}$ Torr show the typical metallic behavior with room temperature R_s of about 20 KΩ. On the other hand the sample grown at low P_{O2} of 1×10^{-5} Torr shows metallic behavior but with very low R_s of about 20 Ω at room temperature, a 3 order of magnitude drop in resistance compared to the high P_{O2} samples. The P_{O2} dependence of $R_s(T)$ shown here is consistent with earlier reports [4, 5]. Stronger effects of growth P_{O2} can be seen in the n_s dependence with temperature for the corresponding samples shown in figure 4.3b.

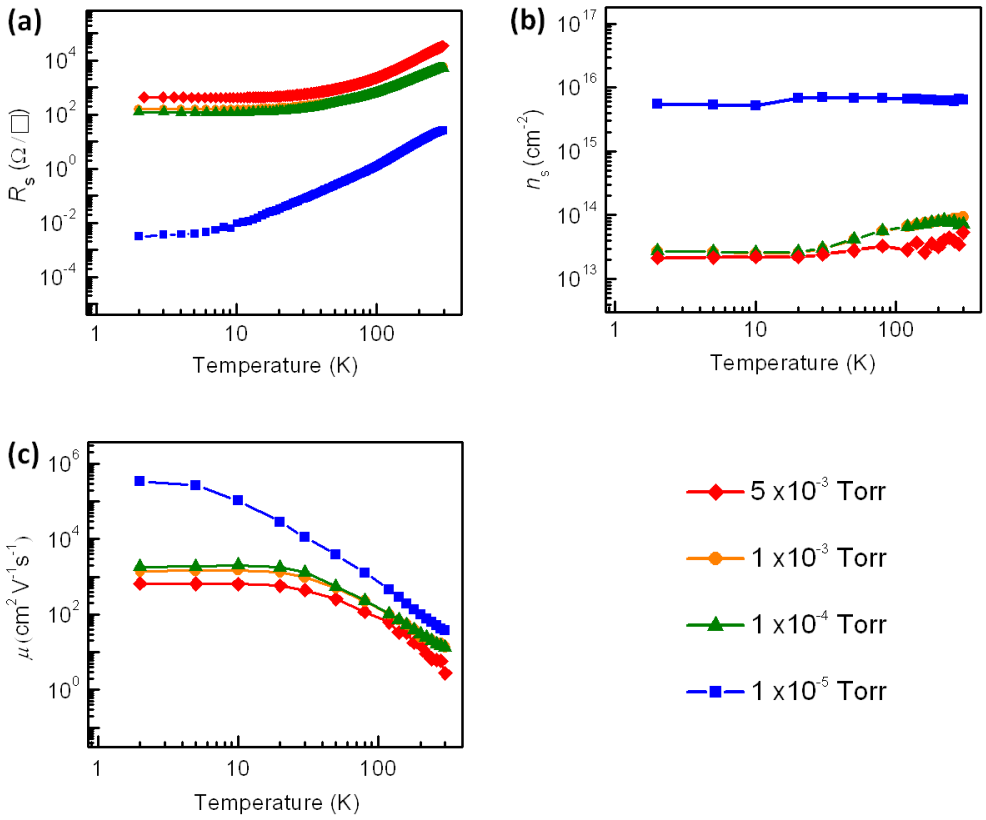

Figure 4.3: Temperature dependence of transport properties of LAO/STO samples grown at different oxygen pressures. (a) Sheet resistance, $R_s(T)$. (b) Carrier density, $n_s(T)$. (c) Mobility, $\mu(T)$.

For the high P_{O2} samples, the n_s is of the order of 5-8 $\times 10^{13}$ cm^{-2} at 300 K and about ~2-3$\times 10^{13}$ cm^{-2} at 2 K, whereas for the low P_{O2} (1×10^{-5} Torr) sample the n_s is about 9×10^{15} cm^{-2} at 300 K and 6×10^{15} cm^{-2} at 2 K. The large n_s observed in low P_{O2} sample arise from the creation of oxygen vacancies due to the surface reduction in STO itself. Figure 4.3c shows the temperature dependence mobility, $\mu(T)$. For the high P_{O2} samples, the μ is of the order of 5 cm^2 V^{-1} s^{-1} at 300 K and 1000 cm^2 V^{-1} s^{-1} at 2 K, whereas for the low P_{O2} sample the μ is about 30 cm^2 V^{-1} s^{-1} at 300 K and 50,000 cm^2 V^{-1} s^{-1} at 2 K showing the high mobility nature of the low $P_{O2\,2}$ grown samples.

Based on the above observation the growth regime can be divided in to three regimes. The P_{O2} range of 1×10^{-5} Torr or less is called the low pressure regime.

Samples prepared in this regime produce a three-dimensional (3D) like conductivity with n_s in the order of 10^{16} cm^{-2}. Further, these samples generally show a Fermi liquid type metallic behavior and often undergo superconductivity at mK temperatures. The samples grown in intermediate P_{O2} ranges of 1×10^{-3} to 1×10^{-4} Torr generally tend to show the magnetic character with localization effects and also low temperature superconductivity. However, the samples deposited under P_{O2} above 1×10^{-3} Torr produce pronounced magnetic effects with strong localization. These high P_{O2} grown samples produce strictly two-dimensional (2D) conductivity with n_s of the order ~10^{13}-10^{14} cm^{-2}. The character of the dimensionality of the carriers described above was investigated and confirmed by a conducting AFM experiment on a cross-section of the LAO/STO interface by Basletic *et al*. [6] where it is found that the dimensionality of the conducting channel is micrometers for the 3D case, and a few nanometers for 2D case. The above dimensionality observations have been investigated further through magneto resistance experiments [7] and this shows that dimensionality is one of the parameters that can be utilized to control the properties of the electron gas.

4.3. Magnetic interactions at the $LaAlO_3/SrTiO_3$ interface

One of the fascinating properties that emerged from P_{O2} phase diagram is the magnetism at this non-magnetic LAO/STO interface. The magnetic effects were first reported by Brinkman *et al*. [5] with a signature of Kondo effect in samples prepared at relatively higher P_{O2}. Subsequently, Ariando *et al*. [8] reported electronic phase separation at this interface by exploiting specific STO surface preparations and P_{O2} and it is shown that the strength of the magnetism depends on growth P_{O2}. Further, the magnetic origin at this interface is confirmed by direct imaging of magnetic patches using scanning SQUID [9].

One common issue with the magnetism is anisotropy. Has the magnetic moment has specific crystallographic preference? In scanning SQUID experiment [9], the magnetic moment distribution near the interface is examined and a signature of

some forms of anisotropy within the plane of interface is found. However, no information about the anisotropy with respect to crystallographic symmetry is found. The origin of the magnetism in the LAO/STO interface is believed to be arising from the localized 3*d* orbitals. Owing to the preferential occupancy, particularly to the Ti $3d_{xy}$ orbitals at the interface, various reports have presumed that the magnetization predominantly is in the plane of interface [8-10]. The magnetism arising from 3*d* orbitals can show a tendency of crystallographic anisotropy due to strong spin-orbit interaction. Thus investigation of anisotropy of magnetic ordering in this system is necessary to map the magnetic phase diagram at the interface.

An effective alternative way for probing these low dimensional and relatively weak magnetic interactions is by the magneto transport measurements. Recently, Dikin *at al*. [11] investigated the magnetic order at the LAO/STO interfaces through in-plane magneto resistance (MR) measurements and showed a hysteresis behavior in the resistance with magnetic field which is a signature for the presence of magnetic ordering. A natural way to further probe this magnetic anisotropy is by investigating the angle dependence of in-plane magneto resistance, *i.e*., anisotropy magneto resistance (AMR) and planar Hall effect (PHE), which directly relate to the magnetic scattering of itinerant electrons associated with the spin-orbit interaction in the system. The LAO/STO interface exhibits a strong spin-orbit interaction [12] due to the broken symmetry near the interface.

In the following a detailed study of various in-plane MR measurements performed on the LAO/STO samples prepared under various P_{O2} is presented (These pressure dependence samples correspond to those shown in figure 4.3). First, comprehensive MR data (including AMR and PHE) is presented for the LAO/STO interface sample deposited at 1×10^{-4} Torr. These MR measurements were performed with respect to various parameters such as magnetic field, temperature and gate electric field. The results are further compared with the AMR data obtained for the LAO/STO samples prepared at low as well as high

P_{O2}, and with that of LAO/STO heterostructure grown on NGO(110) substrate. The acquired data is interpreted with respect to carrier confinement effects on magnetic interactions.

4.3.1 In-plane magneto transport

The in plane magneto transport measurements are summarized in figure 4.4.

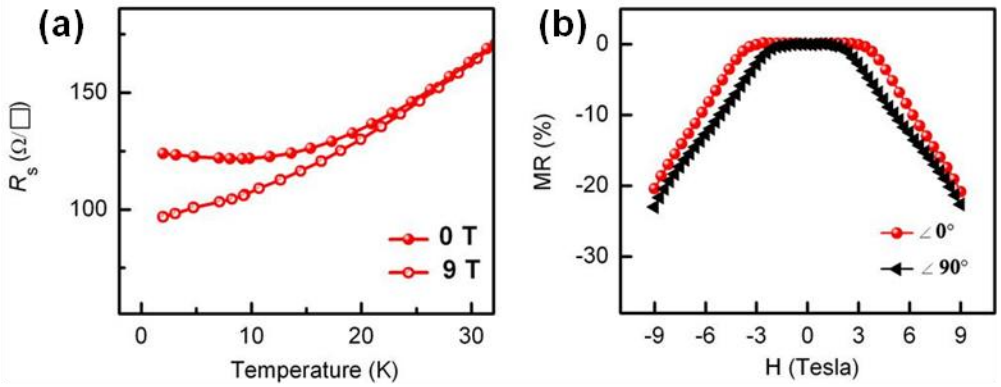

Figure 4.4: Magneto transport properties of LAO/STO interface simple prepared at 1×10^{-4} Torr. (a) The R_s (T) measured with the in-plane magnetic field of 0 and 9 T. (b) In-plane magneto resistance (MR) measured with fixed angle ($\theta = \angle 0^o$, $\angle 90^o$) between ***I*** and ***H*** at 2 K and 9 T.

Figure 4.4a shows R_s (T) measured for the LAO/STO sample deposited at 1×10^{-4} Torr (LAO thickness of 8 uc) with 0 and 9 T magnetic fields applied in-plane to the interface. For the 9 T case, the R_s starts to deviate (decrease) from 0 T case at temperatures at about 25 K, indicates a negative MR. The negative MR is a signature of a spin dependent magnetic scattering. The contribution from conventional orbital and Lorentz scattering to this MR can be excluded as the measurement is performed in in-plane mode, where the Lorentz forces are negligible. Figure 4.4b shows the MR measured at 2 K in two different in-plane modes (***I*** || ***H***, and ***I*** ⊥ ***H***), which clearly show the negative MR in both cases. There appears a critical magnetic field above which the MR starts to change

significantly. The significant difference in MR behavior between these two measurement modes is the change in the critical magnetic field, with critical fields for ***I*** || ***H***, and ***I*** ⊥ ***H*** modes are 1.5 T and 3 T respectively. The origin of this behavior could due to the additional contribution from orbital scatterings specifically in ***I*** ⊥ ***H*** mode. These in-plane MR measurements confirm the presence of magnetic interactions at the LAO/STO interface. The anisotropy property of these magnetic interactions is further investigated through precise in-plane magneto transport measurements namely, AMR and PHE that are discussed in the following.

4.4 Anisotropic magneto resistance and planar Hall effect at the $LaAlO_3/SrTiO_3$ interface

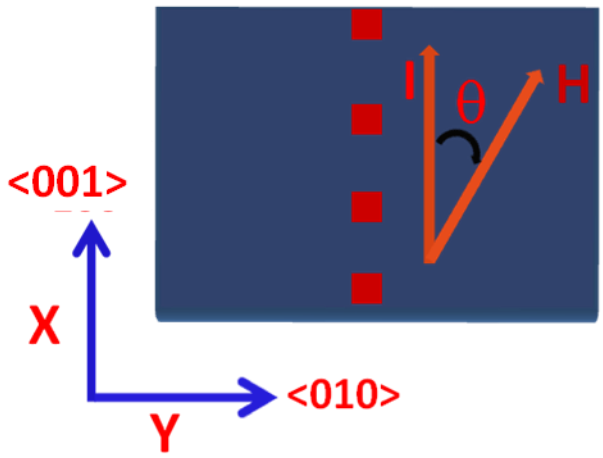

Figure 4.5: Schematic of AMR measurement geometry.

In anisotropic magneto resistance (AMR) measurement, both the magnetic field (***H***) and current (***I***) are in the plane of the sample, and the angle between ***H*** and ***I*** is varied from 0° to 360°. Here, ***I*** is fixed along the <100> crystallographic direction (schematic depicted in figure 4.5). Here the AMR is defined as

AMR=($R(\theta)$-R (0)/$R(0)$) ×100%, θ is the angle between ***H*** and ***I***, and $R(0)$ is the resistance when ***H*** and ***I*** are parallel to each other.

4.4.1 Magnetic field and temperature dependence of AMR

The AMR is investigated first with respect to the magnetic field and temperature. Figure 4.6a shows the AMR measured at 2 K with varying ***H*** from 3 to 9 T on the LAO/STO sample grown at 1×10^{-4} Torr.

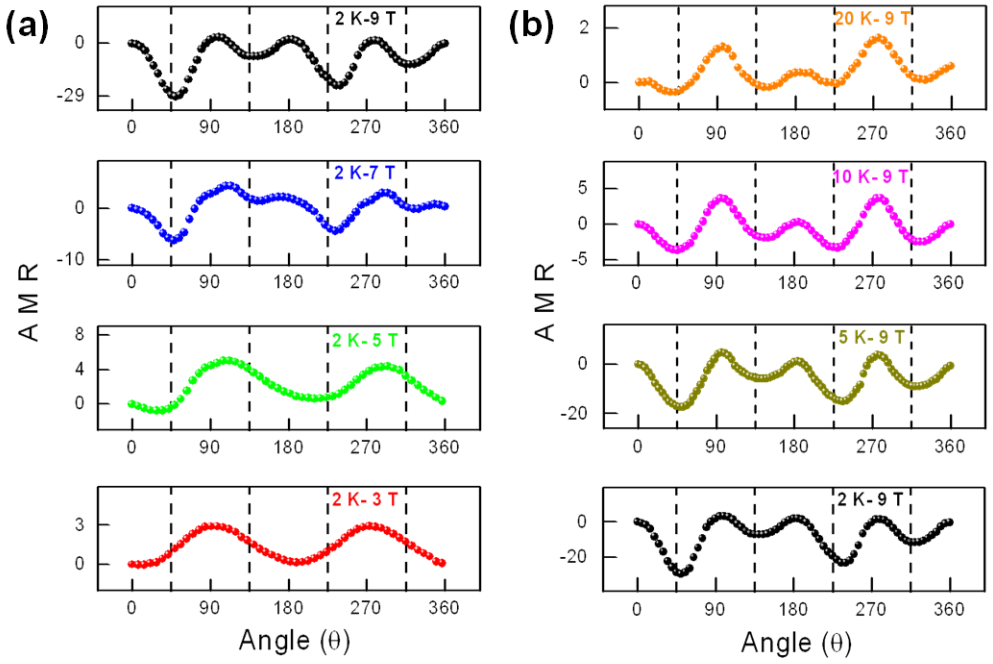

Figure 4.6: (a) AMR measured at 2 K with varying magnetic field 3-9 T. (b) AMR measured at 9 T with varying temperature for the LAO/STO interface sample grown at 1×10^{-4} Torr.

From the figure 4.6a it is clear that AMR shows a significant variation with respect to the angle between ***H*** and ***I***. For the AMR measured at 9 T, a clear fourfold oscillation (AMR oscillation with angle showing four minima/maxima between 0° and 360°) is observed with resistance minima appears at an angle 45°

to the principal {100} directions are repeats every interval of 90°. When ***H*** is decreased, a clear decrease in the amplitude of the fourfold oscillation and simultaneously a gradual transformation from fourfold to twofold (AMR with two minima/maxima) oscillation are observed. At ***H***=3 T, the oscillations turn completely into twofold with resistance maxima appear at 90° and 270° with an interval of 180°. A noticeable observation here is the change of the AMR sign from negative for the fourfold oscillation to positive for the twofold oscillation. The AMR variation is further measured with respect to temperature. Figure 4.6b shows the AMR measured with varying temperature from 2 to 20 K at ***H***=9 T. In this case, the fourfold oscillation in the AMR gradually decreases when the temperature increases and simultaneously a twofold oscillation emerge at higher temperatures. At 20 K the AMR start to transform into a twofold behavior. A similar kind of oscillation behavior in AMR has been previously reported in magnetic systems such as manganites [13-16] and Fe_3O_4 [17]. Very recently, a signature of AMR is also observed at the LAO/STO interfaces [18, 19]. Strikingly, all the above mentioned systems possess *d*-orbital characters. This suggests that the magnetic interactions arising from the *d*-orbitals is crucial for the observed fourfold oscillation.

A phenomenological model is widely used to quantitatively describe the AMR and PHE in various systems [20, 21]. This model is used to explain the AMR behavior in several 3*d* ferromagnetic magnetic systems (details of the model are discussed in chapter 3). In this model, the resistivity tensor is expressed in terms of the direction of current with respect to the applied magnetic field. The fourfold oscillation behavior in the AMR is suggested to be arising from the contribution of higher order terms in the resistivity tensor relating to the crystal symmetry of the system [20]. For the cubic symmetry system, the variation in resistance with angle (θ) is expected to follow the equation containing direction cosines of higher order given by:

$$R_{XX} = C_0 + C_1 \cos^2(\theta + \theta_c) + C_2 \cos^4(\theta + \theta_c) \quad (1)$$

$$R_{XY} = C_3 \sin\theta \cos\theta \quad (2)$$

Here R_{XX} corresponds to the AMR whereas R_{XY} to the PHE. The coefficients C_1, C_2 and C_3 are to arising from the uniaxial and cubic components of magnetization and C_0 and θ_c are additive constants introduced to take the observed asymmetry in the magnitude in the four oscillations into account. Figure 4.7a shows a fitting for the experimental AMR data measured at 2 K and 9 T by equation 1, showing a good agreement with the above formula. Onether striking observation is the asymmetry in the magnitudes between the maxima or minima in the fourfold oscillation. If one considers just the crystalline anisotropy then symmetric amplitudes are expected. However, the fact that we see a strong asymmetry strongly suggests that there is further uniaxial anisotropy present in the system.

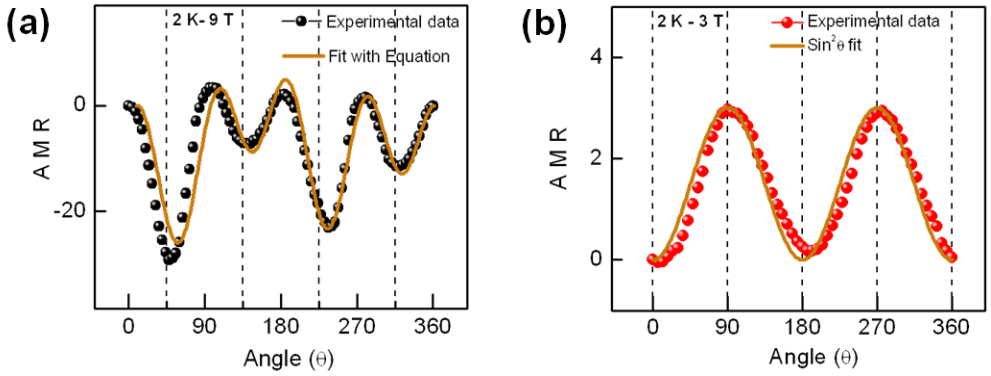

Figure 4.7: (a) A phenomenological model formula fit to the AMR obtained at 9 T and 2 K. (b) $Sin^2\,\theta$ fit for the AMR obtained at 3T and 2 K.

Such anisotropy with respect to the crystal symmetry probably arises because of Fermi surface reconstruction of the various 3*d* orbitals at the interface. The good agreement of experimental data with the model implies the predominant role of crystal symmetry on the magnetic interactions at the LAO/STO interface.

Further, the twofold oscillation in AMR observed at 2 K and 3 T is found to follow a $\sin^2\theta$ dependency. The corresponding $\sin^2\theta$ fit for the twofold oscillation

is shown in figure 4.7b which matches the experimental data accurately. The origin of the twofold oscillation can be from the Lorentz scattering of charge carriers which follows the $\sin^2\theta$ dependency. The transformation of the fourfold to twofold oscillations infers that there are two competing components (spin and charge scatterings) for the AMR, and their contribution to AMR depends on parameters such as magnetic field and temperature. The evolution of fourfold oscillation from twofold oscillation for the magnetic field $\boldsymbol{H} > 3$ T implies that a critical field strength is needed for of the coherent magnetic scattering to overcome the charge scattering. Furthermore, the signature of the four fold AMR starts to diminish for higher temperatures (above 20 K) which could be due to the diminishing of coherence scattering as thermal fluctuations become dominant.

4.4.2 Current dependence of AMR

The AMR was further investigated by varying the magnitude of the current (***I***). Figure 4.8 shows the corresponding AMR behavior measured at 2 K and 9 T for the ***I*** ranging from 0.5 μA-0.5 mA. The data clearly shows that the observed fourfold oscillation behaviour has no ***I*** dependence. This explicitly rules out the possibility of contribution from any activated carrier behavior due to the continuous application of ***I*** and possible thermal effects on sample to the observed AMR behavior. It implies that the orientation and magnitude of the magnetic fields are the only key parameters in the observed AMR.

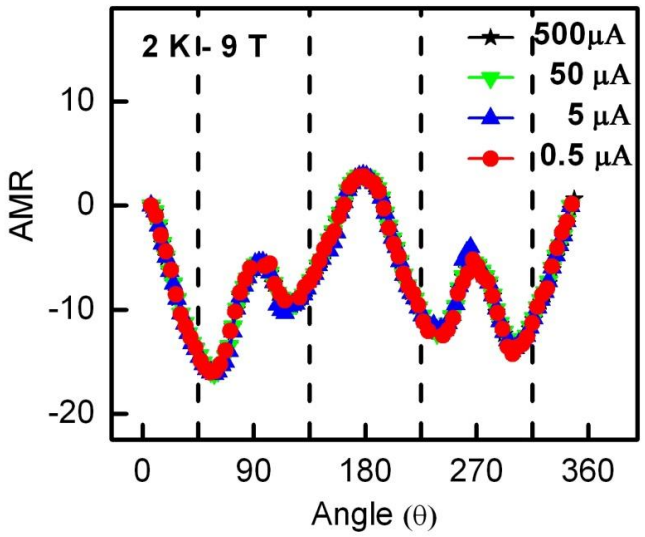

Figure 4.8: AMR measured with different magnitudes of current (***I***) for the LAO/STO interface sample prepared at 1×10^{-4} Torr at 2 K and 9 T.

4.4.3 Electric field effect on AMR

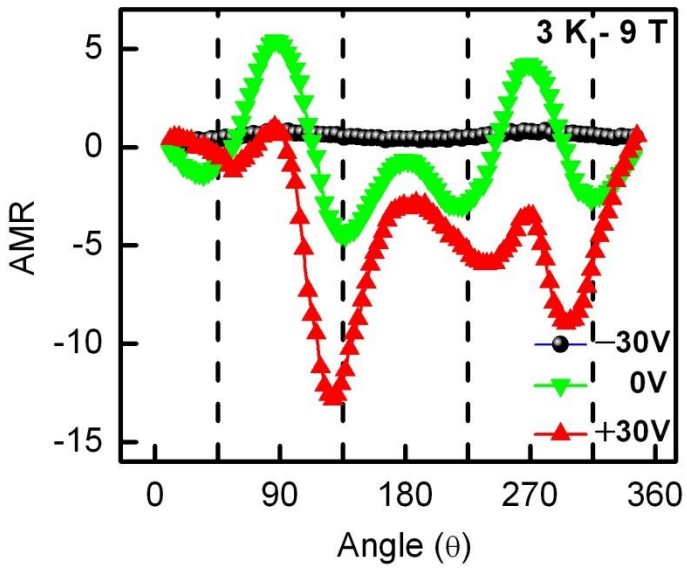

Figure 4.9: AMR measured with various back gate voltages at 3 K and 9 T for the LAO/STO interface prepared at 1×10^{-4} Torr.

At the LAO/STO interfaces, the electric field applied to the interface through back gate voltage was shown to tune the spin-orbit interaction [12] and also the carrier density modulation which is further interpreted to influence the preferential *d*-orbital filling [22]. To examine the influence of spin-orbit interaction on AMR, the gate electric field dependence of the AMR measurements were performed on the LAO/STO sample grown at 1×10^{-4} Torr. Here the gate voltages were applied to the interface through STO substrate as the back gate dielectric material. Figure 4.9 shows the gate electric field dependence of the AMR behavior measured at 3 K and 9 T. As shown in the figure 4.9 for the +30 V gate voltage the strength of the fourfold oscillations is enhanced compared to the +0 V case. On the other hand, the fourfold oscillation in AMR turns into a twofold for the -30 V, showing the distinct effects of gate electric field at these interfaces. It suggests that the gate tunable spin-orbit interaction may be the key in the observation of the AMR behaviour. One possibility for this AMR change is due to the specific orbital fillings, especially the inplane d_{xy} orbitals. The modulation of AMR with electric field effects provides an opportunity to tune the magnetic interactions by electric field at these interfaces. Another effect of an electric field is carrier modulation through accumulation or depletion of charge at the interface, and this may induce the change in the orbital fillings, and spin-orbit interaction at the interface. The applied electric fields are able to induce n_s of about $\sim10^{13}cm^{-2}$. Recently, Joshua *et al*. [22] showed that a critical n_s exist for the LAO/STO interfaces where the preferential occupancy of 3*d*-orbitals is different below and above this critical n_s. This case may applicable in our samples also; however the critical n_s values may also depend on the mobility of the sample. The modulation of AMR with electric field effects further confirm the interface effects to have a key role to the magnetic interactions and it provides an opportunity for tuning the magnetic interactions with electric fields via spin-orbit interaction. It is to note that step edges at the LAO/STO interfaces may contribute to the in plane anisotropy, it is shown that step edge effect follows a sinusoidal dependency with the step edge direction [23]. However, our data show higher order anisotropy with four fold behaviour of a square and fourth power of Cosine function, ruling out

the step edges as the prime origin. Moreover the observed electric field, magnetic field and temperature dependence of AMR can not be explained by the step edge scattering mechanism.

4.4.4 Planar Hall effect

To further understand the anisotropy planar Hall effect (PHE) measurements were performed. The PHE is similar to the AMR, which arises from magnetic related anisotropy. In PHE measurements, ***I*** and ***H*** are in the plane of the sample and the angle between ***H*** and ***I*** is varied between 0° to 360°. Unlike the AMR, here the resistivity is measured using Hall geometry, *i.e.*, transverse resistance, R_{XY}, (depicted in figure 4.10).

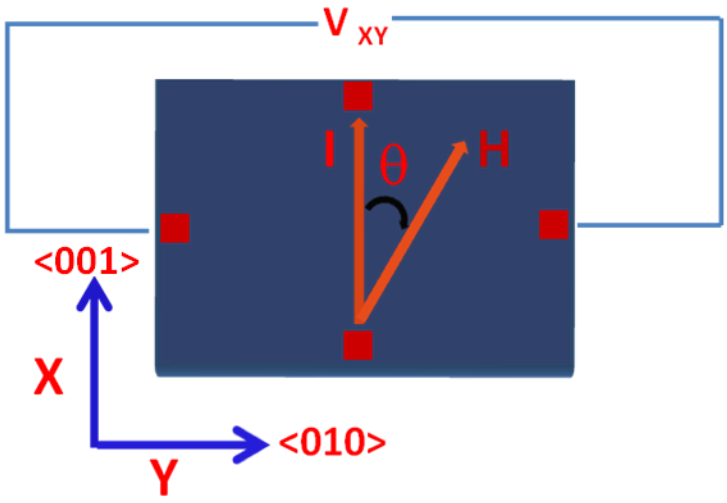

Figure 4.10: Schematic of PHE measurement geometry.

PHE is a very useful technique to investigate magnetism especially for systems which have predominant in-plane magnetizations, in which the perpendicular anomalous Hall effect is difficult to be obtained due to weak magnetism. Figure 4.11a shows R_{xy} measured at 9 T with respect to angle (θ) at various temperatures. The maxima (positive signal) and minima (negative signal) in R_{XY} appear at 45°

to the principal {010} directions with 90° interval. The sign change of Hall signal with angle is a characteristic of PHE. In general, the PHE (R_{XY}) is expected to follow sin 2θ behavior [24, 25]. Figure 4.11b shows a fit to sin 2θ for the PHE measured at 2 K and 9 T, which is in fair agreement with the formula (equation 2) with a slight deviation from the formula with 180° interval. This might be from the contribution of misalignment or contribution from the perpendicular component of MR.

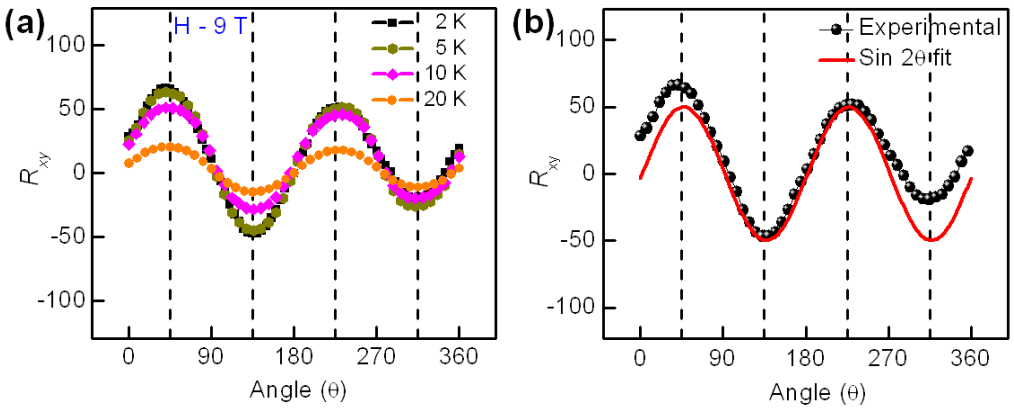

Figure 4.11: (a) PHE measured at 9 T with various temperatures for the LAO/STO interface prepared at 1×10^{-4} Torr. (b) Sin 2θ fit for the PHE obtained at 2 K and 9T.

We note here is that the AMR can be fourfold and/or two fold, but PHE is only twofold. This is consistent with the phenomenological theory by considering cubic symmetry of the system [20, 21]. The large planar Hall signal observed here infers a strong in plane component of magnetic ordering at this interface.

The above experiments give enough hints that magnetic interactions are very sensitive to the interface parameters related to carrier density and interface parameters such as spin-orbit interaction. The carrier confinement of the two dimensional electron gas near the interface does influence the preferential occupancy of the Ti 3*d* orbitals near the interface. Moreover the strength of the spin-orbit interaction near the interface is expected to be strong due to the broken

symmetry effects. However thus far, the interplay between these magnetic phenomena and carrier confinement is less explored at these interfaces. It is noted here that in this P_{O2} growth regime (where we observed the fourfold oscillation in AMR) various reports have demonstrated interface magnetism using various techniques. The strength of the magnetic interaction is shown to be sensitive to sample growth parameters. In the following section we present AMR performed on various samples that include LAO/STO interfaces prepared at different growth P_{O2} and LAO/STO heterostructure grown on NGO (110). The objective of this work is to investigate the different sample configurations and carrier confinement effects on the AMR and thereby on magnetic interactions.

4.4.5 Carrier confinement effects on AMR

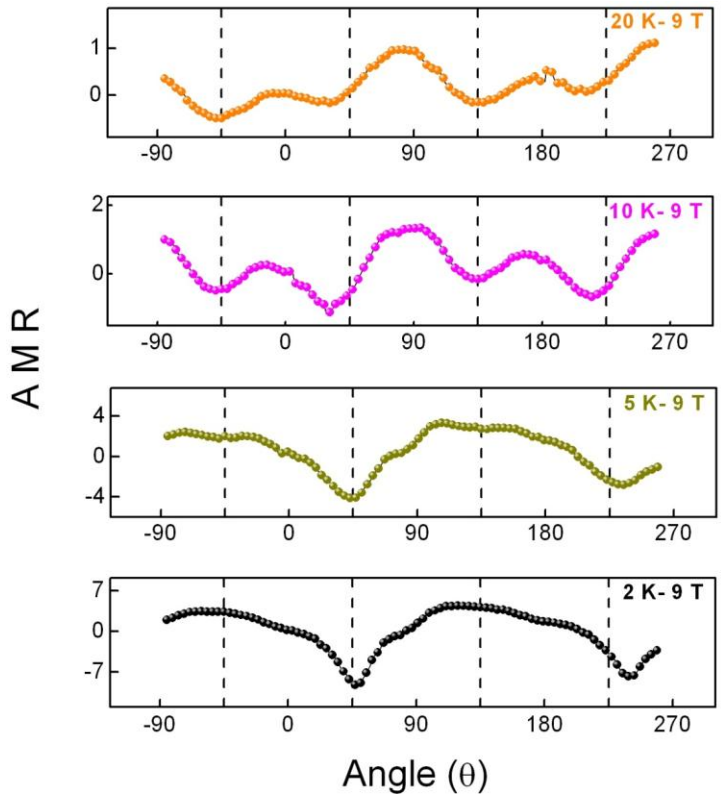

Figure 4.12: AMR measured at 9 T with varying temperature for the LAO/STO interface sample grown at 1×10^{-3} Torr.

Figure 4.12 shows the AMR measured on the sample grown at 1×10^{-3} Torr with varying temperature from 2 to 20 K at $\boldsymbol{H}$=9 T. For the AMR measured at 2 K, the resistance minima appearing at an angle 45° to the principal {100} directions, however with a repetition interval of 180°.

In comparison, there are subtle differences observed from the previous sample (which is grown at 1×10^{-4} Torr). At 2 K and 9 T, the 1×10^{-3} Torr grown sample show further preferential anisotropy, where the magnitude of the AMR is negative at only two angle positions (45° and 135°) instead of four and as the temperature increases the four fold oscillations start to become isotropic with a repetition interval of 90°. Note here that although the carrier density of these two samples is identical (2.4×10^{13} cm^{-2} from figure 4.3b) yet the AMR shows distinct differences suggesting that interface parameters are very crucial. The most important parameters in this case are the spin-orbit interaction, carrier confinement and interface ground state. From the results presented above it is clear that the samples having 2D confined electron gases show strong anisotropy in AMR with fourfold oscillations.

To further investigate the effect of the confinement of the electron gas to the anisotropy, AMR measurements were performed on a LAO/STO sample grown at 1×10^{-5} Torr (low P_{O2} sample) which has 3D like conducting channel (the spread of electrons deep in to the STO). Figure 4.13 shows the AMR measured at 9 T with varying temperatures for the corresponding sample.

Remarkably, in contrast to high P_{O2} samples, it shows only twofold oscillation throughout the temperature range of 2-20 K. However, an anti symmetric behavior in AMR is noticed between 0° to 180° and 180° to 360° at low temperatures and it gradually decreases with increasing temperature suggesting the intrinsic origin for this anti symmetry. This antisymmetry can be attributed to the difference in inter boundary scattering. While the electrons scattered toward the interface encounter a sharp boundary at the interface, those scattered into the STO side will see a relatively graded boundary due to the 3D nature of the

conducting channel. The decrease in anti symmetry with increase in temperature can be understood as at elevated temperatures the radius of the orbital path becomes smaller than the 3D channel width, thus the electron path is governed entirely by Lorentz scattering as it can be seen from the data that at 20 K the AMR follows $Sin^2\theta$ behaviour. The other possibility for the anti symmetry is from spin polarized electrons/moments whose scattering depends on magnetic field direction. The decrease in anti symmetry with increase in temperature can be understood because the polarization strength decreases significantly at elevated temperatures. Similar twofold oscillation behaviour was also reported in the AMR of the Ar-irradiated STO [26] which has a 3D conducting channel (n_s ~1×10^{17} cm^{-2}).

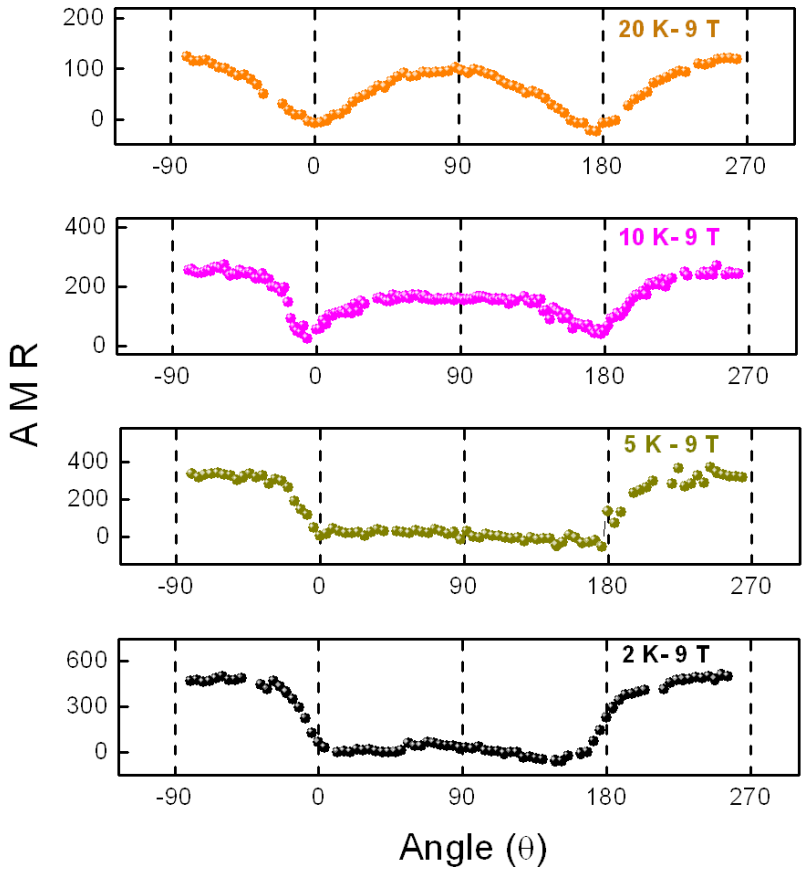

Figure 4.13: AMR measured with varying temperature at 9 T for the LAO/STO interface samples grown at 1×10^{-5} Torr.

To validate the confinement effects, LAO (15 uc)/STO (8 uc) interface was prepared on $NdGaO_3$ (110) substrate a technique employed recently to grow 2DEG on different substrates [27]. The sample shows a metallic behavior with localization behavior at low temperatures. The NdGaO3 substrates are highly insulating and thus in this case the electron gas is confined in STO layers of 8 uc thick. Figure 4.14 shows the AMR measured at 9 T with varying temperature (2-20 K) for the corresponding sample. Evidently, here also a fourfold oscillation is observed in the AMR.

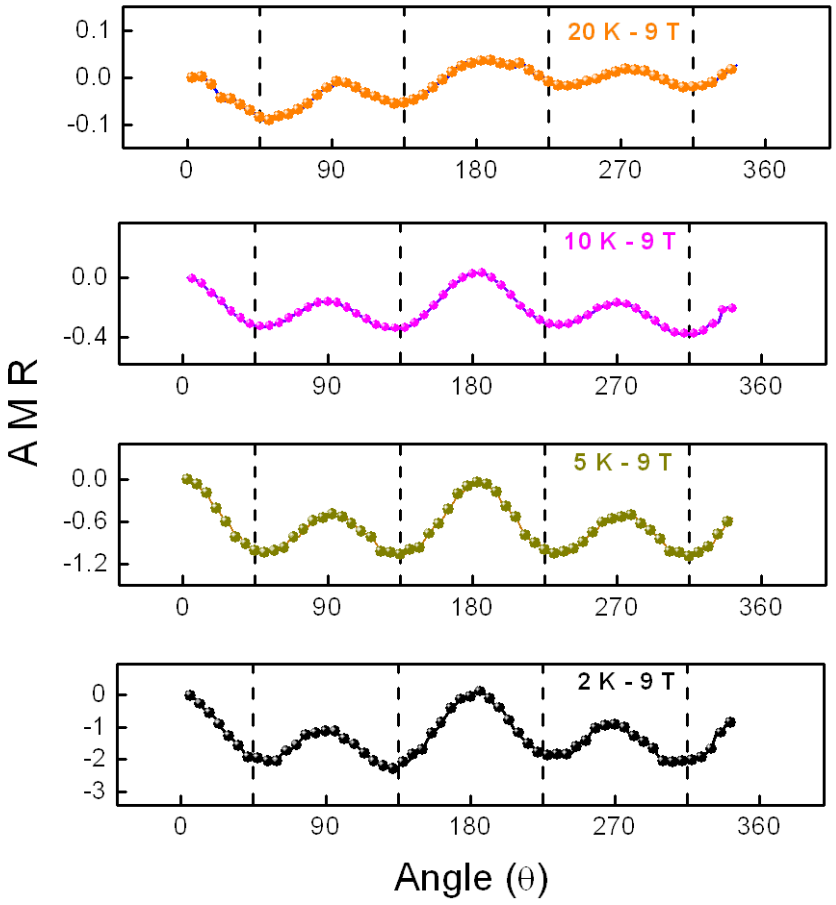

Figure 4.14: AMR measured with varying temperature at 9 T for the LAO/STO interface grown on NGO (110) substrate.

Further the magnitude of AMR gradually diminishes as the temperature increases. This sample shows a clear fourfold oscillation even up to 20 K suggesting that these heterostructures might have pronounced magnetic effects due to the strain states at the interface. As the conducting channel is confined to within 8 uc, thus the strong interface effects are also expected here similar to the high P_{O2} grown LAO/STO samples.

From the above observations, it is evident that the confinement and the n_s of the electron gas at the interface and interface effects such as spin-orbit interaction are very crucial for the fourfold oscillation in AMR. For the case of confined 2DEG, interface effects such as spin-orbit interaction and crystal field would be expected to play a dominant role. Numerous experimental and theoretical reports illustrated that, near the LAO/STO interface, the Ti 3*d* orbitals undergo crystal field induced splitting which is supposed to have a preferential filling [28-30] of *d*-orbitals. It is suggested that in the first few layers of STO [28, 29] from the interface, the $3d_{xy}$ orbitals are the lowest and predominantly occupied and this is supported by the spectroscopic experiments [30]. Further, the fraction of occupied $3d_{xy}$ orbitals (Ti^{3+}) near the interface is expected to have localized character due to lattice coupling and/or disorder which gives rise to magnetic ordering. Therefore the interaction of itinerant electrons to the interface localized in plane $3d_{xy}$ orbitals in the presence of external magnetic field would be the prime source of the observed coherent magnetic scattering. Recently, Trushin *et al.* [31] discussed the combined effects of spin-orbit coupling and symmetry of the system on AMR by considering the interplay between spin-orbit interaction and polarized magnetic moments, and further analyzed the evolution of crystalline AMR with respect to the orientation of current and magnetization in spin-orbit interaction scenario. The experimental observations such as the fourfold oscillations and crystalline AMR (with uniaxial anisotropy among the oscillations) in the case here could support the above scenario at these interfaces. Thus we suggest that the interplay between spin-orbit interaction associated with the symmetry and magnetism would be the key to observe this characteristic AMR behavior. On the other hand in the 3D case, the n_s is of the order of 10^{16} cm^{-2}, and the special extension of carriers is

deeper from the interface into the STO side. The consequence of 3D like conducting channel are; the interface crystal field would be potentially screened by this large n_s due to the strong Coulomb interactions, as a result the 3*d* orbitals would become degenerate in STO, and the strength of the spin-orbit interaction is weakened along with the depth of the electron gas from the interface, and moreover the large n_s in this case may diminish also the magnetic ordering near the interface as it can reduce the carrier localization by minimizing the interface effects. Thus we suggest that due to the weak magnetic interactions among carriers no fourfold oscillation is observed in the AMR in the 3D case. In conclusion, the results presented above establish that the fourfold oscillation appear only for the confined conducting interfaces, and indicates that the magnetic ordering is predominant near the interface and weaker far from the interface.

4.5 Summary

In summary, we have measured AMR and PHE in the LAO/STO system. A fourfold oscillation behavior in the AMR is observed for the confined 2DEG, and a twofold oscillation observed for the 3D case. The origin of the fourfold oscillation is suggested to be arising from magnetic interaction of itinerant electrons with localized magnetic moments coupled to the crystal symmetry. The observation of this behavior only for the confined 2DEG case infers that the magnetic interactions are predominantly at the interface. The observed PHE further signifies that the predominant in-plane component of the magnetization in the systems.

References:

[1] S. Thiel, G. Hammerl, A. Schmehl, C. W. Schneider, and J. Mannhart, "Tunable quasi-two-dimensional electron gases in oxide heterostructures," *Science*, 313, 1942 (2006).

[2] C. Cen, S. Thiel, G. Hammerl, C. W. Schneider, K. E. Andersen, C. S. Hellberg, J. Mannhart, and J. Levy, "Nanoscale control of an interfacial metal–insulator transition at room temperature," *Nature Materials*, 7, 298-302 (2008).

[3] C. Bell, S. Harashima, Y. Hikita, and H. Y. Hwang, "Thickness dependence of the mobility at the $LaAlO_3/SrTiO_3$ interface," *Applied Physics Letters*, 94, 222111 (2009).

[4] A. Brinkman, M. Huijben, M. Van Zalk, J. Huijben, U. Zeitler, J. C. Maan, W. G. Van Der Wiel, G. Rijnders, D. H. A. Blank, and H. Hilgenkamp, "Magnetic effects at the interface between non magnetic oxides," *Nature Materials*, 6, 493-496 (2007).

[5] W. Siemons, G. Koster, H. Yamamoto, W. A. Harrison, G. Lucovsky, T. H. Geballe, D. H. A. Blank, and M. R. Beasley, "Origin of charge density at $LaAlO_3$ on $SrTiO_3$ heterointerfaces: possibility of intrinsic doping," *Physical Review Letters*, 98, 196802 (2007).

[6] M. Basletic, J. -L. Maurice, C. Carrétéro, G. Herranz, O. Copie, M. Bibes, É. Jacquet, K. Bouzehouane, S. Fusil, and A. Barthélémy, "Mapping the spatial distribution of charge carriers in $LaAlO_3/SrTiO_3$ heterostructures," *Nature Materials*, 7, 621(2008).

[7] X. Wang, W. M. Lü, A. Annadi, Z. Q. Liu, K. Gopinadhan, S. Dhar, T. Venkatesan, and Ariando, "Magnetoresistance of two-dimensional and three-dimensional electron gas in $LaAlO_3/SrTiO_3$ heterostructures: Influence of magnetic ordering, interface scattering, and dimensionality," *Physical Review B*, 84, 075312 (2011).

[8] Ariando, X. Wang, G. Baskaran, Z. Q. Liu, J. Huijben, J. B. Yi, A. Annadi, A. Roy Barman, A. Rusydi, Y. P. Feng, J. Ding, H. Hilgenkamp, and T. Venkatesan, "Electronic phase separation at the $LaAlO_3/SrTiO_3$ interface," *Nature Communications*, 2, 188 (2011).

[9] J. A. Bert, B. Kalisky, C. Bell, M. Kim, Y. Hikita, and H. Y. Hwang, "Direct imaging of the coexistence of ferromagnetism and superconductivity at the $LaAlO_3/SrTiO_3$ interface," *Nature Physics*, 7, 767 (2011).

[10] Lu Li, C. Richter, J. Mannhart, and R. C. Ashoori, Coexistence of magnetic order and two-dimensional superconductivity at $LaAlO_3/SrTiO_3$ interfaces, *Nature Physics*, 7, 762 (2011).

[11] D. A. Dikin, M. Mehta, C. W. Bark, C. M. Folkman, C. B. Eom, and V. Chandrasekhar, "Coexistence of Superconductivity and Ferromagnetism in Two dimensions," *Physical Review Letters*, 107, 056802 (2011).

[12] A. D. Caviglia, M. Gabay, S. Gariglio, N. Reyren, C. Cancellieri, and J. -M. Triscone, "Tunable Rashba spin-orbit interaction at oxide Interfaces," *Physical Review Letters*, 104, 126803 (2010).

[13] A. W. Rushforth, K. Vyborny, C. S. King, K. W. Edmonds, R. P. Campion, C. T. Foxon, J. Wunderlich, A. C. Irvine, P. Vasek, V. Novak, K. Olejnik, J. Sinova, T. Jungwirth, and B. L. Gallagher, "Anisotropic Magnetoresistance Components in (Ga,Mn)As," *Physical Review Letters*, 99, 147207(2007).

[14] Y. Q. Zhang, H. Meng, X. W. Wang, X. Wang, H. H. Guo, Y. L. Zhu, T. Yang, and Z. D. Zhang, "Angular dependent magnetoresistance with twofold and fourfold symmetries in A-type antiferromagnetic $Nd_{0.45}Sr_{0.55}MnO_3$ thin film," *Applied Physics Letters*, **97**, 172502 (2010).

[15] M. Bibes, V. Laukhin, S. Valencia, B. Martinez, J. Fontcuberta, O. YuGorbenko, A. R. Kaul, and J. L. Martinez, "Anisotropic magnetoresistance and anomalous Hall effect in manganite thin films," *Journal of Physics: Condensed Matter*, 17, 2733 (2005).

[16] J. D. Fuhr, M. Granada, L. B. Steren, and B. Alascio, "Anisotropic magnetoresistance in manganites: experiment and theory," *Journal of Physics: Condensed Matter*, 22, 146001 (2010).

[17] R. Ramos, S. K. Arora, and I. V. Shvets, "Anomalous anisotropic magnetoresistance in epitaxial Fe_3O_4 thin films on MgO(001)," *Physical Review B*, 78, 214402 (2008).

[18] M. Ben Shalom, C. W. Tai, Y. Lereah, M. Sachs, E. Levy, D. Rakhmilevitch, A. Palevski, and Y. Dagan, "Anisotropic magnetotransport at the $SrTiO_3/LaAlO_3$ interface," *Physical Review B*, 80, 140403(R) (2009).

[19] F. Flekser, M. Ben Shalom, M. Kim, C. Bell, Y. Hikita, H. Y. Hwang, and Y. Dagan, "Magnetotransport effects in polar versus non-polar $SrTiO_3$ based heterostructures," *Physical Review B*, 86, 121104(R) (2012).

[20] T. R. McGuire, and R. I. Potter, "Anisotropic Magnetoresistance in Ferromagnetic 3*d* alloys," *IEEE Transactions on Magnetics*, 11, 1018(1975).

[21] J. Li, S. L. Li, Z. W. Wu, S. Li, H. F. Chu, J. Wang, Y. Zhang, H. Y. Tian, and D. N. Zheng, "A phenomenological approach to the anisotropic magnetoresistance and planar Hall effect in tetragonal La(2/3)Ca(1/3)MnO3 thin films," *Journal of Physics: Condensed Matter*, 22, 146006 (2010).

[22] A. Joshua, S. Pecker, J. Ruhman, E. Altman, S. Ilani, "A universal critical density underlying the physics of electrons at the $LaAlO_3/SrTiO_3$ interface," *Nature Communications*, 3, 1129 (2012).

[23] P. Brinks, W. Siemons, J. E. Kleibeuker, G. Koster, G. Rijnders, and M. Huijben, "Anisotropic electrical transport properties of two-dimensional electron gas at LaAlO3/SrTiO3 interfaces," Applied Physics Letters, 98, 242904 (2011).

[24] A. M. Nazmul, H. T. Lin, S. N. Tran, S. Ohya, and M. Tanaka, "Planar Hall Effect and uniaxial in-plane magnetic anisotropy in Mn δ-doped GaAs⁄p-AlGaAs hetero-structures," *Physical Review B*, 77, 155203 (2008).

[25] S. Nakagawa, I. Sasaki, and M. Naoe, "Magnetization processes of storage and back layers in double-layered perpendicular magnetic recording media observed using anomalous and planar Hall effects," *Journal of Applied Physics*, 91, 8354 (2002).

[26] F. Y. Bruno, J. Tornos, M. Gutierrez del Olmo, G. Sanchez Santolino, N. M. Nemes, M. Garcia-Hernandez, B. Mendez, J. Piqueras, G. Antorrena, L. Morell´on, J. M. De Teresa, M. Clement, E. Iborra, C. Leon, and J. Santamaria, "Anisotropic magnetotransport in $SrTiO_3$ surface electron gases generated by Ar+ irradiation," *Physical Review B*, 83, 245120 (2011).

[27] C. W. Bark, D. A. Felker, Y. Wang, Y. Zhang, H. W. Jang, C. M. Folkman, J. W. Park, S. H. Baek, H. Zhou, D. D. Fong, X. Q. Pan, E. Y. Tsymbal, M. S. Rzchowski, and C. B. Eom, "Tailoring a two-dimensional electron gas at the $LaAlO_3$⁄$SrTiO_3$ (001) interface by epitaxial strain," *Proceedings of the National Academy of Sciences* 108, 12, 4720 (2011).

[28] Z. S. Popovic´, S. Satpathy, and R. M. Martin, "Origin of the Two-Dimensional Electron Gas Carrier Density at the $LaAlO_3$ on $SrTiO_3$ interface," *Physical Review Letters*, 101, 256801 (2008).

[29] P. Delugas, A. Filippetti, and V. Fiorentini, "Spontaneous 2-Dimensional Carrier Confinement at the n-Type $SrTiO_3$/$LaAlO_3$ interface," *Physical Review Letters*, 106, 166807 (2011).

[30] M. Salluzzo, J. C. Cezar, N. B. Brookes, V. Bisogni, G. M. De Luca, C. Richter, S. Thiel, J. Mannhart, M. Huijben, A. Brinkman, G. Rijnders, and G. Ghiringhelli, "Orbital Reconstruction and the Two-Dimensional Electron Gas at the $LaAlO_3$/$SrTiO_3$ interface," *Physical Review Letters*, 102, 166804 (2009).

[31] M. Trushin, K. Výborný, P. Moraczewski, A. A. Kovalev, J. Schliemann, and T. Jungwirth, "Anisotropic magnetoresistance of spin-orbit coupled carriers scattered from polarized magnetic impurities," *Physical Review B*, 80, 134405 (2009).

Chapter 5

Investigation of 2DEG at the interfaces of various combinations of polar and non-polar oxides

Abstract

All of the novel properties that are discussed until now are based on LAO/STO interfaces constructed by polar $LaAlO_3$ layer. To investigate the role of the A and B cationic sites of the ABO_3 polar layer on the interface properties, in this chapter various combinations of polar/non-polar oxides ($NdAlO_3$/ $SrTiO_3$, $PrAlO_3/SrTiO_3$ and $NdGaO_3/SrTiO_3$) interfaces which are otherwise similar in nature to LAO/STO interface are investigated (figure 5.1). All of these polar layers comprise of $(AO)^{+1}$ and $(BO_2)^{-1}$ polar charge layers alternativly along the (100) direction. A polarization discontinuity will be formend when the polar layer is grown on a non polar substrate such as STO.

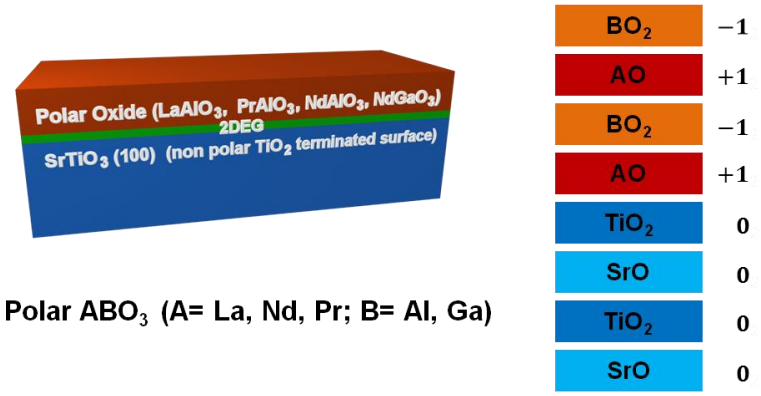

Figure 5.1: Schematic representation of the polar/non-polar $ABO_3/SrTiO_3$ interfaces.

The experimental results reveal that the new combinations $NdAlO_3$/ $SrTiO_3$ (NAO/STO), $PrAlO_3/SrTiO_3$ (PAO/STO) and $NdGaO_3/SrTiO_3$ (NGO/STO) can also support a 2DEG at the interface. Apart from the observation of 2DEG, these

interfaces show some distinct properties in carrier density and mobility where a decrease in carrier density and mobility is observed for the highly strained NAO/STO interface. The combined effects of interface strain provided by the lattice mismatch between the polar layers and STO, and electron correlations arising from octahedral distortions in STO at the interface seem to control the carrier density and mobility of the 2DEG. Further, a NAO film critical thickness metal-insulator transition is observed for the NAO/STO interfaces, suggesting that polarization discontinuity could be the prime origin of the conductivity at these polar/non-polar interfaces. The NAO film thickness dependence transport study reveal an emergence of two-dimensional variable range hopping (VRH) at low temperatures, emphasizing the dominant role of over layer thickness in controlling the transport properties of 2DEG through interface strain. A detailed study on VRH mechanism helps to distinguish localization from other 2D electron transport mechanisms.

5.1. Introduction

The role of the polar LAO layer for the conductivity at the LAO/STO interface is very significant as it has been utilized to manipulate the properties at the LAO/STO interface in many ways such as AFM charge writing [1] and adsorbates as capping [2]. Exploiting interface strain effects, Bark *et al*. [3] demonstrated that strain affects the properties of the 2DEG at the LAO/STO interface by growing interfaces on different substrates with different lattice constants. The combined effects of lattice mismatch (2.3%) between the LAO and STO and electronic effects provided by polar LAO at the LAO/STO interface may play a strong role in controlling the interface properties. In addition, the electrostriction and electromechanical response were observed in LAO/STO heterostructures [4, 5]. Recently, a similar 2DEG is also shown to exist at the $LaGaO_3$/ $SrTiO_3$ interface [6]. In all above observations, the polar nature of the over layer is critical.

The significance of the polar over layer can be further explored by investigating various new combinations of polar/non-polar oxide heterostructures. In this scenario, the different chemical nature and lattice structure of the polar layers enable us to tune the interface properties. Moreover this approach may help in revealing key issues such as the driving mechanism for the formation of 2DEG which is widely believed to be originating from polarization catastrophe, [7] and the localization of carriers at this interface due to the lifting of the degeneracy of the Ti 3*d* states. In the following the investigation of various combinations of polar/non-polar oxide ($NdAlO_3$/ $SrTiO_3$, $PrAlO_3$/$SrTiO_3$ and $NdGaO_3$/ $SrTiO_3$) interfaces and the experimental results are discussed.

5.2. Fabrication of polar and non-polar oxide interfaces ($ABO_3/SrTiO_3$, A= Nd, Pr, La, B= Al, Ga)

Samples were prepared by pulsed laser deposition, ablating *REB*O_3 targets onto TiO_2 terminated STO (100) substrates. Samples were prepared in a range of

oxygen pressure (P_{O2}) 1×10^{-3} to 1×10^{-5} Torr at 800 ^{o}C. The laser (248 nm) energy density was 1.4 J/ cm^2 and repetition rate was 1 Hz. During deposition, the film growth and number of unit cells were monitored by in-situ reflection high energy electron diffraction (RHEED). Figure 5.2a shows RHEED intensity patterns obtained during the growth of the various polar oxides on STO, showing layer by layer growth mode. Figure 5.2b shows an AFM topography image obtained for a sample of 10 uc $NdAlO_3$ on STO. The steps structure which is preserved after the film growth further confirms the layer by layer growth.

Even though all these polar oxides offer substantial lattice mismatch with STO substrate, we have successfully grown them by optimizing deposition conditions. Epitaxial growth of films on STO substrates were further confirmed by high resolution X-ray diffraction (HRXRD).

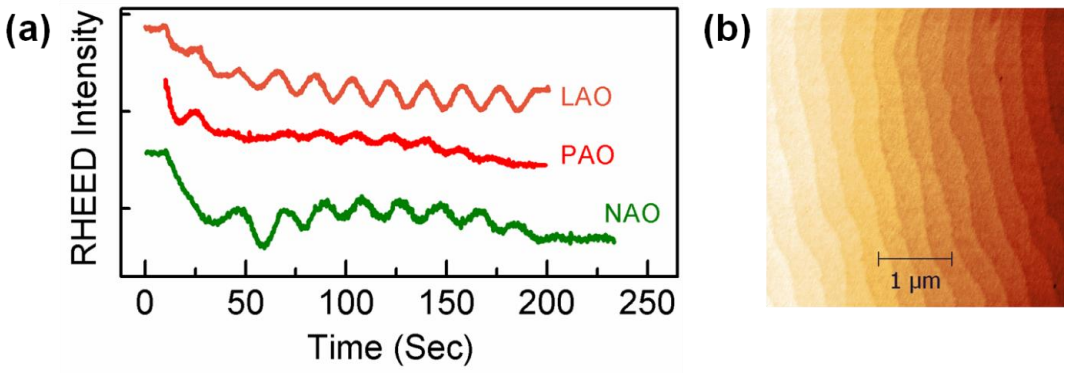

Figure 5.2: (a) RHEED oscillations obtained during the growth of polar oxides on STO substrates. (b) AFM topography image of the NAO/STO 10 uc sample, clerarly show the preserved step flow structure.

First, the transport properties of the NAO/STO interfaces are investigated with respect to the growth oxygen pressure (P_{O2}) .To measure the electrical properties contacts were made with Al wire-bonding directly on the samples, enabling direct to access to the interface. Sheet resistance (R_s) and Hall effect measurements were carried out to obtain carrier density, mobility and other electrical properties.

5.3. Electrical transport of $NdAlO_3$/ $SrTiO_3$ interfaces

Figure 5.3 shows the dependence of sheet resistance, R_s, with temperature for the NAO/STO interface prepared in the P_{O2} range of 1×10^{-3} - 1×10^{-5} Torr. Strikingly, all samples clearly exhibit a conducting property at their interfaces. The high P_{O2} grown samples show strong upturns in R_s at lower temperatures. Interestingly, even the sample grown at P_{O2} of 1×10^{-4} Torr shows strong upturn in the R_s. It is noted here that in the case of LAO/STO (100) interfaces such an upturn emerges only for higher P_{O2} of 1×10^{-3} Torr and "thicker" samples (≥ 15 uc) [8, 9].

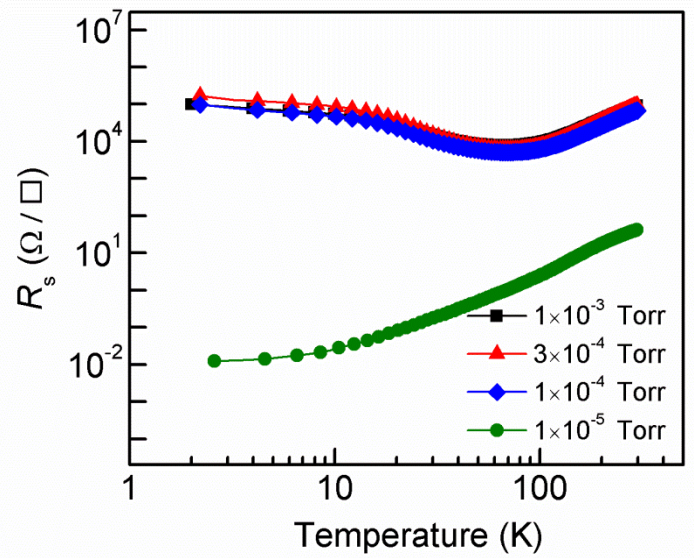

Figure 5.3: Temperature dependence of sheet resistance, R_s for the NAO/STO interfaces grown under different oxygen pressures.

However, the sample grown at P_{O2} of 1×10^{-5} Torr showed higher conductivity which can be understood in terms of the presence of oxygen vacancies at the interface. The carrier density (n_s) and mobility (μ) for the above samples were extracted from Hall measurements. Figures 5.4a and 5.4b show the temperature dependence of n_s, and μ, respectively. For high P_{O2} samples, n_s (300 K) is of the order of 4-5 $\times10^{13}$ cm^{-2}, whereas for the sample grown at P_{O2} of 1×10^{-5} Torr, n_s (300 K) is of the order of 10^{16} cm^{-2}. The higher carrier density in the later case

implies the presence of oxygen vacancies which is a common observation for the interfaces grown at lower P_{O2} [10, 11]. A large carrier freeze-out in n_s with temperature is observed at low temperatures in high P_{O2} samples. Similar kind of behaviour was previously observed in the cases of LAO/STO interfaces [12]. For all samples, μ (300 K) is of the order of 1-8 $cm^2V^{-1}s^{-1}$ comparable to those reported for the LAO/STO (100) interfaces [9,13]. The μ follows T^{-2}-like dependence in the temperature range of 300-100 K, typical behaviour of Fermi liquid.

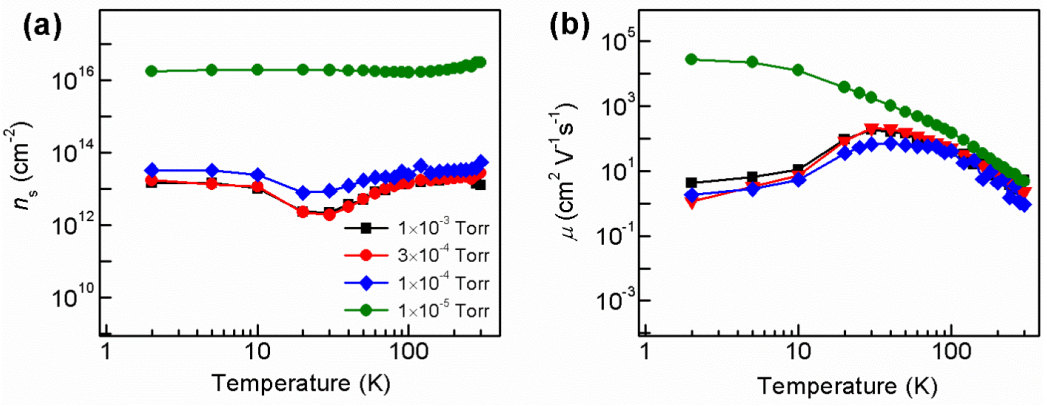

Figure 5.4: Temperature dependence of carrier density n_s and mobility μ for the NAO/STO interfaces grown under different oxygen pressures.

However, a significant difference in μ is observed at low temperatures between samples grown at high and low P_{O2}, where an abrupt drop in μ is observed for the high P_{O2} samples at low temperatures. This generally occurs when strong localization/magnetic scattering effects are present in the system. On the otherhand, an increase in μ is observed throughout the temperature range down to 2 K for the sample grown at P_{O2} of 1×10^{-5} Torr.

Although the transport properties show similar behaviour to LAO/STO interfaces, substantial differences observed in temperature dependence of the n_s and μ

indicate the effect of the different polar layers. To further elucidate the polar layer effects, a comparison study was carried out. For this, samples with $LaAlO_3$, $PrAlO_3$ and $NdGaO_3$ as the polar over layers were grown on STO. For the best comparison all the samples were grown at same thicknesses of 10 uc and under identical growth process (P_{O2} of 1×10^{-3} Torr).

5.4. Comparison of various polar/non polar oxide interfaces

Figure 5.5a shows the temperature dependence of R_s for various polar/non-polar oxide interfaces. Similar to the case of NAO/STO, PAO/STO interfaces also show upturn in R_s at low temperatures. On the other hand, interestingly, LAO/STO and NGO/STO interfaces show a typical metallic behaviour without appreciable upturns in R_s. Further, their R_s at 300 K appears to have a strong dependence on the RE cation of the polar layer, where R_s is larger (90 KΩ) for NAO compared to that of LAO (20 KΩ). Figure 5.5b shows the n_s variation with temperature; LAO/STO and NGO/STO interfaces show minute carrier freeze-out towards low temperatures compared to NAO/STO and PAO/STO, indicating that the interfaces with LAO and NGO have less contribution from activated carriers. However, a carrier recovery below 15 K is observed for the NAO/STO and PAO/STO interfaces, which is possibly due to the difference transport mechanism in this low temperature localized regime. The most remarkable effects are seen in temperature dependence of mobility that is shown in figure 5.5c. For the NAO/STO and PAO/STO interfaces, μ increases initially with decreasing temperature and then drops dramatically for temperatures below 40 K.

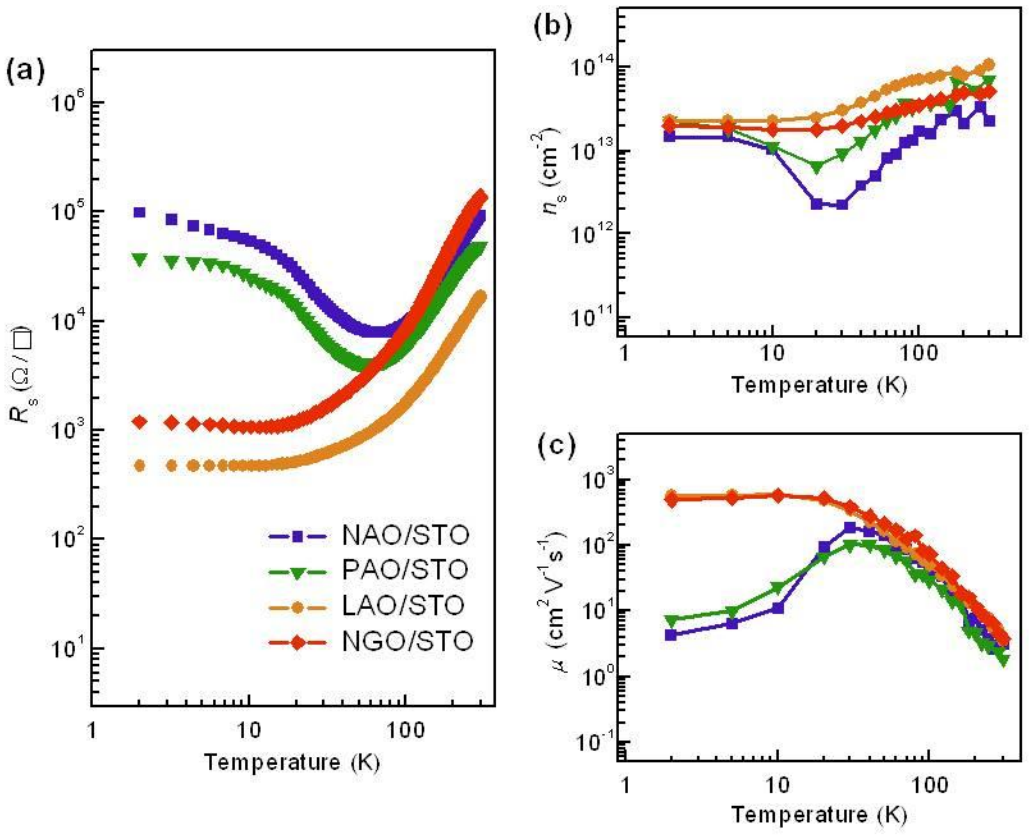

Figure 5.5: Temperature dependence of sheet resistance, R_s, carrier density, n_s, and mobility, μ, for various combinations of polar/non-polar oxide interfaces.

On the other hand, interfaces with LAO and NGO show an increase in μ and tend to saturate at low temperatures. An interesting observation is that even though the n_s (2 K) is nearly the same (~2×10^{13} cm^{-2}) for all the interfaces, R_s and μ exhibit significant divergence, implying a significant influence of the type of polar layer on the charge carriers at the polar/non-polar interface. The possible effects of the polar layers are discussed below.

5.5. Electronic correlation and strain effects

Although these polar layers seem to be similar in nature, yet there are few differences. Firstly, these polar layers comprise of different chemical elements at

A-site (RE cation) and B-site in the perovskite (ABO_3) structure. When the polar layer ($REBO_3$) is deposited on top of the TiO_2 terminated $SrTiO_3$ (100), the first unit cell at the interface on either side can be viewed as a stack of REO/ TiO_2 /SrO layers. In this picture, across the interface, the TiO_2 layer will have a different electronic environment in the presence of different RE cations. Secondly, different polar layers cause different lattice mismatch with STO, which in turns create a different interfacial strain. To further understand these effects, the A-site cationic dependence of the n_s is plotted for corresponding interfaces as shown in figure 5.6.

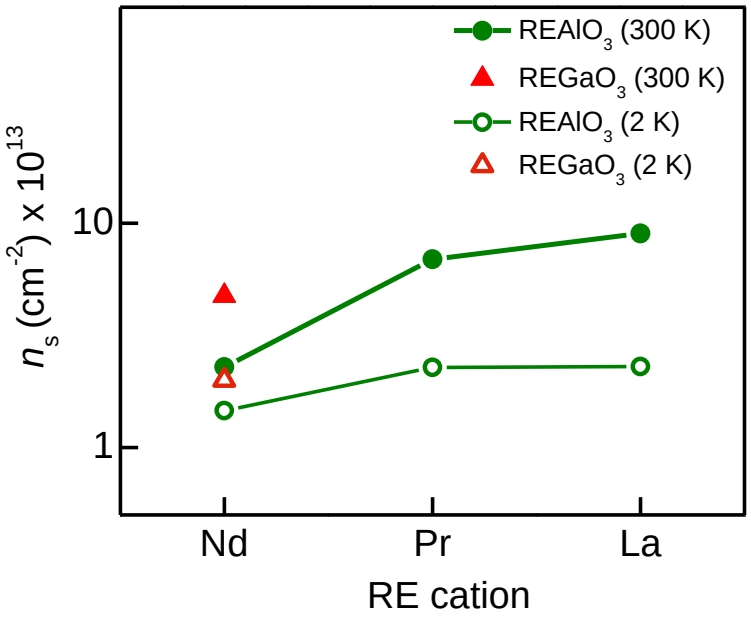

Figure 5.6: Variation in carrier density with Rare Earth (RE) cations at the various polar/non-polar oxide interfaces.

Clearly n_s (300 K) are higher in the case of La based interface and lower for Nd based interfaces, similar to the case of $SrTiO_3$/REO/$SrTiO_3$ heterostructures reported by Jang *et al*. [14]. There it is further shown that the electronic ground state (metallic/insulating) can be controlled by RE cation at the interface and is attributed to the electronic correlations of RE cation to the top STO layer which is

further supported by theoretical calculations. However, in our case here, n_s at 2 K have rather small dependency on the RE cation with n_s is of the order of 1-2 $\times 10^{13}$ cm^{-2} for all interfaces. The RE cation dependency of n_s shown here further suggests the electronic effects arising from polar layer control the charge distribution at the interface.

Now getting back to the mobility case, referring to figure 5.5c, the μ drop was only observed in the case of NAO/STO and not in the NGO/STO (Nd is A-site cation for both cases), implying that we cannot attribute this μ drop to the proximity effects of RE ions at the interface. So the only other difference these polar layers offer is the lattice mismatch at the interface with the STO substrate. A schematic diagram is shown in figure 5.7.

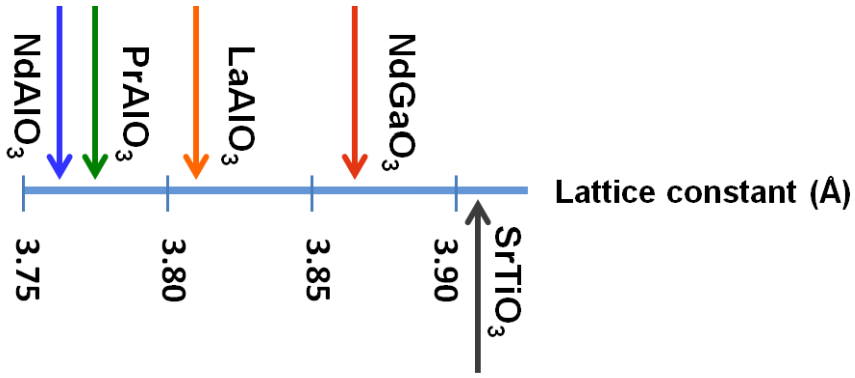

Figure 5.7: Schematic diagram showing the lattice constants of polar oxides and $SrTiO_3$.

Lattice mismatch here is estimated by considering in-plane lattice parameters. Among them the NGO/ STO interface offers the least lattice mismatch (1.6%) and NAO/STO the largest (3.6%).

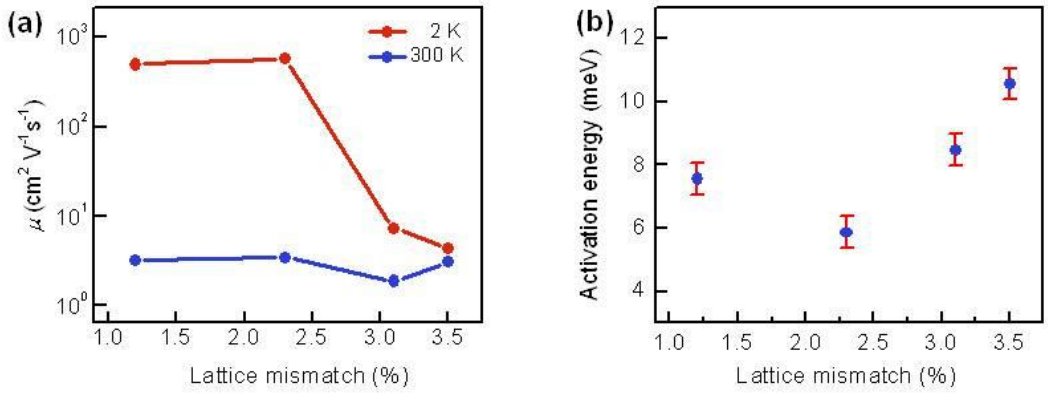

Figure 5.8: (a) Mobility μ and (b) Carrier activation energy as a function of the lattice mismatch at polar/non-polar oxides.

Figure 5.8a shows the μ variation with lattice mismatch; μ (300 K) shows modest dependency to the lattice mismatch with values typically of the order of 1-5 $cm^2V^{-1}s^{-1}$, which suggests the predominant electron-phonon scattering at 300 K. In contrast, μ (2 K) shows strong dependence on lattice mismatch: μ is 500 $cm^2V^{-1}s^{-1}$ for NGO/STO and only 4 $cm^2V^{-1}s^{-1}$ for NAO/STO (a drop of a factor of 100). It appears that the large lattice mismatch is limiting the μ. Recent reports on LAO/STO interface using HRTEM [15] and HRXRD [16] showed that in the top layers of the STO the Ti octahedra are distorted, strongly implying that the top few layers of STO are under the influence of strain provided by the polar over layers through structural coupling across interface. The fundamental issue here is that the charge carriers occupy Ti sites and predominantly reside in the top few layers of STO. The various polar layers offer a range of degree of distortions to the top layers of STO due to the lattice mismatch, therefore the degree of strain/ distortions in these STO layers can be expected to play a crucial role in manipulating the electronic properties at the interface. Consequently, the mobility variation observed here can be ascribed to the degree of strain induced in STO layers by lattice mismatch. Further we note that eventhough the carrier density n_s at 2 K is almost the same (2×10^{13} cm^{-2}) for all interfaces a large variation in μ is observed, suggesting that e-e interactions play a key role in these various

interfaces. However the degree of disorder induced by strain may have an influence to an extent. Thus, we interpret that the combined effects of strain and electron correlations are crucial in controlling the μ. Further, because of a smaller lattice mismatch a higher μ is expected in the case of NGO/STO (1.6%) compared to the case of LAO/STO (2.3%) due to lesser mismatch, however the mobility values are just comparable in both cases. This is attributed to the residual impurity scattering in STO itself. We note that the strain values are estimated by considering the lattice parameters at room temperature for STO and various polar layers. The thermal expansion coeficient for STO and LAO are about 10^{-5} K^{-1} that changes the lattice constants of individual layer by 0.4%. Therefore the variation in strain would be less than that. Further, STO undergoes a cubic to tetragonal phase transition at about 110 K.

As mentioned earlier a large carrier freeze out is observed in a certain temperature range. To examine this, the activation energy is extracted from Arrhenius plots (between 20 and 300 K) of the n_s versus temperature graphs in figure 5.5b. Activation energies of the order of few meV are in agreement with the previous report on LAO/ STO [13]. Figure 5.8b shows activation energy as a function of lattice mismatch. Interestingly, activation energy gradually increases with lattice mismatch and it is largest (16 meV) for the NAO/STO. In general, the activation energy indicates the relative position of carrier donor level from the conduction band in energy scale. Its variation with lattice mismatch may suggest a relative shift in position of donor level. Recently, it has been proposed that strain could lead to distortion of Ti octahedra through octahedral rotation/tilt in STO based heterostructures [14, 15], which in turn could alter the position of energy levels. Since electronic effects are quite sensitive to the degree of octahedral distortions, it is interesting to study the effects of octahedral distortions on novel phases at these interfaces.

The above presented data established that the polar over layers play a key role in governing the interface properties. The Rare earth cation at A-site is shown to influence the carrier density at the interface, and the interface strain offered by

these various polar over layers is shown to control mobility at the interface. From the above section, there is an indication that the 2DEG at various polar/non-polar oxide interfaces exhibit a stronger localization of 2DEG compared to that at the LAO/STO interfaces. The basic difference between NAO/STO and LAO/STO interfaces is that the former one offers larger lattice mismatch of 3.6%. Stronger localization can possibly give rise to different transport properties, and thus its dependence on the NAO over layer thickness is very crucial to be investigated. With this objective, the samples of NAO/STO interfaces with different thickness of NAO were prepared. The transport properties of the corresponding samples are discussed below.

5.6. Thickness dependence study of the $NdAlO_3/SrTiO_3$ interfaces

One of the characteristic features of the 2DEG at the LAO/STO system is the thickness dependence of the insulator-metal transition with a critical thickness of ~ 4 uc of the LAO [17]. Furthermore, in the conventional LAO/STO case, a weak to strong localization [18, 19] and magnetic Kondo behaviour [8] were reported in thicker samples, suggesting that a variety of conduction mechanisms were operating at these interfaces. Moreover superconductivity at these interfaces was also shown to be sensitive to the thickness of the over layer where localization is suggested to be minimum when superconductivity is observed [20]. In order to investigate the NAO over layer thickness effects on transport properties, samples with thicknesses ranging from 1-14 uc were grown. All these samples were grown under identical conditions of oxygen pressure of $1x10^{-3}$ Torr, with energy density of 1.3-1.4 Jcm^{-2}, and with a pulse repetition rate of 1 Hz. During the film growth, the thickness of the NAO is monitored by RHEED. Conductivity for the NAO/STO interfaces as a function of the number of unit cells of NAO is depicted in figure 5.9. The samples show a clear transition from insulating to metallic state at a thickness around 4 uc, with a change in the conductivity of more than three orders of magnitude across the insulator to metal transition.

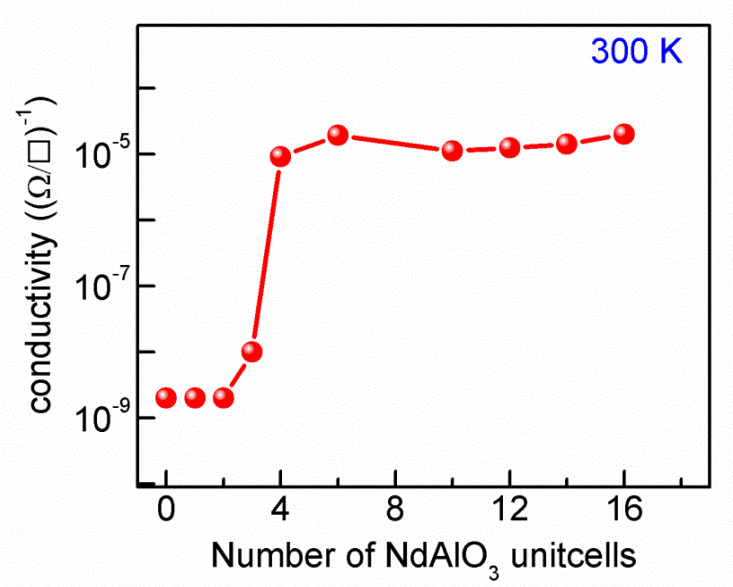

Figure 5.9: NAO layer thickness dependence of conductivity for the NAO/STO interfaces.

The similarity in the insulator to metal transition with the LAO/STO system suggests that same origin for the conductivity is at operation in these interfaces. The thickness dependence of polar layer shown here favours the idea that the electronic reconstruction could also be the driving mechanism in these interfaces; though it is not to completely exclude other possible mechanisms such as intermixing and oxygen vacancy formation [10, 21] from these results.

For thorough investigation of the thickness dependence of NAO over layer samples with thicknesses of 6, 12 and 16 uc were grown on STO (100) substrates. Figure 5.10 shows the R_s variation with temperature for NAO/STO interfaces of various thicknesses. The 6 uc sample shows a typical metallic behavior (albeit a weak upturn at low temperature), whereas thicker samples (12 and 16 uc) show a metallic behavior (300-70 K) but with strong upturns in R_s with resistance minima at about 70 K.

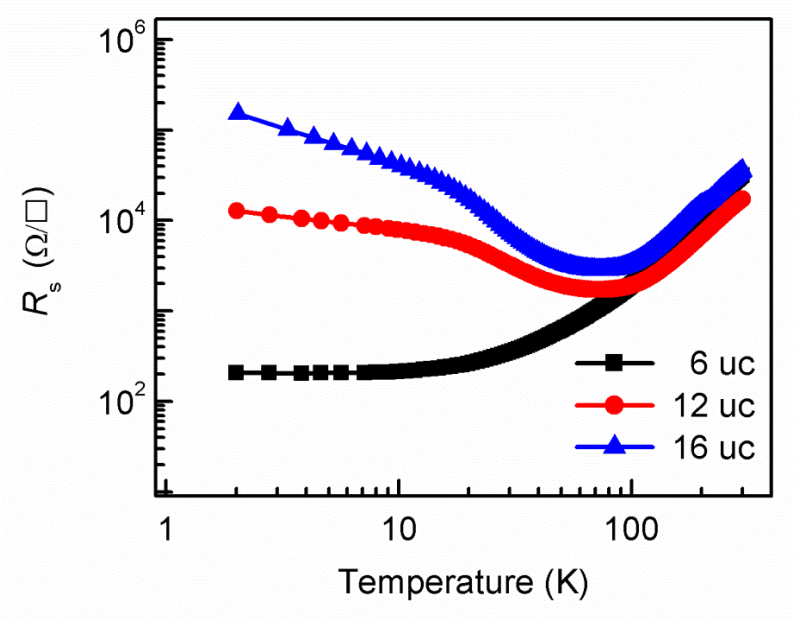

Figure 5.10: Temperature dependence of sheet resistance, R_s for the NAO/STO interfaces with different NAO thicknesses (6, 12, and 16 uc).

The emergence of the upturns with over layer thickness observed here is in agreement with previous reports on LAO/STO though the critical thickness for the LAO/STO samples is about 15 uc [9]. However, a significant observation can be made for the low temperature transport for the thicker NAO/STO samples, *i.e.* below 15 K the variation in R_s is more distinct indicating a different type of transport mechanism operating at low temperatures. Figure 5.11a and 5.11b show the temperature dependence of n_s and μ, respectively, for the corresponding samples. For the thicker samples, n_s decreases in the temperature range of 300-20 K, and this can be attributed to the localization of activated charge carriers at the interface.

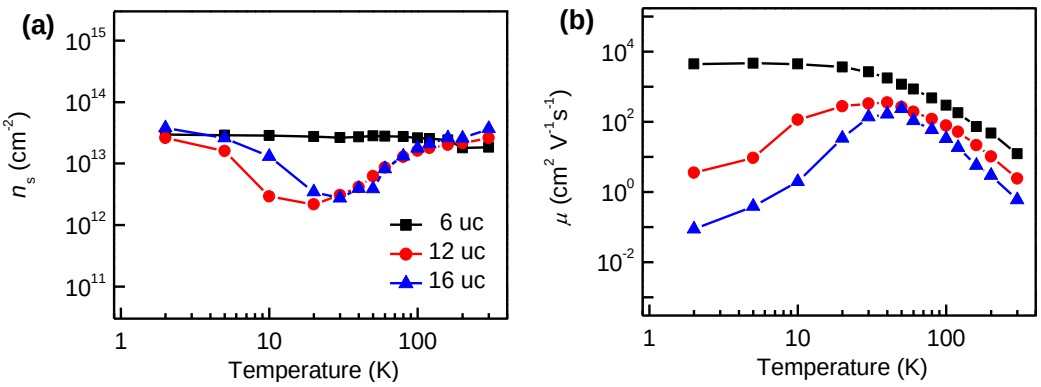

Figure 5.11: Temperature dependence of carrier density n_s and mobility μ for the NAO/STO interfaces with different NAO thicknesses (6, 12, and 16 uc).

n_s in this range can be fit with a simple Arrhenius equation of the form $Ae^{-Ea/T}$, where E_a is the thermal activation energy for the activated charge carriers. The E_a is of the order of 12 meV which is larger compared to 6 meV for the LAO/STO interfaces [13]. As discussed in the previous section the large activation and strong localization observed in thicker samples could be due to the large structural distortions present in these systems arising from the larger interface strain. Further, there is an increase in n_s at low temperatures below 20 K down to 2 K, simultaneously where an increase in R_s is observed. For temperatures below 20 K the increase in both the R_s and n_s implies that the transport mechanism cannot only be simple band (Drude) conduction and indicates that other type of transport mechanism is in operation at low temperatures. Contrary to this, for the 6 uc sample there is no such carrier activation for n_s with temperature. μ for the 6 uc sample increases monotonically from 9 $cm^2V^{-1}s^{-1}$at 300 K to 900 $cm^2V^{-1}s^{-1}$ at 2 K. The relatively high mobility of the 6 uc sample would be favourable for studies of superconductivity. On the other hand, for the thicker samples (12 and 16 uc) the μ at 300 K is about 5 $cm^2V^{-1}s^{-1}$, and it drops significantly at the low temperatures, which gives further evidence for strong localization in these samples. The low temperature behavior of R_s, n_s and μ confirms the strong localization of carriers associated with a change of transport mechanism at low temperatures. In general,

the observed low temperature sharp upturns in R_s can arise from various transport mechanisms namely, variable range hopping (VRH) due to strong localizations, a magnetic Kondo scattering and thermal activation. In order to further verify the transport mechanism in our system, the low temperature variation of R_s is analyzed.

The upturns in R_s could originate from magnetic Kondo effect following the dependence given by $R(T) = R_0 \ln(T/T_{ef})$. However this dependence does not fit our data, indicating that Kondo scattering is not the governing mechanism here. Moreover the non saturating trend of R_s even down to 2 K also further confirms this. For the thicker samples the n_s at 20 K are of the order of $\sim 10^{12}$ cm^{-2} which is one order of magnitude lower than that in the thin 6 uc sample. Hence, it seems that there could be a critical n_s at these interfaces below which the transport mechanism converts to VRH in the strong localization regime. The reduced n_s seen in thicker samples could be due to the large amount of interface strain created by thicker NAO over layers.

5.7. Strong localizations and variable range hopping transport

The observed strong localizations in 2DEG at the interface suggests that the most likely mechanism would be VRH, which is a transport mechanism in which the conduction takes place through hopping of carriers between localized states. The variation of resistance in the VRH regime can be described by the equation

$$R(T) = R_0 \, e^{\left(\frac{T_0}{T}\right)^{\frac{1}{n+1}}}$$

Here n is the dimensionality of the system [22]. Figure 5.12 shows the corresponding 2D VRH (n = 2) fit for the experimental data at low temperatures (40-2 K).

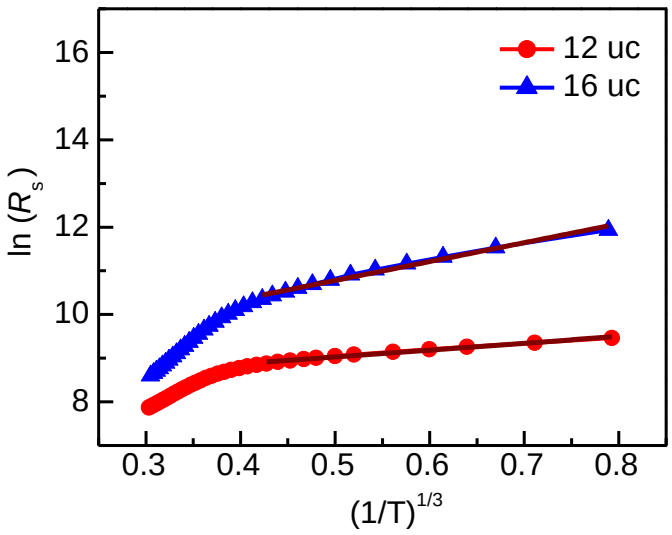

Figure 5.12: The ln (R_s) vs. $(1/T)^{1/3}$ graph for 12 and 16 uc NAO/STO samples, and a 2D variable range hopping (VRH) fit to the experimental data in the temperature range of 2-20 K.

As evidenced from the figure 5.12 the experimental data below 15 K fits well the VRH formula and significantly the $T^{-1/3}$ dependence (n = 2) confirms the 2D nature of the conducting channel. The crossover regime between the metallic and VRH (70-20 K) follows a logarithmic dependence of temperature which may indicate a weak localization regime for the electrons.

The VRH transport mechanism can be further evaluated by magneto transport measurements, since in the hopping transport the carrier conduction is quite sensitive to magnetic fields. Magneto-resistance (MR) measurements were performed on the 12 uc NAO/STO sample at various temperatures with different current (***I***) to magnetic field (***B*** = μ_0***H***) orientations. Figure 5.13 shows the out of plane MR (magnetic field is perpendicular to the current and sample surface) measured at various temperatures. The MR is negative at 2 K with -30 % at 9 T. The negative MR is indeed one of the strong signatures for VRH type transport [23, 24, 25]. Further, the negative MR diminishes with increase in temperature and turns to positive MR for higher temperatures. The negative MR reaches a minimum at about 20 K which is exactly the temperature range where the changes

in trend are simultaneously seen in R_s and n_s. The origin of negative MR in VRH is attributed to the disruption of the interference effects between forward scattering events in the presence of magnetic field.

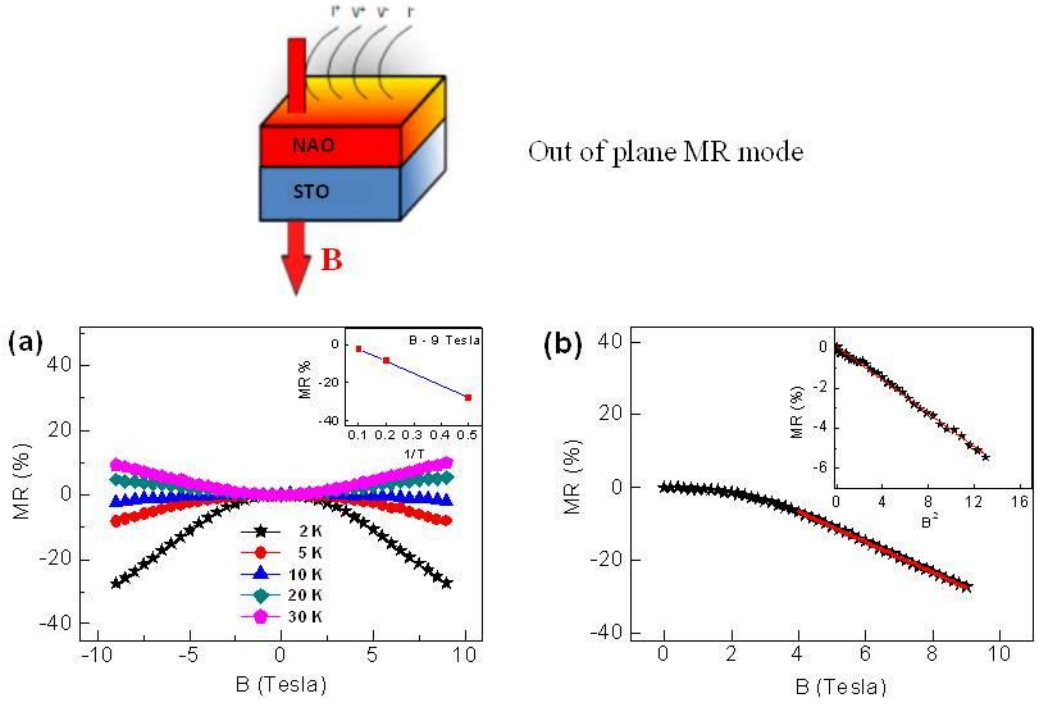

Figure 5.13: (a) Out-of-plane MR measured at different temperatures for 12 uc NAO/STO sample. Inset: scaling of MR at 9 T with temperature for negative MR part. (b) MR (out of plane) measured at 2 K with magnetic field showing linear variation at high magnetic fields and Inset: a B^2 dependence at low magnetic fields.

By considering the interference among the hopping paths between two sites at a distance R_M apart, where R_M is the optimum hopping length, it is shown that interference affects the hopping probability between these two sites. Inset of figure 5.13a shows the temperature dependence of MR in the negative MR regime at 9 T which scales approximately to T^{-1} as expected in the case of 2D VRH [26].

The temperature dependence of hopping length (R_M) basically determines the MR dependence on temperature. Further, the positive MR observed above 20 K arises from Lorentz scattering of electrons in presence of magnetic field, which has been extensively studied for 2DEG at the LAO/STO interface [18, 27, 28]. Figure 5.13b shows the plot of MR as a function of magnetic field, with linear $\boldsymbol{B}$ dependence at high magnetic fields and $\boldsymbol{B}^2$-dependence for low fields (shown in inset of figure 5.13b), which is in accordance with theory and experiments in VRH regime [26, 29]. To exclude the orbital contributions to MR in VRH regime, measurements were further performed in in-plane mode (current and magnetic field are parallel and in the plane of the 2DEG) which is shown in figure 5.14.

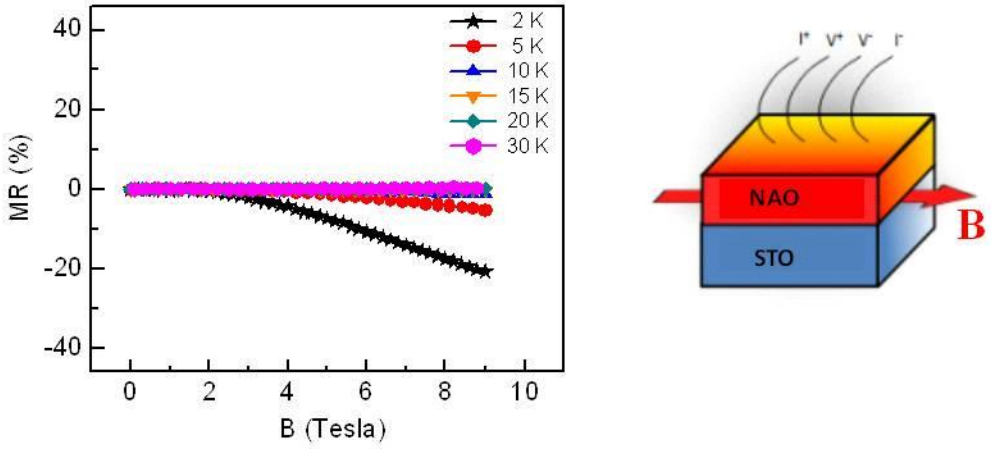

Figure 5.14: In-plane MR measured at different temperatures for 12 uc NAO/STO sample.

In this case, it can be seen that MR is negative for the temperatures below 20 K and diminishes and turns to zero for the temperatures above 20 K. The absence of MR above 20 K suggests the absence of Lorentz scattering of electrons in this in-plane geometry. Figure 5.15 shows the angle dependence of R_s measured at 2 K and 9 T. Here 0 degree corresponds to in plane mode and 90 degree corresponds to out of-plane mode. It can be observed that the R_s show large anisotropy between in-plane and out of-plane modes, which is due to the confinement effect

of the 2DEG. These MR measurements further confirm that the transport mechanism at low temperatures for the thicker samples is governed by VRH and this VRH regime begins to appear for below 20 K which is evidenced by the change in the MR (from positive to negative).

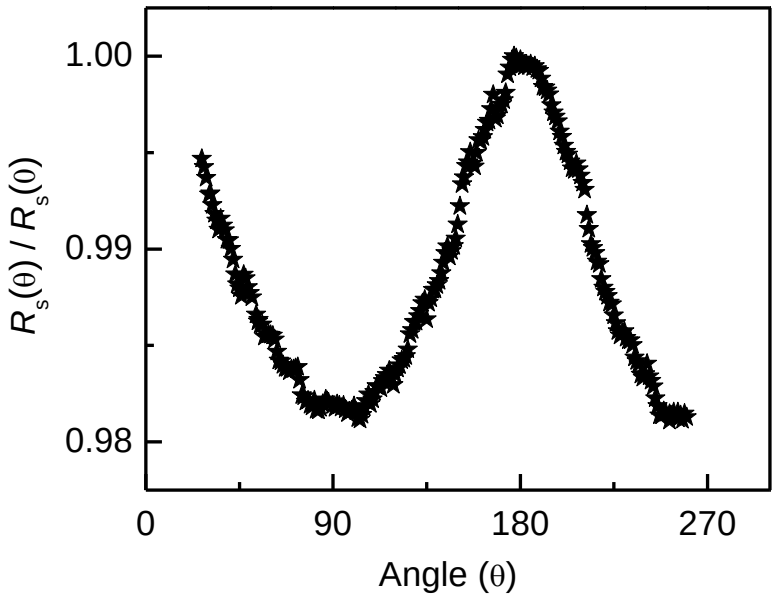

Figure 5.15: Angle dependence of R_s at 2 K and 9 T with angle between magnetic field to current changed from in-plane to out of plane).

Generally, the hopping transport favours over other mechanisms when a considerable amount of carrier localization is present in the system, the carrier confinement would also be crucial in these 2D systems where the absence of lateral transport can further favours the hopping transport. Finally, we comment on the unusual carrier density recovery at low temperatures. The coincidence of the critical temperature with the evolution of VRH regime, where the carrier density increases as the temperature decreases suggests that it may relate to hopping transport. Thus we suggest that the overall carrier density behaviour could be understood by considering two regimes of transport mechanisms; a

regular transport in conduction band via extended states, thermally activated charge carriers where the carrier density decreases with decreasing temperature. We suggest that the lowest lying states are related to strongly localized states with negligible hopping probability to other states. As more and more carriers freeze into localized states, Coloumb interaction between localized states may mobilize initially immobile electrons in this hopping transport regime, thus enhances the mobile carrier density. The other possibility is the change in band fillings at this low temperature regime where heavy bands with high electron density participate in the conduction.

5.8. Summary

In this chapter the observation of 2DEG at new combinations of various polar/non-polar oxides interfaces namely, $NdAlO_3$/ $SrTiO_3$, $PrAlO_3$/$SrTiO_3$ and $NdGaO_3$/ $SrTiO_3$ is demonstrated. This study certainly provides a new insight in in preparing various oxide interfaces with tunable properties at these polar/non-polar oxide combinations. A detailed transport analysis revealed that the properties of the 2DEG can be influenced by the polar over layers. This study indicates that the combined effects of interface strain and electron correlations offered by polar layers are crucial in these oxide interfaces. The lattice mismatch of polar layers to the STO can induce large octahedral distortions in STO and the observed variation in activation energy for carriers in these various polar/non-polar layers could be an indication of such octahedral distortions in STO at the interface. Even though naive thinking suggests is that bulk substrates expected to induce the strain in over layers, however this study shows that at the interface the substrate layers are also influenced by the over layers to an extent that can influence the interface physics and properties. The observations such as rare earth (RE) cation dependence of carrier density, lattice mismatch effects on mobility offered by polar layers may provide an opportunity to tune the properties at selected polar/non-polar oxide interfaces. Further, the observed thickness dependence of metal-insulator transition for the NAO/STO interfaces suggests that polar discontinuity may possibly be the prime origin of conductivity at these

polar/non-polar interfaces. Thickness dependence of localization effects of 2DEG are observed at the NAO/STO interfaces. In the strong localized regime the transport is governed by the VRH. These results further emphasize the dominant role of over layer thickness in controlling the transport properties of 2DEG at these interfaces through interface strain. Moreover the study presented in this report can certainly assist to distinguish the localization from other mechanisms which is very important in understanding the physics of electron transports in two dimensional oxide systems.

References

[1] C. Cen, S. Thiel, G. Hammerl, C. W. Schneider, K. E. Andersen, C. S. Hellberg, J. Mannhart, and J. Levy, "Nanoscale control of an interfacial metal–insulator transition at room temperature," *Nature Materials*, 7, 298-302 (2008).

[2] Y. Xie, Y. Hikita, C. Bell, and H. Y. Hwang, "Control of electronic conduction at an oxide heterointerface using surface polar adsorbates," *Nature communications*, 2,494 (2011).

[3] C. W. Bark, D. A. Felker, Y. Wang, Y. Zhang, H. W. Jang, C. M. Folkman, J. W. Park, S. H. Baek, H. Zhou, D. D. Fong, X. Q. Pan, E. Y. Tsymbal, M. S. Rzchowski, and C. B. Eom "Tailoring a two-dimensional electron gas at the $LaAlO_3/SrTiO_3$ (001) interface by epitaxial strain," *Proceedings of the National Academy of Sciences*, 108, 4720-4724, (2011).

[4] C. Cancellieri, D. Fontaine, S. Gariglio, N. Reyren, A. D. Caviglia, A. Feˆte, S. J. Leake, S. A. Pauli, P. R. Willmott, M. Stengel, Ph. Ghosez, and J.-M. Triscone, "Electrostriction at the $LaAlO_3/SrTiO_3$ interface," *Phys. Rev. Lett*. 107, 056102 (2011).

[5] C. W. Bark, P. Sharma, Y. Wang, S.H. Baek, S. Lee, S. Ryu, C. M. Folkman, T. R.Paudel, A. Kumar, S.V. Kalinin, A. Sokolov, E. Y. Tsymbal, M. S. Rzchowski, A.Gruverman, C.B. Eom, "Switchable Induced Polarization in $LaAlO_3/SrTiO_3$ heterostructures," *Nano Letters*, 12, 1765-1771 (2012).

[6] P. Perna, D. Maccariello, M. Radovic, U. Scotti di Uccio, I. Pallecchi, M. Codda, D. Marré, C. Cantoni, J. Gazquez, M. Varela, S. J. Pennycook, and F. Miletto Granozio, "Conducting interfaces between band insulating oxides: The $LaGaO_3/SrTiO_3$ hetero-structure," *Applied Physics Letters*, 97, 152111 (2010).

[7] N. Nakagawa, H. Y. Hwang, and D. A. Muller, "Why some interfaces cannot be sharp," *Nature Materials*, 5, 204-209 (2006).

[8] A. Brinkman, M. Huijben, M. Van Zalk, J. Huijben, U. Zeitler, J. C. Maan, W. G. Van Der Wiel, G. Rijnders, D. H. A. Blank, and H. Hilgenkamp, "Magnetic effects at the interface between non magnetic oxides," *Nature Materials*, 6, 493-496 (2007).

[9] C. Bell, S. Harashima, Y. Hikita, and H. Y. Hwang, "Thickness dependence of the mobility at the $LaAlO_3/SrTiO_3$ interface," *Applied Physics Letters*, 94, 222111 (2009).

[10] W. Siemons, G. Koster, H. Yamamoto, W. A. Harrison, G. Lucovsky, T. H. Geballe, D. H. A. Blank, and M. R. Beasley, "Origin of charge density at $LaAlO_3$ on $SrTiO_3$ hetero- interfaces: possibility of intrinsic doping," *Physical Review Letters*, 98, 196802 (2007).

[11] A. Kalabukhov, R. Gunnarsson, J. Borjesson, E. Olsson, T. Claeson, and D. Winkler, "Effect of oxygen vacancies in the $SrTiO_3$ on the electrical properties of the $LaAlO_3/SrTiO_3$ interface," *Physical Review B*, 75, 121404(R) (2007).

[12] M. Huijben, G. Koster, H.J.A. Molegraaf, M.K. Kruize, S. Wenderich, J.E. Kleibeuker, A. McCollam, V.K. Guduru, A. Brinkman, H. Hilgenkamp, U. Zeitler, J.C. Maan, D.H.A. Blank, G. Rijnders. "High mobility interface electron gas by defect scavenging in a modulation doped oxide heterostructure," *arXiv: 1008.189*6v1.

[13] M. Huijben, G. Rijinders, D. H. A. Blank, S. Bals, S. V. Aert, J. Verbeeck, G. V. Tendeloo, A. Brinkman, and H. Hilgenkamp, "Electronically coupled complementary interfaces between perovskite band insulators," *Nature Materials*, 5, 556 (2006).

[14] H. W. Jang, D. A. Felker, C. W. Bark, Y. Wang, M. K. Niranjan, C. T. Nelson, Y. Zhang, D. Su, C. M. Folkman, S. H. Baek, S. Lee, K. Janicka, Y. Zhu, X. Q. Pan, D. D. Fong, E. Y. Tsymbal, M. S. Rzchowski, C. B. Eom, "Metallic and insulating oxide interfaces controlled by electronic correlations," *Science*, 331, 886 (2011).

[15] C. L. Jia, S. B. Mi, M. Faley, U. Poppe, J. Schubert, and K. Urban, "Oxygen octahedron reconstruction in the $SrTiO_3/LaAlO_3$ heterointerfaces investigated using aberration-corrected ultrahigh-resolution transmission electron microscopy," *Physical Review B*, 79, 081405(R) (2009).

[16] J. E. Boschker, C. Folkman, C. W. Bark, A. F. Monsen, E. Folven, J. K. Grepstad, E. Wahlstrom, C. B. Eom, and T. Tybell. "Structural coupling across the $LaAlO_3$ /$SrTiO_3$ -interface: High-resolution x-ray diffraction study," *Physical Review B*, 84, 205418 (2011).

[17] S. Thiel, G. Hammerl, A. Schmehl, C. W. Schneider and J. Mannhart, "Tunable quasi-two-dimensional electron gases in oxide heterostructures," *Science*, 313, 1942 (2006).

[18] F. J. Wong, R. V. Chopdekar, and Y. Suzuki, "Disorder and localization at the $LaAlO_3$/ -$SrTiO_3$ interface," *Physical Review B*, 82, 165413 (2010).

[19] T. Hernandez, C. W. Bark, D. A. Felker, C. B. Eom, and M. S. Rzchowski, "Localization of two-dimensional electron gas in $LaAlO_3$/-$SrTiO_3$ heterostructures," *Physical Review B*, 85, 161407 (R) (2012).

[20] N. Reyren, S. Thiel, A. D. Caviglia, L. Fitting Kourkoutis, G. Hammerl, C. Richter, C. W. Schneider, T. Kopp, A. -S. Ruetschi, D. Jaccard, M. Gabay, D. A. Muller, J. -M. Triscone, and J. Mannhart, "Superconducting interfaces between insulating oxides," *Science*, 317, 1196-1199 (2007).

[21] P. R. Wilmott, S. A. Pauli, R. Herger, C. M. Schlepu¨tz, D. Martoccia, B. D. Patterson, B. Delley, R. Clarke, D. Kumah, C. Coinca, and Y. Yacoby, "Structural basis for the conducting interface between $LaAlO_3$ and $SrTiO_3$," *Physical Review Letters*, 99, 155502 (2007).

[22] N. F. Mott, "Conduction in glasses containing transition metal ions," *J. Non-Crystal. Solids*, 1, 1 (1968).

[23] V. I. Nguyen, B. Z. Spivak and B. I. Shklovskii, "Aharonov-Bohm oscillations with normal and superconductive flux-quanta in hopping

conduction," *Pis'ma Zh. Eksp. Teor. Fiz.* 41, 35 (1985) - English translation: *Sov. Phys. JETP Letters*, 41, 42 (1985).

[24] V. I. Nguyen, B. Z. Spivak and B. I. Shklovskii, "Tunnel hops in disordered systems," *Zh. Eksp. Teor. Fiz.* 89, 1770 (1985) - English translation: *Sov. Phys. JETP* 62, 1021 (1985).

[25] U. Sivan, O. Entin-Wohlman, and Y. Imry, "Orbital magnetoconductance in the variable-range–hopping regime," *Physical Review Letters*, 60, 1566 (1988).

[26] W. Schirmacher, "Quantum-interference magnetoconductivity in the variable-range-hopping regime," *Physical Review B*, 41, 2461 (1990).

[27] X. Wang, W. M. Lü, A. Annadi, Z. Q. Liu, K. Gopinadhan, S. Dhar, T. Venkatesan, and Ariando, "Magnetoresistance of two-dimensional and three-dimensional electron gas in $LaAlO_3/SrTiO_3$ heterostructures: Influence of magnetic ordering, interface scattering, and dimensionality," *Physical Review B*, 84, 075312 (2011).

[28] M. Ben Shalom, C. W. Tai, Y. Lereah, M. Sachs, E. Levy, D. Rakhmilevitch, A. Palevski, and Y. Dagan, "Anisotropic magnetotransport at the $SrTiO_3/LaAlO_3$ interface," *Physical Review B*, 80, 140403(R) (2009).

[29] K. Schlenga, H. Bach and K. Westerholt. "Magnetoresistance of $La_{2-x}Ba_xCuO_{4-\delta}$ single crystals with concentrations close to the metal-insulator transition," *Physica C*, 221, 161 (1994).

Chapter 6

Anisotropic two dimensional electron gas at the $LaAlO_3/SrTiO_3$ (110) interface

Abstract

So far the emergent phenomena in LAO/STO based systems were studied specifically only at the interfaces constructed along the (100) crystallographic orientation. The occurrence of conductivity is believed to be driven by polarization discontinuity leading to an electronic reconstruction. In this scenario, the crystal orientation plays an important role and no conductivity would be expected, for example for the interface between $LaAlO_3$ and (110)-oriented $SrTiO_3$, which should not have a polarization discontinuity. Here, it is demonstrated that a high mobility two-dimensional electron gas (2DEG) can also arise at the LAO/STO (110) interface. The (110) interface shows transport properties and $LaAlO_3$ layer critical thickness for the metal-to-insulator transition similar to those of (100) interfaces, but with a strong anisotropic characteristic along the two in-plane crystallographic directions. The anisotropic behaviour is further found to be sensitive to the oxygen growth conditions where the ration of resistance between two in-plane crystallographic directions shows dramatic dependence. Density functional theory calculations reveal that electronic reconstruction, and thus conductivity, is still possible at this (110) interface by considering the energetically favourable (110) interface structure, *i.e.* buckled TiO_2/LaO, in which the polarization discontinuity is still present. Transmission electron microscopy experiments reveal perfect growth of the interface and indicate a further signature of possible buckling of the interface. An alternative zig-zag/buckled interface model for (110) is proposed in place of planar interface. The (110) interface further shows field effect characteristics with external electric fields. The interface shows trans-conductance similar of a field effect transistor

with a significant anisotropy in mobility is observed along crystallographic directions whereas the carrier density is isotropic.

6.1. Introduction

The conductivity of the crystalline LAO/STO (100) interface is mostly interpreted to originate from electronic reconstruction which is a direct consequence of the polarization discontinuity[11] at the interface between the two oxides. The electrostatic charge representation for the LAO/STO case is shown in figure 6.1.

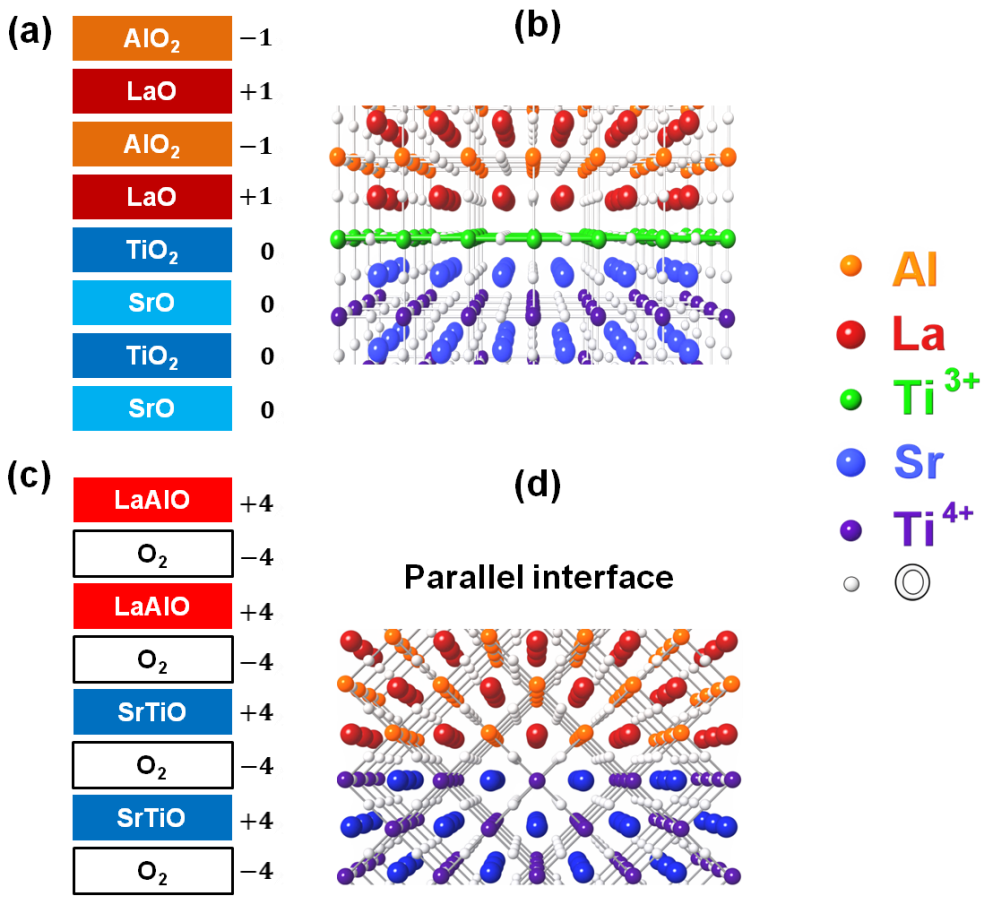

Figure 6.1: Layout of the polar catastrophe model for $LaAlO_3/SrTiO_3$ interface, on (a), (100) and (c), (110)-oriented STO substrates, where planes are segmented as planar charge sheets. In the case of (100), charge transfer is expected while in the case of (110) there is no polarization discontinuity and hence no charge transfer. (b) and (d), Atomic picture of the interfaces for representations (a) and (c), respectively.

In this case, the ABO_3 perovskite structure of the $SrTiO_3$ (100) substrate can be considered as stacks of $(SrO)^0$ and $(TiO_2)^0$ as shown in figure 6.1a, whereas for the $LaAlO_3$ it consists of charged sheets of $(LaO)^{+1}$ and $(AlO_2)^{-1}$, which leads to a polarization discontinuity at the interface between the LAO and STO. According to the polarization discontinuity picture this catastrophe can be avoided by transferring a net charge to the STO at the interface, thus the conductivity at the interface [1]. The atomic representation of figure 6.1a is shown in figure 6.1b with Ti (+3) formation at the interface where the electrons occupy the TiO_2 plane at the interface. On the other hand, for the case of LAO/STO interfaces prepared on $SrTiO_3$ (110) substrates as shown in figure 6.1c, both the STO and LAO can be represented by planar stacks of $(ABO)^{+4}$ and $(O_2)^{-4}$ layers as proposed in [2, 3], which leads to no polarization discontinuity at the interface. The atomic representation of figure 6.1c is shown in figure 6.1d constructed with parallel planes of SrTiO and O_2 planes and LaAlO and O_2 planes, respectively. According to the polar discontinuity picture consequently here no conductivity would be expected for such LAO/STO (110) interfaces. However, no systematic experimental investigation of interfaces with respect to the crystallography has been carried out so far.

6.2. Growth and characterization of $LaAlO_3/SrTiO_3$ (110) thin films

The LAO/STO (110) interface samples were prepared with various LAO thicknesses (N) from 1 to 14 unit cells (uc), and under different P_{O2} ranging from 5×10^{-5} to 5×10^{-3} Torr on atomically flat STO (110) substrates. The LAO films were deposited from a single-crystal LAO target at 720 °C by pulsed laser deposition. The laser (248 nm) energy density was 1.4 J/cm^2 and repetition rate was 1 Hz. During deposition, the film growth was monitored using *in-situ* RHEED. After deposition, all samples were cooled to room temperature at 10 °C/min in oxygen at the deposition pressure. For comparison with the conventional (100) case, LAO/STO (100) samples were grown with 12 uc LAO layers under the same preparation conditions.

For the (100) case, substrates were treated with well-established conditions; buffered HF for 30 sec followed by thermal annealing at 950 °C for 2 hours in air [4, 5]. For the (110)-oriented STO, the substrates were annealed for 3 hours at 1050-1100 °C in air [6]. Figure 6.2a shows an atomic force microscopy (AFM) topography image of the TiO_2 terminated STO (100) substrate surface, with a step height of 0.39 nm, which is the unit cell spacing in STO (100).

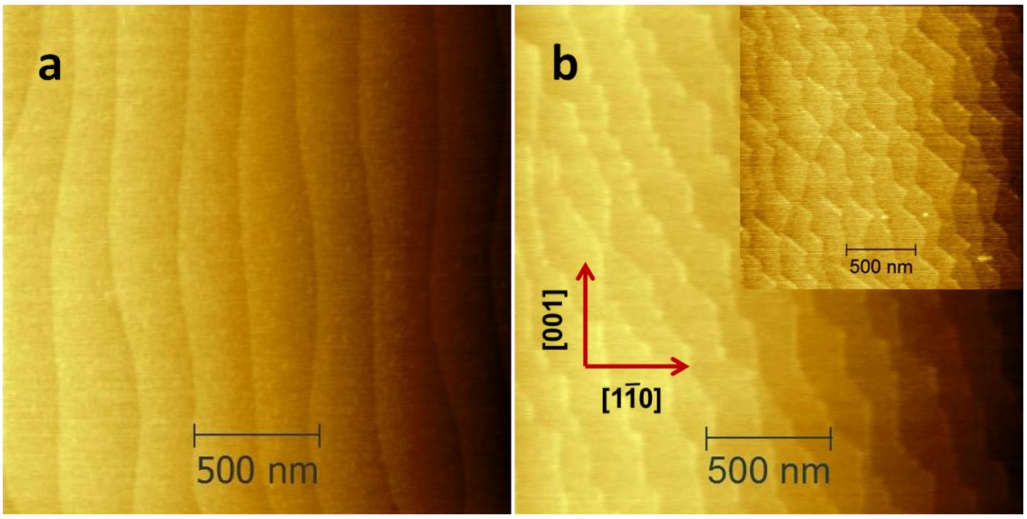

Figure 6.2: Atomic force microscopy (AFM) images of the STO (100) and (110) substrates. Images of step flow surfaces of treated (a) STO (100), and (b) STO (110) substrates. Inset in (b) is the surface morphology of 12 uc LAO/STO (110) sample with visible step flow.

Figure 6.2b shows an AFM image of a treated STO (110) substrate which clearly shows well defined terraces, typically 150-200 nm wide. The step height in this case is about 0.28 nm, which is the unit cell spacing along the [110] direction. The most probable surface termination is expected to be Ti-rich TiO as reported earlier [6]. The step edges appear to be facetted along the [001] and [1$\bar{1}$0] low index crystallographic directions giving rise to the triangular shaped steps [7]. The inset of figure 6.2b shows an AFM topography image after the growth of 12 unit cells

(uc) of LAO on STO (110). The preserved step flow surface clearly indicates quality of the samples with layer by layer growth. Thicker LAO films of about 15 nm were grown to enable confirmation of the growth orientation of the LAO on STO (110) substrates by x-ray diffraction (XRD). Figure 6.3 show the XRD pattern obtained for the (15 nm) LAO/STO (110) film. From the figure it is evident that LAO film grows coherently along the (110) direction.

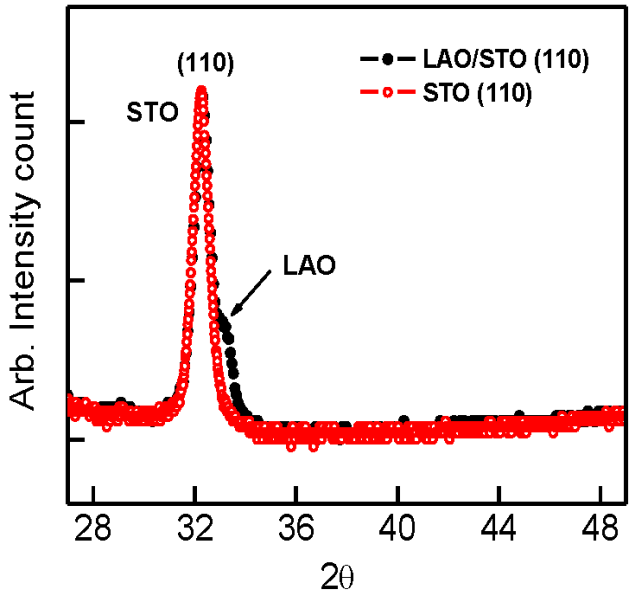

Figure 6.3: XRD pattern for the thin film of (15 nm) LAO/STO (110).

6.3 Electrical transport properties

Electrical characteristics for all the samples such as the sheet resistance, R_s, charge density, n_s, and Hall mobility, μ, were measured using Van der Pauw geometry. Figure 6.4a shows R_s versus temperature for the LAO/STO (110) samples grown at different oxygen partial pressures (P_{O2}) with a fixed thickness of 12 unitcells (uc) LAO. Strikingly, these interfaces show conductivity reminiscent to the (100) case (figure 6.4b), albeit with a larger dispersion with respect to the oxygen pressure during growth. The R_s follows a T^2-like

dependence over a temperature range of 300-100 K and tends to saturate at low temperatures.

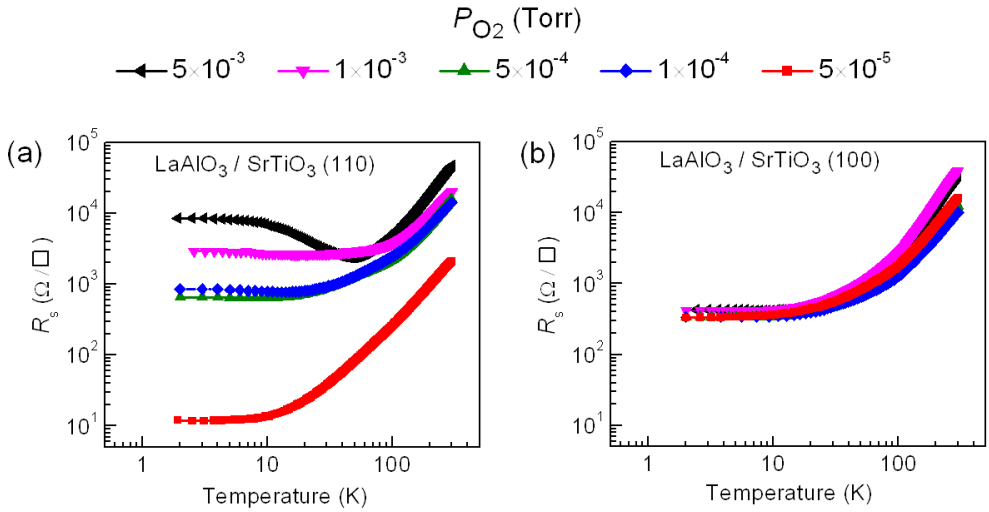

Figure 6.4: Temperature dependence of the sheet resistance R_s (T) of the LAO/STO interfaces, for different oxygen partial pressures (P_{O2}) during growth on (a), (110) and (b), (100)-oriented STO substrates.

The samples grown at higher oxygen pressures show a resistance upturn at lower temperatures, a typical localization/Kondo-behavior indicating the presence of magnetic scattering centers at the interface. While Kondo scattering in the (100) case is reported only for LAO thickness larger than 15 uc [8-10], in the case of (110) it is seen even for 10 uc LAO thickness indicating stronger scattering effects. We note here that for the (100) case the dispersion in the resistivity with oxygen deposition pressures was also reported but for samples with "*thicker*" LAO layers of 20 uc [8], implying different sensitivity to the LAO thickness between these interfaces. Interestingly, there is a temperature shift in the resistance-minimum with the oxygen growth pressure, indicating that the strength of the scattering at the interface is sensitive to the deposition conditions. We note here that resistivity measurements have been carried out down to 2 K, and it is feasible that some of these samples may become superconducting at lower temperatures.

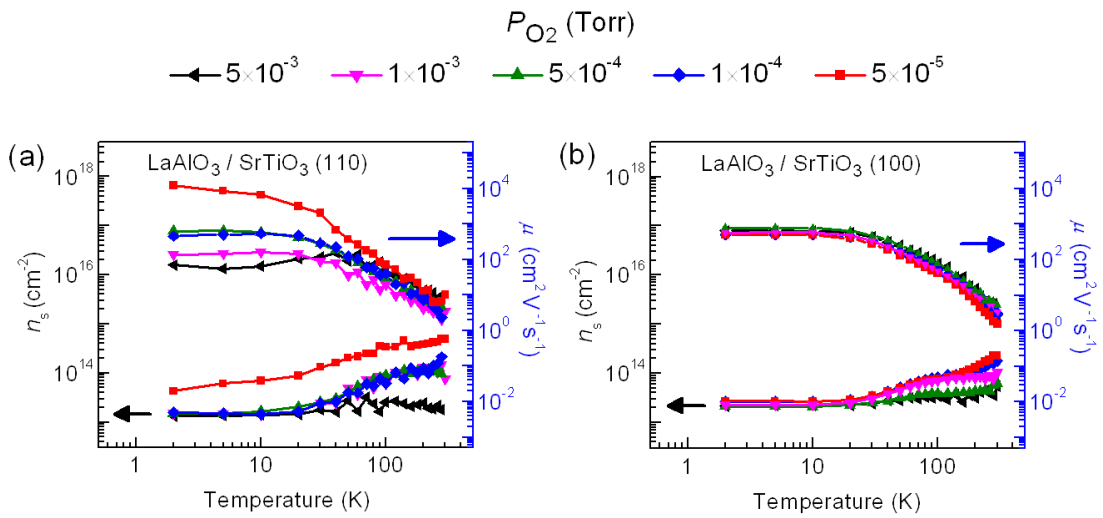

Figure 6.5: (a) Carrier density n_s and mobility μ variation with temperature for LAO/STO (110) and (b) for LAO/STO (100) samples grown at different P_{O2}.

Carrier density and mobility for the samples were extracted from Hall measurements and are summarized in figure 6.5. For the (110) samples (figure 6.5a), n_s decreases with decreasing temperature, for the samples grown at higher partial pressures n_s at low temperature (2 K) tends towards a constant value of about 1.5×10^{13} cm^{-2}, which is somewhat lower than the residual carrier density of about 2.5×10^{13} cm^{-2} for the LAO/STO (100) samples (figure 6.5b). This could be due to the preferred occupancy of the Ti-3d orbitals at the interface which may localize some of the electrons [11, 12]. For the thermally activated charge carriers in the (110)-samples we find activation energy of about 9 meV, whereas in LAO/STO (100) interfaces activation energy of 6.0 meV has been reported [13]. For both orientations, the measured μ follows a power law temperature dependence for T>100 K, as $\mu\sim5\times10^6T^{-2.2}$. All the samples grown at higher pressures show μ values of the order of 200–600 and 2–7 cm^{2}V^{-1}s^{-1} at 2 K and 300 K, respectively. These values correspond well with those reported in literature for the LAO/STO (100) interfaces [9, 14]. We notice a decrease in the μ in the (110)-case, simultaneous with Kondo features becoming visible in the R_s (T) curves. For the (110) sample grown at 5×10^{-5} Torr, the n_s at 300 K is 4.9×10^{14}

cm^{-2}, which has the μ of 12,000 $cm^2V^{-1}s^{-1}$ at 2 K, suggesting contribution from other sources such as oxygen vacancies [14,15] and defect centers present near the interface.

6.4 $LaAlO_3$ thickness dependent insulator-metal transition

One of the characteristic features of the LAO/STO (100) interfaces, and considered as one of the most important arguments for a polarization discontinuity driven mechanism, is the dependence of the sheet conductivity on the number of unit cells of LAO with the observation of an insulator to metal transition at 3-4 uc of LAO layers [16].

To investigate the thickness dependence interface conductivity for the LAO/STO (110) case, the conductivity versus the number of LAO unit cells N grown on the STO (110) substrates is measured and is shown in figure 6.6. For the thickness dependence case all samples were prepared at the same P_{O2} of 1×10^{-3} Torr. As evident from the figure samples are insulating for low N ($N < 3$) and metallic state at higher N ($N \geq 4$) values. For the samples below 3 uc thickness the conductivity is out of measurement limit of the instrument. All of the conducting samples ($N \geq 4$) show nearly equal conductivities. The 3 uc sample showed a slight higher conductivity relative to 1 or 2 uc samples although it still behaves like an insulator. Data points marked in figure 6.6 with open red circle are for a sample initially having 3 uc of LAO (insulating state), followed by the growth of 2 more uc making it 5 uc in total.

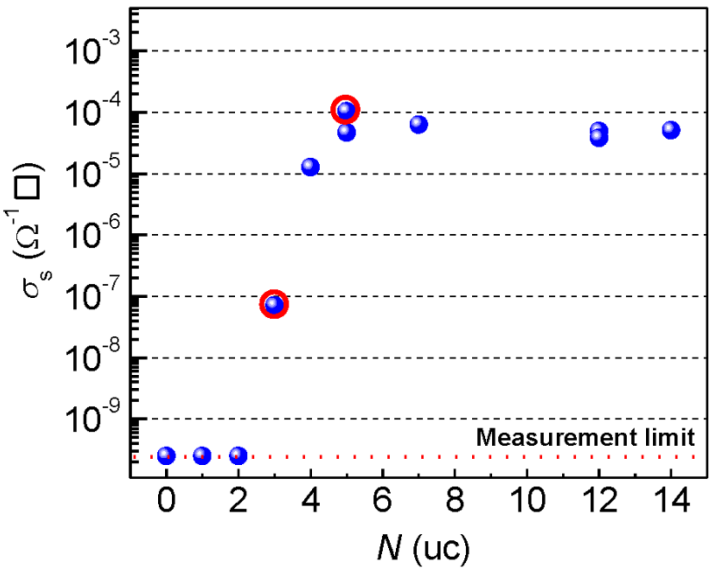

Figure 6.6: $LaAlO_3$ thickness dependence of sheet conductivity. The room temperature sheet conductivity as a function of number of unit cells of $LaAlO_3$ for the LAO/STO (110) samples, clearly showing the insulator to metal transition at about 4 uc (data points marked with open red circle are for a sample initially having 3 uc of $LaAlO_3$, followed by the growth of 2 more uc making it 5 uc in total).

Strikingly, with the thickness of 5 uc, the sample then became metallic from insulating state. The sample with $N = 0$ corresponds to STO (110) substrate which kept under identical growth conditions as the LAO/STO (110) samples.This treated substrate shows an insulating behavior ruling out the self-reduction of STO (110) at high deposition temperatures and pressure as the origin for this conductivity. The fact that there are some similarities between (110) and (100) case, including the insulator to metal transition at around 4 uc of LAO, indicates that a very similar mechanism is at work for the formation of the 2DEGs for both (100) and (110) cases.

At the LAO/STO interfaces the 2DEG was presumed to be the result of a direct manipulation of electronic reconstruction that promote electrons to the conduction band of STO, which requires energy of the order of 3.2 eV. Recent experimental work involving amorphous over layers on STO showing a conductive interface

has brought in the importance of interface chemistry [17]. Under this scenario oxygen diffusion from STO surface during film growth was deemed responsible for the interface conductivity. What was striking was the similarity of the results between the amorphous and crystalline over layers in terms of the saturation in charge density and conductivity with the film thickness. Unlike their crystalline counterparts, however in the case of amorphous over layers, the carriers generated by creation of oxygen vacancies show thermal instability and lose conductivity when subjected to a 150 °C annealing step in air or oxygen atmosphere.

To check the role of oxygen vacancy scenario, we performed subsequent post annealing steps on the as deposited samples. Samples were annealed in oxygen environment at 500 ^{o}C for 2 hour and these crystalline LAO/STO (110) samples preserve the conductivity similar to the conventional LAO/STO (100) samples. However, annealed samples show a reduction in the carrier density from that of as deposited samples. This observation of conductivity at LAO/STO (110) calls into question the polarity issues in these complex oxides. Recently, Stengel *et al.* [18] discussed the issue of polarity in various oxides, especially the case of LAO and STO surfaces, where it is shown that in LAO case, the surface with cleavage planes are shown to be energetically favorable than a simple polar (001) surface. These observations suggest that polar oxides surfaces show a tendency to form stable surfaces. In this scenario, the atomic structure of the interface would be critical to determine polarity effects at this LAO/STO (110) heterostructures.

6.5 Density functional theory

First-principles density functional theory (DFT) calculations for LAO/STO (110) interfaces were performed using the generalized-gradient approximation (GGA) [19] and the projected augmented wave (PAW) method with a plane wave basis set as implemented in the Vienna *Ab* initio Simulation Package (VASP) [20-22]. Density functional theory (DFT) calculations were performed on STO (110) surfaces with various possible atomic surface terminations. Five different surface terminations, i.e., TiO, Sr, O_2, O, and SrTiO terminations were considered. The schematic of the different possible terminations are shown in the figure 6.8.

The stability of these various possible terminations is further analyzed by energy calculations. The results suggest that buckled TiO termination at STO (110) surface is more favorable than a hypothetical polar stoichiometric SrTiO surface consistant with earlier reports [23].

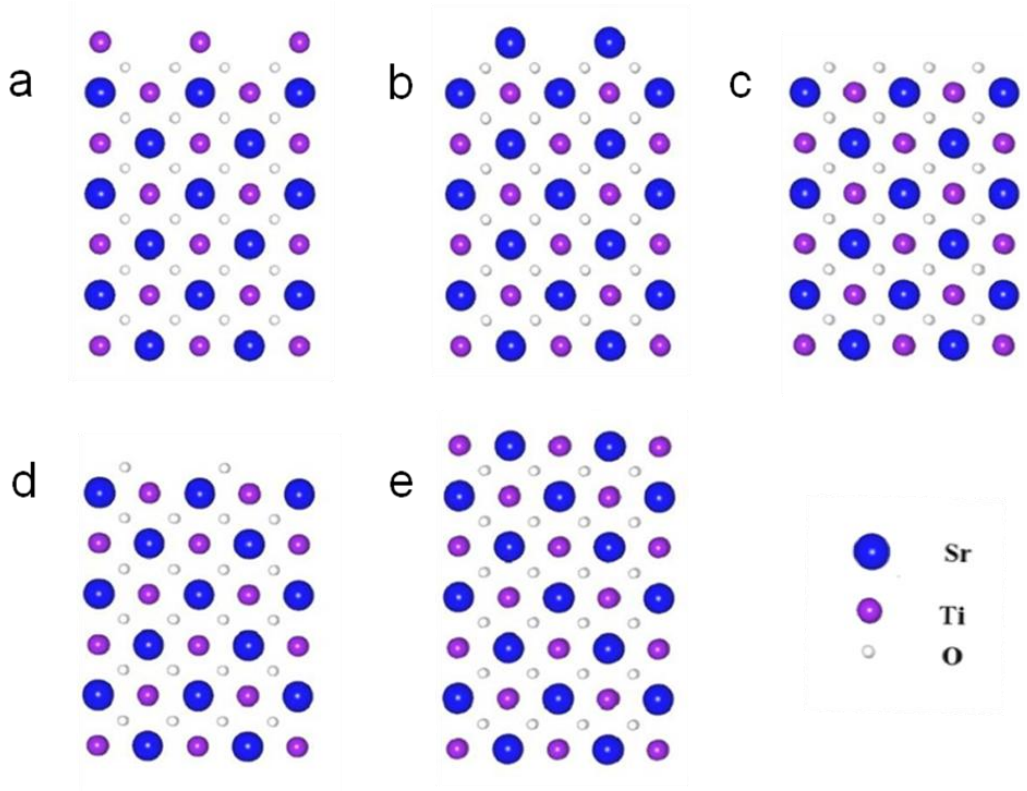

Figure 6.7: Schematic of the various possible terminations considered for the STO (110). (a) TiO, (b) Sr, (c) O_2, (d) O, (e) SrTiO terminations. The calculations showed that the TiO termination is the energetically most stable.

AFM results performed on STO (110) surface indicate the formation of good surface termination (figure 6.2a). Various surface analysis techniques such as time of flight measurements performed on annealed STO (110) revealed that the STO (110) surfaces have Ti-rich termination [6]. The formation of this termination is likely due to surface reconstruction processes. To investigate the possibility of such reconstruction, a careful analysis of RHHED patterns is carried out on

treated STO (110) surfaces prior to the LAO/STO (110) sample preparation. Figure 6.8 shows RHEED patterns obtained on the processed STO (110) surfaces along two orthogonal [001] and [$1\bar{1}0$] surfaces prior to deposition, showing a signature of reconstructed surfaces with respect to the angle of reflection. The RHEED analysis is further carried out by changing the position of the sample surface to e-beam angle, and an evolution of such reconstructed patterns is observed.

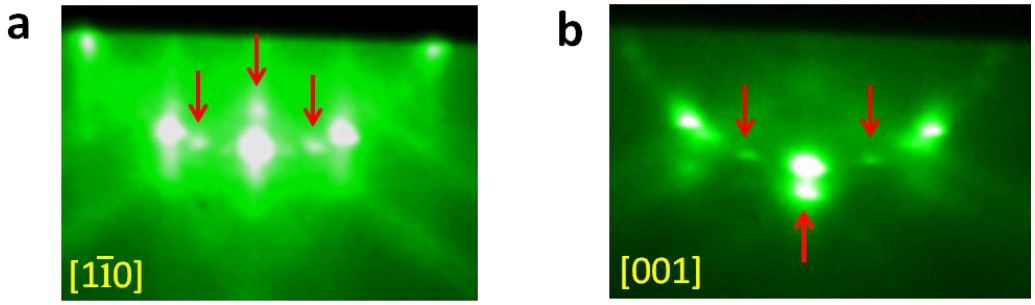

Figure 6.8: (a), and (b) shows the RHEED patterns collected for STO (110) surface prior to deposition along the[$1\bar{1}0$], and [001] directions, respectively, showing the signature of a (*1*×*3*) reconstruction on the surface.

Recently, Enterkin *et al*. [24] reported various surface reconstructions on the STO (110) surface. In general STO (110) surfaces are shown to form various reconstructed (*1*×*n*) structures [24, 25]. However, these (*1*×*n*) reconstructions can be sensitive to the thermodynamics of the processing such as annealing time and temperature. One of the observed (*1*×*3*) reconstructions is shown in figure 6.8. The growth of coherent interfaces on such reconstructed surfaces (the case here) would be interesting to be explored further.

The above results indicate the possibility of formation of stable TiO termination at the STO (110) surface. DFT calculations were performed on the LAO/STO (110) interface with the stable buckled TiO termination. Strikingly, it is found that the

origin for the unexpected conductivity in the (110) case can be explained by considering energetically stable buckled TiO termination. The electronic configuration of interfaces with such a buckled interface structure was modeled by DFT as shown in figure 6.9a. To study the thickness dependence of LAO monolayers deposited on STO (110) substrate, a slab model as shown in figure 6.9a is used.

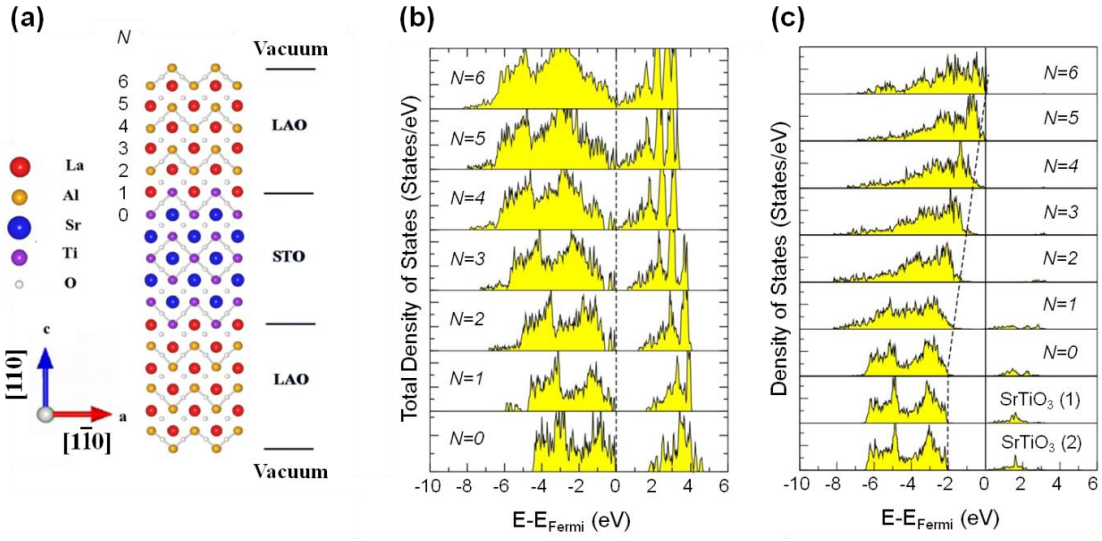

Figure 6.9: Density functional theory calculations. (a) Schematic cell structure of LAO/STO (110) interface with TiO terminated STO (110). (b) The total density of states for different numbers *N* of LAO monolayers deposited on STO (110), clearly shows the band gap decrease with increasing *N* and an insulator to metal transition occurring at 4 uc. (c) The partial density of states for O-2p projected onto each layer for *N*=6 monolayers of LAO deposited onto TiO terminated (110) STO.

To avoid the spurious intrinsic electronic field, inversion symmetry of the slab is assumed to avoid spurious electronic field. In all calculations, a vacuum region of 12 Å between repeated slabs is taken. A kinetic energy cut off is set to be 400 eV for the plane wave basis and the slab is sampled with 8×8×1 k-point grid in combination with the tetrahedron method. While the in-plane lattice constant is fixed at the relaxed lattice constant of bulk STO (*a*=3.944 Å), all coordinates of

atomic positions along the *c*-direction perpendicular to the interface are fully relaxed until the forces become less than 0.01 eV/Å. The convergence of our calculations was carefully checked. These calculations show that the energy gap for bulk STO is about 1.8 eV separating the valence band with O-2p characters and the conduction band mainly composed of Ti-3*d*.

For LAO, the obtained band gap is about 3.2 eV. These estimated values of the band gap are similar to the ones previously reported by DFT calculations [26], and are smaller than the ones observed experimentally. However, the underestimating the energy gap within GGA is well known and the GGA+U approach, for instance, gives an improved description. Indeed as shown in figure 6.9b, an insulator to metal transition with increasing number of LAO mono layers is obtained. The critical thickness for insulator to metal transition is about 4 uc which is in agreement with our experimental observation. This result shows that by viewing the LaO/TiO_2 as buckled layers, the thickness dependence of the insulator to metal transition arising from avoiding the polarization catastrophe can be reproduced [27].

Figure 6.9c shows the partial density of states for O-2p projected onto each layer. From the figure we can see clearly that the top of the valence band moves toward Fermi level as we approach the surface, suggesting that there can still exist intrinsic electrostatic fields to avoid the polar catastrophe due to the polar discontinuity caused by the buckled interface. This intrinsic electrostatic field can induce the insulator-metal transition when this electrostatic potential exceeds the band gap where the O-2p states cross over Ti 3*d* states and makes charge transfer. In our case, this transition occurs at $N < 4$ as shown in figure 6.6. Note, however, the critical value of N might depend on approximations used for calculations. We find by performing GGA+U calculations that the main conclusion are qualitatively the same. Thus, the density functional theory study reveals that the interface between $LaAlO_3$ and the energetically favorable atomic structure of the TiO terminated $SrTiO_3$ (110) can support the conductivity with the interface is represented by an alternate way, namely, the buckled interface in which the polarization discontinuity is still present.

6.6 Transmission electron microscopy of the (110) interface

To investigate the possibility of such proposed buckled atomic structure at the (110) interfaces, we performed cross sectional scanning transmission electron microscopy (STEM) on the LAO/STO (110) interfaces samples for STEM were prepared using cutting, mechanical grinding, polishing and low voltage Ar ion beam milling as a final polishing step. High angle annular dark field STEM images were recorded using a FEI Titan 80-300 microscope with a corrector for spherical aberration of the condenser lenses and a monochromator. The microscope was operated at 300 kV. The electron beam is incident along the [001] direction to the LAO/STO (110) interface.

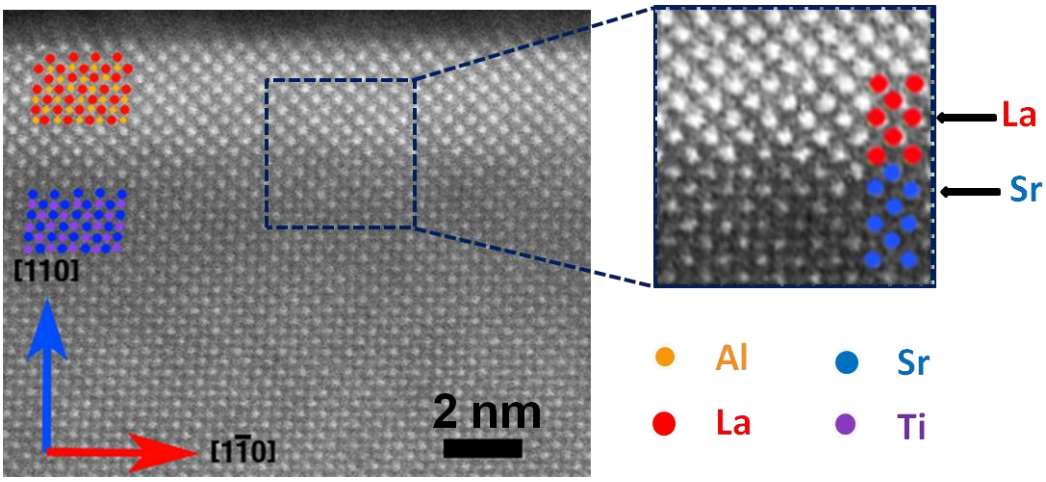

Figure 6.10: High-angle annular dark-field scanning transmission electron microscopy (TEM) images of the LAO film on the STO (110) substrate shows an epitaxial growth of the LAO/STO (110) heterostructure (*A*-site atoms La and Sr are indicated by red and blue, respectively, and the *B*-site Al and Ti by orange and purple, respectively). A magnified view of the elemental mapping across the interface is also shown on the right side.

Figure 6.10 shows a high-angle annular dark-field (HAADF) STEM image of the LAO film grown on the STO (110) substrate. The image shows a perfect epitaxial growth of the LAO across the interface of the heterostructure along the (110)-orientation. The signal from the atom columns depends on the atomic number [28]. The ratio between the signals of the Al and La atom columns is expected to be less than 10%. In addition, the projection along the Al atom columns also includes O atoms further adding to the background signal of the Al columns. We also note that the background intensity is generally higher in LAO compared to the result of (100) interfaces [29].

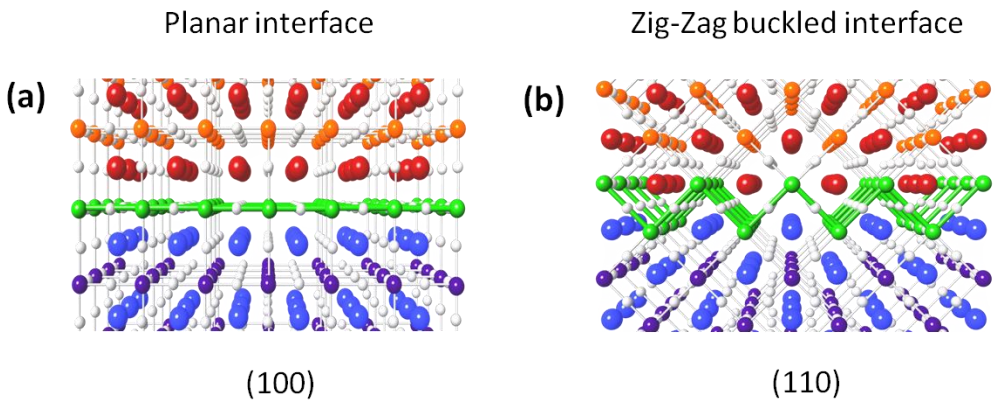

Figure 6.11: Proposed atomic picture for LAO/STO interface on (110)-oriented STO, considering the (110) planes of STO and LAO as buckled sheets.

The Al and Ti (*B*-site) atom columns are visible in the STEM images. However, it is found that it is difficult to use them as indicators of the interface between the LAO and STO film on the basis of poor signal to background ratio. Therefore, the La and Sr (*A*-site) atom columns have been used as indicators for the film/substrate interface. In the figure 6.10, a higher resolution of elemental mapping at the interface representing the arrangement of La (red) and Sr (blue) positions in both LAO and STO is also shown. We notice some of the La and Sr atoms at the interface extend up to 2-4 uc rather than 2 uc as anticipated. Both the sparseness of such extended facets and the absence of connectivity among them rule out other mechanisms for conduction (for example an effective (100)

interface at 45 degrees). However, the proposed buckled zig-zag model cannot be distinguished just by identifying only the *A*-site cations as in our current STEM data. Therefore, one needs to further resolve the chemical identity of the *B*-site cations alongside *A*-site cations in order to confirm the proposed buckled structure. Figure 6.11 show the models for the interfaces along (100) and (110) interfaces. For (100) case the interface represented by a planar interface where the Ti-O chain having a linear chain arrangement whereas a modified interface model is proposed for (110) interface that is a zig-zag buckled interface.

6.7 Anisotropic conductivity at $LaAlO_3/SrTiO_3$ (110) interfaces

Considering all the data presented above, it is remarkable that, the (110)-samples are not only conducting, but also bear remarkable similarities to the conductance properties of the (100) case. However, it is noted that the STO (110) surface is crystallographically anisotropic in terms of atomic arrangement. In most of the transition metal oxide systems, the transition metal and oxygen bonding arrangement is shown to be crucial in transport properties.

The STO (110) surface consists of two orthogonal directions [$1\bar{1}0$] and [001]. In the case of STO (110) the bonding of Ti-O along these two directions is different as shown in figure 6.12c. Directional dependence transport measurements on LAO/STO (110) samples were performed with respect to these crystallographic directions and (figure 6.12). Crystallographic directions of the surface of STO (110) identified as specified by the substrate supplier (Crystec GmbH). Strikingly, along [$1\bar{1}0$] direction (figure 6.12a) strong localization effects are seen at low temperatures while along [001] (figure 6.12b) such localizations are absent. A basic difference between these two directions is the presence of linear Ti-O-Ti chains along [001] and buckled Ti-O-Ti chains along [$1\bar{1}0$] as depicted schematically in figure 6.12c.

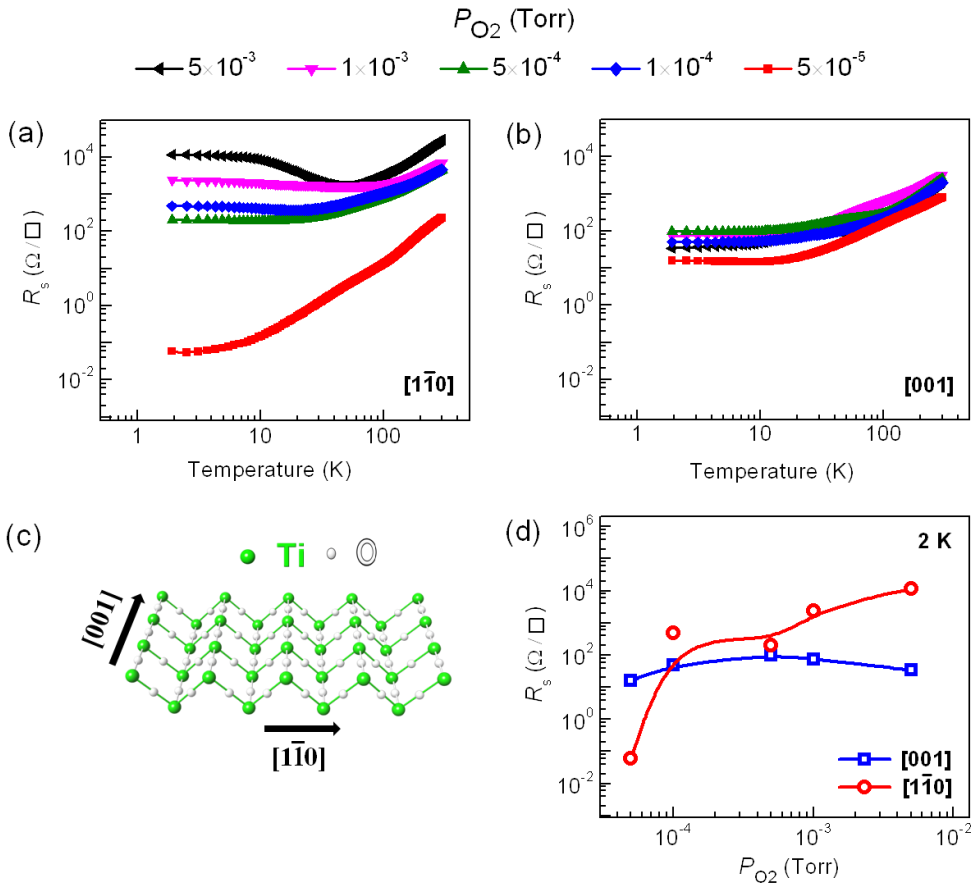

Figure 6.12: Anisotropic conductivity of the LAO/STO (110) interfaces. R_s (T) measured along (a), [1$\bar{1}$0] and (b), [001] directions for the LAO/STO (110) samples grown at different oxygen partial pressures. (c) Schematic view of The Ti chain arrangement along the [1$\bar{1}$0] and [001] directions. (d) Deposition oxygen pressure dependence of R_s at 2 K measured along the [1$\bar{1}$0] and [001] directions.

The deposition pressure dependence of R_s at 2 K is plotted in figure 6.12b for both directions. Clearly, the conductivity along the [1$\bar{1}$0] direction has a much stronger dependence on deposition pressures compared to the [001] direction, indicating the strong role of the Ti-O-Ti chain and their differences along the two orthogonal directions. The growth pressure dependence may also suggest that the defect chemistry along these two directions would be different. It is noted that the sample deposited at P_{O2} of 5×10^{-5} Torr has a considerable oxygen vacancy contribution which is also further showing a dramatic anisotropy along the

crystallographic directions, suggesting that the oxygen vacancy formation at atomic level would be different along these two different directions.

In previous reports on LAO/STO (100) case, the anisotropy is investigated and it is attributed to arise from a possible step edges [30] of the STO (100) substrate. However, the magnitude of this anisotropy is small. It is also shown that there is no systematic dependence of the step edges direction. In order to understand the role of step edges, the anisotropy measurements were performed on LAO/STO (100) samples also. Figure 6.13 shows directional dependence R_s versus temperature, measured along [010] and [001] directions for the LAO/STO (100) samples grown at different P_{O2}. Unlike the case of LAO/STO (110) here a very small anisotropy is observed in (100) case with respect to orthogonal [010] and [001] directions. Since in (100) case the two directions are crystallographically isotropic, thus this small anisotropy in (100) case could arise from step edge scattering.

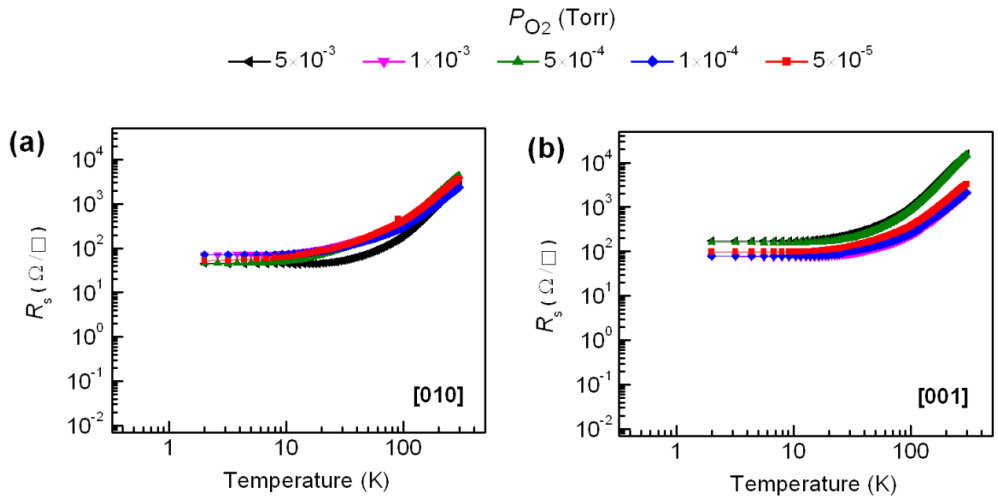

Figure 6.13: Directional dependence electrical transport in case of LAO/STO (100) interfaces. R_s (T) measured along [010] (a), and [001] (b), directions for the LAO/STO (100) samples grown at different oxygen partial pressures.

.

It suggests that step edge scattering can give anisotropy in the system but it is minimal when compared to intrinsic crystallographic anisotropy. The intrinsic carrier localizations arises due to a degree of disorder in the system might also result in anisotropy, but it cannot explain the anisotropy in the case of high conducting sample of 5×10^{-5} Torr. Thus, the large anisotropy seen in (110) must have an intrinsic origin related to the atomic arrangements of atoms, especially to the Ti-O bonding. To quantify the exact magnitude of the intrinsic anisotropy one need to perform nanoscopic transport measurements that can also exclude step edge scattering effects.

6.8 Electric field effect on $LaAlO_3/SrTiO_3$ (110) interfaces

One of the characteristic features of the LAO/STO interfaces is the electric field tuning of interface properties. Various types of electric field measurements were performed. Sample of (5 uc) LAO/STO (110) grown at P_{O2} of 1×10^{-3} Torr is used for the field effect study. Sample interfaces were accessed by directly wire-bonding Al wires.

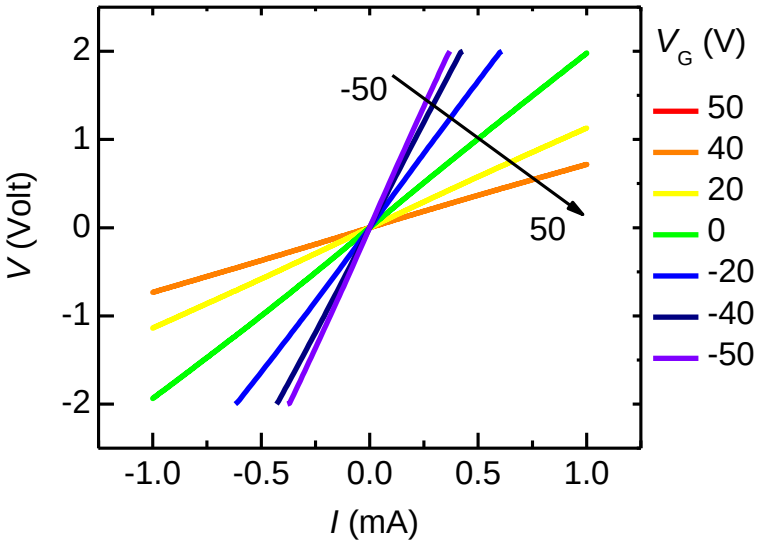

Figure 6.14: The voltage (***V***)-current (***I***) characteristics of the sample along [001] direction at a temperature of 1.9 K.

To apply back gate voltage bias, the source terminal was connected to the back gate and the leakage current through the 0.5 mm thick STO substrate was monitored through source current. Figure 6.14 show the current (I_d)-voltage (V_{ds}) characteristics as a function of V_G. The conductance of the interfaces is ohmic in nature without any evidence of any tunneling characteristics as evident from the linearity of the current-voltage. Figure 6.15 shows the V_G dependence of the resistance of the interface measures along two crystallographic directions showing a considerable field effect. At positive gate bias applied to the interface the resistance of 2DEG decreases, whereas for negative bias the resistance increases more drastically. There appears a hysteresis behavior in the initial sweep of voltages.

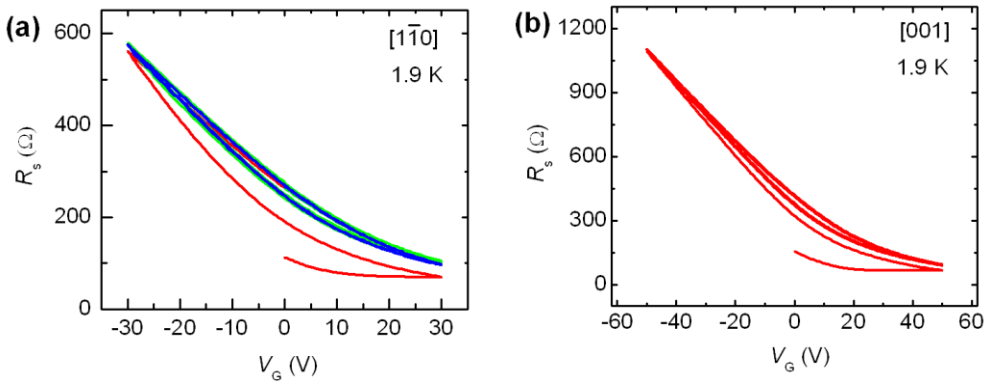

Figure 6.15: Sheet resistance of the LAO/STO (110) interface as a function of back gate voltage in (a) [1$\bar{1}$0] and (b) [001] directions measured at 1.9 K for 5 repeated measurements.

This hysteresis in the resistance is identified to be arising from the charge traps at the interface and this can be diminished significantly by cycling the voltage as shown in the figure. Therefore to go to the field effect ground state of the system, the back gate voltage was swept five times at 1.9 K before the start of each measurement which reduces the hysteresis considerably and also monitors the reproducibility of the results. To investigate the anisotropy behavior that is shown in figure 6.12, properties such as resistance, carrier density and mobility were

investigated with the gate electric field. Figure 6.16a shows the transfer characteristics (source-drain current I_d vs. back gate voltage V_G) of the interface as a function of source voltage V_{ds} at a temperature of 1.9 K in [001] direction.

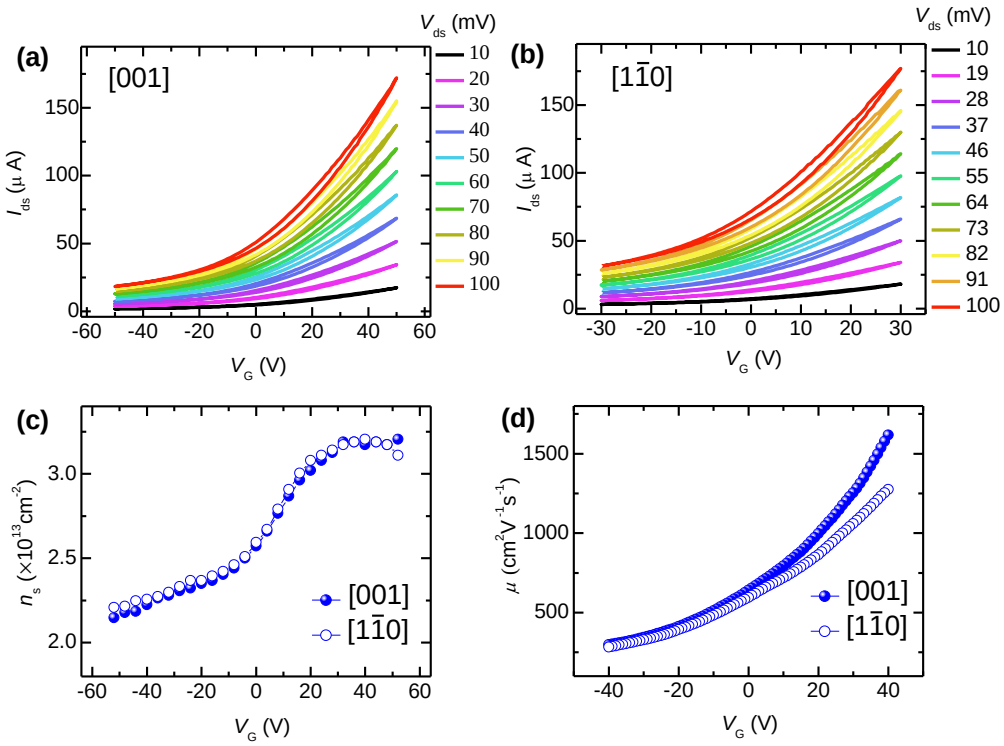

Figure 6.16: Drain current (I_{ds}) vs back gate voltage (V_G) as a function of source-drain voltage (V_{ds}) along (a) [001] and (b) [1$\bar{1}$0] showing the anisotropy in the electrical properties measured at 1.9 K. (c) Carrier density (n_e) and (d) mobility (μ_e) as a function of back gate voltage (V_G) along [001] and [1$\bar{1}$0] directions.

The gain of the transistor is quantified by trans-conductance $g_m$which is defined as

$$g_m = \left|\frac{dI_d}{dV_g}\right|_{V_{ds}}$$

These results show a finite trans-conductance (g_m= 9) for these devices showing possibility for analog electronics. The observation of saturation requires higher gate voltages which were avoided to prevent potential device damage. To

investigate the role of crystallographic orientation, we have measured the transfer characteristics in $[1\bar{1}0]$ direction which is shown in figure 6.16b. The measured trans-conductance indicates that both crystallographic orientations are equally conducting under the present preparation conditions. The hysteresis in the transfer properties is identified to be arising from charge traps at the interface and this can be diminished significantly by cycling the voltage.

It is fact that the electrons at the interface reside at the STO side confined in a few nanometers from the interface. For negative V_G on STO substrate, the electrons are pushed away from the interface whereas in the positive V_G, electrons are attracted to the interface resulting in an increase in the carrier density at the interface. It is reported that there appears a universal carrier density of 1.68×10^{13} cm^{-2} at a critical gate voltage above which the interface tend to form a superconducting ground state at lower temperatures and below which it is insulating [31]. Thus the field effect enables one to tune across the various ground states of this system. Hall measurements were performed and the results fit well with a one band model to extract the carrier density and mobility. Figure 6.16c shows the gate voltage dependant electronic density measured by performing the Hall measurements in both crystallographic directions [001] and $[1\bar{1}0]$ at 1.9 K. Significantly the variation in carrier density along these two directions resulted in similar variation with gate voltages. An electron density of $3.2x10^{13}$ cm^{-2} is observed for a gate voltage of 50 V. We notice a critical density of $2.4x10^{13}$ cm^{-2} at a gate voltage of -5 V. Since in these samples the mobility is somewhat low, this may have resulted in a different critical density than the reported one. The change in the carrier density upon a gate voltage change of 80 V is only a factor of 1.4. Figure 6.16d shows the mobility variation with the gate voltage measured along two directions. It is interesting to note from the figure that the electron mobility can be tuned by varying the gate voltage. Further, the change in the mobility upon a gate voltage change of 80 V is a factor of 5 which suggests that the transport properties at the interface are dominated by electron scattering. The mobility shows a slight anisotropy above the critical voltage in [001] and $[1\bar{1}0]$ directions particularly for positive voltages. With the understanding that above the

critical density, the ground state is superconducting and as such the anisotropy in mobility may suggest possibility for an anisotropic superconductivity in STO (110) samples.

In conclusion both the directional dependent transport measurements and electric field effects strongly suggest that the LAO/STO (110) interfaces show significant anisotropy in the electron transport. The most possible origin for the above observed properties arising from the atomic arrangement of Ti-O bonding along these crystallographic directions.

6.9 Summary

The importance of the (110) interface is better brought out in context with what has been learnt so far with the (100) interfaces. The 2DEG at the $LaAlO_3/SrTiO_3$ (100) interfaces has been studied under a variety of deposition conditions, layer thicknesses and externally applied fields [32, 33]. In most of these experiments the 2DEG was presumed to be the result of a direct manipulation of electrostatic potential at the interface in order to promote electrons to the conduction band of STO, which requires energy of the order of 3.2 eV. However, recently the 2DEG was also demonstrated on the surface of STO by shining UV light [34], vacuum cleaving [35] and chemical reduction of the surface during growth [17]. It is apparent that the 2DEG can be produced by different mechanisms, which can elevate the electron to the conduction band of STO. The real attraction of these crystalline LAO/STO interfaces is that they offer a variety of controllable parameters such as strain [36], correlation effects [37] through structure coupling and large anisotropy (as shown here) which can be used to manipulate the interface properties.

Our experiments and DFT calculations using (110) substrates show that the polarization catastrophe model may still be valid for crystalline LAO/STO interfaces provided the interface is viewed appropriately (buckled interface). Because of the different atomic structure in the (110)-interfaces, the presence of

buckled Ti-O-Ti chains opens up new possibilities which may lead to new phenomena. For example, the anisotropy can be further explored by nano-structuring the 2DEG along the anisotropic crystallographic axis with techniques such as charge writing using atomic force microscopy (AFM) [26] which has already been shown to create new properties. The other effect of the crystallographic anisotropy is on the reported spin-orbit interaction [38] which would further attract a lot of interest to explore the electric field effects on these anisotropic surfaces. Further investigation of the anisotropy on other phenomena (magnetism, superconductivity) will be of interest, which may lead to new physics and device applications.

References:

[1] N. Nakagawa, H. Y. Hwang, and D. H. Muller, "Why some interfaces cannot be sharp," *Nature Materials*, 5, 204-209 (2006).

[2] H. Y. Hwang, "Atomic control of the electronic structure at heterointerfaces. *MRS Bulletin*, 31, 28-35 (2006).

[3] Y. Mukunoki, N. Nakagawa, T. Susaki, and H. Y. Hwang, "Atomically flat (110) $SrTiO_3$ and heteroepitaxy," *Applied Physics Letters*, 86, 171908 (2005).

[4] M. Kawasaki, K. Takahashi, T. Maeda, R. Tsuchiya, M. Shinohara, O. Ishiyama, T. Yonezawa, M. Yoshimoto, H. Koinuma, "Atomic control of the $SrTiO_3$ crystal surface," *Science*, 266, 1540-1542 (1994).

[5] G. Koster, B. L. Kropman, G. J. H. M. Rijnders, D. H. A. Blank, and H. Rogalla, "Quasi-ideal strontium titanate crystal surfaces through formation of strontium hydroxide," *Appl. Phys. Lett*, 73, 2920-2922 (1998).

[6] A. Biswas, P. B. Rossen, C.-H. Yang, W. Siemons, M.-H. Jung, I. K. Yang, R. Ramesh, and Y. H. Jeong, "Universal Ti-rich termination of atomically flat $SrTiO_3$ (001), (110) and (111) surfaces," *Applied Physics Letters*, 98, 051904 (2011).

[7] R. Bachelet, F. Valle, I. C. Infante, F. Sanchez, and J. Fontcuberta, "Step formation, faceting, and bunching in atomically flat $SrTiO_3$ (110) surfaces," *Applied Physics Letters*, 91, 251904 (2007).

[8] A. Brinkman, M. Huijben, M. Van Zalk, J. Huijben, U. Zeitler, J. C. Maan, W. G. Van Der Wiel, G. Rijnders, D. H. A. Blank, and H. Hilgenkamp, "Magnetic effects at the interface between non magnetic oxides," *Nature Materials*, 6, 493-496 (2007).

[9] C. Bell, S. Harashima, Y. Hikita, and H. Y. Hwang, "Thickness dependence of the mobility at the $LaAlO_3/SrTiO_3$ interface," *Applied Physics Letters*, 94, 222111 (2009).

[10] C. Cancellieri, N. Reyren1, S. Gariglio, A. D. Caviglia, A. Fête, and J.-M. Triscone, "Influence of the growth conditions on the $LaAlO_3/SrTiO_3$ interface electronic properties," *Europhysics letters*, 91, 17004 (2010).

[11] Z. S. Popovic, S. Satpathy, and R. M. Martin, "Origin of the two-dimensional electron gas carrier density at the $LaAlO_3$ on $SrTiO_3$ interface," *Physical Review Letteers*, **101**, 256801 (2008).

[12] P. Delugas, A. Filippetti, and V. Fiorentini, "Spontaneous 2-dimensional carrier confine-ment at the n-type $LaAlO_3/SrTiO_3$ interface," *Physical Review Letters*, 106, 166807 (2011).

[13] M. Huijben, G. Rijinders, D. H. A. Blank, S. Bals, S. V. Aert, J. Verbeeck, G. V. Tendeloo, A. Brinkman, and H. Hilgenkamp, "Electronically coupled complementary interfaces between perovskite band insulators," *Nature Materials*, 5, 556 (2006).

[14] A. Kalabukhov, R. Gunnarsson, J. Borjesson, E. Olsson, T. Claeson, and D. Winkler, "Effect of oxygen vacancies in the $SrTiO_3$ on the electrical properties of the $LaAlO_3/SrTiO_3$ interface," *Physical Review B*, 75, 121404(R) (2007).

[15] W. Siemons, G. Koster, H. Yamamoto, W. A. Harrison, G. Lucovsky, T. H. Geballe, D. H. A. Blank, and M. R. Beasley, "Origin of charge density at $LaAlO_3$ on $SrTiO_3$ hetero- interfaces: possibility of intrinsic doping," *Physical Review Letters*, 98, 196802 (2007).

[16] S. Thiel, G. Hammerl, A. Schmehl, C. W. Schneider, and J. Mannhart, "Tunable quasi-two-dimensional electron gases in oxide heterostructures," *Science*, 313, 1942-1945 (2006).

[17] Y. Chen, N. Pryds, J. E. Kleibeuker, G. Koster, J. Sun, E. Stamate, B. Shen, G. Rijnders, and S. Linderoth, "Metallic and insulating interfaces of amorphous $SrTiO_3$-based oxide heterostructures," *Nano Letters*, 11, 3774-3778 (2011).

[18] M. Stengel, "Electrostatic stability of insulating surfaces: Theory and applications," *Physical Review B*, 84, 205432 (2011).

[19] J. P. Perdew, K. Burke, and M. Ernzerhof, "Generalized gradient approximation made simple," *Physical Review Letters*, 77, 3865 (1996).

[20] G. Kresse**,** and J. Hafner, "*Ab* initio molecular dynamics for liquid metals," *Physical Review B*, 47, 558 (1993).

[21] G. Kresse, and J. Furthmüller, "Efficient iterative schemes for *ab* initio total-energy calculations using a plane-wave basis set," *Physical Review B*, 54, 11169 (1996).

[22] P. E. Blöchl, "Projector augmented-wave method," *Physical Review B*, 50, 17953 (1994).

[23] Bottin, F., Finocchi, F. & Noguera, C. Facetting and (*n*×*1*) reconstructions of $SrTiO_3$ (110) surfaces. *Surf. Sci*. **574**, 65-76 (2005).

[24] J. A. Enterkin, *et al.* A homologous series of structures on the surface of $SrTiO_3$ (110). *Nat. Mater.* **9**, 245-248 (2010).

[25] L. Fengmiao *et al.* Reversible transition between thermodynamically stable phases with low density of oxygen vacancies on the $SrTiO_3$ (110) Surface. *Phys. Rev. Lett.* **107**, 036103 (2011).

[26] C. Cen, S. Thiel, G. Hammerl, C. W. Schneider, K. E. Andersen, C. S. Hellberg, J. Mannhart, and J. Levy, "Nanoscale control of an interfacial metal–insulator transition at room temperature," *Nature Materials*, 7, 298-302 (2008).

[27] R. Pentcheva, and W. E. Pickett, "Avoiding the polarization catastrophe in $LaAlO_3$ over layers on $SrTiO_3$ (001) through polar distortion," *Physical Review Letters*, 102, 107602 (2009).

[28] S. J. Pennycook, and D. E. Jesson, "High-resolution Z-contrast imaging of crystals," *Ultramicroscopy*, 37, 14 (1991).

[29] A. Kalabukhov, Yu. A. Boikov, I. T. Serenkov, V. I. Sakharov, J. Börjesson, N. Ljustina, E. Olsson, D. Winkler, and T. Claeson, "Improved cationic stoichiometry and insulating behavior at the interface of $LaAlO_3/SrTiO_3$ formed at high oxygen pressure during pulsed-laser deposition," *EuroPhysics Letters*, 93, 37001 (2011).

[30] P. Brinks, W. Siemons, J. E. Kleibeuker, G. Koster, G. Rijnders, and M. Huijben, "Anisotropic electrical transport properties of two-dimensional electron gas at $LaAlO_3/SrTiO_3$ interfaces," *Applied Physics Letters*, 98, 242904 (2011).

[31] A. Joshua, S. Pecker, J. Ruhman, E. Altman, S. Ilani, "A universal critical density underlying the physics of electrons at the $LaAlO_3/SrTiO_3$ interface," *Nature Communications*, 3, 1129 (2012).

[32] J. Mannhart, D. H. A. Blank, H.Y. Hwang, A. J. Millis, J. -M. Triscone, "Two-dimensional electron gases at oxide interfaces," *MRS bulletin*, 33**,** 1027-1034 (2008).

[33] M. Huijben, A. Brinkman,G. Koster, G. Rijnders, H. Hilgenkamp, and D. H. A. Blank, "Structure-property relation of $SrTiO_3/LaAlO_3$ interfaces," *Advanced Materials*, 21, 1665-1677, (2009).

[34] W. Meevasana, P. D. C. King, R. H. He, S.-K. Mo, M. Hashimoto, A. Tamai, P. Songsiriritthigul, F. Baumberger, and Z.-X. Shen, "Creation and control of a two-dimensional electron liquid at the bare $SrTiO_3$ surface," *Nature Materials*, 10, 114-118 (2011).

[35] A. F. Santander-Syro, A. F. O. Copie, T. Kondo, F. Fortuna, S. Pailhès, R. Weht, X. G. Qiu, F. Bertran, A. Nicolaou, A. Taleb-

Ibrahimi, P. Le Fèvre, G. Herranz, M. Bibes, N. Reyren, Y. Apertet, P. Lecoeur, A. Barthélémy, and M. J. Rozenberg, "Two-dimensional electron gas with universal subbands at the surface of $SrTiO_3$," *Nature*, 469, 189-193 (2011).

[36] C. W. Bark, D. A. Felker, Y. Wang, Y. Zhang, H. W. Jang, C. M. Folkman, J. W. Park, S. H. Baek, H. Zhou, D. D. Fong, X. Q. Pan, E. Y. Tsymbal, M. S. Rzchowski, and C. B. Eom "Tailoring a two-dimensional electron gas at the $LaAlO_3/SrTiO_3$ (001) interface by epitaxial strain," *Proceedings of the National Academy of Sciences*, 108, 4720-4724, (2011).

[37] H. W. Jang, D. A. Felker, C. W. Bark, Y. Wang, M. K. Niranjan, C. T. Nelson, Y. Zhang, D. Su, C. M. Folkman, S. H. Baek, S. Lee, K. Janicka, Y. Zhu, X. Q. Pan, D. D. Fong, E. Y. Tsymbal, M. S. Rzchowski, C. B. Eom, "Metallic and insulating oxide interfaces controlled by electronic correlations," *Science*, 331, 886 (2011).

[38] A. D. Caviglia, M. Gabay, S. Gariglio, N. Reyren, C. Cancellieri, and J. -M. Triscone, "Tunable Rashba spin-orbit interaction at oxide Interfaces," *Physical Review Letters*, 104, 126803 (2010).

Chapter 7

Nature of spin-orbit interaction at the $LaAlO_3/SrTiO_3$ (110) interface

Abstract

The nature of spin-orbit interaction at the LAO/STO (110) interfaces is investigated through gate voltage dependence of magneto conductance measurements. These measurements were performed along both [001] and $[1\bar{1}0]$ crystallographic directions. It is found that a spin relaxation mechanism is operating at this interface, and Rashba type spin-orbit interaction with gate tunability. Further, the (110) interface showed an anisotropic character in spin-orbit interaction (SOI) with respect to the in-plane crystallographic directions. The anisotropy is understood to arise from the difference in the atomic potentials in [001] and $[1\bar{1}0]$ directions due to the Ti t_{2g} orbitals. The angle dependence of magneto-conductance from in-plane to out-of-plane further indicated the existence of other mechanisms together along with Rashba spin-orbit interaction. This study thus provides a further understanding of the nature of the SOI at this interface and could be useful for tailoring the spin-orbit interaction with crystallographic anisotropy.

7.1. Introduction

In recent years, the scientific and technological relevance of spin-orbit interaction (SOI) has become prominent due to its technological importance [1]. The conventional wisdom about SOI is that as the atomic number of an element increases, the spin-orbit interaction also increases typically as the fourth power of the atomic number. However, disruption of the periodic boundary condition in a solid, particularly broken inversion symmetry, can also lead to SOIs and due to this, the interface between two solids witness strong spin-orbit interactions, the classic example is GaAs/GaAlAs [2]. The role of spin-orbit interaction in oxides and oxide interfaces has come to the fore over the last few years owing to the observation of spin-orbit interaction [3,4] at the LAO/STO interface and further the observation of simultaneous existence of superconductivity and ferromagnetism which is intriguing and unconventional. The general notion is that conventional zero momentum (singlet) Cooper pairs are unstable in a magnetic environment. Recently, it has been shown that finite momentum states are stable in the presence of magnetic fields and existence of SOI is inevitable to explain the coexistence of magnetism and superconductivity [5]. Thus, further understanding of the mechanism and tailoring of spin-orbit interaction strength at oxides and oxide interfaces would be very important. However, most of these studies were based on the LAO/STO (100) interface. The investigation of spin–orbit interaction at the interface of LAO/STO (110) is very significant. Since the origin of SOI, especially a Rashba type, is expected to arise from the broken inversion symmetry, a further anisotropy within the plane may also influence the SOI.

There exist contradicting reports on the nature of the SOI at the LAO/STO (100) interface. In one report [3], it is shown that the spin relaxation follows a D'yakonov-Perel' (DP) type relaxation whereas in another report [4], an Elliott-Yafet (EY) relaxation mechanism is suggested leading to ambiguity about the nature of SOI at these interfaces. One explanation however is that there could be more than one possible mechanism. The parameter that distinguishes these mechanisms is the spin relaxation which can originate in two ways, either during

a momentum scattering event or in between the scattering events. The former one is the (EY) mechanism [6] in which spin relaxation time τ_{so} follows $\tau_{so} \sim \tau/(\Delta g)^2$ where τ is the elastic relaxation time and Δg is the difference in the g-factor of electrons between that in a solid and vacuum. The latter is the D'yakonov-Perel' (DP) relaxation mechanism [7] in which $\tau_{so} \sim 1/\tau$ and result from random Bychkov-Rashba like spin-orbit fields. Thus quantitative analysis of SOI is very important for future implications.

To understand the nature of the SOI in LAO/STO (110) interface, samples of LAO with 5 unit cells (uc) were grown on STO (110) substrate at an oxygen partial pressure of $1x10^{-3}$ Torr using pulsed laser deposition. The study is specific to 5 uc LAO sample, which is expected to have a dominating superconducting ground state along with a strong SOI. The transport measurements were carried out in a linear geometry. The interfaces were accessed by directly wire-bonding Al based alloy wires. To apply back gate bias, the source terminal was connected to the back gate and the leakage current through the 0.5 mm thick STO substrate was monitored.

7.2. Spin-orbit interaction with respect to crystallography

The SOI can be investigated through a study of magneto-conductance measurements in the weak localization regime. The negative magneto conductance is a characteristic of the weak antilocalization of the carriers due to SOI and the strength of this interaction is tunable with a back gate voltage. Weak antilocalization has been reported in semiconductor heterostructures [8,9] which exhibit a large SOI. To extract the SOI parameters, the Maekawa-Fukuyama formula for the conductance correction ($\Delta\sigma$) in the diffusive regime is used.

For an applied field $H < H_{so} = \hbar/4eD\tau_{so}$, where D is the diffusion coefficient and τ_{so} is the spin relaxation time, the magneto-conductance is given by

$$\frac{\Delta\sigma(H)}{\sigma_0} = \Psi\left(\frac{H}{H_i + H_{so}}\right) + \frac{1}{2\sqrt{1-\gamma^2}}\Psi\left(\frac{H}{H_i + H_{so}(1+\sqrt{1-\gamma^2})}\right) - \frac{1}{2\sqrt{1-\gamma^2}}\Psi\left(\frac{H}{H_i + H_{so}(1-\sqrt{1-\gamma^2})}\right) \quad \ldots\ldots (7.1)$$

The function $\Psi(z) = \ln z + \psi(1/2 + 1/z)$, where $\psi(x)$ is the digamma function, $\sigma_0 = e^2/\pi h$, $H_i = \hbar/4eD\tau_i$ is the inelastic field with an inelastic relaxation time τ_i. Gate voltage dependent magneto conductance measurements were performed along two directions at 1.9 K.

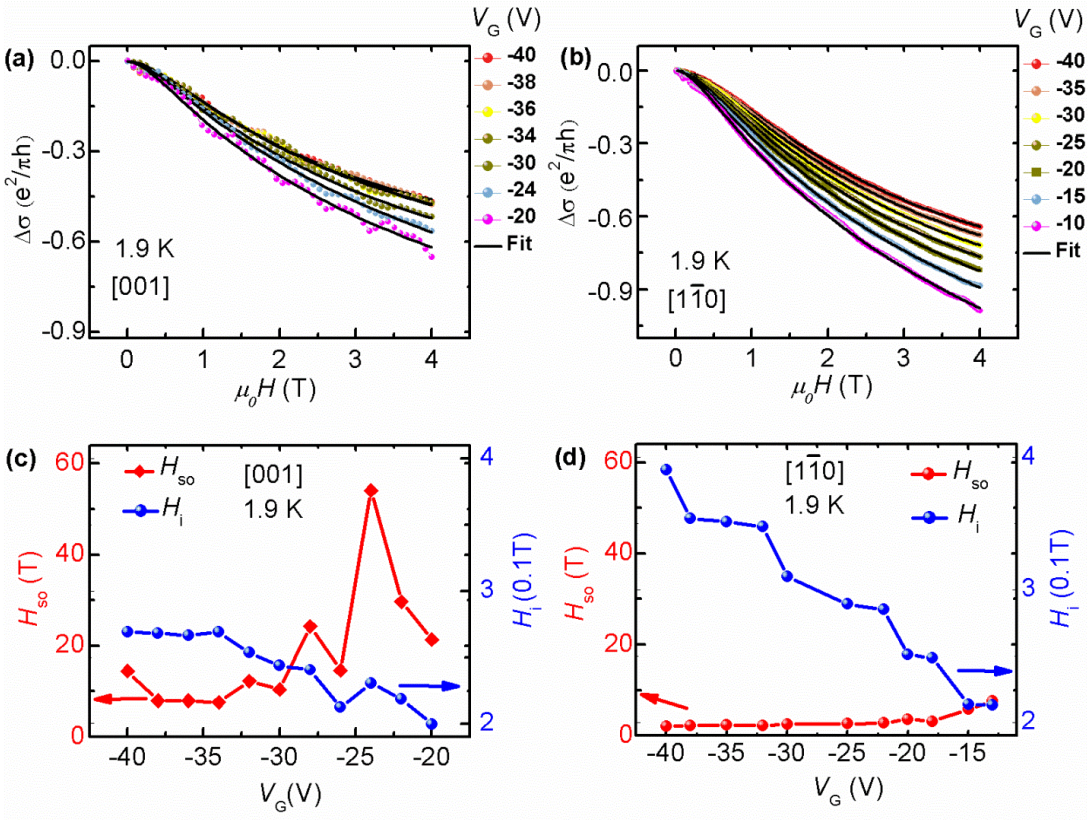

Figure 7.1: Magneto-conductance ($\Delta\sigma$) vs. applied field H as a function of back gate voltage (V_G) along (a) [001] and (b) [1$\bar{1}$0] directions measured at 1.9 K. A fit to Maekawa-Fukuyama theory is also shown in the figure. The estimated spin-orbit field (H_{SO}) and inelastic field (H_i) along (c) [001] and (d) [1$\bar{1}$0] directions as a function of back gate voltage (V_G).

Figure 7.1a shows the magneto conductance ($\Delta\sigma$) as a function of the normal external magnetic field (H) at various gate voltages in [001] direction. It is clear from the figure that the magneto conductance shows a systematic change with gate voltages. The experimental magneto conductance curves were fitted with eqn. (7.1) (Maekawa-Fukuyama theory). Fitting to the equation yield a very good fit for $V_G < 0$, but the fit is very poor for $V_G > 0$ which could be due to an increase in Coulomb interactions. Therefore we restrict our discussion to $V_G < 0$. Figure 7.1b show the magneto-conductance measured with various gate voltages along the $[1\bar{1}0]$ direction. The behavior is similar to [001] direction except with a slightly larger magneto conductance. In this case also the experimental results are fitted well with eqn. (7.1). The extracted parameters of the fittings, SOI field H_{so} and inelastic field $H_{i,}$ are plotted as a function of V_G for [001] and $[1\bar{1}0]$ in figure 7.1c and 7.1d respectively.

Here H_{so} represents a spin relaxation process whereas H_i represents the inelastic scattering process. The SOI field H_{so} shows a gradual increase with increase in V_G in both crystal directions; however their magnitudes are very different implying a significant anisotropy in the spin relaxation. On the other hand the inelastic field H_i decreases with increase in V_G, however their magnitudes are comparable in both directions.

To further determine the nature of the spin relaxation, the spin relaxation time τ_{so} was extracted from H_{so} using $H_{so} = \hbar / 4eD\tau_{so}$ where the diffusion coefficient D is calculated using Einstein relationship, $D = \pi\hbar^2 n_s \mu / m^* e$. Here n_s is the carrier density of the sample which is 1.98×10^{13} cm^{-2}. The effective mass of the electron in both crystallographic orientations is taken as $m^* = 3m_0$ [10], where m_0 is the free electron mass. On the other hand inelastic relaxation time τ_i is calculated using $H_i = \hbar / 4eD\tau_i$. Figure 7.2a shows variation in τ_{so} and τ_i as a function of V_G in [001] and $[1\bar{1}0]$ directions respectively.

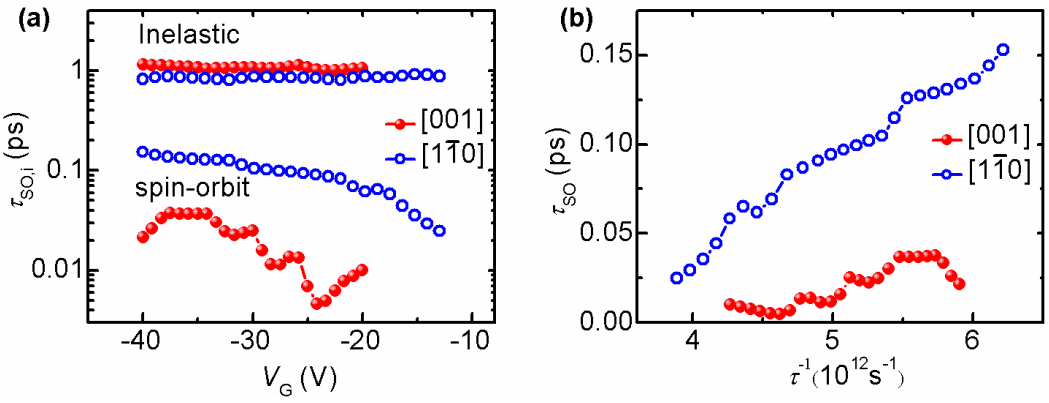

Figure 7.2: Estimated spin relaxation time (τ_{so}) and inelastic relaxation time (τ_i) as a function of back gate voltage (V_G) along (a) [001] and (b) [1$\bar{1}$0] directions.

Clearly, in both directions the τ_i shows very small changeas is the cas of the gate voltage as is the H_i. On the other hand τ_{so} is tunable with the gate voltage. In both directions, τ_{so} is much smaller than the τ_i implying that the spin relaxation is the dominant mechanism in the transport. In addition, the magnitude of τ_{so} is significantly different in [001] and [1$\bar{1}$0] directions further suggesting an anisotropic nature of the spin relaxation mechanism of the LAO/STO (110) system. The spin relaxation time in [1$\bar{1}$0] direction is of the order of 0.2 ps with the spin diffusion length $l_s = \sqrt{D\tau_s}$ is ~10 nm at a V_G = -40 V. whereas in [001] direction at a V_G of -40 V, spin relaxation time is about 0.02 ps with l_s is 3 nm. To understand the nature of mechanism of spin relaxation, it is important to investigate the relation between spin relaxation and elastic relaxation time τ where $\tau = m^*\mu/e$. Figure 7.2b shows the variation in τ_{so} as a function of inverse of τ in [001] and [1$\bar{1}$0] directions respectively. In both directions, clearly there is an inverse relationship between τ_{so} and τ which also exhibits anisotropy. The inversion relationship of τ_{so} with τ confirms the Rashba type SOI at the LAO/STO (110) interface. Eventhough the applied electric fields are very small with respect to the atomic potentials, yet the interface carrier confinements and

filling of various orbitals can be largely influence by the external electric fields could have resulted in this large tenability of SOI at this interface.

7.3. Magnetic field direction dependeece of spin-orbit interaction

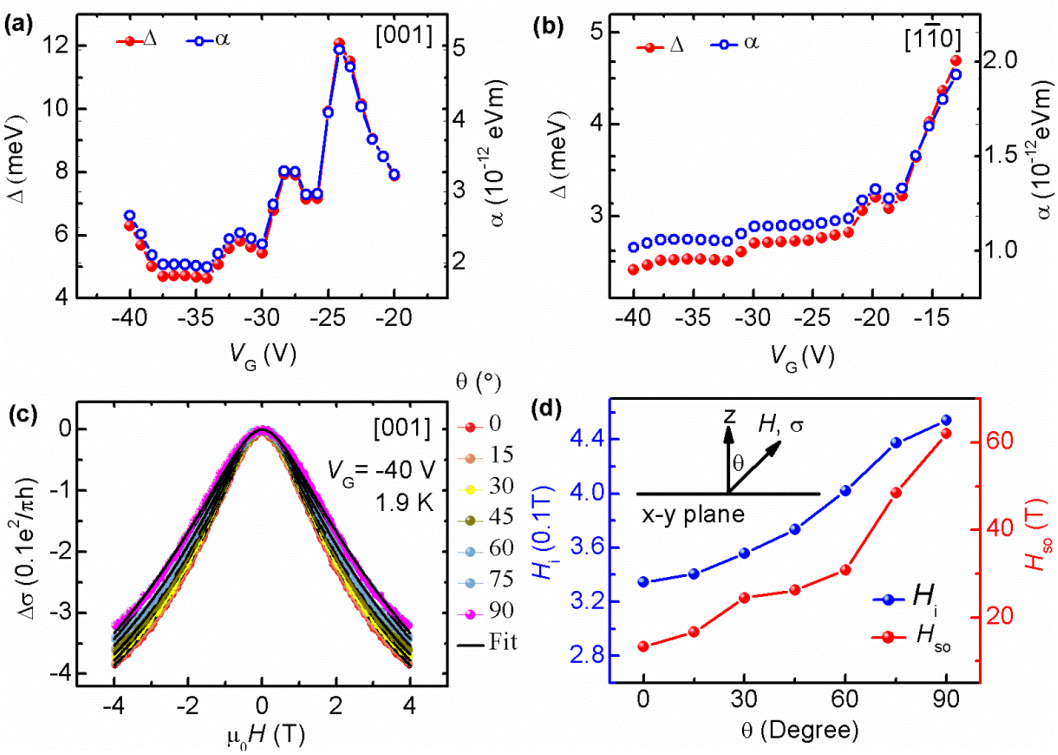

Figure 7.3: Estimated spin splitting (Δ) and coupling constant (α) as a function of back gate voltage (V_G) along (a) [001] and (b) [1$\bar{1}$0]. (c) Magneto-conductance (MC) at different angles of the magnetic field H ranging from out of plane (θ = 0^o) to in plane (θ = 90^o). (d) Fitting parameters, H_{so} and H_i, as a function of the angle of the magnetic field. Inset is a schematic of the co-ordinate system showing the direction of the applied field *H*.

The strength of the SOI, α, is calculated which is related to the spin relaxation time τ_{so} through the relationship $\tau_{so} = \hbar^4 / 8\alpha^2 m_*^2 D$. In the presence of broken inversion symmetry, the dispersion relationship at the Fermi surface exhibits a splitting in the k-vectors for up and down spins. The spin splitting is given by

$\Delta = 2\alpha k_F$ where k_F is the Fermi wave vector which is calculated from carrier density. Figures 7.3a and 7.3b show the spin splitting energy Δ and the strength of the SOI α as a function of the gate voltage. A spin splitting energy of 10 meV is estimated for V_G=-20 V in [001] case whereas this value is lower for $[1\bar{1}0]$ direction. The spin splitting energy reported here is comparable to those of GaAs heterostructures. Since the change in carrier concentration is small for the range of the applied V_G, $\Delta \propto \alpha$, which is clear from figure 7.3a and 7.3b. To clarify the nature of the SOI further, we did magneto conductance measurements at V_G = -40 V by varying the angle (θ) of the applied magnetic field to the interface, from out of plane ($\theta = 0°$) to in plane ($\theta = 90°$) direction which is shown in Figure 7.3c. The magneto-conductance is fitted with eqn. (7.1) which gives a very good fit to the experimental results at all angles. As the magnetic field orientation changes from out of plane to in plane, the negative magneto conductance decreases indicating that the conduction electron spins are affected by the magnetic field. The parameters of the fittings H_{so} and H_i are given in figure 8.3d as a function of the orientation of the magnetic field.

7.4. Summary

The gate tunability of SOI coupling at the LAO/STO (110) interfaces certainly supports the Rashba type SOI at these interfaces. The onother important factor arised from the present study is the anisotropy in SOI in the (110) plane itself. One way to produce the anisotropy in SOI is due to the atomic arrangement at the interface. Along $[1\bar{1}0]$ direction, two Ti atoms are connected by an O atom in a zigzag way, while along [001] direction it is linear. The differences in atomic arrangements may give rise to different potential gradients along respective directions. Since the origin of SOI lies in these potential gradients thus an insitropy in SOI would be expected. Further, generally Rashba effect is expected to be constant for inplane and out of plane measurements, but we see a change in strength of SOI from inplane to out of plane suggesting that there can be other contribution to the spin-orbit interaction other than Rashba type SOI that has been

demonstrated before. Thus far the SOI in semiconductor and heavy element metallic surfaces considers the spin as the source and dominant factor. However, these oxide materials with transition metals pocess an additional orbital concept that may have a significant role in the SOI at these oxide interfaces. Few recent reports suggesting an atomistic SOI and SOI with orbital effects have been proposed at the LAO/STO interfaces.Thus the atomic and orbital arrangements at the interfaces may have a significant role in those scenarios. These additional SOI concepts need to be investigated further for a complete understanding of SOI theory at the oxide interfaces

References

[1] S. Datta, and B. Das, "Electronic analog of the electro-optic modulator," *Applied. Physics Letters*, 56**,** 665 (1990).

[2] J. P. Eisenstein, H. L. Störmer, V. Narayanamurti, A. C. Gossard, and W. Wiegmann, **"**Effect of Inversion Symmetry on the Band Structure of Semiconductor Heterostructures," *Physical Review Letters*, 53, 2579 (1984).

[3] A. D. Caviglia, M. Gabay, S. Gariglio, N. Reyren, C. Cancellieri, and J. -M. Triscone, "Tunable Rashba spin-orbit interaction at oxide Interfaces," *Physical Review Letters*, 104, 126803 (2010).

[4] M. Ben Shalom, M. Sachs, D. Rakhmilevitch, A. Palevski, and Y. Dagan, "Tuning Spin-Orbit Coupling and Superconductivity at the $SrTiO_3/LaAlO_3$ Interface: A Magnetotransport Study," *Physical Review Letters*, 104, 126802 (2010).

[5] K. Michaeli, A. C. Potter, and P. A. Lee, "Superconducting and Ferromagnetic Phases in $SrTiO_3/LaAlO_3$ Oxide Interface Structures: Possibility of Finite Momentum Pairing," *Physical Review Letters*, 108, 117003 (2012).

[6] R. J. Elliott, "Theory of the Effect of Spin-Orbit Coupling on Magnetic Resonance in Some Semiconductors," *Physical Review*, 96, 266-279 (1954).

[7] M. I. D'yakonov and V. I. Perel', Fiz. Tverd. Tela (Leningrad) 13, 3581 (1971) *Sov. Phys. Solid State* 13, 3023 (1972).

[8] P. D. Dresselhaus, C. M. A. Papavassiliou, and R. G. Wheeler, "Observation of spin precession in GaAs inversion layers using antilocalization," *Physical Review Letters*, 68, 106-109 (1992).

[9] J. Nitta, T. Akazaki, and H. Takayanagi, "Gate Control of Spin-Orbit Interaction in an Inverted $In_{0.53}Ga_{0.47}As/In_{0.52}Al_{0.48}As$ Heterostructure," *Physical Review Letters*, 78, 1335-1338 (1997).

[10] L. F. Mattheiss, "Energy Bands for $KNiF_3$, $SrTiO_3$, $KMoO_3$, and $KTaO_3$," *Physical Review B*, 6, 4718-4740 (1972).

Chapter 8

Tuning the interface conductivity at the $LaAlO_3/SrTiO_3$ interfaces using proton beam irradiation

Abstract

The structuring and patterning of the 2DEG at the LAO/STO interface for device measurements and applications have remained a challenging task owing to the difficulties in physically structuring the oxides. Here, the use of energetic low Z-ion (proton/helium) beam exposure for engineering the interface conductivity has been investigated. It is found that this method can be utilized to manipulate the conductivity at the LAO/STO interface by carrier localization, arising from the defects created by the ion beam exposure, eventually producing an insulating state. This process of ion induced defect creation results in structural changes in $SrTiO_3$ which leads to the creation of rapid polarization fluctuations, as revealed by the appearance of first-order polar TO_2, and TO_4 vibrational modes which are associated with Ti-O bonds in the Raman spectra of the irradiated samples. Furthermore, magneto transport measurements reveal that the irradiated (un-irradiated) samples show a negative (positive) magneto-resistance along with simultaneous emergence of first-order (only second order) Raman modes. These experiments allow us to conclude that the interface ground state (metallic/insulating) at the LAO/STO can be controlled by tailoring the defect chemistry of the $SrTiO_3$ with ion beam exposure. Structures with a spatial resolution of 5 μm have been fabricated in a single step using a stencil mask. The ability to create an insulating state locally in the conducting oxides demonstrates a novel way to structure the conducting state without any extra etching or intermediate lithography.

8.1. Introduction

The structuring of the buried 2DEG at the LAO/STO interface is of equal importance for device applications and studies of quantum phenomena. Several methods such as amorphous LAO [1, 2] or AlO_x layer deposition [3] as intermediate steps were employed to structure the conducting regimes. In the above techniques the insulating state is created by additional deposition steps of these insulating oxides. Nanoscale writing of conducting structures has been demonstrated by Atomic force microscopy (AFM) on (3 uc) LAO/STO samples [4]. However, in all these approaches either the presence of residual hard mask in the film along with the number of additional sophisticated process steps, or the stability of the structures in ambient conditions (AFM writing case) is an issue of concern. Lithography along with reactive ion etching (RIE) has been used extensively to fabricate controlled structures of various oxide materials. However, heavy ions present in the commonly used RIE plasma transforms insulating STO to a conductor [5]. Thus, RIE cannot be applied in patterning of LAO/STO interfaces. To achieve high quality devices and also to investigate the above-mentioned exotic phases from these unique interfaces, a reliable and simple patterning process is essential, which thus far has not been realized. The important factor in patterning these conducting interfaces is to create a spatially insulating state. A significant factor is that transition metal oxides are known to show dramatic changes in electronic properties with the metal-oxygen bonds. The best examples are metal-insulator transition systems such as VO_2 [6] and rear earth Nickelates [7] where the atomic bonds govern the electrical ground state. Thus the local structural manipulations involving metal-oxygen bonds in STO may offer a way to manipulate the electrical transport microscopically. Much to the subject of effect of atomic bonds, recent reports indicated that the properties of the LAO/STO system are very sensitive to structural distorsions and epitaxial strain in STO [8]. Thus modifying the STO structure at local level may offer a new way to tune the properties of the LAO/STO interfaces. One possible way to manipulate the lattice structure of a material system locally is by ion beam irradiation where

the nuclear and electronic energy loss of the ion beam can alter the lattice symmetry by possible lattice distortions, and atomic displacements.

In this frame work, a possible manipulation of the properties of 2DEG at LAO/STO interface can be expected due to ion beam irradiation effects especially in STO. In the following, the details of ion beam irradiation experiments performed on LAO/STO interface samples are discussed. The effects of irradiations on the LAO/STO interface properties were investigated using various electrical transport measurements and Raman spectroscopy. Scanning Electron microscope (SEM) was used to image the patterned LAO/STO samples. It is found that the metallic behaviour of the 2DEG changes significantly with proton beam exposure, at a fluence of 2×10^{17} ions cm^{-2} strong localization appeared in the 2DEG, and eventually at a fluence of 6×10^{17} ions cm^{-2} the interface became insulating. This process of metal to insulator transition occurs through localization of mobile electrons via ion induced defects, resulting in structural changes in STO, as revealed by Raman spectroscopy. Raman spectra showed the appearance of first-order modes of STO which indicate the presence of polar regions in the irradiated samples. The creation of a spatially-selective insulating ground state by tuning the process parameters of an energetic ion beam based single step approach enabled us to both pattern and tune the electronic properties of the 2DEG.

8.2. $LaAlO_3/SrTiO_3$ sample preparation for ion beam irradiation

Ion beam irradiation experiments were performed with a 2 MeV proton ion beam produced using 3.5 MV ion beam facility at the Center for Ion Beam Applications (CIBA) at the National University of Singapore. The LAO/STO (100) samples were prepared by pulsed laser deposition by ablating LAO target onto TiO_2 terminated STO (100) substrates. Samples were prepared in a range of oxygen pressure (P_{O2}) of $1\text{-}5\times10^{-3}$ Torr at 750 ^{o}C. To make a systematic comparison, the ion irradiation experiments were performed with different proton fluencies on a single LAO/STO sample that consists of four equal and identical portions (each of them consist the 2DEG and portions are electrically isolated to each other). The

schematic representation is shown in figure 8.1. To achieve samples with four isolated equal portions, first, precise cross lines were made on to the square STO (2×2 mm) substrate surface with a diamond cutter that makes it in to four equal portions. Then LAO film of 8 uc is deposited on the partitioned STO substrate. Each portion of the deposited LAO/STO sample showed a conducting behaviour and conductivity is absent between any two portions. The diamond cut lines here resulted in insulating areas that account for the successful partition of the 2DEG. Three out of the four sections of the same sample were exposed to proton beam and the fourth region was kept un-irradiated (as deposited). The ion fluences used were 1×10^{15}, 1×10^{16} and 2×10^{17} ions cm^{-2} respectively.

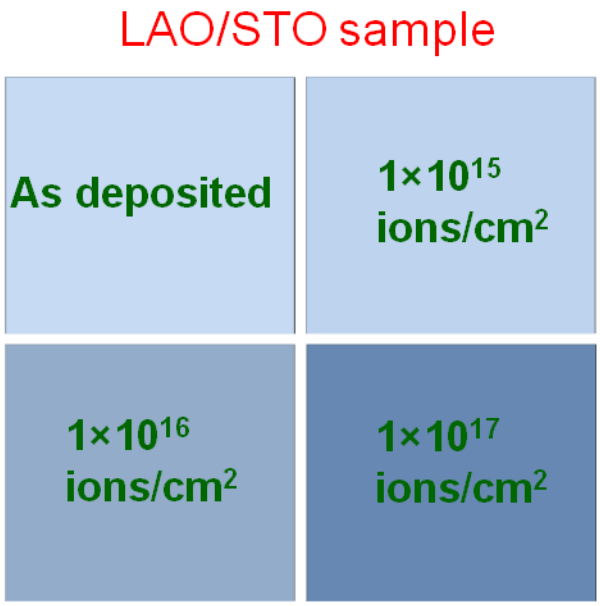

Figure 8.1: A schematic of the LAO/STO sample used for ion beam irradiations. The values represent the ion fluencies used for irradiation.

The proton irradiation experiments and measurements were performed on the (8 uc) LAO/STO sample deposited at P_{O2} of 1×10^{-3} Torr. The typical travelling depth of 2 MeV proton beam is about 26 μm (micro metres) into the STO

substrate. A collimated beam of 2 MeV protons were used to raster-scan under normal incidence over an area of 2×2 mm^2.

8.3. Proton beam irradiation effects on properties of 2DEG

8.3.1 Electric transport and electron localization effects

The electrical transport properties of irradiated portions and as deposited portion of the (8 uc) LAO/STO sections of sample were measured by PPMS. Electrical contacts to the buried 2DEG were provided by Al wire bonding to the interfaces. The temperature dependence of the resistance R (T) for the as-deposited and irradiated sections is shown in Figure 8.2a. The as-deposited section of the sample exhibits a typical metallic behaviour similar to the conventional LAO/STO interfaces at this LAO thickness [9]. Whereas for the irradiated sections, a gradual change in the resistance at 300 K is observed with increase in ion fluence. As the proton fluence is increased, clear localization behaviour in transport starts to emerge at low temperatures with the signature of increased base resistance at 2 K. The sample section irradiated with 2×10^{17} ions cm^{-2} shows strong localization with a resistance of 0.1 MΩ at 2 K, and the resistance minimum in the R (T) curve is found to shift towards higher temperature with an increase in ion fluence. The above R (T) behaviour gives adequate indication that ion exposure has created a high resistive state of the 2DEG through localization of the mobile electrons. The drastic upturns in resistance towards low temperatures is expected for transport mechanisms such as variable range hopping (VRH) in the strong localization regime (discussed in chapter 5) and magnetic Kondo scattering [10] at this interface. The R (T) curve for the case of 2×10^{17} ions cm^{-2} does not show any saturation even down to 2 K (inset of figure 8.2b) inferring that Kondo scattering may not be the governing mechanism.

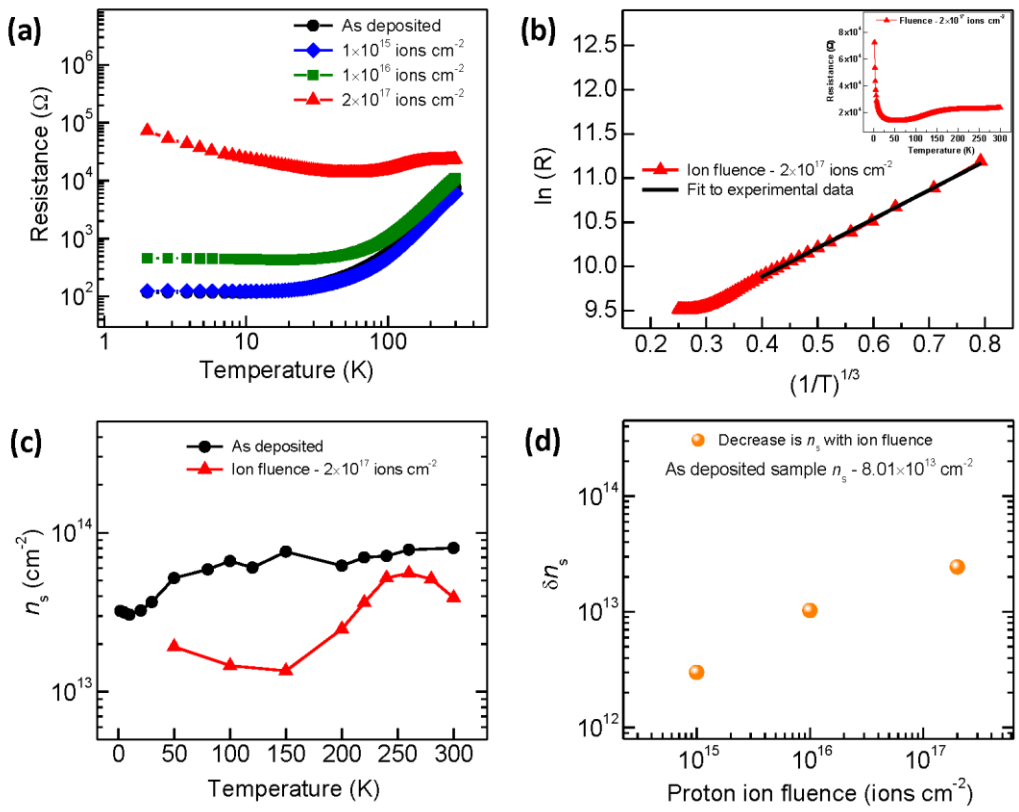

Figure 8.2: Electrical transport of as-deposited and 2 MeV proton beam exposed (8 uc) LAO/STO sample sections. (a) Temperature dependent resistance of as-deposited and ion beam exposed sample sections at different proton fluences. (b) Variable range hopping fit to transport data of ion irradiated with 2×10^{17} ions cm^{-2} fluence, the inset shows the non-saturating behaviour of corresponding sample section. (c) Temperature dependence of carrier density (n_s) for as-deposited and 2×10^{17} ions cm^{-2} ion fluence. (d) Reduction in carrier density δn_s with ion fluence at 300 K, here δn_s defined as the difference in n_s of as-deposited and irradiated sample sections ($\delta n_s = n_{s\ (\text{as-deposited})} - n_{s\ (\text{irradiated})}$).

The low temperature resistance behaviour is further analyzed with respect to the VRH mechanism. In the VRH regime R follows a $(1/T)^{1/n+1}$ (n = dimensionality of the system) dependence. A two-dimensional (n = 2) VRH formula fitting for the experimental data for a fluence of 2×10^{17} ions cm^{-2} case is given in figure 8.2b and the clear $(1/T)^{1/3}$ dependence below 20 K indicates the dominant transport mechanism is VRH in this strong localization regime.

The other important quantity that can give further insight to the localization behaviour is the carrier density (n_s). The n_s for as-deposited and each irradiated section of (8 uc) LAO/STO sample were extracted from Hall Effect measurements. Figure 8.2c shows the temperature dependence of the n_s behaviour for the as-deposited and irradiated with 2×10^{17} ions cm^{-2}. The n_s for the as-deposited section of the sample is about 8×10^{13} cm^{-2} at 300 K and 3×10^{13} cm^{-2} at 2 K. In comparison, the irradiated section shows a significant decrease in n_s to about 5×10^{13} cm^{-2} at 300 K and a further decrease towards low temperatures. The carrier freeze-out towards low temperature further indicates localization effects induced by ion beam exposure. Figure 8.2d shows the extracted decrease in carrier density (δn_s) with proton fluence at 300 K. Here δn_s is defined as the difference in the n_s of as-deposited and n_s of irradiated sections ($\delta n_s = n_{s(\text{as- deposited})} - n_{s(\text{irradiated})}$). From Figure 8.2d it is clear that δn_s increases with the proton fluence with a value of δn_s of about 3×10^{13} cm^{-2} for a fluence of 2×10^{17} ions cm^{-2}. The n_s data clearly indicate that the proton beam exposure with a fluence of 2×10^{17} ions cm^{-2} can reduce as many as 3×10^{13} cm^{-2} mobile carriers of the 2DEG at the interface which is most possibly accomplished by localization of carriers within the lattice of STO. From the above conclusion one may expect that the interface samples having initial $n_s \leq 2\text{-}3\times10^{13}$ cm^{-2} may turn insulating at these ion fluences due to complete localization of carriers. Further to validate this possibility, a conducting LAO/STO sample having an initial carrier density of 1.9×10^{13} cm^{-2} (achieved by controlling the oxygen pressure during the growth) has turned to became insulating with the exposure of proton beam at a fluence of 2×10^{17} ions cm^{-2}.

From the above conclusion one may expect that the interface samples having initial carrier density in the order of $3\text{-}4\times10^{13}$ cm^{-2} may turn in to insulating state at these ion doses due to the complete localization of carriers. To verify the above possibility, new LAO/STO sample was grown at slightly higher P_{O2} of 5×10^{-3} Torr with LAO thickness of 5 uc. The sample n_s is found to be 2×10^{13} cm^{-2} at 300 K which is lower than the previously discussed sample (the reduced n_s achieved by growing the sample at relatively high P_{O2}). A portion of the new sample was

irradiated with the proton ion dose of 2×10^{17} ions cm^{-2}. Strikingly as anticipated this irradiated portion become insulator (exceeding measurement limit of 20 MΩ). The above experiment on the sample with low n_s (2×10^{13} cm^{-2}) confirms that ion irradiation can completely localize the n_s of the order of 3-4$\times10^{13}$ cm^{-2} with ion dose of 2×10^{17} ions cm^{-2}.

8.3.2 Magneto resistance analysis

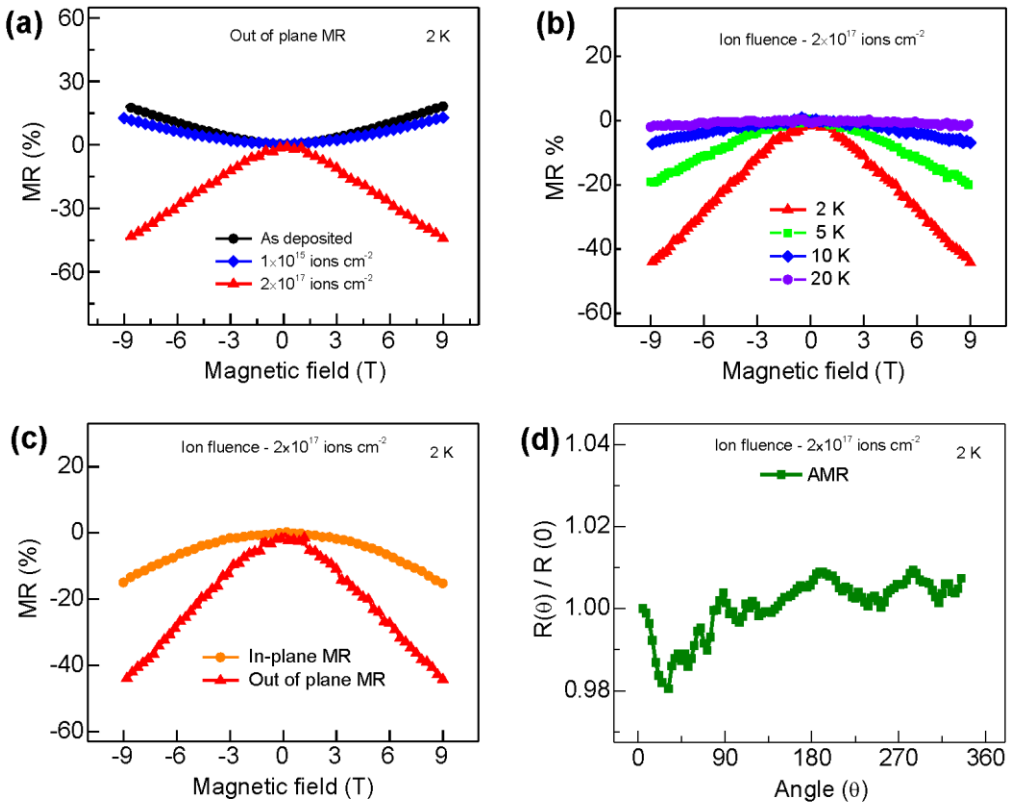

Figure 8.3: Magnetoresistance (MR) of the (8 uc) $LaAlO_3/SrTiO_3$ sample sections with different proton fluences: (a) Out of plane MR at 2 K for different ion fluences. (b) Out of plane MR at 2, 5, 10 and 20 K for the sample section irradiated with 2×10^{17} ions cm^{-2}. (c) In-plane and out of plane MR measured for the sample section in (b) at 2 K. (d) Angle dependent anisotropic magneto resistance measurement for the corresponding sample portion.

To evaluate the localized transport behaviour at low temperature in the above ion exposed samples, a detailed magnetoresistance (MR) study was carried out. MR is a useful tool to investigate the transport mechanisms such as localization and magnetic scattering. MR measurements were performed in various modes such as in-plane, out of plane and anisotropic MR (AMR). Figure 8.3a shows the out of plane MR (magnetic field ***H*** perpendicular to the interface) measured for different ion irradiation fluences and as-deposited sections at 2 K with ***H*** upto 9 T. Both as-deposited and low fluence (1×10^{15} ions cm^{-2}) sections display a positive MR behaviour. Positive MR is a characteristic of orbital scattering in the presence of a magnetic field due to the change in electron transit paths. On the other hand the section exposed with 2×10^{17} ions cm^{-2} fluence shows a negative MR behaviour. Comparison of the MR with respect to ion fluence infers that the MR slowly changes sign from positive to negative with increasing ion fluence, suggesting that it must be correlated with the localization effects discussed earlier in figure 8.2. The large negative and non-saturating MR observed in the irradiated case is a further indication of strong localization behaviour. Electron transport in the strongly localized regime can exhibit a negative MR as a consequence of magnetic field disrupting the self-interference of the electrons and is consistent with the VRH study (discussed in chapter 5). The temperature dependence of the out of plane MR measured for a fluence of 2×10^{17} ions cm^{-2} is shown in Figure 8.3b. The magnitude of MR gradually decreases with increase in temperature which can be understood as the effect of enhanced thermal fluctuations on the scattering process. Figure 8.3c shows the comparison of in-plane (***H*** applied parallel to the interface) and out of plane MR for the 2×10^{17} ions cm^{-2} case where both display a negative MR, however with a difference in MR magnitude. Orbital scattering is excluded in this in-plane geometry due to the absence of Lorentz forces on carriers. The in-plane anisotropic MR (AMR) measurement performed for the 2×10^{17} ions cm^{-2} case and with rotated the ***H*** with respect to current (***I***) direction within the plane of the interface is shown in figure 8.3d. The AMR shows an oscillatory behaviour which is similar to that discussed in chapter 4.

The detailed electron transport and MR analysis discussed above clearly indicates the dependence of ion fluence for carrier localization and point towards the possibility of creating insulating regions in 2DEG. At the LAO/STO interface it is known that the 2DEG is accumulated at the Ti orbitals of STO [11]. Since the ion irradiation produces dramatic changes in the transport of the 2DEG that resides in STO, it is necessary to understand the effects of ion irradiation on STO. Recent reports on STO based interfaces reveal that an atomic distortion of the STO lattice at the interface can manipulate the transport properties of 2DEG significantly [8, 12]. Direct implications of irradiation are that it may create distortions in the crystalline lattice of STO, and/or it may create various types of vacancies and local disorder to an extent in the STO during the various energy-loss processes. A significant observation made with ion irradiation is the optical contrast of the irradiated portions of the sample. The irradiated portions lost the transparency when compare to the as deposited LAO/STO sample portion. In general, ion irradiation can be expected to modify the atomic structure of the materials through electronic and nuclear energy-loss with the atoms of the materials. These atomic structural changes may in turn modify the properties such as optical transparency and electron transport as shown above. In order to investigate the ion irradiation effects on structural and electronic properties of the LAO/STO samples, Raman spectroscopy experiments were carried out.

8.4. Raman spectroscopy of irradiated $LaAlO_3/SrTiO_3$ interface

To understand the possible microscopic structural changes in LAO/STO samples with ion irradiations, Raman spectroscopy experiments were performed on pristine and irradiated portions of the LAO (8 uc) /STO sample. Visible Raman spectroscopy was carried out at room temperature using Renishaw Invia system. The excitation wavelength used was 532 nm and the laser power at the sample was below 1.0 $mWcm^{-2}$ to avoid laser induced damage. A 50X objective lens was used with a laser spot size of ~1 μm and the scattered light from the sample was collected in the back scattering geometry. Raman imaging was carried out using WITec CRM200 Raman system using 532 nm excitation wavelength with a

motorized stage. Raman spectroscopy is used to investigate the vibrational modes of the system.

A material system becomes Raman active only if the vibration is associated with the change in polarizability, for a centro-symmetric system like STO, the first order modes can be Raman active only if the system looses inversion symmetry. In the present case of LAO/STO the thickness of LAO is only 8 uc therefore the Raman spectrum of the LAO/STO sample is expected to be dominated by the modes from the STO substrate only.

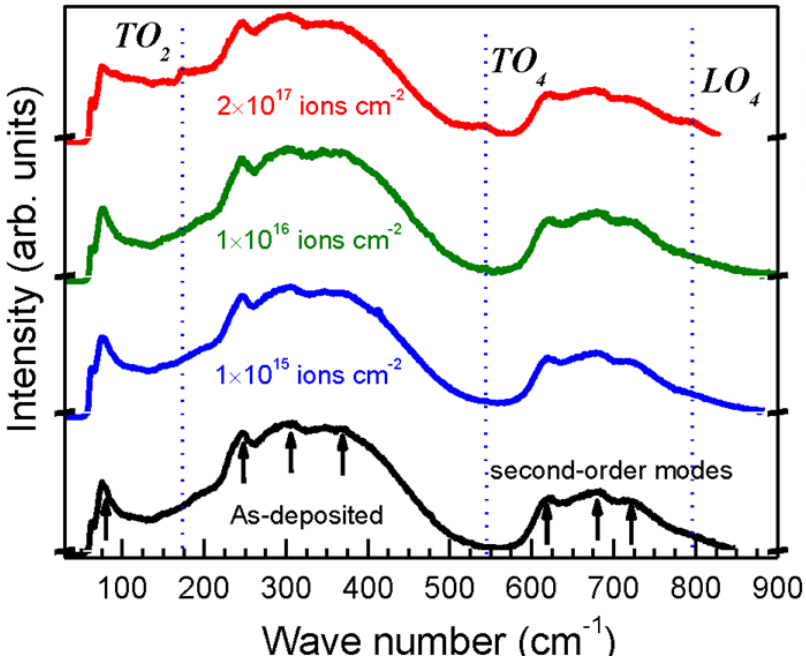

Figure 8.4: Raman spectrum obtained for (8 uc) LAO/STO interface sample portions irradiated with different proton ion doses and as deposited portion. The Transverse TO_2 and TO_4 modes at 165 and 540 cm^{-1} and a longitudinal LO_4 mode at about 800 cm^{-1} emerges with respect to proton ion dose respectively.

STO at room temperature has an ideal cubic perovskite structure with space group *Pm3m* (O_h^1) [13]. There are five atoms per unit cell and each of which is located at a point of inversion symmetry. The atoms are situated on five interpenetrating

simple cubic lattices and at the Brillouin zone center, all the optical phonons in the cubic phase are of odd parity, which accounts for the absence of first-order Raman scattering in STO single crystals [14-16]. Even though the first-order modes are Raman inactive, STO shows a Raman spectrum with broad peaks that are arising from higher-order modes which involves the creation or destruction of two or more first-order modes. Raman spectrum was collected for irradiated and as deposited portions of the (8 uc) LAO/STO sample and is shown in the figure 8.4. As expected the spectrum is dominated by STO modes. In the spectrum, the broad second-order peaks are clearly visible at 75, 200-500 and 600-800 cm^{-1} which arise from the second order-order modes. Significantly, additional peaks start to emerge at 175, 540 and 795 cm^{-1} with increase in irradiation ion fluences (clearly visible for the sample portion irradiated with proton ion fluence of 2×10^{17} ions cm^{-2}). These peaks are identified as symmetry-forbidden first order modes arising from transverse TO_2, TO_4 and longitudinal LO_4 phonons, respectively [17-19]. A significant note here is that the appearance of these Raman modes co-insides with the evolution of localization behaviour in electric transport measurements with respect to the ion irradiation fluence where the highest fluence show maximum effects with change in both Raman spectrum and transport. The appearance of first-order modes in irradiated portions of the sample clearly indicates a lowering of crystal symmetry for the STO and thus the loss of the inversion centre [17-19]. First-order Raman scattering has been observed in thin films, nano-structures of STO, and also in single crystals with lifted centre-of-symmetry by the application of an external electric field [18-20]. The line shape of the TO_2 peak is asymmetric- *i.e.* the scattering intensity increases at the high-energy side and is depressed at the low-energy side of the peak- and this displays a Fano profile [17-19]. Fano effect occurs whenever discrete excitations and a broad continuum interfere coherently. This continuum of excitations in the irradiated sample is polar because it interacts with the polar TO_2 phonon. Such asymmetric line shapes have been observed for polar TO_2 modes in STO thin films and have been ascribed to the interaction of the phonon with a continuum arising from rapid polarization fluctuations [17, 18]. Although TO_4 is also a polar

phonon, its energy is much higher, the density of states for continuum vanishes at this frequency and thus Fano asymmetry has not been observed in the case TO_4 mode [17]. The origin of the TO_2 and TO_4 modes is associated with Ti-O bonding in the STO [18-20]. The appearance of $TO_{2,4}$ modes indicate the presence of polar regions in the case irradiated at a ion fluence of 2×10^{17} ions cm^{-2}.

8.5. Raman spectroscopy of irradiated $SrTiO_3$

In order to further confirm the above spectrum analysis on STO proton irradiation experiment was carried on bare STO substrate (ion fluence is 2×10^{17} ions cm^{-2}). The corresponding Raman spectrum for bare STO substrate and irradiated portion of STO is shown in figure 8.5. Here also a clear emergence of additional modes (marked in figure with line) are seen for the irradiated sample while they are absent for bare STO.

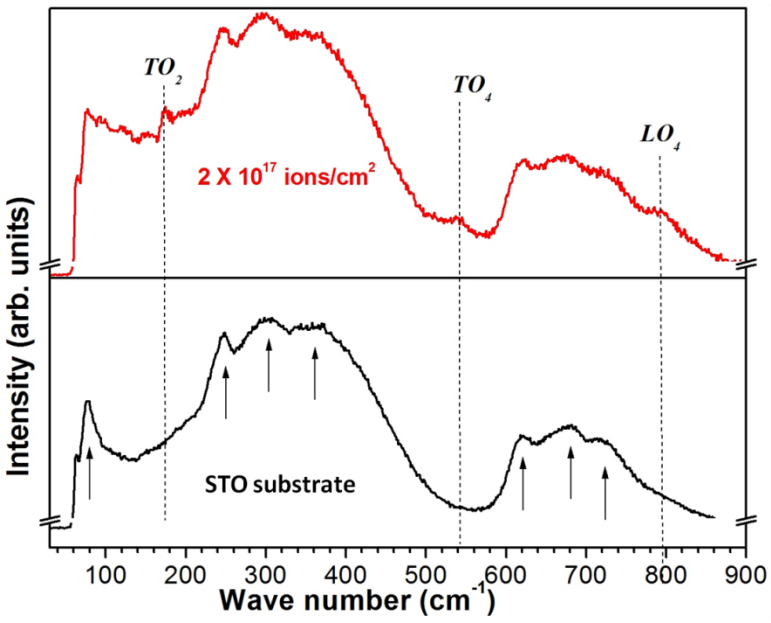

Figure 8.5: Raman spectrum obtained for bare STO sample portion with and without irradiation.

Oxygen ions being the lightest in the STO lattice have maximum displacements compared to Ti, Sr under the exposure of energetic ions. If this is the case, one would expect a reduction in resistance for the irradiated STO. The conductivity of the same sample is measured before and after irradiation, and it does not show any change in the insulating nature of the STO within the sensitivity of our measurements. This confirms that the current irradiation experiments are not creating any significant amount of oxygen vacancies to increase the mobile charges in STO. Eventhough the produced oxygen vacancies may have a chance of getting compensated by the counter produced cationic vacancies of Sr and Ti. An estimate of the defects created by the proton beam can be determined from Monte Carlo simulations (SRIM 2008) using a full damage cascade. Oxygen ions being the lightest in the STO lattice have maximum displacements compared to Ti and Sr under irradiation by energetic ions. If oxygen vacancies were the dominant defects in the MeV proton irradiated STO, one would expect a reduction in resistance for the irradiated STO as observed by Kan *et al.* [5]. The displacement per atom (dpa) for Sr and Ti is found to be half that of oxygen. The oxidation states of O, Ti and Sr are -2, +4 and +2 respectively. Thus the cationic and anionic vacancies will have different charges. The conductivity of the same LAO/STO sample measured before and after irradiation showed an increase in 2DEG resistance with fluence. In a separate experiment, a STO substrate irradiated with a fluence of 2×10^{17} ions cm^{-2} did not show any change in the insulating nature of the STO within the sensitivity of our measurements. This confirms that the current irradiation experiments does not simply create oxygen vacancies alone, but also generate compensating cationic vacancies, and at higher fluences other defect complexes which can trap charges efficiently. This is a benefit as the low Z ion beam will not produce a parallel conducting path in the STO as in the cases with low energy heavy ion irradiations [5].

One significant observation from both transport and Raman measurements is that the sample irradiated with low fluence (1×10^{15} ions cm^{2}) does not show much signature of localization and at the same time no significant changes in Raman spectrum, where as for the high ion dose of 1×10^{17} ions cm^{-2} irradiation case, both

localization behaviours with the formation of polar modes in STO can be noted. It suggests that the emergence of these polar modes in STO must have a correlation with electronic structure of STO. The newly learned mechanism to localize carriers and ability to create insulating state locally as shown above encouraged us to investigate the structuring capability of the LAO/STO interface.

8.6. Structuring of $LaAlO_3/SrTiO_3$ interface

For this, a sample of (8 uc) LAO/STO is grown under identical conditions as the previous sample. Two lines each of which having dimensions of 500 µm width and 2 mm in length were patterned in one of the region.

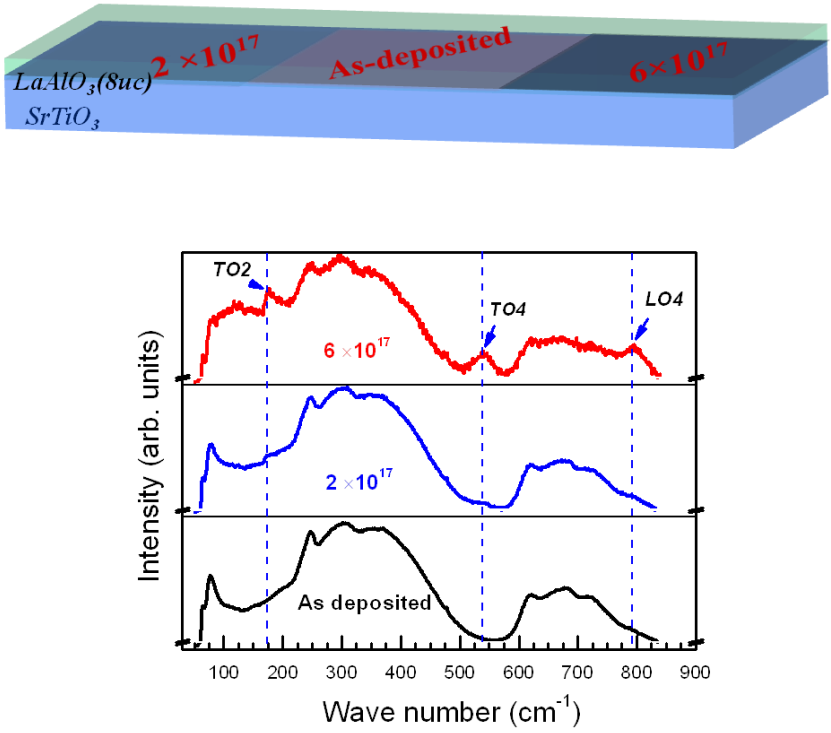

Figure 8.6: Raman spectrum obtained for LAO/STO sample portions irradiated with different proton ion doses. Schematic represents the 500 µm patterns line made with different proton ion dose.

These three regions were formed by employing ion irradiation with different doses as shown in figure 8.6. To confirm the the lattice effects of STO the Raman spectrum is obtained for these three patterned lines. As shown in figure 8.6 the Raman spectrum displays similar behaviour as in the previous case. Note here is that the increased ion dose to 6×10^{17} ions cm^{-2} is strongly reflected with observation of stronger intensity profile for the polar mode peaks in the spectrum also. Further, a Raman spectroscopy image produced using the integrated intensity of TO_4 mode at 540 cm^{-1} of the irradiated sample is shown in figure 8.7.

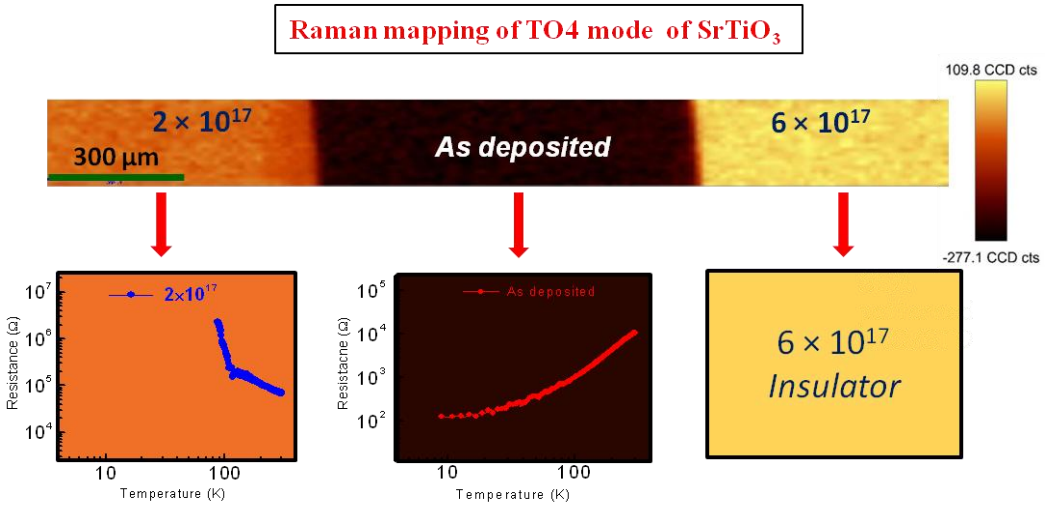

Figure 8.7: Raman spectrum mapped for a TO_4 mode at 540 cm^{-1} for patterned lines (500 µm) of LAO/STO sample portions irradiated with different proton ion doses showing a clear intensity difference with ion irradiation dose. The resistance behaviour with temperature measured for the corresponding patterned lines displaying the metal to insulator transition with increase in proton ion irradiation dose.

The as deposited and the irradiated regions at ion dose of 2×10^{17} ions cm^{-2} and 6×10^{17} ions cm^{-2} are clearly distinguishable in the intensity profile. Here as deposited portion (with electrically conducting state) shows no signal from TO_4 mode. Whereas patterned line with 2×10^{17} ions cm^{-2} (strong localization) show a

significant intensity of TO_4 mode indicating the structural changes in STO at this dose. The highest intensity of the TO_4 mode is observed for the 6×10^{17} ions cm^{-2} doses, which is found to be electrically insulating. Raman imaging thus serves as an indirect mapping of the interface conductivity of the ion-beam patterned LAO/STO system.

To show the patterning capability for device applications, the LAO/STO sample was covered by a stencil mask which is thick enough to stop the ion beam and ion irradiation was performed with the optimized parameters (fluence of 6×10^{17} ions cm^{-2} for 2 MeV protons) to create spatially selected regions exhibiting an insulating state at the interface 2DEG. Figure 8.8a shows a scanning electron microscopy (SEM) image of the patterned LAO/STO sample using a metal stencil mask (made from 0.5 mm thick brass) with a Hall bar geometry (channel width ~150 μm) after 2 MeV proton irradiation. As shown in figure 8.8a, the Hall bar structure has been transferred to the sample with the expected dimensions. Significantly, the SEM image shows the contrast between the irradiated and as-deposited sections. The contrast for the secondary electrons at the conducting (as-deposited) and insulating (irradiated) regimes is due to the difference in the number of secondary electrons reaching the Everhart-Thornley detector used in the SEM. We have also explored low energy helium ion irradiations (500 keV) to create localization and insulating state in conducting LAO/STO interfaces as discussed earlier. An insulating state is found to be created at a fluence of 1×10^{16} ions cm^{-2} and strong localization at 1×10^{15} ions cm^{-2} in the case of helium ions. A pattern was formed with a gold mask for helium ion irradiation and is shown in figure 8.8b. Here, the 5 μm conducting regions (the bright contrast) which are clearly visible in SEM micrographs demonstrate the capability to pattern the interface down to lower dimensions. This demonstrates the ability to pattern the LAO/STO interfaces using low *Z*-ions without any intermediate deposition or etching techniques that were previously employed.

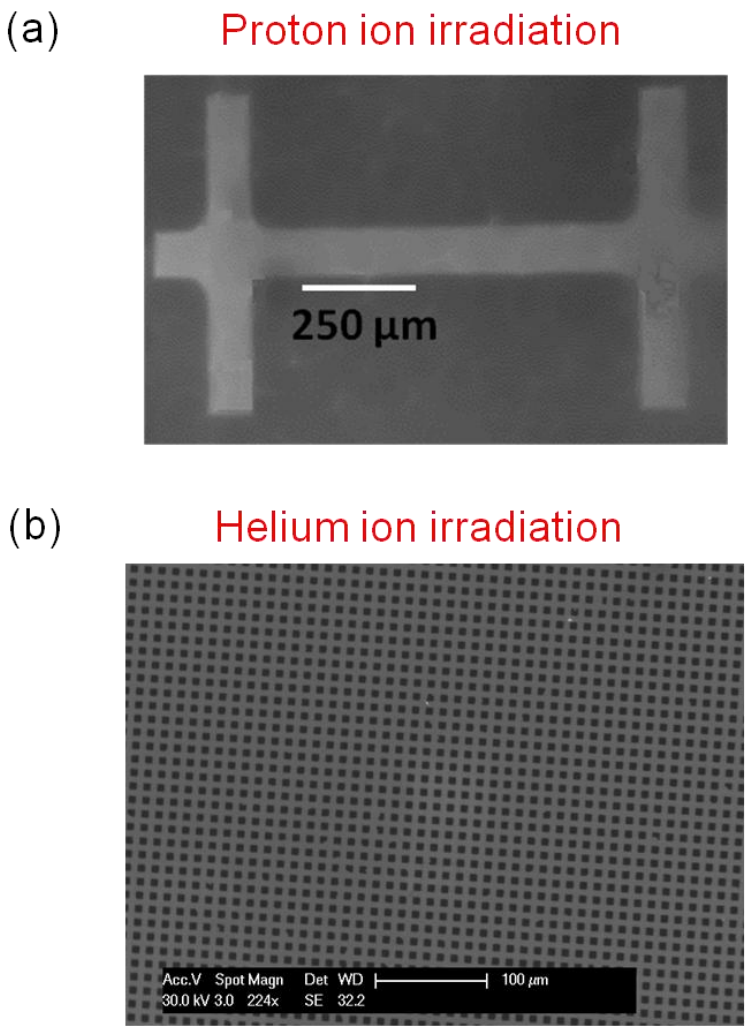

Fugure 8.8: (a) Scanning electron microscopy (SEM) image of the patterned LAO/STO sample: (a) using a 2 MeV proton fluence of 6×10^{17} ions cm^{-2} with a mask of Hall bar geometry (in this case proton beam (6×10^{17} ions cm^{-2}) was irradiated on to the sample using a tensile metal mask; the irradiated portion locally become insulating allows patterning the structure). (b) 500 keV helium ions at a fluence of 1×10^{16} ions cm^{-2} with a gold mask of size 5 µm.

8.7. Summary

In this chapter, it is demonstrated that conductivity of the 2DEG at the LAO/STO can be tuned by the proton beam irradiation. The creation of insulating ground state in 2DEG locally at higher ion fluence as shown here is of important for the device applications. The real advantage of this process is that one can pattern the structures of LAO/STO interfaces locally by employing focussed ion beam writing. It is advantageous to use protons considering the difficulties to structure oxide heterostructures especially involving STO with large *Z* ion beam irradiations such as Ar^+ beam where it has been shown to induce the conductivity in STO by producing large amount of oxygen vacancies which is undesired to STO based two-dimensional electron gas systems. The novel way to avoid this possibility to use low *Z*-element ion irradiations (proton, helium) as demonstrated here may open up new way to create structuring of fascinating interface systems whose properties sensitive to the crystal structure. With the development of helium ion microscope with focused ion beams having spatial resolutions of sub 0.5 nm, direct patterning of fine conducting lines may be possible on the nm scale. The correlation between lattice structure and electronic properties is found to be key to manipulate the properties in these oxide interfaces and may applicable to other oxide systems whose properties are sensitive to the meteal-oxygen bonds.

References

[1] C. W. Schneider, S. Thiel, G. Hammerl, C. Richter, and J. Mannhart, "Microlithography of electron gases formed at interfaces in oxide heterostructures," *Applied Physics Letters*, 89, 122101 (2006).

[2] D. Stornaiuolo, S. Gariglio, N. J. G. Couto, A. Fête, A. D. Caviglia, G. Seyfarth, D. Jaccard, A. F. Morpurgo, and J.-M. Triscone, "In-planeelectronic confinement in superconducting $LaAlO_3/SrTiO_3$ nanostructures," *Applied Physics Letters*, 101, 222601 (2012).

[3] N. Banerjee, M. Huijben, G. Koster, G. Rijnders, "Direct patterning of functional interfaces in oxide heterostructures," *Applied Physics Letters*, 100, 041601 (2012).

[4] C. Cen, S. Thiel, G. Hammerl, C. W. Schneider, K. E. Andersen, C. S. Hellberg, J. Mannhart, and J. Levy, "Nanoscale control of an interfacial metal–insulator transition at room temperature," *Nature Materials*, 7, 298-302 (2008).

[5] D. Kan, T. Terashima, R. Kanda, A. Masuno, K. Tanaka, S. Chu, H. Kan, A. Ishizumi, Y. Kanemitsu, Y. Shimakawa and M. Takano, *Nature Materials*, 4, 816-819 (2005).

[6] N. F. Mott and L. Friedman, "Metal-insulator transitions in VO_2, Ti_2O_3 and $Ti_{2-x}V_xO_3$," *Philosophical Magazine*, 30, 389 (1974).

[7] M. L. Medarde, "Structural, magnetic and electronic properties of $RNiO_3$ perovskites (R = rare earth)," *Journal of Physics: Condensed Matter*, 9, 1679 (1997).

[8] F. Schoofs, M. A. Carpenter, M. E. Vickers, M. Egilmez, T. Fix, J. E. Kleibeuker, J. L. MacManus-Driscoll, M. G. Blamire, Carrier density modulation by structural distortions at modified $LaAlO_3/SrTiO_3$ interfaces. *J. Phys. Condens. Matter*, 25, 175005 (2013).

[9] C. Bell, S. Harashima, Y. Hikita, H. Y. Hwang, "Thickness dependence of the mobility at the $LaAlO_3/SrTiO_3$ interface". *Apllied Physics Letters*, 94, 222111 (2009).

[10] A. Brinkman, M. Huijben, M. Van Zalk, J. Huijben, U. Zeitler, J. C. Maan, W. G. Van Der Wiel, G. Rijnders, D. H. A. Blank, and H. Hilgenkamp, "Magnetic effects at the interface between non magnetic oxides," *Nature Materials*, 6, 493-496 (2007).

[11] M. Salluzzo, J. C. Cezar, N. B. Brookes, V. Bisogni, G. M. De Luca, C. Richter, S. Thiel, J. Mannhart, M. Huijben, A. Brinkman *et al*. "Orbital Reconstruction and the Two-Dimensional Electron Gas at the $LaAlO_3/SrTiO_3$ Interface". *Phys. Rev. Lett.* 102, 166804 (2009).

[12] H. W. Jang, D. A. Felker, C. W. Bark, Y. Wang, M. K. Niranjan, C. T. Nelson, Y. Zhang, D. Su, C. M. Folkman, S. H. Baek, *et al*. "Metallic and insulating oxide interfaces controlled by electronic correlations". *Science* 331, 886 (2011).

[13] R. A. Cowley, "Lattice dynamics and phase transitions of strontium titanate," *Physical Review*, 134, A981-A997 (1964).

[14] W. G. Nilsen, and J. G. Skinner, "Raman spectrum of strontium titanate," *The Journal of Chemical Physics*, 48, 2240-2248 (1968).

[15] A. Tenne. Dmitri, "Raman spectroscopy of ferroelectric thin films and superlattices," *Journal of American Ceramics Society*, 91, 1820–1834 (2008).

[16] Yu. I. Yuzyuk, "Raman scattering spectra of ceramics, films, and superlattices of ferroelectric perovskites: A Review," *Physical Solid State.* 1026-1059 (2012).

[17] A. A. Sirenko, I. A. Akimov, J. R. Fox, A. M. Clark, H. Li, W. Si, and X. X. Xi, "Observation of the first-order Raman Scattering in $SrTiO_3$ thin films," *Physical Review Letters*, 82, 4500 (1999).

[18] B. Sarbajit, Dae. -In. Kim, R. Richard Robinson, P. H. Irving, Y. Mao, S. Wong, "Observation of fano asymmetry in Raman spectra of $SrTiO_3$ and

$Ca_xSr_{1-x}TiO_3$ perovskite nanocubes," *Applied Physics Letters*, 89, 223130 (2006).

[19] X. W. Wu, D. J. Wu, and X. J. Liu, "Negative pressure effects in $SrTiO_3$ nanoparticles investigated by Raman spectroscopy," *Soild State Communications*, 145, 255-258 (2008).

[20] P. A. Fleury, and J. M. Worlock, "Electric-field-induced Raman scattering in $SrTiO_3$ and $KTaO_3$," *Physical Review*, 174, 613-623 (1968).

Chapter 9

Conclusion and scope of future work

9.1 Conclusion

9.1.1 Magnetic interactions

In this thesis work the nature of magnetic interactions at the LAO/STO system were investigated through the AMR and PHE measurements. A fourfold oscillation behavior in the AMR is observed for the confined 2DEG, and a twofold oscillation observed for the 3D case. The origin of the fourfold oscillation primarily arising from magnetic interactions of itinerant electrons with localized magnetic moments coupled to the crystal symmetry via spin-orbit interaction. The observation of this behavior only for the confined 2DEG case infers that the magnetic interactions are predominant at the interface. The observed PHE further signifies that the predominant in-plane component of the magnetization in the system supports the previous observations. The role of spin-orbit interaction is verified by the tunability of magnetic interactions at the interface. The AMR and PHE measurements are very useful as a probe for the magnetic interactions in low dimensional systems.

9.1.2 Strain and correlation effects at polar/non-polar oxide interfaces

It is shown that the new combinations of various polar/non-polar oxides interfaces namely, $NdAlO_3$/ $SrTiO_3$, $PrAlO_3$/$SrTiO_3$ and $NdGaO_3$/ $SrTiO_3$ can also support the 2DEG at the interface. This study offered new interfaces to further investigate and tune the properties at these polar/non-polar oxide interfaces. A detailed transport analysis revealed that the properties of the 2DEG can be influenced by the polar over layers. This study inferred that the combined effects of interface strain and electron correlations offered by polar layers can play a crucial role at these oxide interfaces. The lattice-mismatch of various polar layers with STO can induce considerable octahedral distortions in STO. Even though naive thinking is

that the bulk substrates expected to induce the strain in over layers, however this study shows that at the interface the substrate layers is also influenced by the over layers to an extent that can manipulate the interface physics and properties as the case here. The observations such as rare earth (RE) cation dependence of carrier density, lattice mismatch effects on mobility offered by polar layers may provide an opportunity to tune the properties at selected polar/non-polar oxide interfaces. Further, the observed thickness dependence of metal-insulator transition for the $NdAlO_3/SrTiO_3$ interfaces suggest that polar discontinuity may possibly be the prime origin of conductivity at these polar/non-polar interfaces as well. The thickness dependence of localization effects of 2DEG are observed at the $NdAlO_3/SrTiO_3$ interfaces. In the strong localized regime the transport is governed by variable range hopping. These results emphasize the dominant role of over layer thickness in controlling the transport properties of 2DEG at these interfaces through the interface strain effects. Moreover, the study presented in this report can help in distinguishing localization from other mechanism which is very important in understanding the physics of electron transports in two dimensional oxide systems.

9.1.3 Anisotropic conductivity at (110) interfaces

The importance of the unexpected conductivity demonstrated at (110) interfaces is better brought into context with what has been learnt so far with the (100) interfaces. The 2DEG at the $LaAlO_3/SrTiO_3$ (100) interfaces has been studied under a variety of deposition conditions, layer thicknesses and externally applied fields. In most of these experiments the 2DEG was presumed to be the result of a direct manipulation of electrostatic potential at the interface in order to promote electrons to the conduction band of STO, which requires energy of the order of 3.2 eV. Our experiments and DFT calculations using (110) substrates show that the polarization catastrophe model may still be valid for crystalline LAO/STO interfaces provided the interface is viewed appropriately in (110) case (buckled interface). The real attraction of these LAO/STO (110) interfaces is that they offer

a new physical parameter which is crystalline anisotropy. The demonstrated anisotropy in mobility is very significant for the anisotropic devices at nano-scale.

9.1.4 Tuning the interface conductivity with ion beam irradiation

In this study it is shown that properties of the 2DEG at the LAO/STO can be tuned by the proton beam irradiation technique. The creation of insulating ground state in 2DEG locally as shown here is of important for the device applications. The real advantage of this technique is that one can pattern the structures of LAO/STO interfaces locally by employing focussed ion beam writing. Further, considering the difficulties in patterning of oxide heterostructures especially involving STO with heavy ion beam irradiations such as Ar^{+} beam where it has been shown to induce the conductivity in STO by producing large amount of oxygen vacancies which is undesired to STO based 2-dimensional electron gas system. The novel way to avoid this is to use low *Z*-element ion irradiations as demonstrated may open up new way to create structuring of fascinating interface systems whose properties sensitive to the crystal structure. The correlation between the lattice structure and electronic properties is found to be key to manipulate the properties in these oxide interfaces and may applicable to other oxide systems also whose properties are sensitive to the meteal-oxygen bonds. The patterning ability of the 2DEG with direct ion beam exposure without using any intermediate lithography processing steps as shown here is of technological importance.

9.1.5 Nature of spin-orbit interaction

The observation of quasi-two dimensional electrical conductivity at the $LaAlO_3/SrTiO_3$ (110) interface has generated much interest due to its possible potential in crystallography dictated low dimensional devices. Our angle dependant magneto-conductance results clearly show that there two contributions to the SOI, one originating from the normal component of the conduction electron spin and other from the Rashba effect arising from in-plane spin components. Here we suggest that the interface exhibits a strong anisotropic type z-component

SOI with respect to the crystallography. The anisotropy is understood to arise from the difference in the potentials associated with Ti t_{2g} orbitals along [001] and $[1\bar{1}0]$ directions. Both z-component SOI and Rashba SOI is gate tunable which is technologically very promising. Above all we have shown here a possible route to tune the interface SOI by varying the potential gradient arising from atomic arrangements at these anisotropic interfaces.

9.2 Scope of future work

9.2.1 Role of crystallography on orbital reconstructions and magnetism

The demonstrated strong magnetic interactions at the interface with respect to carrier confinement and electric fields are very important for the implementaiton of spintronic based concepts to the LAO/STO interfaces. The present study shows that these properties are very sensitive to the dimensionality and growth condition of the interfaces is very crucial to realize these magnetic interactions. The present study can be further explored with respect to the crystallography. Based on recent observation of 2DEG at other oriented interfaces (including our study of 2DEG at (110)-oriented interfaces), theroritical reports further suggested that magnetic ordering could depend on interface orientation where the orbital hybridizations play a crucial role. One best way to cross check these predictions is by performing these anisotropic measurements on various oriented interfaces such as along (110) and (111). The comparision study may give the information about such orbital hybridization picture at these interfaces.

9.2.2 Exploring the 2DEG properties at anisotropic surfaces

In this thesis work it is further demonstrated that the 2DEG show highly anisotropic nature with respect to the crystallographic directions. The presence of linear and zig-zag Ti-O-Ti chains along two directions opens up new possibilities for nanoscale quantum phenomena. For example, the anisotropy can be further explored by nano-structuring the 2DEG along the anisotropic crystallographic directions with techniques such as conducting atomic force microscopy (AFM)

charge writing which is already shown to create new properties. Further, investigation of the anisotropy on other phenomena (magnetism, superconductivity) will be of interest which may lead to new physics and device applications. Further, given the fact that the spin-orbit interactions can arise from the symmetry breaking near the interfaces and these in-plane anisotropic interfaces readily offer symmetry breaking within the plane of interface which would further attract a lot of interest to explore the electric field effects on these anisotropic surfaces. In this thesis work we have shown the signature of such anisotropic nature of spin-orbit interactions. These experimental observations can be further explored through theoretical understanding of the spin-orbit interaction concept. In complex oxides, spin as well as orbital degrees of freedom are very sensitive to the external stimuli; therefore one needs further investigation of spin-orbit interactions. Further analysis of spin-orbit interactions with respect to the crystallography is of importance.

9.2.3 Towards single step nano-structuring of interfaces with ion beams

Using an ion beam (proton/helium), a single-step structuring capability of LAO/STO interfaces down to 5 μm using a hard mask.exposure technique has been demonstrated. However focussing of these ion beams, utility of hard masks with lateral dimentions limits the structuring. This can be overcome by using the newly developed focused ion beam microscopes for example helium ion microscope which has a capability of focussing the energetic ions beams down to nanometer level. As a future direction these interfaces can be tested for the patterning with the helium ion microscope. Further, tailoring interface conductivity locally by tuning the interface defect chemistry is a novelty of this work. This ion beam exposure technique can be explored on other complex oxides that are sensitive to the metal-oxygen bonds. For example rare earth nickels oxides and vanadium oxide systems, whose properties are very sensitive to the chemical bonds. The possible manipulation of local structure in these materials may allow tuning the material properties and may allow patterning them also.